



Principles of Lipschitz continuity in neural networks

by

Róisín Luo

**A thesis presented in fulfillment of the requirements for the degree of
Doctor of Philosophy**

at

Ollscoil na Gaillimhe
University of Galway
Ireland

and

Taighde Éireann – Research Ireland
Irish National Centre for Research Training in AI (CRT-AI)

Doctoral Supervisors: Dr. Colm O’Riordan
Dr. James McDermott

Scoil na Ríomheolaíochta
School of Computer Science

September, 2025

Internal Examiner: Prof. Niall Madden

School of Mathematical and Statistical Sciences

University of Galway, Ireland

External Examiner: Dist. Prof. Padhraic Smyth

Hasso Plattner Endowed Chair in Artificial Intelligence

Department of Computer Science (Vice-Chair)

Department of Statistics

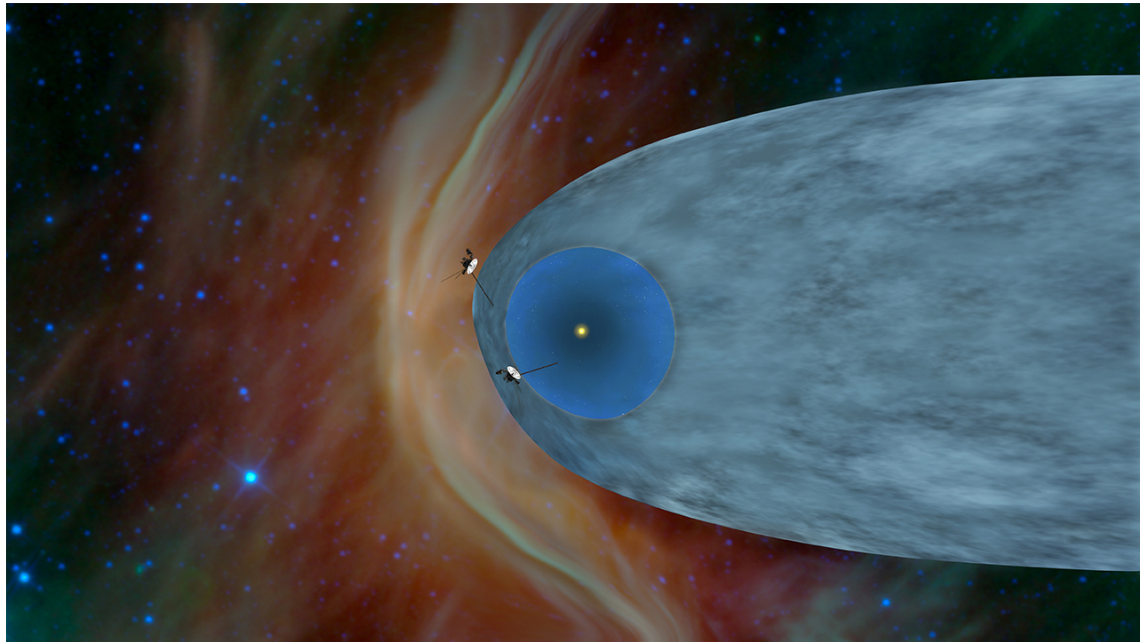
School of Information and Computer Sciences

University of California, Irvine

Cite as:

Róisín Luo. Principles of Lipschitz continuity in neural networks. Doctoral Thesis, Research Ireland – Centre for Research Training in Artificial Intelligence (CRT-AI), University of Galway, Ireland, September, 2025.

To my beloved grandparents.



Voyagers: Edge of the Bubble (NASA/JPL-Caltech)¹. Two tiny spacecraft — the Voyagers — manifest our spirit of exploration to an extraordinary level, a spirit that defines us as human beings. They have been sailing outward into vast interstellar space, reaching the frontier of our solar system, where the star winds meet the solar winds from our world, forming a vast bubble. Within this bubble lies every story, every life, every dream we have ever known — yet the Voyagers press onward, carrying our boldness and wonder into the vast, eternal, and spectacular sea between the stars, destined for an eternal journey, a testament to our instinct to go beyond the horizon where no human has gone before.

I am only stardust — learning to think, to chase dreams.

¹ Image use follows the *NASA Images and Media Usage Guidelines*.

“Nunquam praescriptos transibunt sidera fines
— Nothing exceeds the limits of the stars.”

Jules Henri Poincaré, 1890

RESEARCH FUNDING

This Ph.D. training program is a part of the Centre for Research Training in Artificial Intelligence (**CRT-AI**), funded by **Taighde Éireann – Research Ireland** under Grant Number 18/CRT/6223.

ABSTRACT

Deep learning has achieved remarkable success across a wide range of domains, significantly expanding the frontiers of what is achievable in artificial intelligence. Yet, despite these advances, critical challenges remain — most notably, ensuring **robustness** to small input perturbations and **generalization** to out-of-distribution data. These critical challenges underscore the need to understand the underlying fundamental principles that govern robustness and generalization. This understanding is indispensable for establishing deep learning systems that are: **reliable** — performing consistently under expected conditions on in-distribution data; **resilient** — capable of recovering from unexpected conditions such as noise or adversarial attacks; and **trustworthy** — behaving transparently, ethically, in alignment with intended use, and technically robust, particularly in safety-critical applications.

Among the theoretical tools available, **Lipschitz continuity** plays a pivotal role in governing the fundamental properties of neural networks related to robustness and generalization. It quantifies the worst-case sensitivity of network's outputs to small input perturbations. While its importance is widely acknowledged, prior research has predominantly focused on empirical regularization approaches based on Lipschitz constraints, leaving the underlying principles less explored. This thesis seeks to advance a principled understanding of the **principles of Lipschitz continuity in neural networks** within the paradigm of machine learning, examined from **two complementary perspectives**: an **internal** perspective — focusing on the temporal evolution of Lipschitz continuity in neural networks during training (*i.e.*, **training dynamics**); and an **external** perspective — investigating how Lipschitz continuity modulates the behavior of neural networks with respect to features in the input data, particularly its role in governing frequency signal propagation (*i.e.*, **modulation of frequency signal propagation**).

Guided by these perspectives, the thesis formulates three primary research questions: **(RQ1) State of Knowledge** — what is the state of knowledge of Lipschitz continuity in neural networks? **(RQ2) Training Dynamics** — how does Lipschitz continuity in neural networks evolve during the training process? **(RQ3) Modulation of Frequency Signal Propagation** — how does Lipschitz continuity modulate frequency signal propagation in neural networks?

CONTENTS

1	INTRODUCTION	1
1.1	Research questions	4
1.2	Thesis Presentation Format	5
1.3	Content Organization	6
1.4	Contributions	9
2	LITERATURE REVIEW	11
	Abstract	11
2.1	Introduction	12
2.1.1	Scope	13
2.1.2	Contributions	14
2.2	Theoretical Foundations	15
2.2.1	Preliminaries	15
2.2.2	1-Lipschitz Orthogonal Matrix	16
2.2.2.1	Matrix Orthogonalization	17
2.2.3	Functional Inequalities	19
2.2.4	Sub-Differential Convex Functions	20
2.2.5	Lipschitz Continuity of Activation Functions	21
2.2.6	Lipschitz Continuity of Dot-Product Self-Attention	23
2.2.6.1	Locally Lipschitz Continuous	24
2.2.6.2	Globally Non-Lipschitz Continuous	25
2.2.7	Lipschitz Continuity of Neural Networks	26
2.2.7.1	Lipschitz Continuity for a Directed Acyclic Graph (DAG)	28
2.2.7.2	Lipschitz Constant of Non-Biconnected DAG	31
2.2.7.3	Lipschitz Constant of Residual Network	32
2.2.8	Complexity-Theoretic Generalization Bound	33
2.2.8.1	Rademacher Complexity and its Bounds	34
2.2.9	Training Dynamics of Lipschitz Continuity	36
2.3	Estimation Methods	39
2.3.1	Power Iteration for Single Linear Unit	39
2.3.2	Extreme Value Theory	40
2.3.3	Coordinate-Wise Gradient	42
2.3.4	Spectral Alignment	44
2.3.5	Convex Optimization Relaxation	45
2.3.6	Integer Programming for ReLU Networks	46
2.4	Regularization Approaches	48

2.4.1	Weight Regularization	49
2.4.1.1	Spectral-Norm Regularization	49
2.4.1.2	Weight Clipping	49
2.4.1.3	Orthogonal Weight	50
2.4.2	Gradient Regularization	50
2.4.3	Activation Regularization	51
2.4.3.1	Group-Sorting Activation	51
2.4.3.2	Contraction Activation and Invertible Residual Map	53
2.4.4	Class-Margin Regularization	55
2.4.5	Architectural Regularization	56
2.4.5.1	Orthogonalizing Convolution	56
2.4.5.2	Orthogonality with Lie Unitary Group	58
2.4.5.3	Lipschitz Continuous Transformer	60
2.4.5.4	Jacobian Norm Minimization	62
2.5	Certifiable Robustness	65
2.5.1	Formal Robustness Guarantees	65
2.5.2	Certifiable Robustness via Global Lipschitz Bound	68
2.5.3	Certifiable Robustness via Local Lipschitz Bound	69
2.5.4	Certifiable Robustness in Language Models	69
2.6	Conclusions	70
2.A	Appendix	71
2.B	Proofs: Lipschitz Constants of Activation Functions	71
2.B.1	Proof: Lipschitz Constant of Sigmoid	71
2.B.2	Proof: Lipschitz Constant of Tanh	72
2.B.3	Proof: Lipschitz Constant of Softplus	74
2.B.4	Proof: Lipschitz Constant of Swish	75
2.B.5	Proof: Lipschitz constant of GELU	76
2.B.6	Proof: Lipschitz constant of Softmax	78
3	OPERATOR-THEORETIC PERTURBATION ANALYSIS	81
	Abstract	81
3.1	Introduction	82
3.1.1	Perturbation Theory	83
3.1.2	Schematic Overview	85
3.1.3	Contributions	87
3.2	Fréchet Derivative and Layout Convention	87
3.2.1	Matrix and Spectral Decomposition	88
3.2.2	Differentiability Condition	88
3.2.3	Matrix Fréchet Derivative as Multilinear Operator	89

3.2.4	Representation Convention for Matrix-Valued Functionals	90
3.2.4.1	Representation Convention for Jacobian of Matrix-Valued Functional	91
3.2.4.2	Representation Convention for Hessian of Matrix-Valued Functional	92
3.3	Refined Asymptotic Eigenvalue Expansion	94
3.4	Infinitesimal Higher-Order Spectral Variations	104
3.5	Special Case ($n = 1$): Closed-Form Singular-Value Jacobian	108
3.6	Special Case ($n = 2$): Closed-Form Singular-Value Hessian	110
3.7	Numerical Experiments	122
3.8	Conclusion	126
4	STOCHASTIC DYNAMIC ANALYSIS OF LIPSCHITZ CONTINUITY	127
	Abstract	128
4.1	Introduction	129
4.1.1	Contributions	132
4.2	Preliminaries	132
4.3	Vectorized SDE for Continuous-Time SGD	134
4.4	Estimating batch gradient noise	136
4.4.1	Unbiased batch gradient noise estimator	137
4.4.2	Estimating variance and covariance	138
4.4.3	Computing square root	139
4.5	Temporal evolution of Lipschitz upper bound	140
4.6	Theoretical analysis	142
4.6.1	First- and second-order operator-norm derivatives	142
4.6.2	Layer-specific dynamics	145
4.6.3	Network-specific dynamics	147
4.6.4	Statistical characterization	149
4.7	Framework validation	151
4.8	Theoretical implications	151
4.8.1	Key factors driving dynamics	153
4.8.2	Parameter initialization	153
4.8.3	Unbounded growth near-convergence	154
4.8.4	Noisy gradient regularization	155
4.8.5	Uniform label corruption	156
4.8.6	Batch size	157
4.8.7	Mini-batch sampling trajectory	159
4.9	Limitations and future work	159
4.10	Conclusions	159

4.A Appendix	161
4.B Network configuration	161
4.C Regularization configuration	161
4.D Full validation experiment	162
5 FOURIER ANALYSIS OF LIPSCHITZ CONTINUITY	165
Abstract	165
5.1 Introduction	166
5.2 Preliminaries	167
5.3 Fourier Analysis	170
5.3.1 Fourier Representation of Lipschitz Continuity Bound	170
5.3.1.1 Experiment of Directional Frequency Response	172
5.3.1.2 Numerical Validation – Synthesized Function	173
5.3.1.3 Numerical Validation – Well-Defined Example	174
5.3.2 Small Frequency Perturbation in Input Spaces	178
5.3.2.1 Numerical Validation – Well-Defined Example	179
5.3.3 Variational Mutual Information Gap in Image Classifiers	182
5.4 Empirical Study	183
5.4.1 Role of High-Frequency Components	183
5.4.2 Flatness of Loss Landscape	186
5.5 Conclusions	186
6 INTERPRETING GLOBAL ROBUSTNESS	187
Abstract	187
6.1 Introduction	188
6.2 Notations	191
6.3 Method	193
6.3.1 Spectral coalitional game	194
6.3.2 Spectral coalition filtering	195
6.3.3 Characteristic function design	197
6.3.4 Spectral robustness score (SRS)	198
6.4 Experiments	200
6.4.1 Correlation to robustness metrics	200
6.4.2 Studying architectural robustness	203
6.4.3 Interpreting how supervision noise levels affect model robustness .	204
6.5 Related work	205
6.6 Limitations	208
6.7 Conclusions	208
6.A Appendix	209
6.B Fairness division axioms	209

6.B.1	Spectral signal-to-noise ratio (SNR)	210
6.B.2	Absence assignment scheme	211
6.B.3	Proof for Spectral Coalition Information Identity Theorem	213
6.C	Information quantity relationship in spectral coalitions	214
6.C.1	Partitioning spectrum with ℓ_∞ ball over ℓ_2 ball	215
6.C.2	Normalizing summarized SIDs	216
6.C.3	How many samples are sufficient?	217
7	FUTURE WORK	219
7.1	Introduction	219
7.2	Spectral-gap regularization	219
7.3	Spectrum-gradient alignment	220
7.4	Conclusions	220
8	CONCLUSIONS	221
8.1	Research Summary	222
8.2	Closing Remarks	224
	BIBLIOGRAPHY	225

LIST OF FIGURES

Figure 1.1	Principles of Lipschitz Continuity Manifest in Paradigm of Machine Learning	2
Figure 1.2	Thesis Thematic Structure	6
Figure 2.1	Example of Feedforward DAG Network	28
Figure 2.2	Non-Biconnected DAG Network	31
Figure 2.3	Structure of Residual Module	33
Figure 3.1	Theoretical Framework for Infinitesimal Spectral Variations	84
Figure 3.2	Numerical Experiments for Singular-Value Jacobian	123
Figure 3.3	Numerical Experiments for Singular-Value Hessian	124
Figure 3.4	Errors for Singular-Value Hessian	125
Figure 4.1	Optimization-Induced Stochastic Dynamics of Lipschitz Continuity	130
Figure 4.2	Numerical Validation of Our Mathematical Framework in Characterizing Optimization-Induced Stochastic Dynamics of Lipschitz Continuity	131
Figure 4.3	Stochastic Dynamics of Lipschitz Continuity Near Convergence .	143
Figure 4.4	Predicted Effect of Trajectory in Mini-Batch Sampling on Lipschitz Continuity	152
Figure 4.5	Predicted Effect of Batch Size on Variance of Lipschitz Continuity	152
Figure 4.6	Predicted Effect of Gradient Magnitude and Perturbation	152
Figure 4.7	Predicted Effect of Uniform Label Corruption	152
Figure 4.8	Full Numerical Validation of Our Mathematical Framework on CIFAR-10	163
Figure 5.1	Directional Frequency Analysis of Three-Layer MLP	172
Figure 5.2	Spectral Bound of Lipschitz Continuity with Synthesized Multi-Sine Functions	174
Figure 5.3	Spectral Lipschitz Continuity Representation Bounds Frequency-Band Perturbation	177
Figure 5.4	Low- and High-Frequency Signals Induce Low- and High Gradient Norms	180
Figure 5.5	Empirical and Theoretical Lipschitz Constants with respect to Frequency Signals in Training Data	184
Figure 5.6	Frequency Signals in Training Data Shape Loss Landscape Flatness	185

Figure 6.1	Power-Law-Like Energy Spectral Density Distribution of Natural Images Over Frequency	189
Figure 6.2	Spectral Signal-to-Noise (SNR) Characterization with respect to Corruptions and Adversarial Attacks	191
Figure 6.3	Frequency Signals Shape Robustness in Training	192
Figure 6.4	Framework of Applying Shapley Value Theory	194
Figure 6.5	Implementation Scheme of Spectral Coalition Filtering in Spectral Game	196
Figure 6.6	Examples of Spectral Coalitions	197
Figure 6.7	Spectral Importance Distributions of Trained Models and Un-Trained Models	199
Figure 6.8	Scalarized Spectral Robustness Scores Correlate with Mean Corruption Errors in Literature	200
Figure 6.9	Scalarized Spectral Robustness Scores Correlates with Mean Prediction Errors in Adversarial Attacks	201
Figure 6.10	Scalarized Spectral Robustness Scores Correlates with Mean Prediction Errors in Corruptions	202
Figure 6.11	Effects of Architectural Elements on Robustness	203
Figure 6.12	Effect of Label Noise on Robustness	205
Figure 6.13	Three Absence Assignment Strategies in Spectral Game	212
Figure 6.14	Information Quantity Relationship in Spectral Game	214
Figure 6.15	Two Spectral Band Partitioning Schemes in Spectral Game	215
Figure 6.16	Convergence of Relative Estimation Errors in Spectral Game	217

LIST OF TABLES

Table 2.1	Lipschitz constants of activation functions.	22
Table 4.1	ConvNet configuration. The layer marked as ‘(*)’ is configurable with respect to experimental needs. There are five parameterized layers (<i>i.e.</i> # 1, # 4, # 8, # 12 and # 15).	161
Table 4.2	MLP configuration. There are three parameterized layers (<i>i.e.</i> # 1, # 3, and # 5).	161
Table 4.3	Regularization configuration.	161
Table 5.1	MLP configuration used in the directional frequency response experiment.	173
Table 5.2	ConvNet configuration for the experiments exploring the connection between frequency signal propagation and Lipschitz continuity.	183

LIST OF THEOREMS

2.2.20	Theorem (Lipschitz Bound for DAG Network)	28
2.2.21	Theorem (Lipschitz Bound for Non-Biconnected DAG Network)	31
2.5.1	Theorem (Lipschitz Margin Robustness Radius in ℓ_2 -Normed Spaces) .	65
2.5.3	Theorem (Lipschitz Margin Robustness Radius in Conjugate-Normed Spaces)	67
3.1.1	Theorem (Matrix Singular Value Decomposition (Full Form))	85
3.1.2	Theorem (Spectrum of Jordan–Wielandt Embedding)	85
3.2.4	Theorem (Uniqueness of α -Times Fréchet Derivative (Yosida, 2012; Spivak, 2018))	90
3.3.2	Theorem (Kato’s Weighted Mean of Eigenvalue Expansions (Kato, 1995, Ch. II, §2.2))	94
3.3.3	Theorem (Refined Closed-Form Asymptotic Expansion of Simple Isolated Eigenvalue in Self-Adjoint Operator)	96
3.4.1	Theorem (Analytic Perturbation for Holomorphic Operators)	104
3.4.2	Theorem (Higher-Order Infinitesimal Spectral Variation)	104
4.6.5	Theorem (Layer-Specific Dynamics)	145
4.6.6	Theorem (Logarithmic Network-Specific Dynamics)	147
4.6.7	Theorem (Integral-Form Dynamics of Lipschitz Continuity)	149
4.6.8	Theorem (Statistics of Lipschitz Continuity)	149
5.3.1	Theorem (Spectral Bound of Lipschitz Continuity)	170
6.3.6	Theorem (Spectral coalition information identity)	198

LIST OF LEMMAS

2.2.5	Lemma (Lipschitz Constant Bounds Gradient Norm)	16
2.2.14	Lemma (Local Lipschitz Constant of Sub-Differential Function)	21
3.2.1	Lemma (Essential Matrix Identities)	88
3.5.1	Lemma (Closed-Form Singular-Value Jacobian)	108
3.6.1	Lemma (Closed-Form Singular-Value Hessian)	111
4.6.2	Lemma (Operator-Norm Jacobian)	144
4.6.3	Lemma (Operator-Norm Hessian (Róisín Luo et al., 2025c))	144
4.6.10	Lemma (Moment-Generating Function of $Z(t)$)	150
5.3.4	Lemma (Spectral-Band Perturbation Bound)	178

LIST OF PROPOSITIONS

2.2.8	Proposition (Lipschitz Constant of Semi-Orthogonal Matrix)	16
2.2.9	Proposition (Lipschitz Constant of Function Composition)	19
2.2.10	Proposition (Lipschitz Constant of Function Addition)	19
2.2.11	Proposition (Lipschitz Constant of Function Concatenation)	19
2.2.16	Proposition (Lipschitz Constant of a Linear Layer)	26
2.2.17	Proposition (Spectral-Norm via Singular Value Decomposition)	27
2.2.18	Proposition (Lipschitz Constant Upper Bound of Feedforward Neural Network)	27
4.4.1	Proposition (Unbiased Batch Gradient Noise Estimator)	137
4.4.2	Proposition (Diagonal and Off-Diagonal Elements of Batch Gradient Noise)	138
4.4.3	Proposition (Square Root Approximation of Covariance Matrix) . . .	139
4.5.1	Proposition (Lipschitz Continuity Bound in Feed-Forward Network) .	140
4.5.2	Proposition (Operator Norm of Linear Unit)	141
4.8.1	Proposition (Unbounded Growth Near-Convergence)	154
4.8.2	Proposition (Uncertainty Under Large Batch)	157

LIST OF DEFINITIONS

2.2.1	Definition (p-Norm in Finite-Dimensional Vector Spaces)	15
2.2.2	Definition (Globally K-Lipschitz Continuous)	15
2.2.3	Definition (Globally $K_{p \rightarrow q}$ -Lipschitz Continuous)	15
2.2.7	Definition (Skew-Hermitian & Skew-Symmetric Matrix)	16
2.2.12	Definition (Generalized Gradient)	20
2.2.13	Definition (Clarke Sub-Gradient)	20
2.2.15	Definition (Feedforward Network)	26
2.2.23	Definition (Generalization Gap)	33
2.2.24	Definition (Rademacher Complexity (Mohri et al., 2018, Definition 3.1, § 3))	34
3.2.3	Definition (α -Times Continuously Fréchet Differentiable Matrix Map)	89
3.3.1	Definition (Space of Bounded Linear Operators)	94
4.1.1	Definition (Globally K-Lipschitz Continuous (Yosida, 2012))	129
4.3.2	Definition (Vectorized SDE for Continuous-Time SGD)	135
4.5.3	Definition (Stochastic Dynamical System of Lipschitz Continuity Bound)	141
6.3.1	Definition (Spectral coalition filtering)	196
6.3.3	Definition (Spectral coalition filtering over set)	197
6.3.4	Definition (Characteristic function)	197
6.4.1	Definition (Mean prediction error)	200

DECLARATION

I, *Róisín Luo*, declare that this thesis, titled “*Principles of Lipschitz continuity in neural networks*”, is composed by myself, that the work contained herein is my own except where explicitly stated otherwise in the text, and that this work has not been submitted for any other degree or professional qualification.

Galway, September, 2025

Róisín Luo

LIST OF PUBLICATIONS

Articles Compiled in This Thesis

This thesis compiles and presents the following selected articles — published or under review as of the date of submission — into a **self-contained, modular, coherent, monograph-style** presentation format, all centered on the **principles of Lipschitz continuity in neural networks**:

I **Róisín Luo**, J. McDermott, and C. O’Riordan. **Lipschitz Continuity in Deep Learning: A Systematic Review of Theoretical Foundations, Estimation Methods, Regularization Approaches and Certifiable Robustness**. Manuscript is under review at Transactions on Machine Learning Research (TMLR), 2025b

II **Róisín Luo**, C. O’Riordan, and J. McDermott. **Higher-Order Singular-Value Derivatives of Real Rectangular Matrices**. *Journal of Mathematical Analysis and Applications (JMAA)*, page 130236, 2025c. ISSN 0022-247X. doi: 10.1016/j.jmaa.2025.130236. URL <https://doi.org/10.1016/j.jmaa.2025.130236>

III **Róisín Luo**, J. McDermott, C. Gagné, Q. Sun, and C. O’Riordan. **Optimization-Induced Dynamics of Lipschitz Continuity in Neural Networks**. Manuscript is under review at Journal of Machine Learning Research (JMLR), 2025a. URL <https://arxiv.org/abs/2506.18588>

IV **Róisín Luo**, J. McDermott, and C. O’Riordan. **Interpreting Global Perturbation Robustness of Image Models using Axiomatic Spectral Importance Decomposition**. *Transactions on Machine Learning Research (TMLR)*, 2024b. ISSN 2835-8856. URL <https://arxiv.org/abs/2408.01139>. Presented at The Thirteenth International Conference on Learning Representations (ICLR 2025), Singapore

Articles Not Compiled in This Thesis

Although the following published conference articles and the manuscript in preparation were produced during the Ph.D. training of the author, they are not included in this thesis due to their topics and the thesis's length constraints:

V **Róisín Luo**, A. Drimbarean, J. McDermott, and C. O'Riordan. **Reclaiming Residual Knowledge: A Novel Paradigm to Low-Bit Quantization**. In *The 35th British Machine Vision Conference, BMVC 2024, Glasgow, UK, November 25-28, 2024*. BMVA, 2024a. URL <https://arxiv.org/abs/2408.00923>

1

INTRODUCTION

Deep learning (Goodfellow et al., 2016) has achieved remarkable success across a diversity of domains, including computer vision (Krizhevsky et al., 2012; He et al., 2016; Dosovitskiy et al., 2021), natural language processing (Hochreiter and Schmidhuber, 1997; Vaswani et al., 2017; Radford et al., 2019; Devlin et al., 2019; Brown et al., 2020; OpenAI et al., 2024; DeepSeek-AI et al., 2025), and graph representation learning (Perozzi et al., 2014; Veličković et al., 2018; Xu et al., 2019a). These successes have largely expanded the frontiers of what is achievable in artificial intelligence, enabling powerful capabilities across a wide range of tasks, as well as modeling paradigms such as generative modeling (Hinton and Salakhutdinov, 2006; Goodfellow et al., 2014; Dinh et al., 2017; Ho et al., 2020; Song et al., 2021; Lipman et al., 2023).

Despite these remarkable advances, critical challenges persist, notably in ensuring **robustness** to small input perturbations and **generalization** to out-of-distribution data (Szegedy et al., 2014; Goodfellow et al., 2015; Hendrycks and Dietterich, 2019; Ilyas et al., 2019; Recht et al., 2019; Róisín Luo et al., 2024b). These critical challenges highlight the need to understand the underlying fundamental principles that govern **robustness** and **generalization**, and to establish deep learning systems that are **reliable** — performing consistently under expected conditions on in-distribution data (NIST, 2023), **resilient** — capable of recovering from unexpected conditions such as noise or adversarial attacks (NIST, 2023), and **trustworthy** — behaving transparently, ethically, in alignment with intended use, and technically robust (European Commission, 2019; European Parliament and Council, 2024) — in safety-critical applications.

The paradigm of machine learning (Goodfellow et al., 2016), illustrated in Figure 1.1, typically comprises the *data* $x \in \mathcal{X} \subseteq \mathbb{R}^m$, *supervision signal* $y \in \mathcal{Y}$, a *learned function* $f(x; \Theta)$ with output space $\tilde{\mathcal{Y}} \subseteq \mathbb{R}^n$:

$$f : \mathcal{X} \times \Theta \rightarrow \tilde{\mathcal{Y}}, \quad (1.1)$$

parameterized by:

$$\Theta := \{\Theta^{(1)}, \Theta^{(2)}, \dots\} \in \Theta \subseteq \mathbb{R}^p, \quad (1.2)$$

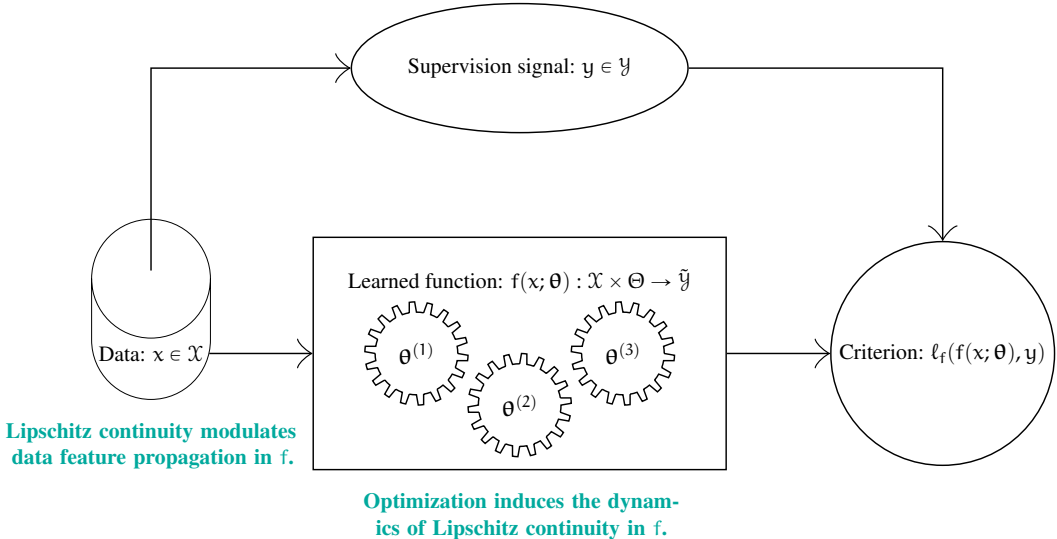


Figure 1.1: Principles of Lipschitz Continuity Manifest in Paradigm of Machine Learning.

In the paradigm of machine learning, we consider *data* $x \in \mathcal{X}$, *supervision signal* $y \in \mathcal{Y}$, a *learned function* $f : \mathcal{X} \times \Theta \rightarrow \tilde{\mathcal{Y}}$ — where $\tilde{\mathcal{Y}}$ is output space — parameterized by $\theta^{(\ell)} \in \mathbb{R}^{d_\ell}$ and $\Theta := \mathbb{R}^{d_1 \times d_2 \times \dots \times d_L}$, and a *criterion* $\ell_f : (f(x, \theta), y) \rightarrow \mathbb{R}$. The Lipschitz constant K_f of f in this paradigm is determined by factors such as the hypothesis class for f , learning algorithm, parameters θ , training data $(\mathcal{X}, \mathcal{Y})$, etc. It also modulates the behavior of f with respect to the input features. This thesis investigates the **principles of Lipschitz continuity** in this paradigm from a **complementary dichotomy of perspectives**: an **internal** perspective — focusing on the temporal evolution of Lipschitz continuity in neural networks during training; and an **external** perspective — examining how Lipschitz continuity modulates the behavior of f with respect to the features in input data, particularly its role in governing frequency signal propagation in neural networks.

and a *criterion*:

$$\ell_f : (f(x; \theta), y) \rightarrow \mathbb{R}. \quad (1.3)$$

Note that the *supervision signals* differ across learning paradigms, for example:

- (i) **Supervised Learning.** The *supervision signals* are explicitly provided as *labels* by the dataset;
- (ii) **Self-Supervised Learning.** The *supervision signals* are derived from inherent structure or priors in the data — for example, in contrastive learning, an augmented view of an image can serve as the label for the original image (Chen et al., 2020);
- (iii) **Reinforcement Learning.** The *supervision signals* are manifested as *reward signals* from the interactions with the environment, which are often noisy, sparse, and delayed (Sutton et al., 1998, Preface & § 1).

Among the theoretical tools available, **Lipschitz continuity** (Rudin, 1976, Theorem 9.19, § 9) plays a pivotal role in governing the fundamental properties of the function f in this paradigm related to robustness and generalization. The *Lipschitz constant* K_f of f , with respect to the ℓ_2 -norm, defined as:

$$K_f := \sup_{\forall u \neq v} \frac{\|f(u) - f(v)\|_2}{\|u - v\|_2}, \quad (1.4)$$

measures the worst-case sensitivity of the network to small input perturbations. Equivalently, it bounds the maximum rate of change of f with respect to its inputs in the ℓ_2 -norm (Rudin, 1976, Theorem 9.19, § 9):

$$K_f \geq \sup_x \|\nabla_x f(x)\|_2, \quad (1.5)$$

where $\nabla_x(\cdot)$ denotes a differential operator acting on (\cdot) with respect to x . A lower Lipschitz constant K_f ensures a smoother mapping f , enhancing the network's ability to generalize to unseen data. Moreover, Lipschitz continuity forms a theoretical foundation for **certifiable robustness** — where safety guarantees under bounded perturbations can be formally proven — in safety-critical applications.

While Lipschitz continuity is crucial in governing the fundamental properties of neural networks related to robustness and generalization, prior research has largely concentrated on empirical aspects, such as regularization techniques (Miyato et al., 2018; Arjovsky et al., 2017; Cisse et al., 2017; Anil et al., 2019), leaving the underlying principles less explored. This thesis is motivated by the absence of theoretical underpinnings of the principles of Lipschitz continuity in neural networks — a foundation that is critical for establishing reliable, resilient, and trustworthy deep learning systems. To address this gap, it seeks to advance a principled understanding of the **principles of Lipschitz continuity in neural networks** within the paradigm of machine learning, examined from a **complementary dichotomy of perspectives**:

an **internal** perspective — focusing on the temporal evolution of Lipschitz continuity in neural networks during training (*i.e.*, **Training Dynamics**);

an **external** perspective — investigating how Lipschitz continuity modulates the behavior of neural networks with respect to features in the input data, particularly its role in governing frequency signal propagation (*i.e.*, **Modulation of Frequency Signal Propagation**).

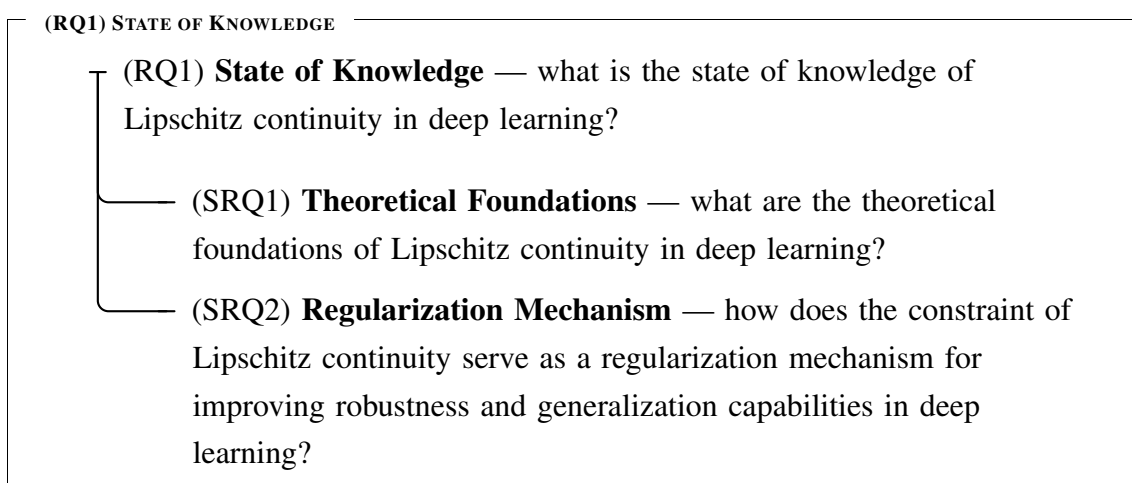
Together, these complementary perspectives form the basis of the primary research questions presented in Section 1.1 and underscore the principles under investigation within this thesis.

1.1 Research questions

This thesis is centered around an overarching inquiry from a complementary dichotomy of **internal** and **external** perspectives:

What are the principles of Lipschitz continuity in neural networks, from its temporal evolution during training (an internal perspective) to its modulation of frequency signal propagation (an external perspective)?

To support this central inquiry, it investigates three primary research questions (RQs) with a structured approach, each gives rise to a set of secondary research questions (SRQs), which are explored in one or two dedicated chapters.



(RQ2) TRAINING DYNAMICS — AN INTERNAL PERSPECTIVE

- (RQ2) **Training Dynamics** — how does Lipschitz continuity of neural networks evolve over time during training?
- (SRQ3) **Parameter Space Perturbation** — how do the spectral properties (*e.g.* singular values) of parameter matrices change in training? During training, the optimization process updates parameter matrices, thereby altering the spectral structures accordingly.
- (SRQ4) **Stochastic Dynamic Analysis of Lipschitz Continuity** — how does Lipschitz continuity evolve over time during training in neural networks?

(RQ3) MODULATION OF FREQUENCY SIGNAL PROPAGATION — AN EXTERNAL PERSPECTIVE

- (RQ3) **Modulation of Frequency Signal Propagation** — how does Lipschitz continuity modulate the frequency signal propagation in neural networks, and how does it help us for understanding the global robustness of image models?
- (SRQ5) **Fourier Analysis of Lipschitz Continuity** — how does Lipschitz continuity modulate frequency signal propagation in image models?
- (SRQ6) **Interpreting Global Robustness** — how can global robustness be explained through the lens of spectral bias in Lipschitz continuity?

1.2 Thesis Presentation Format

This thesis compiles and presents a selection of research articles — published or under review as of the date of submission — into a **self-contained, modular, coherent, monograph-style** presentation format, all centered on the principles of Lipschitz continuity in neural networks. The research was conducted cumulatively during the Ph.D. training. Portions of the chapter content, which address the research questions, are reused either verbatim or with minor modifications from the selected articles, in accordance with institutional guidelines and the policies of the relevant publishers. Each core chapter is presented in the style of a standalone journal article, including an **abstract, introduction**, and other standard components in journal articles. For consistency with the original publi-

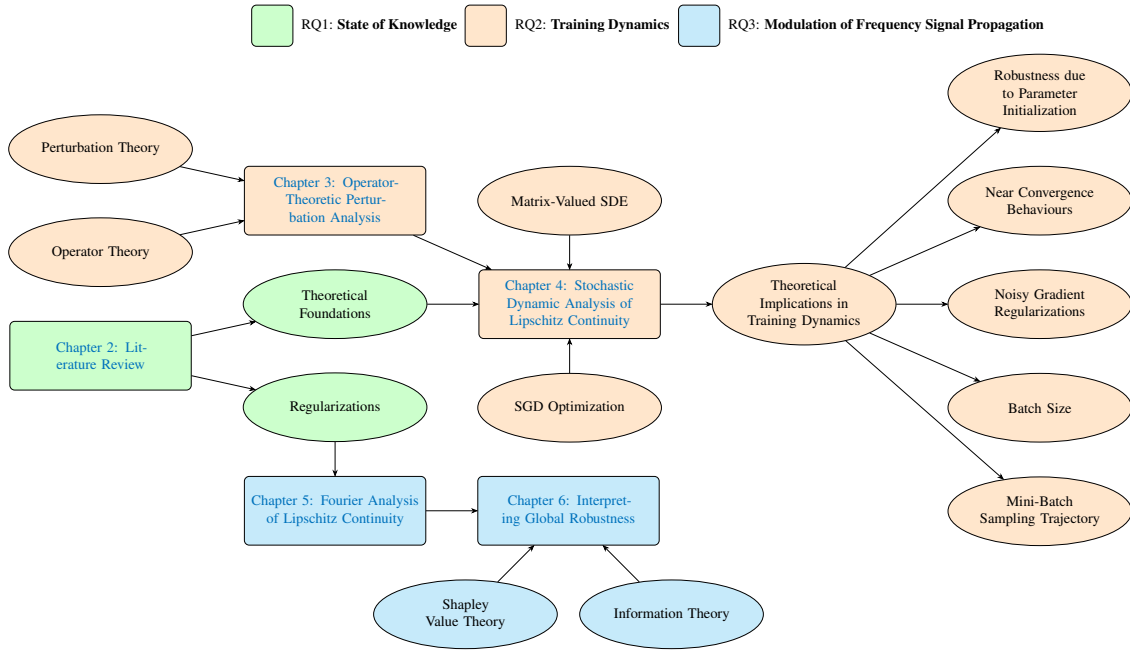


Figure 1.2: Thesis Thematic Structure. A high-level conceptual diagram outlining the thematic connections between chapters. This thesis investigates the principles of Lipschitz continuity in neural networks through a structured approach guided by three primary research questions. Each primary question gives rise to two secondary research questions and is addressed in one or two dedicated chapters.

cations, the term **paper** is used throughout to refer to the current chapter, and the literature review may include results from our research, either published or available as preprints. Permissions for reuses have been obtained from all co-authors in all articles.

1.3 Content Organization

The research questions collectively establish a cohesive thematic investigation into the principles of Lipschitz continuity in neural networks. Figure 1.2 illustrates how each question aligns with the core chapters and jointly guides the development of the overarching theoretical framework. The structure of the thesis is outlined below.

(RQ1) State of Knowledge. What is the state of knowledge of Lipschitz continuity in deep learning? This research question is addressed by surveying the landscape of Lipschitz continuity in deep learning, covering its theoretical foundations, estimation methods, regularization approaches, and role in certifiable robustness. This research question is addressed by surveying the landscape of Lipschitz continuity in deep learning, covering its

theoretical foundations, estimation methods, regularization approaches, and role in certifiable robustness.

(SRQ1) Theoretical Foundations ([Chapter 2: Literature Review](#)) — what are the theoretical foundations of Lipschitz continuity in deep learning? This is answered in [Chapter 2: Literature Review](#), which is based on an article:

- (i) [Róisín Luo](#), J. McDermott, and C. O’Riordan. **Lipschitz Continuity in Deep Learning: A Systematic Review of Theoretical Foundations, Estimation Methods, Regularization Approaches and Certifiable Robustness**. Manuscript is under review at *Transactions on Machine Learning Research (TMLR)*, 2025b .

(SRQ2) Regularization Mechanism ([Chapter 2: Literature Review](#)) — how does Lipschitz continuity serve as a regularization mechanism for improving robustness and generalization capabilities in deep learning? This is answered in [Chapter 2: Literature Review](#), which is based on an article:

- (i) [Róisín Luo](#), J. McDermott, and C. O’Riordan. **Lipschitz Continuity in Deep Learning: A Systematic Review of Theoretical Foundations, Estimation Methods, Regularization Approaches and Certifiable Robustness**. Manuscript is under review at *Transactions on Machine Learning Research (TMLR)*, 2025b .

(RQ2) Training Dynamics. How does Lipschitz continuity evolve over time during the training in neural networks? To the best of our knowledge, as of the date of submission, this constitutes the first theoretical framework to characterize the temporal evolution of Lipschitz continuity in neural networks leveraging perturbation theory ([Kato, 1995](#); [Róisín Luo et al., 2025c](#)) and a system of stochastic differential equations (SDEs).

(SRQ3) Parameter Space Perturbation ([Chapter 3: Operator-Theoretic Perturbation Analysis](#)) — how do the spectral properties (*i.e.* singular values) of parameter matrices change in training? During training, the optimization process updates parameter matrices, thereby altering the spectral structures accordingly. This is addressed in [Chapter 3: Operator-Theoretic Perturbation Analysis](#), which is based on an article:

- (ii) [Róisín Luo](#), C. O’Riordan, and J. McDermott. **Higher-Order Singular-Value Derivatives of Real Rectangular Matrices**. *Journal of Mathematical Analysis and Applications (JMAA)*, page 130236, 2025c. ISSN

0022-247X. doi: 10.1016/j.jmaa.2025.130236. URL <https://doi.org/10.1016/j.jmaa.2025.130236>.

(SRQ4) Stochastic Dynamic Analysis of Lipschitz Continuity ([Chapter 4: Stochastic Dynamic Analysis of Lipschitz Continuity](#)) — how does Lipschitz continuity evolve over time during training in neural networks? This is answered in [Chapter 4: Stochastic Dynamic Analysis of Lipschitz Continuity](#), which is based on an article:

- (iii) [Róisín Luo](#), J. McDermott, C. Gagné, Q. Sun, and C. O’Riordan. [Optimization-Induced Dynamics of Lipschitz Continuity in Neural Networks](#). Manuscript is under review at [Journal of Machine Learning Research \(JMLR\)](#), 2025a. URL <https://arxiv.org/abs/2506.18588>.

(RQ3) Modulation of Frequency Signal Propagation. How does Lipschitz continuity modulate the frequency signal propagation in neural networks, and how does it help us for understanding the global robustness of image models?

(SRQ5) Fourier Analysis of Lipschitz Continuity ([Chapter 5: Fourier Analysis of Lipschitz Continuity](#)) — how does Lipschitz continuity modulate frequency signal propagation in image models? This is answered in [Chapter 5: Fourier Analysis of Lipschitz Continuity](#).

(SRQ6) Interpreting Global Robustness ([Chapter 6: Interpreting Global Robustness](#)) — how can global robustness be explained through the lens of spectral bias in Lipschitz continuity? This is answered in [Chapter 6: Interpreting Global Robustness](#), which is based on an article:

- (iv) [Róisín Luo](#), J. McDermott, and C. O’Riordan. [Interpreting Global Perturbation Robustness of Image Models using Axiomatic Spectral Importance Decomposition](#). [Transactions on Machine Learning Research \(TMLR\)](#), 2024b. ISSN 2835-8856. URL <https://arxiv.org/abs/2408.01139>. Presented at [The Thirteenth International Conference on Learning Representations \(ICLR 2025\)](#), Singapore .

1.4 Contributions

The main contributions are summarized as follows:

- (i) **Comprehensive literature study.** We present an extensive survey on Lipschitz continuity in deep learning, covering theoretical foundations, estimation methods, regularization approaches, and certifiable robustness. This survey serves to consolidate existing knowledge.
- (ii) **Operator-Theoretic Perturbation Analysis.** We develop a formal operator-theoretic framework for analyzing spectral variations of parameter matrices in training. This framework enables precise characterization of parameter matrices during training.
- (iii) **Stochastic analysis of Lipschitz dynamics.** We introduce a theoretical framework that characterizes the temporal evolution of Lipschitz continuity of neural networks during training. This framework is formulated using a system of stochastic differential equations (SDEs) and enables a rigorous analysis of how Lipschitz continuity evolves throughout training. Our analysis identifies key factors that govern the temporal evolution of Lipschitz continuity of neural networks.
- (iv) **Interpreting Global Robustness.** We begin by analyzing Lipschitz continuity through the lens of Fourier analysis, revealing how it modulates frequency signal propagation in neural networks. Building on this foundation, we introduce a novel perspective for interpreting the global robustness of image models — incorporating information theory and Shapley value theory — by linking the spectral bias of Lipschitz continuity to robustness against input perturbations.

2 | LITERATURE REVIEW

Copyright Disclaimer. This chapter includes content adapted from the following article:

1. **Róisín Luo**, J. McDermott, and C. O’Riordan. **Lipschitz Continuity in Deep Learning: A Systematic Review of Theoretical Foundations, Estimation Methods, Regularization Approaches and Certifiable Robustness**. Manuscript is under review at Transactions on Machine Learning Research (TMLR), 2025b

Portions of the content are reused verbatim or with minor edits, in accordance with institutional guidelines and the policies of the relevant publishers. Permission from all co-authors has been obtained.

Guiding Research Question. This chapter addresses the primary research question — **(RQ1) State of Knowledge** — by answering two interrelated secondary research questions through a comprehensive literature study: **(SRQ1) Theoretical Foundations** and **(SRQ2) Regularization Mechanism**.

Reproducibility. https://github.com/roisincrtai/activation_lipschitz

ABSTRACT

Lipschitz continuity is a fundamental property of neural networks that characterizes their sensitivity to input perturbations. It plays a pivotal role in deep learning, governing **robustness**, **generalization** and **optimization dynamics**. Despite its importance, research on Lipschitz continuity is scattered across various domains, lacking a unified perspective. This paper addresses this gap by providing a systematic review of Lipschitz continuity in deep learning. We explore its **theoretical foundations**, **estimation methods**, **regularization approaches**, and **certifiable robustness**. By reviewing existing research through the lens of Lipschitz continuity, this survey serves as a comprehensive reference

for researchers and practitioners seeking a deeper understanding of Lipschitz continuity and its implications in deep learning.

2.1 Introduction

Deep learning has achieved remarkable success across various domains, including computer vision, natural language processing, and graph-based learning. Advances in state-of-the-art architectures, such as convolutional neural networks (CNNs) (Krizhevsky et al., 2012), transformers (Vaswani et al., 2017; Brown et al., 2020), and graph neural networks (GNNs) (Kipf and Welling, 2017), as well as their large-scale applications, including large language models (LLMs) (Brown et al., 2020; Chowdhery et al., 2023; Touvron et al., 2023; OpenAI et al., 2024; DeepSeek-AI et al., 2025) and large vision-language models (LVLMs) (Radford et al., 2021; Li et al., 2022a; Anil et al., 2025), have significantly expanded the frontiers of deep learning, enabling powerful capabilities across a wide range of tasks.

Beyond their remarkable success, ensuring safety, robustness (Madry et al., 2018) and generalization, remains a critical challenge. These properties are intrinsically linked to the sensitivity of neural networks to input perturbations (Madry et al., 2018; Tsipras et al., 2019; Hendrycks and Dietterich, 2019; Amerehi and Healy, 2025), which can significantly impact their reliability in real-world applications. For instance, adversarial vulnerabilities (Goodfellow et al., 2015; Carlini and Wagner, 2017), and out-of-distribution (OOD) generalization (Sokolić et al., 2017; Neyshabur et al., 2017; Bartlett et al., 2017; Hendrycks et al., 2021) are major concerns in developing reliable deep learning models. A fundamental mathematical concept that characterizes network sensitivity and governs these properties is **Lipschitz continuity**, which measures the upper bound of the outputs of neural networks to inputs.

Although numerous studies have explored Lipschitz continuity from both theoretical (Bartlett et al., 2017; Róisín Luo et al., 2025a) and applied (Arjovsky et al., 2017; Gulrajani et al., 2017; Miyato et al., 2018) perspectives, a unified survey that consolidates these insights is still lacking. Existing works primarily focus on isolated aspects, such as adversarial robustness (Szegedy et al., 2014; Madry et al., 2018; Weng et al., 2018b), regularization (Arjovsky et al., 2017; Gulrajani et al., 2017), or theoretical bounds without practical considerations (Bartlett et al., 2017). The absence of a comprehensive survey integrating these perspectives leaves a critical gap in the literature. To address this, we provide a systematic review of Lipschitz continuity in deep learning, covering its **theoretical foundations, estimation methods, regularization approaches in optimization and architecture**.

ture, and **certifiable robustness**. By synthesizing key findings across these domains, this survey serves as a valuable resource for researchers and practitioners seeking a deeper understanding of Lipschitz continuity and its role in trustworthy learning systems. Beyond conducting a survey, we also critically distill the existing knowledge, present it in a more accessible manner, and provide the results or proofs **missing** or **incorrect** in the literature.

2.1.1 Scope

This survey aims to consolidate existing knowledge across these domains, providing a comprehensive resource for researchers and practitioners seeking to understand and leverage Lipschitz continuity in deep learning. To ensure a high-quality review, we focus primarily on the literature published in prestigious and other well-regarded sources. The scope of this survey is organized as below:

1. Section 2.2: **Theoretical Foundations** presents the formal definitions and fundamental properties of Lipschitz continuity, followed by key theoretical developments in deep learning. It covers the mathematical foundations, Lipschitz properties of activation functions and neural networks, Lipschitz analysis of multi-head self-attention, complexity-theoretic generalization bounds, and advances in training dynamics.
2. Section 2.3: **Estimation Methods** surveys the principal methods for estimating the Lipschitz constants of neural networks, including derivative bound propagation, spectral alignment, convex optimization relaxations, and relaxed integer programming approaches.
3. Section 2.4: **Regularization Approaches** reviews approaches for enforcing Lipschitz continuity in neural networks through both optimization-based and architectural approaches, covering weight regularization, gradient regularization, activation regularization, and class-margin regularization.
4. Section 2.5: **Certifiable Robustness** examines methods for achieving certifiable robustness through Lipschitz bounds, including the theoretical foundations of Lipschitz-margin robustness radii, certification via global Lipschitz bounds, certification via local Lipschitz bounds and certificated robustness in LLMs.

2.1.2 Contributions

Our key contributions are as follows:

1. **A Unified Systematic Review.** We close a critical gap in the literature by conducting a comprehensive survey of Lipschitz continuity in deep learning. Our review unites disparate research threads — spanning theoretical foundations, estimation methods, regularization approaches, architectural designs, and certified robustness — into a coherent framework that highlights their interconnections from the lens of Lipschitz continuity.
2. **Comprehensive Analysis.** We provide in-depth examinations of existing techniques organized into four categories:
 - **Theoretical Foundations.** We review the formal definitions and properties of Lipschitz continuity, analyze Lipschitz behavior of activations and network architectures, and synthesize key results on generalization bounds, optimization convergence, and training-induced Lipschitz dynamics.
 - **Estimation Methods.** From power-iteration spectral-norm approximations and extreme-value theory to randomized and interval-analysis approaches, we compare each method’s tightness, computational overhead, and scalability to modern architectures.
 - **Regularization Approaches.** We critically assess gradient-based penalties, spectral normalization, orthogonal and Parseval constraints, and novel Lipschitz bounded activations, examining their theoretical guarantees, implementation trade-offs, and empirical effects on robustness, generalization, and training dynamics.
 - **Certifiable Robustness.** We survey Lipschitz-based certification frameworks — covering global and local Lipschitz bounds, path-based and convex-relaxation certificates, randomized smoothing, and Lipschitz constrained architectures — analyzing their provable guarantees, computational requirements, and applicability to real-world deep models.
3. **Results and Proofs.** We contribute new and complementary results, including corrected Lipschitz constants for common activation functions (validated by our numerical experiments) and a Lipschitz continuity bound for arbitrary neural networks represented as directed acyclic graphs (DAGs). Furthermore, we provide theoretical results **missing or incorrect** from prior work, such as rigorous proofs of the closed-form expressions for the Lipschitz constants of common activation functions and a

general perturbation bound for certifiable robustness based on Hölder's conjugacy relation.

2.2 Theoretical Foundations

Lipschitz continuity is a foundational concept in deep learning theory, offering a rigorous framework for quantifying a neural network's sensitivity to input perturbations. It plays a central role in understanding robustness, generalization, and optimization dynamics. Throughout, we use operator $\text{Lip}_p[\bullet]$ to denote the p -norm Lipschitz constant for \bullet , and use operator $\text{Lip}[\bullet]$ to denote the 2-norm Lipschitz constant for \bullet .

2.2.1 Preliminaries

Definition 2.2.1 (p -Norm in Finite-Dimensional Vector Spaces). Let $V \subseteq \mathbb{R}^d$ be a finite-dimensional vector space. The p -norm (*i.e.* ℓ_p -norm) in V is defined as:

$$\|z\|_p = \begin{cases} \left(\sum_{i=1}^d |z_i|^p \right)^{1/p}, & \text{if } 1 \leq p < \infty, \\ \max_{i=1,\dots,d} |z_i|, & \text{if } p = \infty, \end{cases} \quad (2.1)$$

where $z = (z_1, z_2, \dots, z_d) \in V$ (Rudin, 1987, Definition 3.6, § 3).

Definition 2.2.2 (Globally K -Lipschitz Continuous). Let $f : X \mapsto Y$ be a function, where $X \subseteq \mathbb{R}^d$ and $Y \subseteq \mathbb{R}^c$. The function f is said to be *globally K -Lipschitz continuous* (with respect to the 2-norm) if there exists a constant scalar $K > 0$ such that:

$$\|f(u) - f(v)\|_2 \leq K\|u - v\|_2, \quad \forall u, v \in X, \quad (2.2)$$

(Rudin, 1976, Theorem 9.19, § 9). Throughout, unless specified otherwise, the *Lipschitz norm* is assumed to be the 2-norm.

Definition 2.2.3 (Globally $K_{p \rightarrow q}$ -Lipschitz Continuous). Let:

$$1 \leq p, q \leq \infty \quad (2.3)$$

be two scalars. A function $f : X \rightarrow Y$, with $X \subseteq \mathbb{R}^d$ and $Y \subseteq \mathbb{R}^c$, is said to be $K_{p \rightarrow q}$ -Lipschitz continuous if there exists a constant $K_{p \rightarrow q} > 0$ such that:

$$\|f(u) - f(v)\|_q \leq K_{p \rightarrow q} \|u - v\|_p, \quad \forall u, v \in X, \quad (2.4)$$

where $\|\cdot\|_p$ and $\|\cdot\|_q$ denote the ℓ_p and ℓ_q norms, respectively. Particularly, $K_{2 \rightarrow 2}$ -Lipschitz continuous reduces to K-Lipschitz continuous with respect to 2-norm.

Remark 2.2.4. Definition 2.2.3 (Globally $K_{p \rightarrow q}$ -Lipschitz Continuous) is non-standard in the mathematical literature; however, it is useful for discussions of certifiable robustness in the context of deep learning.

Lemma 2.2.5 (Lipschitz Constant Bounds Gradient Norm). *Let $f : \mathbb{R}^m \rightarrow \mathbb{R}$ be a differentiable function. Then f is K-Lipschitz continuous (with respect to the 2-norm) if and only if*

$$K \geq \sup_{x \in \text{dom}(f)} \|\nabla f(x)\|_2, \quad (2.5)$$

(Rudin, 1976, Theorem 9.19, § 9). In the case $0 < K < 1$, the function f is called a contraction map. In particular, for the case that $\text{dom}(f)$ is a convex set — any points connected through the Mean Value Theorem remain within $\text{dom}(f)$, thus the tight bound is achieved such that:

$$K = \sup_{x \in \text{dom}(f)} \|\nabla f(x)\|_2. \quad (2.6)$$

Remark 2.2.6. In Lemma 2.2.5 (Lipschitz Constant Bounds Gradient Norm), of the deep learning sense, the domain of a neural network $f : \mathbb{R}^m \rightarrow \mathbb{R}$ can be assumed to be a convex set on \mathbb{R}^m . Consequently, the tight Lipschitz bound is attained.

2.2.2 1-Lipschitz Orthogonal Matrix

Definition 2.2.7 (Skew-Hermitian & Skew-Symmetric Matrix). A matrix A is referred to as a *skew-hermitian matrix*, if A satisfies:

$$A = -A^*. \quad (2.7)$$

Particularly, if A is a real matrix, then A is also referred to as a *skew-symmetric matrix*.

Proposition 2.2.8 (Lipschitz Constant of Semi-Orthogonal Matrix). *If a matrix $W \in \mathbb{R}^{m \times n}$ with:*

$$W^\top W = I_n \quad \text{or} \quad WW^\top = I_m, \quad (2.8)$$

then W is semi-orthogonal with Lipschitz constant 1. If $m \geq n$, W is an isometric map over the entire \mathbb{R}^n ; if $m < n$, W is a contraction map on $\ker(W)$ strictly.

Proof. **Case 1: $m \geq n$ (Isometric Map).** For $\forall x, y \in \mathbb{R}^n$:

$$\|W(x - y)\|_2^2 = (W(x - y))^\top W(x - y) \quad (2.9)$$

$$= (x - y)^\top W^\top W(x - y) \quad (2.10)$$

$$= (x - y)^\top I_n(x - y) \quad (2.11)$$

$$= \|x - y\|_2^2, \quad (2.12)$$

then by definition:

$$\text{Lip}[W] = \sup_{x \neq y} \frac{\|W(x - y)\|_2}{\|x - y\|_2} = 1. \quad (2.13)$$

Case 1: $m < n$ (Contraction on Kernel). For $\exists x - y \in \ker(W)$, such that:

$$\|W(x - y)\|_2 = 0 < \|x - y\|_2, \quad (2.14)$$

then W is a contraction map on the kernel $\ker(W)$ strictly.

□

2.2.2.1 Matrix Orthogonalization

We also survey useful matrix orthogonalization algorithms below.

Lie Group Exponential Map. Let:

$$U(n) = \left\{ A \in \mathbb{C}^{n \times n} \mid A^* A = I \right\} \quad (2.15)$$

be an unitary group and:

$$u(n) = \{ B \in \mathbb{R}^{n \times n} : B = -B^* \} \quad (2.16)$$

be a *Skew-Hermitian* group. Then the *Lie Exponential Map* connects $u(n)$ and $U(n)$:

$$\exp(A) = I + A + \frac{1}{2}A^2 + \dots, \quad (2.17)$$

which is surjective. For a matrix W , its corresponding skew-Hermitian matrix can be constructed by taking:

$$B = W - W^* \quad (2.18)$$

(Lezcano-Casado and Martínez-Rubio, 2019).

Cayley Transform. If $B \in \mathbb{R}^{n \times n}$ is a *skew-symmetric* matrix, the surjective map:

$$\phi(B) = (I + \frac{1}{2}B)(I - \frac{1}{2}B)^{-1} \quad (2.19)$$

is referred to as the *Cayley map* which transforms B to an orthogonal matrix $\phi(B)$ (Cayley, 1846; Trockman and Kolter, 2021).

Björck Orthogonalization Approximation. Suppose $W_0 \in \mathbb{R}^{n \times n}$ is not an orthogonal matrix. Let W_k be an iterative sequence such that W_k is the closest orthogonal matrix to W_0 as $k \rightarrow \infty$. *Björck Orthogonalization* (Björck and Bowie, 1971) is a differentiable method to iteratively solve the closest orthogonal matrix to a given matrix W_0 . Chernodub and Nowicki (2017) use *Björck Orthogonalization* in an optimization problem for constraining the orthogonality of parameter matrices (Chernodub and Nowicki, 2017). *Björck Orthogonalization* (Björck and Bowie, 1971) is defined by:

$$W_{k+1} = W_k \left(I + \frac{1}{2}Q_k + \cdots + (-1)^p \binom{-\frac{1}{2}}{p} Q_k^p \right), \quad (2.20)$$

where W_k is the k -th iterative result, p is a chosen hyper-parameter, $\binom{-\frac{1}{2}}{p}$ is binomial coefficient, and Q_k is:

$$Q_k = I - W_k^\top W_k. \quad (2.21)$$

As $n \rightarrow \infty$, $W_k^\top W_k$ converges to I_n . For a rectangular matrix $W_0 \in \mathbb{R}^{m \times n}$, if $\text{rank}(W_0) = n$, the convergence still holds:

$$W_k^\top W_k \rightarrow I_n \quad \text{as} \quad n \rightarrow \infty. \quad (2.22)$$

2.2.3 Functional Inequalities

Proposition 2.2.9 (Lipschitz Constant of Function Composition). *Let $f : X \rightarrow Y$ and $g : Y \rightarrow Z$ be two bounded functions. Then the Lipschitz constant of their composition $g \circ f : X \rightarrow Z$ admits:*

$$\text{Lip}_p[g \circ f] \leq \text{Lip}_p[g] \text{ Lip}_p[f]. \quad (2.23)$$

Proof.

$$\text{Lip}_p[g \circ f] = \sup_{\|x-y\|_p \neq 0} \frac{\|f(g(x)) - f(g(y))\|_p}{\|x-y\|_p} \quad (2.24)$$

$$\leq \text{Lip}_p[f] \sup_{\|x-y\|_p \neq 0} \frac{\|g(x) - g(y)\|_p}{\|x-y\|_p} \quad (2.25)$$

$$= \text{Lip}_p[f] \text{ Lip}_p[g]. \quad (2.26)$$

□

Proposition 2.2.10 (Lipschitz Constant of Function Addition). *Let f and g be two bounded functions on $\text{dom}(g) \cap \text{dom}(f)$. Then the Lipschitz constant of $g + f$ admits:*

$$\text{Lip}_p[g + f] \leq \text{Lip}_p[g] + \text{Lip}_p[f]. \quad (2.27)$$

Proof.

$$\text{Lip}_p[g + f] = \sup_{\|x-y\|_p \neq 0} \frac{\|f(x) + g(x) - [f(y) + g(y)]\|_p}{\|x-y\|_p} \quad (2.28)$$

$$= \sup_{\|x-y\|_p \neq 0} \frac{\|f(x) - f(y) + g(x) - g(y)\|_p}{\|x-y\|_p} \quad (2.29)$$

$$\leq \sup_{\|x-y\|_p \neq 0} \frac{\|f(x) - f(y)\|_p}{\|x-y\|_p} + \sup_{\|x-y\|_p \neq 0} \frac{\|g(x) - g(y)\|_p}{\|x-y\|_p} \quad (2.30)$$

$$= \text{Lip}_p[g] + \text{Lip}_p[f]. \quad (2.31)$$

□

Proposition 2.2.11 (Lipschitz Constant of Function Concatenation). *Let $f : \mathbb{R}^d \rightarrow \mathbb{R}^m$ and $g : \mathbb{R}^d \rightarrow \mathbb{R}^n$ be two Lipschitz continuous functions. Let:*

$$(f \oplus g)(x) := \begin{bmatrix} f(x) \\ g(x) \end{bmatrix} \in \mathbb{R}^{m+n} \quad (2.32)$$

be a function by concatenating the outputs of f and g . Then, the following inequality holds true:

$$\left(\text{Lip}_p [f \oplus g] \right)^p \leq \left(\text{Lip}_p [f] \right)^p + \left(\text{Lip}_p [g] \right)^p. \quad (2.33)$$

Proof. For any $x, y \in \mathbb{R}^d$, we have:

$$\| (f \oplus g)(x) - (f \oplus g)(y) \|_p^p = \left\| \begin{bmatrix} f(x) \\ g(x) \end{bmatrix} - \begin{bmatrix} f(y) \\ g(y) \end{bmatrix} \right\|_p^p \quad (2.34)$$

$$= \sum_{i=1}^m (|f(x) - f(y)|^p)_i + \sum_{j=1}^n (|g(x) - g(y)|^p)_j \quad (2.35)$$

$$\leq \left(\left(\text{Lip}_p [f] \right)^p + \left(\text{Lip}_p [g] \right)^p \right) \|x - y\|_p^p. \quad (2.36)$$

Hence:

$$\left(\text{Lip}_p [f \oplus g] \right)^p = \sup_{x \neq y} \frac{\| (f \oplus g)(x) - (f \oplus g)(y) \|_p^p}{\|x - y\|_p^p} \quad (2.37)$$

$$\leq \left(\text{Lip}_p [f] \right)^p + \left(\text{Lip}_p [g] \right)^p. \quad (2.38)$$

□

2.2.4 Sub-Differential Convex Functions

For a function that is not differentiable but is locally Lipschitz continuous — such as the ReLU activation — the Clarke sub-differential provides a generalized notion of gradient that allows one to analyze and bound local Lipschitz constants (Clarke, 1975).

Definition 2.2.12 (Generalized Gradient). Let $f : \mathbb{R}^m \rightarrow \mathbb{R}$ be a function on X . The sub-differential of f at point x is a set, satisfying:

$$\partial_s f(x) = \left\{ g \mid \forall x, y \in X, \exists g \in \mathbb{R}^m \text{ s.t. } f(y) \geq f(x) + \langle g, y - x \rangle \right\}. \quad (2.39)$$

If f is convex, then:

$$\partial_s f(x) \neq \emptyset \quad \text{and} \quad \partial_s f(x) = \{ \nabla f(x^*) \mid \forall x^* \rightarrow x \}. \quad (2.40)$$

Definition 2.2.13 (Clarke Sub-Gradient). Let $f : \mathbb{R}^m \rightarrow \mathbb{R}$ be a proper convex function on X . If f is locally Lipschitz continuous on X , then by Rademacher's theorem it is

differentiable almost everywhere. The Clarke sub-differential f at a point x is defined as the convex hull of all limit points of gradients at differentiable points approaching x . That is, a vector g lies in the Clarke sub-differential at x if there exists a sequence of points $x_k \rightarrow x$ ($k \in \mathbb{N}$) at which f is differentiable such that the gradients $\nabla f(x_k)$ converge to g . Then the Clarke sub-differential is a convex hull, satisfying:

$$\partial f(x) = \text{conv} \left\{ g \mid \exists \text{ a sequence } (x_k) \rightarrow x \text{ as } k \rightarrow \infty, \nabla f(x_k) \rightarrow g \right\} \quad (2.41)$$

(Clarke, 1975, Definition 1.1). If f is convex, then $\partial f(x) = \partial_s f(x)$. This definition also extends to vector-valued functions (Clarke, 1990).

Lemma 2.2.14 (Local Lipschitz Constant of Sub-Differential Function). *Let $f : \mathbb{R}^m \rightarrow \mathbb{R}^n$ be a convex function differentiable almost everywhere on X . Then the $p \rightarrow q$ local Lipschitz constant of f on X is given as:*

$$\text{Lip}_{p \rightarrow q} [f; X] = \sup_{G \in \partial f(x)} \sup_{\|v\|_p \neq 0} \frac{\|G^\top v\|_q}{\|v\|_p} = \sup_{G \in \partial f(x)} \sup_{\|v\|_p = 1} \|G^\top\|_q, \quad (2.42)$$

such that:

$$\|f(x) - f(y)\|_q \leq \text{Lip}_{p \rightarrow q} [f; X] \|x - y\|_p, \quad (2.43)$$

for $\forall x, y \in X$ in the sense of Clarke sub-gradient (Jordan and Dimakis, 2020; Boyd et al., 2022).

2.2.5 Lipschitz Continuity of Activation Functions

An activation function:

$$\phi : \mathbb{R}^d \rightarrow \mathbb{R}^d \quad (2.44)$$

is a nonlinear mapping applied after neuron's output at a layer, enabling neural networks to learn complex patterns. For example, if ϕ is piecewise defined as:

$$\phi(x) = \begin{cases} x, & \text{if } x > 0, \\ 0, & \text{otherwise} \end{cases}$$

then the ϕ is referred to as *ReLU* activation function (Nair and Hinton, 2010).

The Lipschitz constants of commonly used activation functions are provided in Table 2.1. The constants are derived as the supremum of the 2-norm of the derivatives of activation functions. Proofs are provided in the Appendix 2.B. To numerically validate the results, we have conducted experiments by maximizing the gradient norm using Lemma 2.2.5 for a further sanity check.

Notes. The Lipschitz constant for the *softmax* function reported in the literature (Gouk et al., 2021) and *Sigmoid* function reported in the literature (Virmaux and Scaman, 2018) as 1. We show in Appendix 2.B.6 that the exact Lipschitz constant of *softmax* is indeed $\frac{1}{2}$, validated by our numerical experiment. This result has been reported a recent concurrent literature (Nair, 2025). We also show in Appendix 2.B.1 that exact Lipschitz constant of *sigmoid* is indeed $\frac{1}{4}$, validated by our numerical experiment. For *Leaky ReLU* and *ELU*, the parameter α is typically chosen with $\alpha < 1$, so their effective Lipschitz constants are usually 1 in practice.

Auto-Differentiation based Numerical Method. Suppose $f : \mathbb{R}^d \rightarrow \mathbb{R}$ be a first- and second-order differentiable neural network under domain convex condition (Remark 2.2.6). Leverage the autograd mechanism of PyTorch, we use gradient descent — *e.g.*, Adam (Kingma and Ba, 2017) — to numerically approximate the supremum:

$$\text{Lip}[f] = \sup_x \|f'(x)\|_2, \quad (2.45)$$

using Lemma 2.2.5.

Table 2.1: Lipschitz constants of activation functions.

Activation	Definition	Lipschitz Constant & Proof	Citations
ReLU	$\max(0, x)$	1	Nair and Hinton (2010, Sec. 2); Virmaux and Scaman (2018, Sec. 5)
Leaky ReLU	$\max(\alpha x, x)$	$\max(1, \alpha)$	Maas et al. (2013, Sec. 2); Virmaux and Scaman (2018, Sec. 5)
Sigmoid	$\frac{1}{1+e^{-x}}$	$\frac{1}{4}$ (Appendix 2.B.1)	Virmaux and Scaman (2018, Sec. 5)
Tanh	$\tanh(x)$	1 (Appendix 2.B.2)	Cybenko (1989); Virmaux and Scaman (2018, Sec. 5)
Softplus	$\log(1 + e^x)$	1 (Appendix 2.B.3)	Dugas et al. (2000, Sec. 2); Virmaux and Scaman (2018, Sec. 5)
ELU	$\begin{cases} x & x > 0 \\ \alpha(e^x - 1) & x \leq 0 \end{cases}$	$\max(1, \alpha)$	Clevert et al. (2016, Sec. 3)
Swish	$x \cdot \sigma(x)$	≈ 1.1 (Appendix 2.B.4)	Ramachandran et al. (2018, Sec. 1)
GELU	$\frac{x}{2} \left(1 + \text{erf} \left(\frac{x}{\sqrt{2}} \right) \right)$	≈ 1.1 (Appendix 2.B.5)	Hendrycks and Gimpel (2016, Sec. 2)
Softmax	$\text{softmax}(x_i) = \frac{e^{x_i}}{\sum_j e^{x_j}}$	$\frac{1}{2}$ (Appendix 2.B.6)	Gouk et al. (2021, Sec. 3.3)

2.2.6 Lipschitz Continuity of Dot-Product Self-Attention

LLMs (Brown et al., 2020; Chowdhery et al., 2023; Touvron et al., 2023; OpenAI et al., 2024; DeepSeek-AI et al., 2025), built on transformer architectures (Vaswani et al., 2017), rely heavily on dot-product self-attention mechanisms, whose Lipschitz continuity governs their sensitivity to input perturbations, such as token-level adversarial attacks. Dot-product self-attention mechanisms form the core of transformer architectures, enabling effective modeling of long-range dependencies in sequences for applications such as natural language processing and vision-language tasks.

Single-Head Dot-Product Self-Attention. For an input sequence matrix $x \in \mathbb{R}^{n \times d}$, where n is the sequence length and d is the input dimension, a self-attention layer computes the output as

$$\text{Attention}(x) = \underbrace{\text{softmax}\left(\frac{QK^\top}{\sqrt{d}}\right)}_{\text{row-wise softmax}} V \in \mathbb{R}^{n \times m}, \quad (2.46)$$

(Vaswani et al., 2017, Equation 1) where

$$Q = xW_Q \in \mathbb{R}^{n \times m}, \quad K = xW_K \in \mathbb{R}^{n \times m}, \quad V = xW_V \in \mathbb{R}^{n \times m}, \quad (2.47)$$

are the *query*, *key*, and *value* matrices, with weight matrices:

$$W_Q, W_K, W_V \in \mathbb{R}^{d \times m}, \quad (2.48)$$

and m denotes the hidden dimension. The softmax is applied row-wise to normalize attention scores. The scaling factor $\frac{1}{\sqrt{d}}$ stabilizes the computation numerically.

Multi-Head Dot-Product Self-Attention. In practice, transformers employ h parallel self-attention heads to jointly attend to information from different representation subspaces (Vaswani et al., 2017). Each head i has its own projection matrices:

$$W_{Q,i}, W_{K,i}, W_{V,i} \in \mathbb{R}^{d \times m_i}, \quad (2.49)$$

where $m_i = \frac{m}{h}$, h denotes the number of heads, and produces an output for head i :

$$\text{Attention}_i(x) \in \mathbb{R}^{n \times m_i}. \quad (2.50)$$

The outputs are concatenated:

$$\text{Attention}(x) = [\text{Attention}_1(x), \text{Attention}_2(x), \dots, \text{Attention}_h(x)] \in \mathbb{R}^{n \times m}, \quad (2.51)$$

produces the final output.

2.2.6.1 Locally Lipschitz Continuous

Standard dot-product self-attention is locally Lipschitz continuous, and several works have derived explicit upper bounds for its local Lipschitz constant. Let $\mathcal{B}(x_0, \delta) = \{x \mid \|x - x_0\|_2 < \delta\}$ denote a ball centered x_0 with a radius δ . [Hu et al.](#) show that for the dot-product self-attention layer within a ball $\mathcal{B}_2(x, \delta)$ is locally Lipschitz continuous bounded by:

$$\text{Lip}[\text{Attention}; \mathcal{B}_2(x, \delta)] \leq n(n+1) \left(\|x\|_2 + \delta \right)^2 \left[\|W_V\|_2 \|W_Q\|_2 \|W_K^\top\|_2 + \|W_V\|_2 \right], \quad (2.52)$$

where $x \in \mathbb{R}^{n \times d}$, n is the sequence length, d is the input dimension, $W_K, W_Q, W_V \in \mathbb{R}^{d \times m}$ are the *key*, *query* and *value* parameter matrices, and δ is a 2-norm radius ([Hu et al.](#), 2024, Theorem 2). [Castin et al.](#) provide a tighter bound by \sqrt{n} up to a constant factor, showing that within a ball $\mathcal{B}_2(0, \delta)$, the Lipschitz constant of dot-product self-attention is bounded by:

$$\text{Lip}[\text{Attention}; \mathcal{B}_2(0, \delta)] \leq \sqrt{3} \|W_V\|_2 \left[\left\| \frac{W_K^\top W_Q}{\sqrt{d}} \right\|_2^2 \delta^4 (4n+1) + n \right]^{\frac{1}{2}}, \quad (2.53)$$

where A is the attention score matrix ([Castin et al.](#), 2024, Theorem 3.3).

Most recently, [Yudin et al. \(2025\)](#) refine the bound by explicitly incorporating the Jacobian of the softmax function, given by:

$$\mathcal{M}(P_x) := \nabla \text{softmax}(x) = \text{diag}(P_x) - P_x^\top P_x, \quad (2.54)$$

where:

$$P_x = \left(\frac{e^{x_i}}{\sum_j e^{x_j}} \right), \quad (2.55)$$

leading that the Lipschitz constant for a single head is bounded by:

$$\text{Lip}[\text{Attention}] \leq \|W_V\|_2 \left(\|P\|_2 + 2\|x\|_2^2 \|A\|_2 \max_i \|\mathcal{M}(P_{i,:})\|_2 \right) \quad (2.56)$$

with:

$$P = \text{softmax}(xAx^\top) \in \mathbb{R}^{n \times n} \quad \text{and} \quad A = \frac{W_Q W_K^\top}{\sqrt{d}} \in \mathbb{R}^{d \times d} \quad (2.57)$$

(Yudin et al., 2025, Theorem 3).

2.2.6.2 Globally Non-Lipschitz Continuous

It is worth noting that the Lipschitz constants of both single-head and multi-head dot-product self-attention are not globally bounded. This is because the Lipschitz bound for dot-product self-attention grows with the input sequence length, implying that the dot-product self-attention is not globally Lipschitz continuous (Kim et al., 2021, Theorem 3.1). Kim et al. show that, for a sequence length n , input dimension d , and h heads, the 2-norm Lipschitz bound is:

$$\text{Lip}[\text{Attention}] \leq \frac{\sqrt{n}}{\sqrt{d/h}} \left[4\phi^{-1}(n-1) + 1 \right] \left(\sqrt{\sum_{h_i} \|W_{Q,h_i}\|_2^2 \|W_{V,h_i}\|_2^2} \right) \|W_O\|_2, \quad (2.58)$$

and the ∞ -norm Lipschitz bound:

$$\begin{aligned} \text{Lip}_\infty[\text{Attention}] &\leq \left[4\phi^{-1}(n-1) + \frac{1}{d/h} \right] \\ &\quad \|W_O^\top\|_\infty \max_{h_i} \|W_{Q,h_i}\|_\infty \|W_{Q,h_i}^\top\|_\infty \max_{h_j} \|W_{V,h_j}^\top\|_\infty, \end{aligned} \quad (2.59)$$

where:

$$\phi(x) = x \exp(x+1) \quad (2.60)$$

is an invertible univariate function on $x > 0$, W_{Q,h_i} is the *query* parameter matrix for head h_i , W_{V,h_i} is the *value* parameter matrix for head h_i , and W_O is the projection parameter

matrix (Kim et al., 2021, Theorem 3.2). They further conclude that their results can lead that the 2-norm Lipschitz bound is at the scale:

$$\text{Lip}[\text{Attention}] \sim O(\sqrt{n} \log n), \quad (2.61)$$

and the ∞ -norm Lipschitz bound is at the scale:

$$\text{Lip}_\infty[\text{Attention}] \sim O(\log n) \quad (2.62)$$

(Kim et al., 2021, Theorem 3.2). The bounds in (Kim et al., 2021, Theorem 3.2) are complemented by concurrent work (Vuckovic et al., 2020) with a measure-theoretical framework. Vuckovic et al. show that the 1-norm Lipschitz bound is at the scale:

$$\text{Lip}_1[\text{Attention}] \sim O(\sqrt{\log n}) \quad (2.63)$$

(Vuckovic et al., 2020, Theorem 29 & Corollary 30).

2.2.7 Lipschitz Continuity of Neural Networks

Definition 2.2.15 (Feedforward Network). Let $f : \mathbb{R}^m \rightarrow \mathbb{R}^n$ denote a feedforward neural network consisting of L layers, defined as the composition:

$$f := h^{(L)} \circ \dots \circ h^{(2)} \circ h^{(1)}, \quad (2.64)$$

where each layer $h^{(\ell)}$ is composed of a linear transformation $\phi^{(\ell)}(\cdot)$ followed by a non-linear activation function $\rho^{(\ell)}(\cdot)$:

$$h^{(\ell)} := \rho^{(\ell)} \circ \phi^{(\ell)}. \quad (2.65)$$

Proposition 2.2.16 (Lipschitz Constant of a Linear Layer). *Let $\phi^{(\ell)} : \mathbb{R}^{m_\ell} \rightarrow \mathbb{R}^{n_\ell}$ denote a linear transformation implemented either as a convolutional layer:*

$$\phi^{(\ell)}(z^{(\ell-1)}) = \Theta^{(\ell)} \odot z^{(\ell-1)} + b^{(\ell)}, \quad (2.66)$$

or as a fully connected (dense) layer:

$$\phi^{(\ell)}(z^{(\ell-1)}) = \Theta^{(\ell)} z^{(\ell-1)} + b^{(\ell)}, \quad (2.67)$$

where $\Theta^{(\ell)}$ is the weight matrix (or convolution kernel), $b^{(\ell)}$ is the bias term, \circledast denotes the convolution operator, and $z^{(\ell-1)}$ is the output from the previous layer. The Lipschitz constant of $\phi^{(\ell)}$ with respect to the Euclidean norm is given by:

$$\text{Lip}[\phi^{(\ell)}] = \|\Theta^{(\ell)}\|_2, \quad (2.68)$$

where $\|\Theta^{(\ell)}\|_2$ denotes the spectral-norm of the associated linear operator.

Proposition 2.2.17 (Spectral-Norm via Singular Value Decomposition). *Let $\Theta \in \mathbb{R}^{n \times m}$ be a matrix, admitting a truncated singular value decomposition (SVD):*

$$\Theta = \sum_{i=1}^r \sigma_i \mathbf{u}_i \mathbf{v}_i^\top, \quad \text{with} \quad \sigma_1 > \sigma_2 > \dots > \sigma_r > 0, \quad r = \text{rank}(\Theta), \quad (2.69)$$

where σ_i are the singular values, and \mathbf{u}_i , \mathbf{v}_i are the left and right singular vectors, respectively. Then, the spectral-norm of Θ (i.e., its operator norm induced by the Euclidean norm) is given by the largest singular value:

$$\|\Theta\|_2 = \sigma_1 \quad (2.70)$$

(*Horn and Johnson, 2012, Example 5.6.6, § 5*).

Proposition 2.2.18 (Lipschitz Constant Upper Bound of Feedforward Neural Network). *Let $f : \mathbb{R}^m \rightarrow \mathbb{R}^n$ be an L -layer feedforward neural network composed of linear transformations $\phi^{(\ell)}$ and activation functions $\rho^{(\ell)}$. The Lipschitz constant of f with respect to the Euclidean norm is defined as:*

$$\text{Lip}[f] = \sup_{\forall u \neq v} \frac{\|f(u) - f(v)\|_2}{\|u - v\|_2}, \quad (2.71)$$

which immediately admits an upper bound by applying [Proposition 2.2.9 \(Lipschitz Constant of Function Composition\)](#):

$$\text{Lip}[f] \leq \prod_{\ell=1}^L \text{Lip}[\rho^{(\ell)}] \prod_{\ell=1}^L \text{Lip}[\phi^{(\ell)}] \quad (2.72)$$

(*Róisín Luo et al., 2025a, Proposition 8, § 5*).

Corollary 2.2.19 (Spectral-Norm Upper Bound of Feedforward Neural Network). *For an ℓ -layer feedforward network f with only linear or convolutional layers and 1-Lipschitz*

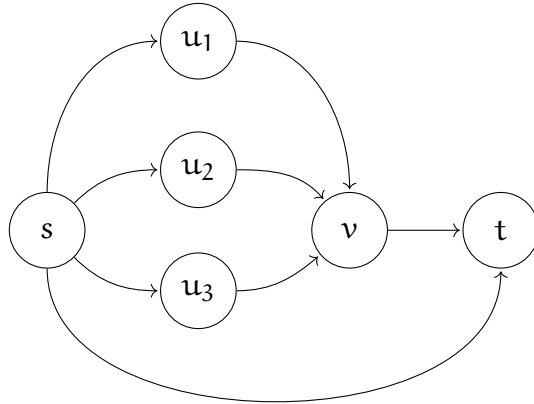


Figure 2.1: Example of Feedforward DAG Network. There are four computational paths: $s \rightarrow u_1 \rightarrow v \rightarrow t$, $s \rightarrow u_2 \rightarrow v \rightarrow t$, $s \rightarrow u_3 \rightarrow v \rightarrow t$, and $s \rightarrow t$. A node is a module in the DAG neural network f .

activation functions, combining Proposition 2.2.16 and Proposition 2.2.18 immediately yields a spectral-norm product bound:

$$\text{Lip}[f] \leq \prod_{\ell=1}^L \|\theta^{(\ell)}\|_2, \quad (2.73)$$

where $\theta^{(\ell)}$ is the ℓ -th layer parameter matrix.

2.2.7.1 Lipschitz Continuity for a Directed Acyclic Graph (DAG)

To the best of our knowledge, the existing literature does not present an explicit Lipschitz bound for a general feedforward network with skip connections. Prior literature such as (Miyato et al., 2018; Virmaux and Scaman, 2018) focuses strictly on sequential architectures, while norm-based capacity measures such as the path norm (Neyshabur et al., 2015) implicitly involve path enumeration but are not formulated as direct Lipschitz bounds. More recent path-metric bounds (Gonon et al., 2025) apply to arbitrary DAGs but are expressed in a rescaling-invariant metric form rather than the simple sum-over-paths structure we consider.

Figure 2.1 provides an illustrative example of a DAG network. To complement the survey, we derive an explicit bound in Theorem 2.2.20 using graph-theoretic method. To the best of our knowledge, this result has not previously appeared in the literature.

Theorem 2.2.20 (Lipschitz Bound for DAG Network). *Let $G = (V, E)$ be a finite directed acyclic graph (DAG) representing a feedforward neural network with unique input node $s \in V$ and output node $t \in V$. Each node $v \in V$ is a module h_v that is Lipschitz*

continuous with constant $\text{Lip}[h_v]$. An edge $(u \rightarrow v) \in E$ represents the computation of h_v immediately after h_u . Let $x_{v_i} : x \rightarrow x_{v_i}(x)$ represent the output at a node $v_i \in V$. The network is evaluated additively along incoming edges:

$$x_s(x) = x, \quad (2.74)$$

$$x_v(x) = \sum_{(u \rightarrow v) \in E} h_v(x_u(x)), \quad v \neq s. \quad (2.75)$$

A computational path p from s to t is an ordered sequence of nodes

$$p = (v_0 = s, v_1, \dots, v_{L_p} = t), \quad (2.76)$$

where $(v_{i-1} \rightarrow v_i) \in E$ for all $i = 1, \dots, L_p$. Define for each edge $(u \rightarrow v)$ the constant

$$C_{(u \rightarrow v)} := \text{Lip}[h_v], \quad (2.77)$$

and for a path p set

$$C_p := \prod_{i=1}^{L_p} \text{Lip}[h_{v_i}] = \prod_{i=1}^{L_p} C_{(v_{i-1} \rightarrow v_i)}. \quad (2.78)$$

Let \mathcal{P} be the set of all such paths from s to t . Then the Lipschitz constant of the overall network $f(x) := x_t(x)$ satisfies

$$\text{Lip}[f] \leq \sum_{p \in \mathcal{P}} C_p. \quad (2.79)$$

Proof. Fix any topological order of V . For $v \in V$, define the scalar

$$S(v) := \begin{cases} 1, & v = s, \\ \sum_{(u \rightarrow v) \in E} C_{(u \rightarrow v)} S(u), & v \neq s. \end{cases} \quad (2.80)$$

Claim: for all $v \in V$,

$$\text{Lip}[x_v] \leq S(v). \quad (2.81)$$

We prove (2.81) by induction along the topological order.

Base case ($v = s$). $x_s(x) = x$, hence $\text{Lip}[x_s] = 1 = S(s)$.

Inductive step. Let $v \neq s$ and assume (2.81) holds for all predecessors u of v . Applying Minkowski inequality, for any x, y in the input space,

$$\|x_v(x) - x_v(y)\| = \left\| \sum_{(u \rightarrow v)} h_v(x_u(x)) - \sum_{(u \rightarrow v)} h_v(x_u(y)) \right\| \quad (2.82)$$

$$\leq \sum_{(u \rightarrow v)} \|h_v(x_u(x)) - h_v(x_u(y))\| \quad (2.83)$$

$$\leq \sum_{(u \rightarrow v)} \text{Lip}[h_v] \|x_u(x) - x_u(y)\| \quad (2.84)$$

$$\leq \sum_{(u \rightarrow v)} \text{Lip}[h_v] \text{Lip}[x_u] \|x - y\| \quad (2.85)$$

$$= \sum_{(u \rightarrow v)} C_{(u \rightarrow v)} \text{Lip}[x_u] \|x - y\| \quad (2.86)$$

$$\leq \left(\sum_{(u \rightarrow v)} C_{(u \rightarrow v)} S(u) \right) \|x - y\| = S(v) \|x - y\|, \quad (2.87)$$

since inductive hypothesis:

$$\text{Lip}[x_u] \leq S(u). \quad (2.88)$$

Thus $\text{Lip}[x_v] \leq S(v)$. In particular,

$$\text{Lip}[f] = \text{Lip}[x_t] \leq S(t). \quad (2.89)$$

It remains to show $S(t) = \sum_{p \in \mathcal{P}} C_p$. More generally:

Lemma (Path expansion of S). For every $v \in V$,

$$S(v) = \sum_{p \in \mathcal{P}(s \rightarrow v)} \prod_{e \in p} C_e, \quad (2.90)$$

where $\mathcal{P}(s \rightarrow v)$ is the set of all directed paths from s to v .

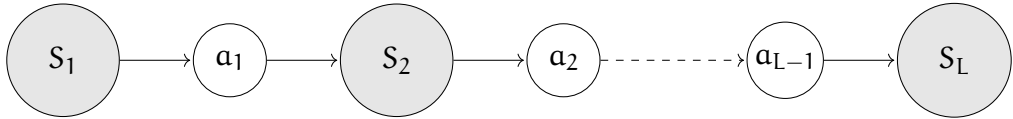


Figure 2.2: Topology of non-biconnected DAG network. If a DAG is separated into two sub-DAGs by the removal of a vertex a_i , then a_i is referred to as a *cut vertex* (or *articulation point*), and the DAG is said to be *non-biconnected*. This diagram shows the topology for a DAG that contains $L - 1$ articulation points a_1, a_2, \dots, a_{L-1} and L corresponding sub-DAGs S_1, S_2, \dots, S_L .

Proof of Lemma. Proceed again by induction in topological order. For $v = s$, $\mathcal{P}(s \rightarrow s)$ contains only the empty path with product 1, so (2.90) holds. Assume (2.90) holds for all predecessors u of v . Then

$$S(v) = \sum_{(u \rightarrow v)} C_{(u \rightarrow v)} S(u) = \sum_{(u \rightarrow v)} C_{(u \rightarrow v)} \left(\sum_{p \in \mathcal{P}(s \rightarrow u)} \prod_{e \in p} C_e \right) \quad (2.91)$$

$$= \sum_{(u \rightarrow v)} \sum_{p \in \mathcal{P}(s \rightarrow u)} \left(\prod_{e \in p} C_e \right) C_{(u \rightarrow v)}. \quad (2.92)$$

Concatenating each $p \in \mathcal{P}(s \rightarrow u)$ with the edge $(u \rightarrow v)$ yields a bijection onto $\mathcal{P}(s \rightarrow v)$, and multiplies the edge constants accordingly; thus (2.90) holds for v . \square

Applying the lemma at $v = t$ gives $S(t) = \sum_{p \in \mathcal{P}} C_p$, and hence

$$\text{Lip}[f] \leq S(t) = \sum_{p \in \mathcal{P}} \prod_{i=1}^{L_p} \text{Lip}[h_{v_i}]. \quad (2.93)$$

\square

2.2.7.2 Lipschitz Constant of Non-Biconnected DAG

If a DAG is separated into two disconnected sub-DAGs by the removal of a vertex, then the removed vertex is referred to as *cut vertex* or *articulation point*. Modern deep learning architectures often give rise to computation DAGs that are not biconnected: the DAGs can be separated into multiple subgraphs by removing a small set of vertices.

Theorem 2.2.21 (Lipschitz Bound for Non-Biconnected DAG Network). *Figure 2.2 shows the typical non-biconnected DAG topology found in modern deep learning architectures.*

The DAG contains a set of cut vertexes a_1, a_2, \dots, a_{L-1} and biconnected DAGs S_1, S_2, \dots, S_L . Suppose the DAG network f in Figure 2.2 is:

$$f = S_L \circ a_{L-1} \circ \dots \circ a_2 \circ S_2 \circ a_1 \circ S_1, \quad (2.94)$$

then it is not difficult to show that the Lipschitz constant bound of this DAG is:

$$\text{Lip}[f] \leq \left(\prod_{i=1}^L \text{Lip}[S_i] \right) \left(\prod_{j=1}^{L-1} \text{Lip}[a_i] \right), \quad (2.95)$$

where each the Lipschitz bound of sub-DAG $\text{Lip}[S_i]$ is given by Theorem 2.2.20 (Lipschitz Bound for DAG Network).

Remark 2.2.22. Theorem 2.2.21 (Lipschitz Bound for Non-Biconnected DAG Network) is particularly valuable for estimating the Lipschitz bound of a deep model. In contrast to path-based bound of Theorem 2.2.20 (Lipschitz Bound for DAG Network), which can be quite loose due to its combinatorial dependence on the number of paths, Theorem 2.2.21 yields significantly tighter and more structurally informed bounds.

2.2.7.3 Lipschitz Constant of Residual Network

Residual networks (He et al., 2016) address the optimization challenges of very deep neural architectures by introducing *residual modules*, which is illustrated in Figure 2.3. Each module m_{res} has the structure:

$$m_{\text{res}}(x) = x + \phi(x), \quad (2.96)$$

which consists a non-identity unit ϕ and an identity skip connection. The resulting residual mapping $m_{\text{res}}(x)$ maintains stable gradient flow, mitigates vanishing-gradient effects, and enables the training of substantially deeper networks without degradation. This simple architectural principle has proven highly effective and forms the backbone of many state-of-the-art deep learning models. Using Theorem 2.2.20 (Lipschitz Bound for DAG Network), it is not difficult to show that the Lipschitz constant bound of this structure is:

$$\text{Lip}[m_{\text{res}}] \leq \text{Lip}[s] + \text{Lip}[\phi] = 1 + \text{Lip}[\phi], \quad (2.97)$$

which recovers the same results in (Behrmann et al., 2019, Lemma 2, § 2), (Gouk et al., 2021, § 3.4) and Proposition 2.2.9 (Lipschitz Constant of Function Composition) by setting s to an identity map.

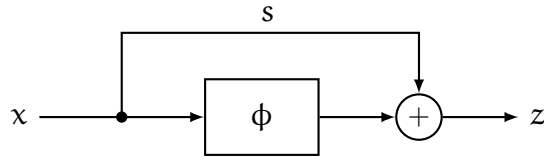


Figure 2.3: A residual module $m(x) = x + \phi(x)$ consists of a non-identity unit $\phi : x \mapsto \phi(x)$ and an identity skip connection unit $s : x \mapsto x$.

2.2.8 Complexity-Theoretic Generalization Bound

Notations. Let \mathcal{H} be a hypothesis family and $\mathcal{H} \ni h : X \rightarrow Y$ be a hypothesis. Let $\ell : Y \times Y \rightarrow \mathbb{R}$ be a loss function. For each $\ell(h(x), y)$, we can associate ℓ and h with a map $G \ni g : X \times Y \rightarrow \mathbb{R}$, where G is the family of loss functions associated to with hypothesis family \mathcal{H} .

The generalization capacity of a neural network is fundamentally governed by its Lipschitz constant (Mohri et al., 2018). To quantify this capacity for a hypothesis, the concept of *generalization gap* is often used to measure the error between *true risk* and *empirical risk* (Definition 2.2.23). This gap for a model $h \in \mathcal{H}$ is proportional to its empirical Rademacher complexity of the hypothesis family \mathcal{H} , and the empirical Rademacher complexity is proportional to the Lipschitz constant $\text{Lip}[\mathcal{H}] := \sup_{h \in \mathcal{H}} \text{Lip}[h]$ of the hypothesis family:

$$\text{Generalization gap of } h \sim \text{Rademacher complexity} \sim O(\text{Lip}[\mathcal{H}]) \quad (2.98)$$

(Mohri et al. (2018, § 3); Shalev-Shwartz and Ben-David (2014, Part IV)). A smaller Lipschitz constant enforces smoother mappings, reducing the complexity of the function class and mitigating overfitting, thereby enhancing robustness to noise and adversarial perturbations (Neyshabur et al., 2015; Gouk et al., 2021; Castin et al., 2024).

Definition 2.2.23 (Generalization Gap). Let $S := \{(x_i, y_i)\}_{i=1}^m$ be a dataset where (x_i, y_i) is sampled *i.i.d.* from an unknown distribution \mathcal{D}_X . The true (population) risk for hypothesis h is defined as:

$$R(h) := \mathbb{E}_{(x,y) \sim \mathcal{D}_X} [\ell(h(x), y)], \quad (2.99)$$

and the empirical risk on S is defined as:

$$R_S(h) := \frac{1}{m} \sum_{i=1}^m \ell(h(x_i), y_i) \quad (2.100)$$

(Mohri et al. (2018, § 3); Shalev-Shwartz and Ben-David (2014, Part IV)). Accordingly, the generalization gap on S is given by:

$$R(h) - R_S(h). \quad (2.101)$$

2.2.8.1 Rademacher Complexity and its Bounds

In learning theory, *Rademacher complexity* quantifies the expressiveness of a hypothesis family $G := \{g : X \rightarrow \mathbb{R}\}$ by measuring how well the G can fit data associated with random labels (Mohri et al., 2018, § 3.1). Let $S = (x_1, x_2, \dots, x_m)$ be a dataset of size m with each $x_i \in X$ drawn i.i.d. from an unknown distribution \mathcal{D}_X . Let $h : X \rightarrow \mathbb{R}$ be a hypothesis that assigns a real-valued score to each input. Let $\sigma_1, \dots, \sigma_m$ be m independent *Rademacher variables*, i.e., random variables uniformly distributed over $\{-1, +1\}$ (Mohri et al., 2018, § 3.1). For random labels $\sigma_1, \dots, \sigma_m$ assigned to S , the maximal correlation between the labels and the predictions of hypotheses in \mathcal{H} is given by

$$\sup_{g \in G} \frac{1}{m} \sum_{i=1}^m \sigma_i g(x_i). \quad (2.102)$$

By assigning all possible random labels to the dataset S , we can thus define *Rademacher Complexity* for hypothesis family G , stated in Definition 2.2.24 (Rademacher Complexity (Mohri et al., 2018, Definition 3.1, § 3)).

Definition 2.2.24 (Rademacher Complexity (Mohri et al., 2018, Definition 3.1, § 3)). The *empirical Rademacher complexity* of G with respect to S is defined as

$$\hat{\mathfrak{R}}_S(G) := \mathbb{E}_\sigma \left[\sup_{g \in G} \frac{1}{m} \sum_{i=1}^m \sigma_i g(x_i) \right], \quad (2.103)$$

and the (expected) *Rademacher complexity* is the expectation of $\hat{\mathfrak{R}}_S(G)$ over all dataset S of size m :

$$\mathfrak{R}_m(G) := \mathbb{E}_{S \sim \mathcal{D}_X^m} \left[\hat{\mathfrak{R}}_S(G) \right], \quad (2.104)$$

where $S \sim \mathcal{D}_X^m$ denotes m samples i.i.d. drawn from \mathcal{D} .

In the paradigm of machine learning, for the case of the hypothesis family $\ell \circ \mathcal{H}$ is the composition of a model $h \in \mathcal{H} := \{h : \mathbb{R}^n \rightarrow \mathbb{R}\}$ and loss function $\ell : \mathbb{R} \rightarrow \mathbb{R}$:

$$\ell \circ \mathcal{H} := \{\ell \circ h \mid h \in \mathcal{H}\}, \quad (2.105)$$

by Talagrand's Contraction Lemma (Mohri et al., 2018, Lemma 4.2, § 4), the empirical Rademacher complexity of $\ell \circ \mathcal{H}$ on S admits:

$$\hat{\mathfrak{R}}_S(\ell \circ \mathcal{H}) \leq \text{Lip}[\ell] \hat{\mathfrak{R}}_S(\mathcal{H}). \quad (2.106)$$

For any $\delta > 0$, with probability at least $1 - \delta$, the generalization gap for $h \in \mathcal{H}$ on S is bounded by empirical Rademacher complexity of $\ell \circ \mathcal{H}$:

$$R(h) - R_S(h) \leq 2 \hat{\mathfrak{R}}_S(\ell \circ \mathcal{H}) + 3 \sqrt{\frac{\log \frac{2}{\delta}}{2m}} \leq 2 \text{Lip}[\ell] \hat{\mathfrak{R}}_S(\mathcal{H}) + 3 \sqrt{\frac{\log \frac{2}{\delta}}{2m}} \quad (2.107)$$

(Mohri et al., 2018, Theorem 3.1 & Theorem 3.3, § 3). If \mathcal{H} is a $K_{\mathcal{H}}$ -Lipschitz continuous hypothesis family, that is:

$$\mathcal{H} := \{h : \mathbb{R}^n \rightarrow \mathbb{R} \mid \text{Lip}[h] \leq K_{\mathcal{H}}\}, \quad (2.108)$$

and let:

$$\Phi := \{\phi : \mathbb{R}^n \rightarrow \mathbb{R}^n \mid \phi \text{ is a coordinate-wise identity map}\} \quad (2.109)$$

be an coordinate-wise identity hypothesis family. By using vector contraction theorem (Maurer, 2016, Equation 1 & Corollary 4), $\hat{\mathfrak{R}}_S(\mathcal{H})$ holds an inequality:

$$\hat{\mathfrak{R}}_S(\mathcal{H}) = \hat{\mathfrak{R}}_S(\mathcal{H} \circ \Phi) \leq \sqrt{2} K_{\mathcal{H}} \hat{\mathfrak{R}}_S(\Phi), \quad (2.110)$$

where $\hat{\mathfrak{R}}_S(\Phi)$ is bounded by the 2-norm dataset diameter $\max_{x \in S} \|x\|_2$ of S :

$$\hat{\mathfrak{R}}_S(\Phi) = \mathbb{E}_{\sigma} \left[\sup \frac{1}{m} \sum_{i=1}^m \sigma_i x_i \right] \leq \frac{\sqrt{\sup \sum_{i=1}^m \|x_i\|_2^2}}{m} = \frac{\max_{x \in S} \|x\|_2}{\sqrt{m}}, \quad (2.111)$$

this immediately yields:

$$R(h) - R_S(h) \leq O(K_{\mathcal{H}}). \quad (2.112)$$

The literature on norm-based generalization bounds (Bartlett et al., 2017; Golowich et al., 2018) also shows that the empirical Rademacher complexity of general neural networks with ReLU activations can be bounded by the product of the layerwise parameter 2-norms, which in turn provides an upper bound on the Lipschitz constant of the hypothesis family. For example, Bartlett et al. show that the lower bound of the empirical Rademacher complexity depends on an upper bound $K_{\mathcal{H}}^{+, \ell_2}$ of Lipschitz constant $K_{\mathcal{H}}$ of an L-layer network:

$$K_{\mathcal{H}} \leq K_{\mathcal{H}}^{+, \ell_2} := O\left(\prod_{\ell=1}^L \|\theta^{(\ell)}\|_2\right), \quad (2.113)$$

where $\|\theta^{(\ell)}\|_2$ is the 2-norm of the ℓ -th layer parameter matrix, this leads:

$$\hat{\mathfrak{R}}_S(\mathcal{H}) \geq O(K_{\mathcal{H}}^{+, \ell_2}), \quad (2.114)$$

(Bartlett et al., 2017, Theorem 3.4., § 3.3). The Lipschitz upper bound $K_{\mathcal{H}}^{+, \ell_2}$ is given by the product of the spectral-norms of parameter matrices (Proposition 2.2.18). Golowich et al. explicitly show that, for ReLU networks, the $\hat{\mathfrak{R}}_S(\mathcal{H})$ is bounded by:

$$\hat{\mathfrak{R}}_S(\mathcal{H}) \leq O\left(\frac{K_{\mathcal{H}}^{+, \ell_2}}{\sqrt{m}}\right) \quad (2.115)$$

(Golowich et al., 2018, Theorem 2).

2.2.9 Training Dynamics of Lipschitz Continuity

The Lipschitz continuity of a parameterized network evolves as optimization updates its parameters. Consequently, the optimization process induces the dynamics of the network's Lipschitz continuity. While existing work in deep learning theory has largely focused on bounding the Lipschitz constants of neural networks, understanding how Lipschitz continuity evolves throughout training remains an open problem. Only a few studies have begun to explore this aspect. In particular, Róisín Luo et al. (2025a) introduces the concept of *optimization-induced dynamics* establishes a continuous-time stochastic framework that explicitly links the optimization process to the time-varying Lipschitz continuity bound of deep networks. The literature (Róisín Luo et al., 2025a) uses the operator-theoretical results regarding how the largest singular values of parameter matrices vary with respect to perturbations from the literature (Róisín Luo et al., 2025c), along with the theory from high-dimensional stochastic differential equations (SDEs) from stochastic analysis, for establishing a mathematical framework modeling the evo-

lution of a spectral-norm based Lipschitz continuity upper bound. They further validate their theoretical framework with experiments across datasets and regularization scenarios.

Consider an L -layer feed-forward neural network $f : \mathbb{R}^m \rightarrow \mathbb{R}$ with 1-Lipschitz activation functions (e.g., ReLU). Let $\Theta^{(\ell)}(t) \in \mathbb{R}^{m_\ell \times n_\ell}$ be the ℓ -layer parameter matrix at time t and $\Theta(t)$ be the collection of $\Theta^{(\ell)}(t)$ for all layers. Let $\mathcal{L}_f(\Theta(t))$ be the loss expectation for the f with parameters $\Theta(t)$ at time t . Suppose that $\Sigma_t^{(\ell)} \in \mathbb{R}^{(m_\ell n_\ell) \times (m_\ell n_\ell)}$ is the layer-wise covariance matrix of stochastic gradient noise, arising from mini-batch sampling. Let $K^{(\ell)}(t)$ be the Lipschitz constant at layer ℓ . Let $K(t)$ be the network Lipschitz spectral-norm bound. [Róisín Luo et al. \(2025a\)](#) show that the continuous-time dynamics of the parameters under stochastic gradient descent (SGD) with a sufficiently small learning rate $\eta > 0$ are given by a system of SDEs ([Róisín Luo et al., 2025a](#), Definition 10):

$$\begin{cases} d\text{vec}(\Theta^{(\ell)}(t)) = -\text{vec} \left[\nabla^{(\ell)} \mathcal{L}_f(\Theta(t)) \right] dt + \sqrt{\eta} \left[\Sigma_t^{(\ell)} \right]^{\frac{1}{2}} dB_t^{(\ell)} \\ K^{(\ell)}(t) = \|\Theta^{(\ell)}(t)\|_{\text{op}} \\ Z(t) = \sum_{l=1}^L \log K^{(l)}(t) \\ K(t) = e^{Z(t)} \end{cases}$$

where:

- $\text{vec} : \mathbb{R}^{m \times n} \rightarrow \mathbb{R}^{mn}$ represents major-column vectorization operator.
- $\|\cdot\|_{\text{op}}$ the matrix operator (spectral) norm.
- $\nabla^{(\ell)} \mathcal{L}_f(\Theta(t))$ is the gradient of the loss with respect to the ℓ -th layer parameters.
- $B_t^{(\ell)}$ is a standard $(m_\ell n_\ell)$ -dimensional Wiener process.

This stochastic dynamical system characterizes, in continuous time, the evolution of both layer-wise and network-level Lipschitz continuity bounds induced by the optimization process. [Róisín Luo et al. \(2025a, Theorem 15\)](#) show that the layer-wise dynamics decompose into three *driving forces*:

$$\frac{dK^{(\ell)}(t)}{K^{(\ell)}(t)} = \left(\mu^{(\ell)}(t) + \kappa^{(\ell)}(t) \right) dt + \lambda^{(\ell)}(t)^\top dB_t^{(\ell)}, \quad (2.116)$$

where $dB_t^{(\ell)} \sim \mathcal{N}(0, I_{m_\ell n_\ell} dt)$ represents the increment of a standard Wiener process in $\mathbb{R}^{m_\ell n_\ell}$, and the three *driving forces* are:

1. Optimization-induced drift:

$$\mu^{(\ell)}(t) = \frac{\left\langle J_{\text{op}}^{(\ell)}(t), -\text{vec}[\nabla^{(\ell)} \mathcal{L}_f(\theta(t))] \right\rangle}{\sigma_1^{(\ell)}(t)}, \quad (2.117)$$

where $J_{\text{op}}^{(\ell)}(t)$ is the Jacobian of the operator norm with respect to $\text{vec}(\theta^{(\ell)}(t))$ and $\sigma_1^{(\ell)}(t)$ is its largest singular value. This term captures the deterministic component of Lipschitz evolution driven by the mean gradient flow. This shows that the alignment of the gradient $\nabla^{(\ell)} \mathcal{L}_f(\theta(t))$ and principal direction of the ℓ -th layer parameter matrix $J_{\text{op}}^{(\ell)}(t)$ at time t determines the contribution of the optimization to the increment of the layer-wise Lipschitz constant.

2. Noise-curvature entropy production:

$$\kappa^{(\ell)}(t) = \frac{\eta}{2 \sigma_1^{(\ell)}(t)} \left\langle H_{\text{op}}^{(\ell)}(t), \Sigma_t^{(\ell)} \right\rangle \geq 0, \quad (2.118)$$

where $H_{\text{op}}^{(\ell)}(t)$ is the Hessian of the operator norm and $\Sigma_t^{(\ell)}$ is the gradient-noise covariance. This non-negative term quantifies irreversible growth of the Lipschitz bound due to the interaction between stochastic gradient noise and curvature.

3. Diffusion-modulation intensity:

$$\lambda^{(\ell)}(t) = \frac{\sqrt{\eta}}{\sigma_1^{(\ell)}(t)} \left[\Sigma_t^{(\ell)} \right]^{1/2\top} J_{\text{op}}^{(\ell)}(t), \quad (2.119)$$

which controls the variance of Lipschitz evolution by scaling the Wiener noise term from mini-batch sampling.

[Róisín Luo et al. \(2025a, Theorem 16\)](#) show that, at the network level, these quantities aggregate as:

$$\mu_Z(t) = \sum_{\ell=1}^L \mu^{(\ell)}(t), \quad \kappa_Z(t) = \sum_{\ell=1}^L \kappa^{(\ell)}(t), \quad \lambda_Z(t) = \left[\sum_{\ell=1}^L \|\lambda^{(\ell)}(t)\|_2^2 \right]^{\frac{1}{2}}, \quad (2.120)$$

governing the deterministic trend, irreversible growth, and stochastic fluctuations of the overall Lipschitz bound $K(t)$.

Their framework is particularly useful for interpreting the behaviors of neural networks, such as the near-convergence behavior, noisy supervision and mini-batch sampling trajectories. [Róisín Luo et al. \(2025a, § 8\)](#) show that:

1. The Lipschitz constant bound irreversibly increase since the term *noise-curvature entropy production* $\kappa_Z(t)$ is *non-negative*, which increases the system entropy ([Róisín Luo et al., 2025a](#), § 8.3).
2. The magnitude of supervision noise affects the Lipschitz bound ([Róisín Luo et al., 2025a](#), § 8.4 & 8.5). In particular, larger supervision noise leads to a lower Lipschitz bound for the network. This is because the supervision noise shrinks the *optimization-induced drift* $\mu_Z(t)$.
3. Mini-batch trajectories do not affect the variance of the Lipschitz bound if batch size is sufficiently large ([Róisín Luo et al., 2025a](#), § 8.6).

Remark 2.2.25. The dynamical analysis of Lipschitz continuity in deep learning models remains an open research problem. For instance, the dynamics under small-batch training remains poorly understood.

2.3 Estimation Methods

Proposition 2.2.18 gives an upper bound of the Lipschitz constant of a network ([Miyato et al., 2018](#); [Róisín Luo et al., 2025a](#)). However, exact computation of the Lipschitz constant

$$K = \sup_{x \neq y} \frac{\|f(x) - f(y)\|_2}{\|x - y\|_2} = \sup_x \|\nabla f(x)\|_2 \quad (2.121)$$

is generally NP-hard ([Virmaux and Scaman, 2018](#); [Jordan and Dimakis, 2020](#)). This section surveys major estimation and bounding techniques, ranging from statistical sampling to certified convex relaxations. We group them into *Power Iteration*, *Extreme Value Theory*, *Derivative Bound Propagation*, *Spectral Alignment*, *Convex Optimization Relaxations*, and *Exact/Relaxed MILP formulations*.

2.3.1 Power Iteration for Single Linear Unit

Power Iteration ([Mises and Pollaczek-Geiringer, 1929](#)) is also known as the Von Mises iteration ([Mises and Pollaczek-Geiringer, 1929](#)). It is the standard way to estimate the Lipschitz constant for a linear layer — fully-connected or convolutional, by approximating the spectral-norm of weight matrices, which bounds the layer Lipschitz constant (Proposition 2.2.16) [Miyato et al. \(2018\)](#); [Sedghi et al. \(2019\)](#); [Kim et al. \(2021\)](#); [Róisín Luo et al. \(2025a\)](#)). Another desirable property of *power iteration* in optimization is that *power*

iteration is differentiable. For example, Miyato et al. (2018) and Miyato et al. (2018) use *power iteration* for computing the largest singular values of parameter matrices, in which the differentiability of *power iteration* allows the gradient propagation for gradient based optimization.

Suppose that $W \in \mathbb{R}^{m \times m}$ is the parameter matrix of a fully-connected layer or a convolutional layer, then the largest singular value $\sigma_1(W)$ is its operator norm:

$$\text{Lip}[W] = \sigma_1(W). \quad (2.122)$$

Computing the exact value of $\sigma_1(W)$ for a large $m \times m$ matrix W is computationally expensive, as classical algorithms require $O(m^3)$ time. However, the largest singular value can be approximated using *power iteration* by assuming the existence of a uniquely dominant singular value (Golub and Van Loan, 2013, § 7.3). Starting with random unit vectors u_0, v_0 , one step of power iteration updates

$$v_{k+1} \leftarrow \frac{W^\top u_k}{\|W^\top u_k\|_2}, \quad u_{k+1} \leftarrow \frac{Wv_k}{\|Wv_k\|_2}, \quad (2.123)$$

and uses

$$\hat{\sigma}_1^{(k+1)} = u_{k+1}^\top W v_{k+1} \quad (2.124)$$

as a differentiable estimate of $\sigma_1(W)$ at step $k + 1$. At the iteration number T , the estimated Lipschitz constant of W is approximated as:

$$\text{Lip}[W] \approx u_T^\top W v_T, \quad (2.125)$$

where T is the number of iterations. The estimation error is proportional to:

$$|\sigma_1 - \hat{\sigma}_1^{(T)}| = O\left(\left[\frac{\sigma_2}{\sigma_1}\right]^T\right), \quad (2.126)$$

where σ_1 and σ_2 are the largest, and second largest singular values, respectively (Golub and Van Loan, 2013, Equation 7.3.5, § 7.3).

2.3.2 Extreme Value Theory

CLEVER (Weng et al., 2018b) — *Cross-Lipschitz Extreme Value for nEwork Robustness* — converts the problem of estimating the attack-independent robustness into the problem of estimating the *local* Lipschitz constant by sampling gradient norms in a neigh-

borhood of the input (Weng et al., 2018b). This is because the q -norm Lipschitz constant of a network $g : \mathbb{R}^m \rightarrow \mathbb{R}$ is determined by:

$$\text{Lip}_q[g] = \sup_x \|\nabla g(x)\|_q, \quad (2.127)$$

for any inputs x and y :

$$|g(x) - g(y)| \leq \text{Lip}_q[f] \|x - y\|_p \quad (2.128)$$

(Weng et al., 2018b, Lemma 3.1) where $1 \leq p, q \leq \infty$ satisfy the Hölder conjugacy relation (Rudin, 1976, § 6):

$$\frac{1}{p} + \frac{1}{q} = 1. \quad (2.129)$$

Adversarial Perturbation Bound. Weng et al. (2018b) further show that the local Lipschitz constant can be used for deriving the adversarial perturbation bound. Let

$$f : \mathbb{R}^m \rightarrow \mathbb{R}^k \quad (2.130)$$

be a k -class classifier and f_i be the i -th prediction. Let:

$$c(x) = \arg \max_{1 \leq i \leq k} f_i(x) \quad (2.131)$$

be the prediction. Then the p -norm adversarial perturbation $\|\delta\|_p$ to an input x_0 is bounded above by:

$$\|\delta\|_p \leq \min_{j \neq c} \frac{f_c(x_0) - f_j(x_0)}{\text{Lip}_q[f_j]}, \quad (2.132)$$

where the local Lipschitz constant $\text{Lip}_q[f_j]$ can be estimated through:

$$\text{Lip}_q[f_j] = \max_{x \in B_p(x_0, \delta)} \|\nabla f_j(x)\|_q \quad (2.133)$$

and $B_p(x_0, \delta)$ is a p -norm ball centered at x_0 with a radius δ (Weng et al., 2018b, Theorem 3.2).

Distribution of Extreme Value $\max_{x \in B_p(x_0, \delta)} \|\nabla f_j(x)\|_q$. Estimating:

$$\max_{x \in B_p(x_0, \delta)} \|\nabla_x f_j(x)\|_q \quad (2.134)$$

can be through sampling $x \in B_p(x_0, \delta)$. Suppose the n samples are $\{x^{(1)}, x^{(2)}, \dots, x^{(n)}\}$. Their gradient q -norms are $\{\|\nabla f_j(x^{(1)})\|_q, \|\nabla f_j(x^{(2)})\|_q, \dots, \|\nabla f_j(x^{(n)})\|_q\}$. [Weng et al. \(2018b\)](#) show that the extreme value of the gradient q -norm:

$$Y := \lim_{n \rightarrow \infty} \max_{x^{(i)} \in B_p(x_0, \delta)} \left\{ \|\nabla f_j(x^{(1)})\|_q, \|\nabla f_j(x^{(2)})\|_q, \dots, \|\nabla f_j(x^{(n)})\|_q \right\} \quad (2.135)$$

can only be a distribution P_Y of three distribution classes — *Gumbel class (Type I)*, *Fréchet class (Type II)* and *Reverse Weibull class (Type III)* — according to Fisher-Tippett-Gnedenko Theorem ([Weng et al., 2018b](#), Theorem 4.1). The extreme value $\max \|\nabla f_j(x^{(1)})\|_q$ is thus converted to estimating the mean of the distribution P_Y :

$$\text{Lip}_q [f_j] \approx \mathbb{E}_{Y \sim P_Y} [Y]. \quad (2.136)$$

2.3.3 Coordinate-Wise Gradient

Fast-Lip ([Weng et al., 2018a](#)) derives a lower bound of local Lipschitz constant in the form of coordinate-wise gradients by analyzing the activation patterns of ReLU networks. Let n_k denote the number of neurons at the k -th layer of an m -layer network and Let n_0 be the input dimension. Let $\phi_k : \mathbb{R}^{n_0} \rightarrow \mathbb{R}^{n_k}$ be the map from input to the output of k -th layer. Let σ be the coordinate-wise activation function. Then the relation between the $(k-1)$ -th layer and the k -th layer can be written as:

$$\phi_k(x) = \sigma(W^{(k)} \phi_{k-1}(x) + b^{(k)}), \quad (2.137)$$

where $W^{(k)} \in \mathbb{R}^{n_k \times n_{k-1}}$ is the k -th layer parameter matrix, and $b^{(k)} \in \mathbb{R}^{n_k}$ is the bias. Set $f(x) = \phi_m(x)$ and let $f_j(x)$ denote the j -th output of f . [Weng et al. \(2018a\)](#) start from analyzing the ReLU activation patterns and then deriving gradient bounds under this setting for bounding local Lipschitz constant.

Activation Patterns of ReLU Networks. Let $l_r^{(k)}$ and $u_r^{(k)}$ denote the lower and upper bound for the r -th neuron in the k -th layer and let $z_r^{(k)}$ be the pre-activation at the k -th layer, given as:

$$z_r^{(k)} = W_{r,:}^{(k)} \phi_{k-1}(x) + b_r^{(k)}, \quad (2.138)$$

where $W_{r,:}^{(k)}$ denotes the r -th row of $W^{(k)}$ (Weng et al., 2018a, § 3.2). For the neurons indexed by $[n_k] := \{1, 2, \dots, n_k\}$, then there are only three activation patterns:

1. **Always Activated.** Neurons are always activated: $\mathcal{I}_k^+ := \{r \in [n_k] \mid u_r^{(k)} \geq l_r^{(k)} \geq 0\}$.
2. **Always Inactivated.** Neurons are always inactivated: $\mathcal{I}_k^- := \{r \in [n_k] \mid l_r^{(k)} \leq u_r^{(k)} \leq 0\}$.
3. **Either Activated or Inactivated.** Neurons are either activated or inactivated: $\mathcal{I}_k := \{r \in [n_k] \mid l_r^{(k)} \leq 0 \leq u_r^{(k)}\}$.

Gradient Analysis of ReLU Networks. Gradient norm carries the information for local Lipschitz constant. Weng et al. (2018a) then analyze the coordinate-wise gradients of ReLU networks with a manner of layer-wise. Using the activation patterns of ReLU networks, the k -th layer output can be rewritten into:

$$\phi_k(x) = \Lambda^{(k)} \left(W^{(k)} \phi_{k-1}(x) + b^{(k)} \right), \quad (2.139)$$

where $\Lambda^{(k)}$ is the activation pattern matrix:

$$\Lambda_{r,r}^{(k)} = \begin{cases} 1 \text{ or } 0, & \text{if } r \in \mathcal{I}_k \\ 1, & \text{if } r \in \mathcal{I}_k^+ \\ 0, & \text{if } r \in \mathcal{I}_k^- \end{cases} \quad (2.140)$$

Let $\Lambda_a^{(k)}$ be the diagonal activation matrix for neurons in the k -th layer that are always activated and set $\Lambda_u^{(k)} := \Lambda^{(k)} - \Lambda_a^{(k)}$. Starting by analyzing the bound of the gradient $\nabla \phi_k(x)$ coordinate-wisely in a 2-layer ReLU network, Weng et al. (2018a) show that an inequality for gradient q -norm holds:

$$\max_{x \in B_p(x_0, \epsilon)} \left| [\nabla f_j(x)]_k \right| \leq \max \left(C_{j,k}^{(1)} + L_{j,k}^{(1)}, C_{j,k}^{(1)} + U_{j,k}^{(1)} \right), \quad (2.141)$$

where:

$$C_{j,k}^{(1)} = W_{j,:}^{(2)} \Lambda_a^{(1)} W_{:,k}^{(1)}, \quad (2.142)$$

$$L_{j,k}^{(1)} = \sum_{i \in \mathcal{I}_1, W_{j,i}^{(2)} W_{i,k}^{(2)} < 0} W_{j,i}^{(2)} W_{i,k}^{(2)}, \quad \text{and} \quad U_{j,k}^{(1)} = \sum_{i \in \mathcal{I}_1, W_{j,i}^{(2)} W_{i,k}^{(2)} > 0} W_{j,i}^{(2)} W_{i,k}^{(2)}. \quad (2.143)$$

Then the gradient q -norm can be bounded above by:

$$\text{Lip}_q [f_j; B_p(x_0, \epsilon)] = \max_{x \in B_p(x_0, \epsilon)} \|\nabla f_j(x)\|_q \leq \left[\sum_k \left(\max_{x \in B_p(x_0, \epsilon)} \|\nabla f_j(x)\|_k \right) \right]^{\frac{1}{q}}, \quad (2.144)$$

yielding a local Lipschitz constant upper bound. This method is referred to as **Fast-Lip** in [Weng et al. \(2018a\)](#).

2.3.4 Spectral Alignment

SeqLip ([Virmaux and Scaman, 2018](#)) refines the upper bound of an L -layer sequential network f with 1-Lipschitz activation functions:

$$\text{Lip}[f]^+ = \prod_{\ell=1}^L \|W^{(\ell)}\|_2, \quad (2.145)$$

where $W^{(\ell)} \in \mathbb{R}^{n_\ell \times n_{\ell+1}}$ is the ℓ -th layer parameter matrix, and $\text{Lip}[f]^+$ is referred to as **AutoLip** bound in [Virmaux and Scaman \(2018\)](#). By taking into account the spectral alignment between the parameter matrices of two consecutive layers, the bound is then refined as:

$$\begin{aligned} \text{Lip}[f] &\leq \text{Lip}[f]^+ \\ &\underbrace{\left(\prod_{\ell=1}^{L-1} \sqrt{(1 - r_\ell - r_{\ell+1})} \max_{t^{(\ell)} \in [0,1]^{n_\ell}} \langle t^{(\ell)} \cdot v_1^{(\ell+1)}, u_1^{(\ell)} \rangle^2 + r_\ell + r_{\ell+1} + r_\ell r_{\ell+1} \right)}_{\text{spectral alignment}} \end{aligned} \quad (2.146)$$

where $t^{(\ell)}[0, 1]^{n_\ell}$ represents the ℓ -th layer gradient patterns from activation functions for n_ℓ neurons — the coordinate-wise gradient of an activation function such as ReLU falls in $[0, 1]$, $u_1^{(\ell)}$ is the first left-singular vector for $W^{(\ell)}$, $v_1^{(\ell+1)}$ is the first right-singular vector

for $W^{(\ell+1)}$, and $r_\ell = \frac{\sigma_2^{(\ell)}}{\sigma_1^{(\ell)}}$ is the ratio of the second largest singular value to the first largest singular value for $W^{(\ell+1)}$ (Virmaux and Scaman, 2018, Theorem 3).

Virmaux and Scaman (2018) also show that, if $u, v \in \mathbb{R}^n$ are two independent random vectors taken uniformly from $S^{n-1} = \{x \in \mathbb{R}^n \mid \|x\|_2 = 1\}$, the following limit:

$$\lim_{n \rightarrow \infty} \max_{t \in [0,1]^n} |\langle t \cdot u, v \rangle| = \frac{1}{\pi} \quad (2.147)$$

holds *almost surely*. Under this independent assumption, the bound reduces to:

$$\text{Lip}[f] \leq \frac{\text{Lip}[f]^+}{\pi^{L-1}} \quad (2.148)$$

(Virmaux and Scaman, 2018, Lemma 2). In real setting, the singular vectors are not independent across layers.

2.3.5 Convex Optimization Relaxation

LipSDP (Fazlyab et al., 2019) interpret activation functions as gradients of convex potential functions, satisfying certain properties described by quadratic constraints. Therefore, Lipschitz constant estimation problem is treated as a semidefinite program (SDP) problem.

Let $f : \mathbb{R}^{n_0} \rightarrow \mathbb{R}^{n_L}$ be an L-layer feed-forward network, recursively defined as:

$$\begin{cases} x^{(0)} = x \\ x^{(k+1)} = \phi(W^{(k)}x^{(k)} + b^{(k)}) \end{cases}, \quad (2.149)$$

where $x^{(\ell)}$ is the output at the ℓ -th layer, $W^{(\ell)} \in \mathbb{R}^{n_{\ell+1} \times n_\ell}$ is the parameter matrix at the ℓ -th layer, $b^{(\ell)} \in \mathbb{R}^{n_{\ell+1}}$ is the bias at the ℓ -th layer, and ϕ is the coordinate-wise activation function. For a single layer network:

$$f(x) = W^{(1)}\phi(W^{(0)}x + b^{(0)} + b^{(1)}), \quad (2.150)$$

Fazlyab et al. (2019) shows that the Lipschitz constant of f is given by a SDP problem:

$$\text{Lip}[f] \leq \sqrt{\rho}, \quad (2.151)$$

defined by:

$$\text{minimize } \rho \quad (2.152)$$

$$\text{subject to } M(\rho, T) \leq 0 \quad T \in T_n, \quad (2.153)$$

where ϕ is *slope-restricted* on $[\alpha, \beta]$:

$$\alpha \leq \frac{\phi_j(x) - \phi_j(y)}{x - y} \leq \beta \quad \forall x, y \in \mathbb{R} \quad (2.154)$$

and:

$$M(\rho, T) := \begin{bmatrix} -2\alpha\beta(W^{(0)})^\top TW^{(0)} & (\alpha + \beta)(W^{(0)})^\top \\ (\alpha + \beta)TW^{(0)} & -2T + (W^{(1)})^\top W^{(1)} \end{bmatrix} \leq 0 \quad (2.155)$$

holds true for $T \in T_n$ (Fazlyab et al., 2019, Theorem 1). For more general L-layer fully-connected network, Fazlyab et al. (2019) show that $M(\rho, T)$ is:

$$M(\rho, T) = \begin{bmatrix} A \\ B \end{bmatrix}^\top \begin{bmatrix} -2\alpha\beta T & (\alpha + \beta)T \\ (\alpha + \beta)T & -2T \end{bmatrix} \begin{bmatrix} A \\ B \end{bmatrix} + \begin{bmatrix} -\rho I_{n_0} & 0 & \cdots & 0 \\ 0 & 0 & \cdots & 0 \\ \vdots & \vdots & \ddots & \vdots \\ 0 & 0 & \cdots & (W^{(L)})^\top W^{(L)} \end{bmatrix} \leq 0, \quad (2.156)$$

where:

$$A = \begin{bmatrix} W^{(0)} & 0 & \cdots & 0 & 0 \\ 0 & W^{(1)} & \cdots & 0 & 0 \\ \vdots & \vdots & \ddots & \vdots & \vdots \\ 0 & 0 & \cdots & W^{(L-1)} & 0 \end{bmatrix}, \quad B = \begin{bmatrix} 0 & I_{n_1} & 0 & \cdots & 0 \\ 0 & 0 & I_{n_2} & \cdots & 0 \\ \vdots & \vdots & \vdots & \ddots & \vdots \\ 0 & 0 & 0 & \cdots & I_{n_L} \end{bmatrix}, \quad (2.157)$$

and:

$$C = \begin{bmatrix} 0 & \cdots & 0 & W^{(L)} \end{bmatrix}, \quad b = \left[(b^{(0)})^\top \cdots (b^{(L-1)})^\top \right]^\top \quad (2.158)$$

(Fazlyab et al., 2019, Theorem 2).

2.3.6 Integer Programming for ReLU Networks

It is well known that computing the Lipschitz constant of an arbitrary scalar- or vector-valued function is NP-hard (Virmaux and Scaman, 2018; Jordan and Dimakis, 2020). A

common approximation is to estimate the Lipschitz constant using gradient norms, where the Jacobians can be explicitly derived via the chain rule. However, nondifferentiabilities, *e.g.*, those arising in ReLU networks, can introduce inaccuracies into these estimates. An alternative approach is to formulate the Lipschitz bounding problem as an integer programming problem, which avoids such inaccuracies by directly bounding the Jacobians.

LipMIP (**Jordan and Dimakis, 2020**) is a method that provably exactly compute 2-norm and ∞ -norm Lipschitz constants of non-smooth ReLU networks. We summarize their method by simplifying their notations. Let $f : \mathbb{R}^d \rightarrow \mathbb{R}$ be a ReLU network. Let σ be activation function. Then, an L -layer ReLU network is recursively defined as:

$$\begin{cases} f(x) = \sigma(Z_L(x)) \\ Z^{(\ell)}(x) = W^{(\ell)} \sigma(Z^{(\ell-1)}(x)) + b^{(\ell)} \\ Z^{(0)} = x \end{cases}, \quad (2.159)$$

where $W^{(\ell)} \in \mathbb{R}^{n_\ell \times n_{\ell-1}}$ is the ℓ -th layer parameter matrix, and $Z^{(\ell)}(x)$ is the output of the ℓ -th layer neurons. Let $\partial f(x)$ be the Clarke sub-differential convex hull of f at point x — see Section 2.2.4 (**Sub-Differential Convex Functions**). For example:

$$\partial \sigma(0) = [0, 1]. \quad (2.160)$$

Let $\partial f(X)$:

$$\partial f(X) = \left\{ g \mid g \in \partial f(x), x \in X \right\} \quad (2.161)$$

be the set-valued Clarke sub-differentials at set X . Let $\nabla^\# f(\bullet)$ be the pushforward set that the sub-gradients of ReLU activation at value 0 come from the hull set $\partial \sigma(0)$:

$$\nabla^\# f(\bullet) = \left\{ \nabla f(\bullet) \mid \text{the sub-differentials of activations come from the hull set } \partial \sigma(0) \right\}. \quad (2.162)$$

Thus for a ReLU network, the *feasible set* for its gradients on X are given as:

$$\nabla^\# f(X) = \left\{ G \in \nabla^\# f(x) \mid x \in X \right\}. \quad (2.163)$$

Jordan and Dimakis (2020) show that the push forward set sub-gradient $\nabla^\# f(x)$ is the Clarke sub-gradient hull $\partial f(x)$, that is:

$$\nabla^\# f(x) = \partial f(x) \quad (2.164)$$

(Jordan and Dimakis, 2020, Theorem 2). Then the local $p \rightarrow q$ Lipschitz constant of f on X is given as:

$$\text{Lip}_{p \rightarrow q}[f; X] = \sup_{G \in \nabla^{\#} f(X)} \sup_{\|v\|_p \leq 1} \frac{\|G^T v\|_q}{\|v\|_p} = \sup_{G \in \nabla^{\#} f(X)} \|G^T\|_q. \quad (2.165)$$

Finding the Lipschitz constant on X can be formulated as an integer programming problem on the feasible set $\nabla^{\#} f(X)$. Let $n = \sum_{\ell=1}^L n_{\ell}$ be the number of neurons in f . The set:

$$\left\{ \|G^T\|_q \mid G \in \nabla^{\#} f(X) \right\} \quad (2.166)$$

is then represented as a mixed-integer programming problem for maximizing $\|G^T\|_q$ by solving the combinations of input $x \in X$ and ReLU's sub-gradient $a \in [0, 1]^n$ on a mixed-integer polytope in $X \times [0, 1]^n$, such that $\nabla^{\#} f(x)$ is represented with some A , B and c :

$$\nabla^{\#} f(x) = Ax + Ba < c \quad (2.167)$$

by analyzing gradients with chain rules on ReLU networks (Jordan and Dimakis, 2020, Definition 6 & Lemma 1). This problem can be solved by off-the-shelf MIP solvers.

2.4 Regularization Approaches

A variety of techniques have been developed to explicitly or implicitly enforce Lipschitz continuity in deep neural networks. These approaches can be categorized into:

- (i) Section 2.4.1: **Weight Regularization** — constraining or regularizing weight matrices during initialization and training;
- (ii) Section 2.4.2: **Gradient Regularization** — penalizing or normalizing gradient norms during training;
- (iii) Section 2.4.3: **Activation Regularization** — designing or constraining activation functions to be Lipschitz-bounded;
- (iv) Section 2.4.4: **Class-Margin Regularization** — implicitly enforcing Lipschitz constraints via maximizing class decision boundaries;
- (v) Section 2.4.5: **Architectural Regularization** — enforcing Lipschitz constraints by designing architectures, particularly for transformers.

2.4.1 Weight Regularization

This subsection reviews methods that control the Lipschitz constant by directly constraining or regularizing the network’s weight parameters, either at initialization or during training.

2.4.1.1 Spectral-Norm Regularization

Spectral-norm regularization constrains the Lipschitz constant of a neural network by bounding the spectral-norm of its weight matrices, which is the largest singular value of the matrix (Proposition 2.2.16). Miyato et al. (2018) propose normalizing the weight matrix W of a linear layer by:

$$W \leftarrow \frac{W}{\|W\|_2}, \quad (2.168)$$

ensuring a Lipschitz constant of at most 1 for the layer (Miyato et al., 2018, § 3). This method, later adopted by Miyato et al. in generative adversarial networks (GANs) (Goodfellow et al., 2014), for improving the generations (Miyato et al., 2018, § 2.1).

2.4.1.2 Weight Clipping

Weight clipping is a straightforward method to enforce Lipschitz continuity by limiting the magnitude of weight matrices. This is because for a matrix W , the operator-norm variation $\|W\|_{\text{op}}$ in ℓ_2 for W under perturbation ΔW is bounded above by:

$$\|W\|_{\text{op}} = \sigma_1(W) = \langle u_1 v_1^\top, \Delta W \rangle \leq \|u_1 v_1^\top\|_2 \|\Delta W\|_2, \quad (2.169)$$

with Cauchy–Schwarz inequality, where $\sigma_1(W)$ is the largest singular value of W , u_1, v_1 are the left- and right-singular vectors corresponding the largest singular value (Róisín Luo et al., 2025c, Lemma 5.1).

In the setting of GANs, Arjovsky et al. (2017) show that the discriminator f of a GAN evaluates the Wasserstein distance $W(\mathbb{P}, \mathbb{Q})$ between two distributions \mathbb{P} and \mathbb{Q} . The Kantorovich–Rubinstein duality (Villani et al., 2008) tells that:

$$W(\mathbb{P}, \mathbb{Q}) = K \sup_{\text{Lip}[f] \leq K} \mathbb{E}_{x \sim \mathbb{P}}[f(x)] - \mathbb{E}_{y \sim \mathbb{Q}}[f(y)] \quad (2.170)$$

(Arjovsky et al., 2017, Equation 2). Therefore reducing the Lipschitz constant K can reduce the Wasserstein distance $W(P, Q)$. Arjovsky et al. (2017) propose clipping weights to a fixed range:

$$W \leftarrow \text{clip}(W, -c, +c) \quad (2.171)$$

(Arjovsky et al., 2017, Algorithm 1), where c is a small positive constant (e.g., $c = 0.01$). Weight clipping is computationally efficient, but can lead to exploding or vanishing gradients if c is too small, reducing model capacity, as criticized in the a later literature (Gulrajani et al., 2017).

2.4.1.3 Orthogonal Weight

Parseval Networks (Cisse et al., 2017). Parseval networks enforce approximate orthonormality on weight matrices to bound their spectral-norms (Cisse et al., 2017). For a weight matrix $W^{(\ell)}$ in layer ℓ , Cisse et al. (2017) minimize the 2-norm of the deviation from orthonormality:

$$\|W^{(\ell)\top}W^{(\ell)} - I\|_F, \quad (2.172)$$

ensuring $\|W^{(\ell)}\|_2 \leq 1$ (Cisse et al., 2017, § 4.2). For a feedforward network with L layers and 1-Lipschitz activations (e.g., ReLU), the global Lipschitz constant is bounded by:

$$K \leq \prod_{\ell=1}^L \|W^{(\ell)}\|_2 \leq 1 \quad (2.173)$$

(Proposition 2.2.18). Cisse et al. (2017) argue that the robustness to adversarial attacks is enhanced since the reduced sensitivity to perturbations.

2.4.2 Gradient Regularization

Gradient-based regularization methods enforce Lipschitz continuity by constraining the gradient norm of the loss function or network output with respect to inputs, ensuring smooth decision boundaries and robustness. Note that, for a network f on convex X , its 2-norm Lipschitz constant on X is given by:

$$\text{Lip}[f] = \sup_{x \in X} \|\nabla f(x)\|_2, \quad (2.174)$$

see 2.2.5 (Lipschitz Constant Bounds Gradient Norm). Theoretically, constraining $\|\nabla f(x)\|_2$ can bound Lipschitz constant of f .

For example, [Gulrajani et al. \(2017\)](#) argue that bounding Lipschitz constant by weight clipping can lead exploding or vanishing gradients, and reduce capacity of the critic in a GAN. They then introduce a regularization method by directly bounding the gradients of the critic network D through:

$$\mathbb{E}_{x \sim \mathbb{P}_X} \left[(\|\nabla D(x)\|_2 - 1)^2 \right], \quad (2.175)$$

where \mathbb{P}_X is the distribution of training sample set X ([Gulrajani et al., 2017](#), § 4).

2.4.3 Activation Regularization

Activation regularization methods modulates Lipschitz continuity by constraining the properties of activation functions or their outputs. Such approaches may impose explicit norm bounds, design activations that are inherently norm-preserving, or apply penalties to activation magnitudes, thereby limiting the contribution of nonlinearities to the overall Lipschitz constant of the network.

2.4.3.1 Group-Sorting Activation

Bounding the Lipschitz constant of a network by ensuring 1-Lipschitz for affine units through spectral-norm constraints can improve robustness ([Miyato et al., 2018](#)). However, this often comes at the cost of reduced expressiveness ([Anil et al., 2019](#)). [Anil et al. \(2019\)](#) first show that, to remain expressive in a spectral-norm constrained network, the network must preserve the gradient norms at each layer ([Anil et al., 2019](#)). ReLU networks can only satisfy this for positive values, this is because:

$$\frac{\partial \text{ReLU}(x)}{\partial x} = \begin{cases} 1, & x > 0 \\ (0, 1), & \text{in sub-differential sense} \\ 0, & x < 0 \end{cases} \quad (2.176)$$

To preserve the gradient norms at activation layer, [Anil et al. \(2019\)](#) use a general purpose 1-Lipschitz activation function **GroupSort**(x) which is homogeneous:

$$\text{GroupSort}(\alpha x) = \alpha \text{GroupSort}(x) \quad (2.177)$$

(Anil et al., 2019). **GroupSort** activation separates a pre-activation x into k groups:

$$x = (\underbrace{x_1, \dots, x_{g_1}}_{\text{group 1}}, \underbrace{x_{g_1+1}, \dots, x_{g_2}}_{\text{group 2}}, \dots, \underbrace{x_{g_{k-1}+1}, \dots, x_{g_k}}_{\text{group } k}), \quad (2.178)$$

and sorts each group into ascending order:

$$\mathbf{GroupSort}(x) = (\underbrace{x_{s_1}, \dots, x_{s_{g_1}}}_{\text{group 1}}, \underbrace{x_{s_{g_1}+1}, \dots, x_{s_{g_2}}}_{\text{group 2}}, \dots, \underbrace{x_{s_{g_{k-1}}+1}, \dots, x_{s_{g_k}}}_{\text{group } k}), \quad (2.179)$$

where the i -th sorted group satisfies:

$$x_{s_{g_{i-1}}+1} \leq x_{s_{g_{i-1}}+2} \leq \dots \leq x_{s_{g_i}} \quad (2.180)$$

(Anil et al., 2019). For the pre-activation in a linear unit:

$$Wx \quad (2.181)$$

where $W \in \mathbb{R}^{m \times n}$ and $x \in \mathbb{R}^n$, if the linear unit is with spectral-norm constraint such that:

$$\|W\|_2 = 1, \quad (2.182)$$

GroupSort activation directly gives rise an 1-Lipschitz constant activation:

$$\sup_{\|x\|_2=1} \|\mathbf{GroupSort}(Wx)\|_2 = \sup_{\|x\|_2=1} \|Wx\|_2 = \|W\|_2. \quad (2.183)$$

When the group size is 2, Anil et al. (2019) refers to this special case as **MaxMin**, which is equivalent to the Orthogonal Permutation Linear Unit (OPLU) (Chernodub and Nowicki, 2017); when the group size is the entire input, this is referred to as **FullSort** in the literature (Chernodub and Nowicki, 2017).

To train a network with **GroupSort** activations and guarantee that all linear units are exactly 1-Lipschitz during optimization instead of bounded by 1 (Cisse et al., 2017; Gulrajani et al., 2017), Chernodub and Nowicki (2017) approximate the updated parameter matrix W_0 with a closest orthogonal matrix through a differentiable, iterative algorithm,

referred to as *Björck Orthogonalization* (Björck and Bowie, 1971). This algorithm is defined by:

$$W_{k+1} = W_k \left(I + \frac{1}{2} Q_k + \cdots + (-1)^p \begin{pmatrix} -\frac{1}{2} \\ p \end{pmatrix} Q_k^p \right), \quad (2.184)$$

where W_k is the k -th iterative result, p is a chosen hyper-parameter and Q_k is:

$$Q_k = I - W_k^\top W_k \quad (2.185)$$

(Chernodub and Nowicki, 2017, § 4.2.1). As a result, the iteration at step T leads to:

$$W_T^\top W_T \approx I, \quad (2.186)$$

which provably ensures the linear unit with parameter matrix W is 1-Lipschitz continuous:

$$\|W_T\|_2 \approx 1. \quad (2.187)$$

2.4.3.2 Contraction Activation and Invertible Residual Map

Flow-based models or flows learn to transform a source distribution p_X to target distribution p_Z , consisting of invertible networks (Rezende and Mohamed, 2015). Ensuring that the transformation is invertible and its Jacobian are computable is a straightforward way for ensuring invertibility:

$$\log p_X(x) = \log p_Z(z) + \log |\det J_F(x)| \quad (2.188)$$

where $F : \mathbb{R}^m \rightarrow \mathbb{R}^m$ is an invertible map and $J_F(x)$ is the Jacobian of F at x (Van Den Berg et al., 2018; Dinh et al., 2017). Different from explicit computation of Jacobian, Behrmann et al. (2019) propose a method for inverting residual networks (He et al., 2016) by ensuring the Lipschitz constants be less than 1, so that the residual networks are *contraction maps* (Behrmann et al., 2019; Perugachi-Diaz et al., 2021).

Inverting Residual Layer. Let

$$F(x) = x + g(x) \quad (2.189)$$

be a residual layer where $F : \mathbb{R}^m \rightarrow \mathbb{R}^m$, $g : \mathbb{R}^m \rightarrow \mathbb{R}^m$ and $x \in \mathbb{R}^m$. Let g be a contraction map:

$$\text{Lip}[g] < 1. \quad (2.190)$$

Suppose that the inversion F^{-1} exists and set $y = F(x)$, so that:

$$F^{-1}(x) = x = y - g(x). \quad (2.191)$$

Set:

$$T(x) = y - g(x), \quad (2.192)$$

note that:

$$\text{Lip}[T] = \text{Lip}[g] < 1 \quad (2.193)$$

is a contraction mapping. Using *Banach contraction principle* or *Banach fixed-point theorem*, set $x_0 = y$, the $F^{-1}(y)$ can be approximated through:

$$x_{k+1} = y - g(x_k) \quad (2.194)$$

iteratively. The **essential condition** for inverting g is that g must be a contraction map:

$$\text{Lip}[g] < 1. \quad (2.195)$$

Contraction Activation. Chen et al. (2019) first introduce **LipSwish** activation function for inverting residual networks, defined as:

$$\text{LipSwish}(x) = \frac{x\sigma(\beta x)}{1.1}, \quad (2.196)$$

where σ is the sigmoid function, and $\beta > 0$ is a learnable negative constant, initialized with 0.5. **LipSwish** has a Lipschitz constant at most 1. However, the negative axis of **LipSwish** has zero gradients almost everywhere. In a 1-Lipschitz continuous network, the Jacobian norm across two consecutive layers is reduced to be at most one, which limits the network's expressiveness and referred to as *gradient norm attenuation* problem (Anil et al., 2019; Li et al., 2019a). To mitigate this problem, Perugachi-Diaz et al. (2021)

use specially designed activation function **CLipSwish** by concatenating two **LipSwish** functions. The **CLipSwish** is therefore given as:

$$\Phi(x) = \begin{bmatrix} \text{LipSwish}(x) \\ \text{LipSwish}(-x) \end{bmatrix}, \quad \text{CLipSwish}(x) = \frac{\Phi(x)}{\text{Lip}[\Phi]} \leq 1, \quad (2.197)$$

where $\text{Lip}[\Phi] \approx 1.004$ (Perugachi-Diaz et al., 2021, § 3.4). This concatenation overcomes the gradient attenuation problem introduced by **LipSwish** since the negative axis has zero gradients almost everywhere while ensuring the activation is a contraction map.

2.4.4 Class-Margin Regularization

The goal of adversarial defense in classification task is to ensure that, for a k -class classifier $f : \mathbb{R}^d \rightarrow \mathbb{R}^k$, and an input $x \in \mathbb{R}^d$, a bounded perturbation $\|\epsilon_x\|_2 < c$ does not alter the prediction:

$$\arg \max_{i \in [k] = \{1, 2, \dots, k\}} f_i(x + \epsilon_x), \quad (2.198)$$

where $f_i(x)$ denotes the output at the i -th coordinate. The margin $m(x)$ is defined as:

$$m(x) = f_i(x) - \max_{j \neq i} f_j(x), \quad (2.199)$$

where i is the ground-truth (Tsuzuku et al., 2018, § 4.1). Then, a guaranteed 2-norm perturbation bound does not alter the prediction, if:

$$\|\epsilon_x\|_2 \leq \frac{m(x)}{\sqrt{2} \text{Lip}[f]} \quad (2.200)$$

(Szegedy et al., 2014; Cisse et al., 2017). This implies that the class margin must be at least:

$$m(x) = f_i(x) - \max_{j \neq i} f_j(x) \geq \sqrt{2} \text{Lip}[f] \quad (2.201)$$

(Tsuzuku et al., 2018, Proposition 1 & 2). Suppose i is the ground-truth for x , in training stage, Perugachi-Diaz et al. (2021) adjust each class margin $j \neq i$ by:

$$f_j(x) \leftarrow f_j(x) + \sqrt{2} c \text{Lip}[f], \quad (2.202)$$

where c is a guaranteed perturbation bound (Perugachi-Diaz et al., 2021, Algorithm 1). For each linear unit $\phi : \mathbb{R}^m \rightarrow \mathbb{R}^n$ in the network, and let $u \in \mathbb{R}^m$ be drawn i.i.d. from $\mathcal{N}(0, 1)$. Perugachi-Diaz et al. (2021) use a general method for estimating the Lipschitz constant of ϕ iteratively by:

$$u_k \leftarrow \frac{u_k}{\|u_k\|_2}, \quad v_k \leftarrow \phi(u_k), \quad u_{k+1} \leftarrow \frac{1}{2} \frac{\partial \|v_k\|_2^2}{\partial u}. \quad (2.203)$$

At the end of the iteration T , the Lipschitz constant of ϕ is given by:

$$\text{Lip} [\phi] \approx \|u_T\|_2, \quad (2.204)$$

almost surely (Perugachi-Diaz et al., 2021).

2.4.5 Architectural Regularization

Lipschitz continuity can also be constrained through architectural design choices, including activation functions, parameter structures, initialization schemes, and optimization. As a complement to regularization approaches that do not fall into one single category, we survey these approaches in this section.

2.4.5.1 Orthogonalizing Convolution

Parameter orthogonality in neural networks can directly yield 1-Lipschitz continuous (Proposition 2.2.8) ([Lipschitz Constant of Semi-Orthogonal Matrix](#)). This is because, for a matrix $W \in \mathbb{R}^{m \times n}$, an semi-orthogonal matrix W preserves the 2-norm:

$$W^\top W = I_n \quad \text{or} \quad W W^\top = I_m \quad \implies \quad \text{Lip} [W] = 1, \quad (2.205)$$

if $m \geq n$ and $W^\top W = I_n$, W is an isometric map; if $m < n$ and $W W^\top = I_m$, W is a contraction map on the kernel $\ker(W)$ strictly (Proposition 2.2.8) ([Lipschitz Constant of Semi-Orthogonal Matrix](#)).

Extending Semi-Orthogonality to Convolution. Let $W \in \mathbb{R}^{c_{\text{out}} \times c_{\text{in}} \times n \times n}$ be a convolutional filter where c_{out} is the number of output channels, c_{in} is the number of input

channels, and $n \times n$ are the input dimensions. The action on an input $x \in \mathbb{R}^{c_{\text{in}} \times n \times n}$ is denoted by:

$$W \circledast x : \mathbb{R}^{c_{\text{in}} \times n \times n} \rightarrow \mathbb{R}^{c_{\text{out}} \times n \times n}. \quad (2.206)$$

Using the norm preserving concept for 1-Lipschitz maps on ℓ_2 , for $\forall x \in \mathbb{R}^{c_{\text{in}} \times n \times n}$, if the 2-norms are preserved:

$$\|W \circledast x\|_2 = \|x\|_2, \quad (2.207)$$

then the convolutional filter W is referred to as semi-orthogonal (Trockman and Kolter, 2021).

Filter Orthogonalization via Cayley Transform. However, convolutional operation is not matrix multiplication, to apply the existing results from matrix theory, Trockman and Kolter (2021) harness the *Convolutional Theorem* (Jain, 1989) for converting the convolutional operation in spatial domain to multiplication in frequency domain by:

$$\mathcal{F}[W \circledast x][:, i, j] = \mathcal{F}[W][:, :, i, j] \mathcal{F}[x][:, :, i, j] = \widehat{W}[:, i, j] \widehat{x}[:, i, j], \quad (2.208)$$

where \mathcal{F} represents Fourier transform, $\widehat{W} = \mathcal{F}[W]$, $\widehat{x} = \mathcal{F}[x]$, $[:, :, i, j]$ and $[:, i, j]$ are slicing operations by fixing indices (i, j) (Trockman and Kolter, 2021, Equation 3 & 4, § 4). Note that $\widehat{W}[:, :, i, j]$ is not orthogonal or semi-orthogonal, Trockman and Kolter (2021) use a bijective *Cayley Transform* for deriving an orthogonal matrix $Q[:, :, i, j]$ from $\widehat{W}[:, :, i, j]$ by:

$$Q[:, :, i, j] = (I - A[:, :, i, j])(I + A[:, :, i, j])^{-1}, \quad (2.209)$$

where:

$$A[:, :, i, j] = \widehat{W}[:, :, i, j] - \widehat{W}[:, :, i, j]^*, \quad (2.210)$$

and $A[:, :, i, j]$ is referred to as *skew-symmetric* matrix (Trockman and Kolter, 2021). Conceptually, the convolution on frequency domain is then computed through:

$$\mathcal{F}[W \circledast x][:, i, j] = Q[:, :, i, j] \widehat{x}[:, i, j] \quad (2.211)$$

$$= (I - A[:, :, i, j])(I + A[:, :, i, j])^{-1} \widehat{x}[:, i, j], \quad (2.212)$$

then $Q[:, :, i, j] \hat{x}[:, i, j]$ is inverted back to spatial domain by:

$$\mathcal{F}^{-1} [Q[:, :, i, j] \hat{x}[:, i, j]], \quad (2.213)$$

which leads to the convolution 1-Lipschitz continuous.

2.4.5.2 Orthogonality with Lie Unitary Group

Lezcano-Casado and Martínez-Rubio (2019) introduce a method, stemming from Lie group theory, through the exponential map, for ensuring 1-Lipschitz by construction. Orthogonal constraints networks can improve the robustness and generalization capabilities (Huang et al., 2018; Bansal et al., 2018). For a matrix A , if $AA^* = I$, then the matrix A is referred to as an unitary matrix. Unitary matrices allow to solve the exploding or vanish gradients (Arjovsky et al., 2016, 2017). In the sense of Lie algebra, these unitary matrices form a special orthogonal group on field \mathbb{R} :

$$SO(n) = \left\{ A \in \mathbb{R}^{n \times n} \mid A^T A = I \right\} \quad (2.214)$$

and unitary group on field \mathbb{C} :

$$U(n) = \left\{ A \in \mathbb{C}^{n \times n} \mid A^* A = I \right\} \quad (2.215)$$

(Lezcano-Casado and Martínez-Rubio, 2019, § 3.1). We are interested of converting a parameter matrix $W \in \mathbb{R}^{n \times n}$ to on $SO(n)$ or $U(n)$. Lezcano-Casado and Martínez-Rubio (2019) harness the concept of *skew-symmetric matrix* group (Definition 2.2.7 (Skew-Hermitian & Skew-Symmetric Matrix)) as a bridge:

$$\mathfrak{so}(n) = \left\{ B \in \mathbb{R}^{n \times n} : B = -B^T \right\} \quad (2.216)$$

and:

$$\mathfrak{u}(n) = \left\{ B \in \mathbb{R}^{n \times n} : B = -B^* \right\}. \quad (2.217)$$

Taking:

$$B = W - W^T \quad (2.218)$$

can easily send a parameter matrix W to $\mathfrak{u}(n)$.

Connecting to Lie Orthogonal Group. Then there exist an exponential *surjective* map between two groups:

$$\exp : \mathfrak{so}(n) \rightarrow SO(n) \quad (2.219)$$

and:

$$\exp : \mathfrak{u}(n) \rightarrow U(n), \quad (2.220)$$

which is defined as:

$$\exp(B) = I + B + \frac{1}{2}B^2 + \dots \quad (2.221)$$

(Lezcano-Casado and Martínez-Rubio, 2019, § 3.2). Then a network $f(x; W)$ is parameterized on the Lie group $SN(n)$ by an algebraic mapping chain:

$$W \in \mathbb{R}^{n \times n} \xrightarrow{B=W-W^\top} B \in \mathfrak{so}(n) \xrightarrow{A=\exp(B)} A \in SO(n), \quad (2.222)$$

and the optimization problem becomes:

$$\min_A f(x; A) \iff \min_B f(x; \exp(B)) \quad (2.223)$$

(Lezcano-Casado and Martínez-Rubio, 2019, § 3.3).

Optimizing on Lie Orthogonal Group. The Lie group $SO(n)$ forms a Riemannian manifold, to optimize a function f on the Riemannian manifold $SO(n)$:

$$f : \mathcal{X} \times SO(n) \rightarrow \mathbb{R}, \quad (2.224)$$

where \mathcal{X} is input space, one may use *Riemannian gradient descent* (Absil et al., 2007). Given a point on the manifold $A \in SO(n)$, $\mathcal{T}_A SO(n)$ is the tangent space at A with induced metric, and a gradient $\Omega \in \mathcal{T}_A SO(n)$, then the geodesic update is:

$$A \leftarrow A \exp(-\eta A^* \Omega), \quad (2.225)$$

where η is a learning rate $\eta > 0$ (Lezcano-Casado and Martínez-Rubio, 2019). Computing the Riemannian exponential map is expensive, Lezcano-Casado and Martínez-Rubio (2019) use a first-order approximation, *i.e.*, *Cayley map*, for the update instead:

$$A \leftarrow A \phi(-\eta A^* \Omega), \quad (2.226)$$

where ϕ is the *Cayley map*:

$$\phi(A) = (I + \frac{1}{2}A)(I - \frac{1}{2}A)^{-1} \quad (2.227)$$

(Wisdom et al., 2016; Vorontsov et al., 2017). Finally, this induces an update rule on $B \in \mathfrak{so}(n)$:

$$\exp(B) \leftarrow \exp\left(B - \eta \nabla f(x; \exp(B))\right) \quad (2.228)$$

where $\nabla f(x; \exp(B))$ is the usual gradient with Euclidean metric. In a specially designed recurrent neural network (RNN), Lezcano-Casado and Martínez-Rubio (2019) transform the matrix exponential maps skew-symmetric matrices to orthogonal matrices transforming an optimization problem with orthogonal constraints (Lezcano-Casado and Martínez-Rubio, 2019). Particularly, Lezcano-Casado and Martínez-Rubio (2019) use Padé approximants and the scale-squaring trick to compute machine-precision approximations of the matrix exponential and its gradient (Lezcano-Casado and Martínez-Rubio, 2019). As a result, the optimization remains in the group and the Lipschitz constants of the updated matrices remain 1 by design.

2.4.5.3 Lipschitz Continuous Transformer

Qi et al. (2023) demonstrate that enforcing Lipschitz continuity in Transformer architecture (Vaswani et al., 2017) is more crucial for ensuring training stability in contrast to the tricks such as *learning rate warmup*, *layer normalization*, *attention formulation*, and *weight initialization* (Qi et al., 2023). Their proposed method, referred to as **LipsFormer**, replaces the Transformer parts with their Lipschitz continuous counterparts: *CenterNorm* for *LayerNorm*, *spectral initialization* for *Xavier initialization*, *scaled cosine similarity attention* for *dot-product attention*, and *weighted residual shortcut* for *residual connection* (Qi et al., 2023). These modifications result in a Transformer architecture with a provably bounded Lipschitz constant.

CenterNorm instead of LayerNorm. LayerNorm (Ba et al., 2016) is widely used in Transformer, defined as:

$$LN(x) = \gamma \odot z + \beta, \quad (2.229)$$

and:

$$z = \frac{y}{\text{std}(y)}, \quad y = \left(I_d - \frac{1}{d} \mathbf{1}_d \mathbf{1}_d^\top \right) x, \quad (2.230)$$

where $x \in \mathbb{R}^d$ is input, I_d is an identity matrix in $\mathbb{R}^{d \times d}$, $\mathbf{1}_d$ is an all-ones vector in \mathbb{R}^d , $\text{std}(y)$ is the standard deviation of y , \odot is element-wise product, α and β are learnable parameters initialized to 1 and 0 respectively (Qi et al., 2023). The Jacobian of z with respect to x is given as:

$$\frac{\partial z}{\partial x} = \frac{1}{\text{std}(y)} \left(I_d - \frac{1}{d} \mathbf{1}_d \mathbf{1}_d^\top \right) \left(I_d - \frac{y y^\top}{\|y\|_2^2} \right), \quad (2.231)$$

which shows that **LayerNorm** is not Lipschitz continuous when $\text{std}(y) \rightarrow 0$. To address this problem, Qi et al. (2023) introduce **CenterNorm**, defined as:

$$CN(x) = \gamma \odot \frac{d}{d-1} \left(I_d - \frac{1}{d} \mathbf{1}_d \mathbf{1}_d^\top \right) x + \beta, \quad (2.232)$$

which admits a Lipschitz constant:

$$\text{Lip}[CN] = \frac{d}{d-1} \approx 1 \quad (2.233)$$

for sufficient large d , $\alpha = 1$, and $\beta = 0$ (Qi et al., 2023).

Scaled Cosine Similarity Attention (SCSA). Kim et al. (2021) show that standard dot-product self-attention is not globally Lipschitz continuous since the Lipschitz constant depends on sequence length which is not bounded (Kim et al., 2021), see also Section 2.2.6 (Lipschitz Continuity of Dot-Product Self-Attention). To address this problem, Qi et al. (2023) replace standard dot-product attention part with **SCSA**, defined as:

$$SCSA(x; v, \tau) = v P V, \quad P = \text{softmax}(\tau Q K^\top), \quad (2.234)$$

where K, Q, V are row-wise normalized in ℓ_2 (Qi et al., 2023, § 4.1.2).

Remark 2.4.1. It is worth noting that their method reduces the Lipschitz constant of the attention module; however, the module remains not globally Lipschitz continuous since the Lipschitz constant still depends on sequence length n :

$$\text{Lip}_2[SCSA] \leq O(n), \quad \text{and} \quad \text{Lip}_\infty[SCSA] \leq O(n^2) \quad (2.235)$$

(Qi et al., 2023, Theorem 1).

Weighted Residual Shortcut. For a residual module:

$$h(x) = x + g(x), \quad (2.236)$$

where $g : \mathbb{R}^d \rightarrow \mathbb{R}^d$, $h : \mathbb{R}^d \rightarrow \mathbb{R}^d$ and $x \in \mathbb{R}^d$, the Lipschitz constant of h is bounded by:

$$\text{Lip}[h] \leq 1 + \text{Lip}[g], \quad (2.237)$$

see Section 2.2.7.3 (Lipschitz Constant of Residual Network). To further reduce the Lipschitz constant introduced by residual module, Qi et al. (2023) replaces the standard residual module with:

$$\text{WRS}(x) = x + \alpha \odot g(x), \quad (2.238)$$

where α is a learnable parameter, initialized to a small value $[0.1, 0.2]$ (Qi et al., 2023).

Note that the result:

$$\text{Lip}[\text{WRS}] = 1 + \max(\alpha) \quad (2.239)$$

in the Qi et al. (2023, § 4.1.3) is incorrect mathematically. The Lipschitz constant of WRS in residual module should be bounded by:

$$\text{Lip}[\text{WRS}] \leq 1 + \max(\alpha). \quad (2.240)$$

Spectral-based Weight Initialization. Qi et al. (2023) further normalize the parameters at initialization by spectral-norm. Let W be a parameter matrix, the W is normalized by:

$$W \leftarrow \frac{W}{\|W\|_2} \quad (2.241)$$

(Qi et al., 2023, § 4.1.4).

2.4.5.4 Jacobian Norm Minimization

Constraining the Lipschitz constant of Transformer architecture for stable optimization and robustness remains an open research problem. Yudin et al. (2025) first derive an explicit tight local Lipschitz constant for self-attention module in Transformer architecture by analyzing the Jacobian of softmax (Yudin et al., 2025). Building on top of the Jaco-

bian analysis, they present **JaSMin** (Jacobian Softmax norm Minimization) for enhancing Transformer's robustness by constraining the local Lipschitz constant (Yudin et al., 2025).

Bounding Lipschitz through Softmax Jacobian. Consider the softmax function:

$$\text{softmax} : \mathbb{R}^d \rightarrow \mathbb{R}^d, \quad (2.242)$$

then the Jacobian of the softmax function is:

$$\mathcal{M}(P_x) := \nabla \text{softmax}(x) = \text{diag}(P_x) - P_x^\top P_x, \quad (2.243)$$

where:

$$P_x = \left(\frac{e^{x_i}}{\sum_j e^{x_j}} \right). \quad (2.244)$$

Yudin et al. (2025) incorporate this Jacobian expression of the softmax function into self-attention, leading a Lipschitz constant bound for a single head:

$$\text{Lip}[\text{Attention}] \leq \|W_V\|_2 \left(\|P\|_2 + 2\|x\|_2^2 \|A\|_2 \max_i \|\mathcal{M}(P_{i,:})\|_2 \right) \quad (2.245)$$

with:

$$P = \text{softmax}(x A x^\top) \in \mathbb{R}^{n \times n} \quad \text{and} \quad A = \frac{W_Q W_K^\top}{\sqrt{d}} \in \mathbb{R}^{d \times d} \quad (2.246)$$

(Yudin et al., 2025, Theorem 3). It worthy noting that the local Lipschitz constant contains a term:

$$\text{Lip}[\text{Attention}] \leq O\left(\max_i \|\mathcal{M}(P_{i,:})\|_2\right), \quad (2.247)$$

which shows that softmax Jacobian norm determines an upper bound of the local Lipschitz constant.

Jacobian Softmax Norm Minimization. To approximate the Jacobian norm more efficiently, Yudin et al. (2025) introduce a surrogate function g that captures the partial

ordering of the singular values of softmax mappings. For $x \in \mathbb{R}_{>0}^n$, let $x_{(k)}$ be the k -th largest component of x . Define:

$$g_k(x) := x_{(k)}(1 - x_{(k)} + x_{(k+1)}), \quad (2.248)$$

for $k = 1, 2, \dots, n-1$ (Yudin et al., 2025, Definition 1). Let $A = \text{diag}(x) - xx^\top$, then the following inequality holds true:

$$x_{(1)} \geq g_1(x) \geq \sigma_1(A) \geq x_{(2)} \geq g_2(x) \geq \sigma_2(A) \geq x_{(n)} \geq g_n(x) \geq \sigma_n(A) \geq 0 \quad (2.249)$$

(Yudin et al., 2025, Theorem 4).

Building on the derived bound, Yudin et al. (2025) propose an efficient regularization loss expressed in terms of the function g with two forms:

$$\mathcal{L}_{\text{JaSMin}(k=0)} = \sum_{\ell=1}^L \sum_{h_i=1}^h \max_j \log \left[g_1 \left(P_{j,:}^{\ell,i} \right) \right], \quad (2.250)$$

and:

$$\mathcal{L}_{\text{JaSMin}(k)} = \sum_{\ell=1}^L \sum_{h_i=1}^h \max_j \log \left[\frac{g_1 \left(P_{j,:}^{\ell,i} \right)}{g_k \left(P_{j,:}^{\ell,i} \right)} \right], \quad (2.251)$$

where $P_{j,:}^{\ell,i}$ represents the softmax map for the ℓ -th attention module ($1 \leq \ell \leq L$), i -th head ($1 \leq i \leq h$), and the j -th row of the map (Yudin et al., 2025, § 4). They also show that for g_1/g_k is bounded below γ :

$$\frac{g_1 \left(P_{j,:}^{\ell,i} \right)}{g_k \left(P_{j,:}^{\ell,i} \right)} \leq \gamma, \quad (2.252)$$

for $1 \leq \gamma \leq \frac{k}{4}$. Then the softmax Jacobian 2-norm is bounded by:

$$\|\mathcal{M}(P_{j,:}^{\ell,i})\|_2 \leq O\left(\frac{\gamma}{k}\right) \quad (2.253)$$

(Yudin et al., 2025, Proposition 1).

2.5 Certifiable Robustness

Certifiable robustness, a cornerstone of trustworthy deep learning, guarantees that a neural network's predictions remain consistent under adversarial perturbations within a specified norm ball. Unlike empirical defenses like adversarial training, which lack formal guarantees, Lipschitz-based certification methods leverage the Lipschitz constant to bound sensitivity to input changes, ensuring provable robustness. While some literature, such as (Clevert et al., 2016), have been introduced previously from the perspectives — such as **theoretical foundations, estimation methods and regularization approaches**, we may revisit some of them in this section from the perspective of **certifiable robustness**.

2.5.1 Formal Robustness Guarantees

In the setting of an n -class classifier f with Lipschitz constant K , a central question in adversarial defense is to determine the largest perturbation norm that leaves the prediction unchanged.

Theorem 2.5.1 (Lipschitz Margin Robustness Radius in ℓ_2 -Normed Spaces). *Let $f : \mathbb{R}^d \rightarrow \mathbb{R}^n$ be a classifier. Let f_i be the i -th output. Let $c = \arg \max_i f_i(x)$ be the predicted class for x . Define the (one-versus-rest) margin*

$$m(x) := f_c(x) - \max_{j \neq c} f_j(x). \quad (2.254)$$

Assume that f is K -Lipschitz from the input ℓ_2 norm to the output ℓ_2 norm, i.e.,

$$\|f(x) - f(y)\|_2 \leq K \|x - y\|_2 \quad \text{for all } x, y. \quad (2.255)$$

Then for any perturbation δ with

$$\|\delta\|_2 < \frac{m(x)}{\sqrt{2}K}, \quad (2.256)$$

the prediction is unchanged:

$$\arg \max_i f_i(x + \delta) = c. \quad (2.257)$$

Remark 2.5.2. This result is particularly useful for analyzing the adversarial defense problem. Similar results have been discussed in the literature (Szegedy et al., 2014; Hein and

Andriushchenko, 2017; Cisse et al., 2017; Tsuzuku et al., 2018; Perugachi-Diaz et al., 2021).

Proof. Let $e_i \in \mathbb{R}^n$ denote the i -th standard basis vector, *i.e.*, e_i has a 1 in the i -th position and 0 elsewhere. Then

$$f_i(x) = e_i^\top f(x). \quad (2.258)$$

For each $j \neq c$, define the pairwise margin function:

$$g_j(x) := f_c(x) - f_j(x) = (e_c - e_j)^\top f(x). \quad (2.259)$$

By Hölder's inequality,

$$|g_j(x) - g_j(y)| = |(e_c - e_j)^\top (f(x) - f(y))| \quad (2.260)$$

$$\leq \|e_c - e_j\|_2 \cdot \|f(x) - f(y)\|_2 \quad (2.261)$$

$$\leq \sqrt{2} \cdot K \cdot \|x - y\|_2, \quad (2.262)$$

so each g_j is $\sqrt{2}K$ -Lipschitz:

$$\text{Lip}[g_j] = \sqrt{2}K. \quad (2.263)$$

Note that the margin $m(x)$ can be expressed as

$$m(x) = f_c(x) - \max_{j \neq c} f_j(x) = \min_{j \neq c} g_j(x). \quad (2.264)$$

Now let $\delta \in \mathbb{R}^d$ be a perturbation satisfying

$$\|\delta\|_2 < \frac{m(x)}{\sqrt{2}K}. \quad (2.265)$$

Then for all $j \neq c$,

$$g_j(x + \delta) \geq g_j(x) - \text{Lip}[g_j] \cdot \|\delta\|_2 \quad (2.266)$$

$$> m(x) - \sqrt{2}K \cdot \frac{m(x)}{\sqrt{2}K} = 0. \quad (2.267)$$

Hence, $f_c(x + \delta) > f_j(x + \delta)$ for all $j \neq c$, which implies

$$\arg \max_i f_i(x + \delta) = c. \quad (2.268)$$

□

Theorem 2.5.3 (Lipschitz Margin Robustness Radius in Conjugate-Normed Spaces). *Let $f: \mathbb{R}^d \rightarrow \mathbb{R}^n$ be a classifier with predicted class $c = \arg \max_i f_i(x)$ and one-versus-rest margin*

$$m(x) := f_c(x) - \max_{j \neq c} f_j(x). \quad (2.269)$$

Assume f is K -Lipschitz from the input ℓ_p norm to the output ℓ_q norm:

$$\|f(x) - f(y)\|_q \leq K \|x - y\|_p. \quad (2.270)$$

Let p be the dual exponent of q , i.e., $\frac{1}{q} + \frac{1}{p} = 1$. Then the classification of x is certifiably robust to any perturbation δ with

$$\|\delta\|_p < r_{\text{cert}}(x) := \frac{m(x)}{2^{\frac{1}{p}} K}, \quad (2.271)$$

where $e_i \in \mathbb{R}^n$ denotes the i -th standard basis vector — e.g., one-hot vector.

Remark 2.5.4. Similar results have been discussed in the literature (Hein and Andriushchenko, 2017; Weng et al., 2018b).

Proof. Let $e_i \in \mathbb{R}^n$ denote the i -th standard basis vector, i.e., e_i has a 1 in the i -th position and 0 elsewhere. Then

$$f_i(x) = e_i^\top f(x). \quad (2.272)$$

For each $j \neq c$, define the pairwise margin function:

$$g_j(x) := f_c(x) - f_j(x) = (e_c - e_j)^\top f(x). \quad (2.273)$$

By Hölder's inequality and the Lipschitz property of f ,

$$|g_j(x) - g_j(y)| \leq \|e_c - e_j\|_p \|f(x) - f(y)\|_q \quad (2.274)$$

$$\leq K \|e_c - e_j\|_p \|x - y\|_p. \quad (2.275)$$

Thus the Lipschitz constant of g_j is:

$$\text{Lip}[g_j] \leq K \|e_c - e_j\|_p. \quad (2.276)$$

If:

$$\|x' - x\|_p < \frac{g_j(x)}{\text{Lip}[g_j]}, \quad (2.277)$$

for all $j \neq c$, then $g_j(x') > 0$ for all $j \neq c$, preserving the predicted class. Taking the minimum over j yields

$$r_{\text{cert}}(x) = \min_{j \neq c} \frac{g_j(x)}{\text{Lip}[g_j]} \geq \frac{m(x)}{K \max_{j \neq c} \|e_c - e_j\|_p} = \min_{j \neq c} \frac{g_j(x)}{\text{Lip}[g_j]} \geq \frac{m(x)}{K 2^{\frac{1}{p}}}. \quad (2.278)$$

□

Remark 2.5.5. Note that:

$$\alpha = \max_{j \neq c} \|e_c - e_j\|_p = 2^{\frac{1}{p}}, \quad (2.279)$$

common output norm choices yield:

$$\ell_2 \text{ output norm: } \alpha = \sqrt{2} \quad \Rightarrow \quad r_{\text{cert}} \geq \frac{m(x)}{\sqrt{2} K}, \quad (2.280)$$

$$\ell_\infty \text{ output norm: } \alpha = 1 \quad \Rightarrow \quad r_{\text{cert}} \geq \frac{m(x)}{K}, \quad (2.281)$$

$$\ell_1 \text{ output norm: } \alpha = 2 \quad \Rightarrow \quad r_{\text{cert}} \geq \frac{m(x)}{2K}. \quad (2.282)$$

Note that the number of classes n affects the certified radius only through the margin $m(x)$; it does not appear explicitly in the bound.

2.5.2 Certifiable Robustness via Global Lipschitz Bound

For a network f with 1-Lipschitz activations and $W^{(\ell)}$ is the ℓ -th layer parameter matrix, the spectral-norm product bounds the Lipschitz constant of f globally:

$$\text{Lip}[f] \leq \prod_{\ell=1}^L \|W^{(\ell)}\|_2, \quad (2.283)$$

providing a *certified global bound*. This is computationally cheap but typically loose. **Se-qLip** (Virmaux and Scaman, 2018) refines this spectral product by incorporating singular-vector alignment between layers, also producing certified global bounds. **LipSDP** (Fazlyab et al., 2019) interprets activation functions as gradients of convex potential functions, satisfying certain properties described by quadratic constraints. Therefore, Lipschitz constant estimation problem is treated as a semi-definite program (SDP) problem.

2.5.3 Certifiable Robustness via Local Lipschitz Bound

Local Lipschitz bounds are computed over a neighborhood. **Fast-Lip** (Weng et al., 2018a) analyze the activation patterns of ReLU networks and derive a gradient norm based local Lipschitz bound. **CLEVER** (Weng et al., 2018b) estimates local constants via extreme value theory on sampled gradient norms; this improves tightness but does not yield a formal certificate. MILP-based methods (Jordan and Dimakis, 2020) encode the exact piecewise-linear constraints of ReLU networks within the ball, yielding exact local Lipschitz constants (and thus exact certified radii), but are limited to small networks.

2.5.4 Certifiable Robustness in Language Models

Proper Distance Metrics for Text. Language models typically operate on text sequences as inputs, for which the conventional notion of a Lipschitz constant over \mathbb{R} with ℓ_p norm does not directly apply. The *Levenshtein distance* (Levenshtein, 1966) measures the number of character replacements, insertions or deletions needed in order to transform a sequence x to sequence y . It is a proper metric that satisfies all axioms of a metric space:

1. **Non-Negativity.** $d_{lev}(x, y) \geq 0$;
2. **Identity.** $d_{lev}(x, y) = 0 \iff x = y$;
3. **Symmetry.** $d_{lev}(x, y) = d_{lev}(y, x)$;
4. **Triangle Inequality.** $d_{lev}(x, z) \leq d_{lev}(x, y) + d_{lev}(y, z)$;

where $d_{lev}(x, y)$ denotes the Levenshtein distance between two sequence x and y . Thereby it provides a principled foundation for discussing Lipschitz continuity in the context of language models. For tokenized text — where each vocabulary item is represented as a one-hot vector — a variant of the *Levenshtein distance*, known as the *ERP distance*, has been proposed for comparing sequences of one-hot vectors (Chen and Ng, 2004).

Rocamora et al. (2025) introduce **LipsLev**, a method for training convolutional text classifiers that are *1-Lipschitz* in the sense of Levenshtein distance for Lipschitz constant based defense (Rocamora et al., 2025). That is, for a classifier $f : S \rightarrow \mathbb{R}^c$, two one-hot vector-valued sequences $x \in \mathbb{R}^{n \times d} \subset S$ and $y \in \mathbb{R}^{m \times d} \subset S$ where n, m are sequence lengths and d is one-hot vector dimension, the classification margin must hold:

$$|f_i(x) - f_j(y)| \leq K_{\text{lev}} d_{\text{lev}}(x, y) \quad (2.284)$$

for a constant $K_{\text{lev}} > 1$, so that the prediction does not change under perturbation radius $d_{\text{lev}}(x, y) < R$ (Rocamora et al., 2025, Theorem 3.3). They then train a 1-Lipschitz classifier over text sequences — in the sense of the Levenshtein distance — by normalizing each layer’s outputs through division by its corresponding Lipschitz constant (Rocamora et al., 2025, § 3.3).

2.6 Conclusions

Lipschitz continuity serves as a cornerstone for enhancing the robustness, generalization, and optimization stability of deep neural networks, providing a rigorous mathematical framework to quantify and control sensitivity to input perturbations. This comprehensive survey synthesizes key insights across theoretical foundations, estimation techniques, regularization approaches, and certifiable robustness, highlighting their interconnections and practical implications. By unifying disparate research threads, we address a critical gap in the literature, offering a cohesive resource for researchers and practitioners. Challenges remain in balancing bound tightness with computational scalability, preserving model expressivity under constraints, and extending certifications to diverse norms and large-scale architectures like transformers, paving the way for future advancements in trustworthy deep learning systems.

2.A Appendix

2.B Proofs: Lipschitz Constants of Activation Functions

2.B.1 Proof: Lipschitz Constant of Sigmoid

Proof. Consider the sigmoid function:

$$\text{Sigmoid}(x) = f(x) = (1 + e^{-x})^{-1}. \quad (2.285)$$

Let $u = 1 + e^{-x}$, so $f(x) = u^{-1}$. The derivative is:

$$f'(x) = -\frac{1}{u^2} \cdot \frac{du}{dx}. \quad (2.286)$$

Compute $\frac{du}{dx}$:

$$u = 1 + e^{-x}, \quad \frac{du}{dx} = -e^{-x}. \quad (2.287)$$

Thus:

$$f'(x) = -\frac{1}{(1 + e^{-x})^2} \cdot (-e^{-x}) = \frac{e^{-x}}{(1 + e^{-x})^2}. \quad (2.288)$$

Express the derivative in terms of $f(x)$:

$$1 - f(x) = \frac{e^{-x}}{1 + e^{-x}}, \quad (2.289)$$

and:

$$f'(x) = \frac{1}{1 + e^{-x}} \cdot \frac{e^{-x}}{1 + e^{-x}} = f(x)(1 - f(x)). \quad (2.290)$$

Thus:

$$|f'(x)| = f(x)(1 - f(x)). \quad (2.291)$$

Maximize the Derivative. Since $0 < f(x) < 1$, we maximize $g(z) = z(1 - z)$ for $z = f(x) \in (0, 1)$:

$$g'(z) = 1 - 2z = 0 \implies z = \frac{1}{2}, \quad (2.292)$$

thus:

$$g\left(\frac{1}{2}\right) = \frac{1}{2} \cdot \frac{1}{2} = \frac{1}{4}. \quad (2.293)$$

Find when $f(x) = \frac{1}{2}$:

$$\frac{1}{1 + e^{-x}} = \frac{1}{2} \implies e^{-x} = 1 \implies x = 0, \quad (2.294)$$

at $x = 0$:

$$f'(0) = \frac{1}{2} \cdot \frac{1}{2} = \frac{1}{4}. \quad (2.295)$$

As $x \rightarrow \infty$, $e^{-x} \rightarrow 0$, so $f'(x) \rightarrow 0$. As $x \rightarrow -\infty$, $e^{-x} \rightarrow \infty$, so:

$$f'(x) \approx \frac{e^{-x}}{e^{-2x}} = e^x \rightarrow 0. \quad (2.296)$$

Hence:

$$\text{Lip} [\text{Sigmoid}(x)] = \sup_x |f'(x)| = \frac{1}{4}. \quad (2.297)$$

□

2.B.2 Proof: Lipschitz Constant of Tanh

Proof. The tanh is defined as:

$$f(x) = \tanh(x) = \frac{e^x - e^{-x}}{e^x + e^{-x}}, \quad (2.298)$$

for all $x, y \in \mathbb{R}$.

Let $g(x) = \sinh(x)$, $h(x) = \cosh(x)$, so $f(x) = \frac{g(x)}{h(x)}$. The derivative is:

$$f'(x) = \frac{g'(x)h(x) - g(x)h'(x)}{h(x)^2}. \quad (2.299)$$

Since $g'(x) = \cosh(x)$, $h'(x) = \sinh(x)$, and $h(x)^2 = \cosh^2(x)$:

$$f'(x) = \frac{\cosh(x) \cdot \cosh(x) - \sinh(x) \cdot \sinh(x)}{\cosh^2(x)} = \frac{\cosh^2(x) - \sinh^2(x)}{\cosh^2(x)}. \quad (2.300)$$

Using the identity $\cosh^2(x) - \sinh^2(x) = 1$:

$$f'(x) = \frac{1}{\cosh^2(x)} = \operatorname{sech}^2(x). \quad (2.301)$$

Since $\cosh(x) \geq 1$, we have:

$$|f'(x)| = \operatorname{sech}^2(x). \quad (2.302)$$

Express the derivative in terms of $f(x)$:

$$f'(x) = \operatorname{sech}^2(x) = 1 - \tanh^2(x) = 1 - f(x)^2. \quad (2.303)$$

Since $-1 \leq f(x) \leq 1$, we have $|f'(x)| = 1 - f(x)^2 \leq 1$.

Maximize the Derivative. Maximize $|f'(x)| = \operatorname{sech}^2(x)$:

$$\cosh(x) = \frac{e^x + e^{-x}}{2}. \quad (2.304)$$

At $x = 0$:

$$\cosh(0) = \frac{e^0 + e^0}{2} = 1, \quad \operatorname{sech}^2(0) = \frac{1}{\cosh^2(0)} = 1. \quad (2.305)$$

As $|x| \rightarrow \infty$, $\cosh(x) \approx \frac{e^{|x|}}{2}$, so:

$$\operatorname{sech}^2(x) \approx \frac{4}{e^{2|x|}} \rightarrow 0. \quad (2.306)$$

The supremum of $|f'(x)|$ is 1 at $x = 0$. Alternatively, since $f(x)^2 \leq 1$, the supremum of $1 - f(x)^2$ occurs when $f(x) = 0$:

$$\tanh(0) = 0, \quad f'(0) = 1 - 0^2 = 1. \quad (2.307)$$

Hence:

$$\text{Lip}[\tanh(x)] = \sup_x |f'(x)| = 1. \quad (2.308)$$

□

2.B.3 Proof: Lipschitz Constant of Softplus

Proof. Consider the softplus function:

$$f(x) = \ln(1 + e^x). \quad (2.309)$$

The derivative is:

$$f'(x) = \frac{d}{dx} \ln(1 + e^x) = \frac{e^x}{1 + e^x}. \quad (2.310)$$

Since $e^x > 0$ and $1 + e^x > 1$, we have $f'(x) > 0$, so:

$$|f'(x)| = \frac{e^x}{1 + e^x}. \quad (2.311)$$

Maximize the Derivative. To find the Lipschitz constant, we need to compute:

$$K = \sup_{x \in \mathbb{R}} \frac{e^x}{1 + e^x}. \quad (2.312)$$

Notice that $\frac{e^x}{1 + e^x}$ is the sigmoid function, which ranges between 0 and 1. Analyze its behavior:

1. As $x \rightarrow \infty$, e^x grows large, so:

$$\frac{e^x}{1 + e^x} \approx \frac{e^x}{e^x} = 1. \quad (2.313)$$

2. As $x \rightarrow -\infty$, $e^x \rightarrow 0$, so:

$$\frac{e^x}{1 + e^x} \rightarrow \frac{0}{1} = 0. \quad (2.314)$$

To confirm the supremum, consider the function $g(x) = \frac{e^x}{1 + e^x}$. Its derivative is:

$$g'(x) = \frac{e^x(1 + e^x) - e^x \cdot e^x}{(1 + e^x)^2} = \frac{e^x}{(1 + e^x)^2}. \quad (2.315)$$

Since $g'(x) > 0$ for all x , $g(x)$ is strictly increasing, approaching 0 as $x \rightarrow -\infty$ and 1 as $x \rightarrow \infty$. Thus:

$$\sup_{x \in \mathbb{R}} \frac{e^x}{1 + e^x} = 1 \quad (2.316)$$

Hence:

$$\text{Lip} [\text{Softplus}(x)] = \sup_x |f'(x)| = 1. \quad (2.317)$$

□

2.B.4 Proof: Lipschitz Constant of Swish

Proof. Let

$$f(x) = x \sigma(x), \quad \sigma(x) = \frac{1}{1 + e^{-x}}. \quad (2.318)$$

The derivative is

$$g(x) := f'(x) = \sigma(x) + x \sigma(x)(1 - \sigma(x)). \quad (2.319)$$

Since $\sigma(-x) = 1 - \sigma(x)$, we have

$$g(-x) = 1 - g(x). \quad (2.320)$$

Using $\sigma(x) = \frac{1}{2}(1 + \tanh(\frac{x}{2}))$ and $\sigma(x)(1 - \sigma(x)) = \frac{1}{4} \operatorname{sech}^2(\frac{x}{2})$,

$$g(x) = \frac{1}{2}\left(1 + \tanh\frac{x}{2}\right) + \frac{x}{4} \operatorname{sech}^2\frac{x}{2}. \quad (2.321)$$

Differentiating,

$$g'(x) = \frac{1}{4} \operatorname{sech}^2 \frac{x}{2} \left(2 - x \tanh \frac{x}{2} \right), \quad (2.322)$$

so the maximizer $x^* > 0$ satisfies

$$x^* \tanh \frac{x^*}{2} = 2. \quad (2.323)$$

Using $\tanh \left(\frac{x^*}{2} \right) = \frac{2}{x^*}$ and

$$\operatorname{sech}^2 \frac{x^*}{2} = \frac{(x^*)^2 - 4}{(x^*)^2}. \quad (2.324)$$

Thus

$$K = g(x^*) = \frac{1}{2} + \frac{x^*}{4}. \quad (2.325)$$

Since $g(-x) = 1 - g(x)$, x^* gives the global maximum of $|g|$, solving $x^* \tanh \frac{x^*}{2} = 2$ gives:

$$x^* \approx 2.3993572805 \dots . \quad (2.326)$$

Hence:

$$\operatorname{Lip} [\operatorname{Siwsh}(x)] = \sup_x |f'(x)| \approx 1.09983932 \dots \quad (2.327)$$

□

2.B.5 Proof: Lipschitz constant of GELU

Proof. Let:

$$f(x) = x \Phi(x), \quad (2.328)$$

where:

$$\Phi(x) = \frac{1}{2} (1 + \operatorname{erf}(x/\sqrt{2})) \quad (2.329)$$

is the standard normal CDF and:

$$\Phi(x) = \frac{1}{\sqrt{2\pi}} e^{-x^2/2} \quad (2.330)$$

is its PDF.

Differentiate:

$$g(x) := f'(x) = \Phi(x) + x \phi(x). \quad (2.331)$$

Note the symmetry $\Phi(-x) = 1 - \Phi(x)$ and $\phi(-x) = \phi(x)$, hence

$$g(-x) = 1 - g(x). \quad (2.332)$$

Compute the critical points:

$$g'(x) = \phi(x) + \phi(x) + x \phi'(x) = 2\phi(x) - x^2\phi(x) = \phi(x)(2 - x^2). \quad (2.333)$$

Since $\phi(x) > 0$, we have $g'(x) > 0$ for $|x| < \sqrt{2}$ and $g'(x) < 0$ for $|x| > \sqrt{2}$. Hence g attains its unique global maximum at $x^* = \sqrt{2}$ and minimum at $-\sqrt{2}$.

Since $g(-x) = 1 - g(x)$, the minimum equals $1 - g(\sqrt{2})$, so indeed $\sup_x |g(x)| = g(\sqrt{2})$.

Evaluate at:

$$x = \sqrt{2} \approx 1.414224\cdots, \quad (2.334)$$

hence:

$$\text{Lip}[\text{GELU}(x)] = \sup_x |f'(x)| \quad (2.335)$$

$$= g(\sqrt{2}) \quad (2.336)$$

$$= \Phi(\sqrt{2}) + \sqrt{2}\phi(\sqrt{2}) \quad (2.337)$$

$$= \frac{1}{2}(1 + \text{erf}(1)) + \frac{e^{-1}}{\sqrt{\pi}} \quad (2.338)$$

$$\approx 1.128904145. \quad (2.339)$$

□

2.B.6 Proof: Lipschitz constant of Softmax

Proof. Let

$$\text{softmax}(z)_i = \frac{e^{z_i}}{\sum_{j=1}^n e^{z_j}}, \quad (2.340)$$

and:

$$p := \text{softmax}(z) \in \Delta^{n-1}, \quad (2.341)$$

where Δ^{n-1} is the probability simplex in \mathbb{R}^n (*i.e.*, the set of all probability vectors of length n):

$$\Delta^{n-1} := \{ p \in \mathbb{R}^n \mid p_i \geq 0, \sum_{i=1}^n p_i = 1 \}. \quad (2.342)$$

The Jacobian is

$$J(z) = \nabla \text{softmax}(z) = \text{diag}(p) - p p^\top, \quad (2.343)$$

which is symmetric positive semidefinite (PSD) and satisfies:

$$J(z) \mathbf{1} = 0. \quad (2.344)$$

Hence the Lipschitz constant K is:

$$K = \sup_{z \in \mathbb{R}^n} \|J(z)\|_2 = \sup_{p \in \Delta^{n-1}} \lambda_{\max}(\text{diag}(p) - p p^\top). \quad (2.345)$$

where λ_{\max} is the largest singular value of $\text{diag}(p) - p p^\top$.

For any unit vector $v \in \mathbb{R}^n$,

$$v^\top J(z) v = v^\top \text{diag}(p) v - (p^\top v)^2 = \sum_{i=1}^n p_i v_i^2 - \left(\sum_{i=1}^n p_i v_i \right)^2 = \text{Var}_{i \sim p}[v_i]. \quad (2.346)$$

Therefore

$$\|J(z)\|_2 = \sup_{\|v\|_2=1} \text{Var}_{i \sim p}[v_i]. \quad (2.347)$$

By Popoviciu's inequality on variances, for any random variable X supported in $[a, b]$,

$$\text{Var}[X] \leq \frac{(b - a)^2}{4}, \quad (2.348)$$

with equality attained by a two-point distribution at the endpoints.

Applying this to $X = v_i$ under p , we get

$$\text{Var}_{i \sim p}[v_i] \leq \frac{(\max_i v_i - \min_i v_i)^2}{4}. \quad (2.349)$$

Maximizing the RHS over $\|v\|_2 = 1$ yields $\max_i v_i - \min_i v_i \leq \sqrt{2}$, with equality for

$$v = \frac{1}{\sqrt{2}}(e_a - e_b) \quad \text{for some distinct } a, b, \quad (2.350)$$

so that

$$\sup_{\|v\|_2=1} \text{Var}_{i \sim p}[v_i] \leq \frac{(\sqrt{2})^2}{4} = \frac{1}{2}. \quad (2.351)$$

This upper bound is (arbitrarily) attainable by choosing p supported on the two indices a, b with $p_a = p_b = \frac{1}{2}$ and $p_i \rightarrow 0$ for $i \notin \{a, b\}$ (which is approached by softmax logits $z_a = z_b \gg z_{i \notin \{a, b\}}$). In that case,

$$J = \begin{bmatrix} \frac{1}{4} & -\frac{1}{4} \\ -\frac{1}{4} & \frac{1}{4} \end{bmatrix} \oplus 0_{n-2}, \quad (2.352)$$

whose largest eigenvalue is $\frac{1}{2}$.

Hence:

$$\text{Lip}[\text{Softmax}(x)] = \sup_z \|J(z)\|_2 = \frac{1}{2}, \quad (2.353)$$

independent of $n \geq 2$.

□

3

OPERATOR-THEORETIC PERTURBATION ANALYSIS

Copyright Disclaimer. This chapter includes content adapted from the following article:

(i) **Róisín Luo**, C. O’Riordan, and J. McDermott. **Higher-Order Singular-Value Derivatives of Real Rectangular Matrices.** *Journal of Mathematical Analysis and Applications (JMAA)*, page 130236, 2025c. ISSN 0022-247X. doi: 10.1016/j.jmaa.2025.130236. URL <https://doi.org/10.1016/j.jmaa.2025.130236>

Portions of the content are reused verbatim or with minor edits, in accordance with institutional guidelines and the policies of the relevant publishers. Permission from all co-authors has been obtained.

Guiding Research Question. This chapter addresses the secondary research question — **(SRQ3) Parameter Space Perturbation**, in service of the primary research question — **(RQ2) Training Dynamics**. Using tools from operator theory and perturbation theory, it establishes a theoretical framework for analyzing perturbations in matrices. In the next chapter, the analytic operator-norm Hessian formulation enables further theoretical analysis of the temporal evolution of Lipschitz continuity in neural networks.

Reproducibility. https://github.com/roisincrtai/highorder_spectral_variation_analysis

ABSTRACT

Higher-order derivatives of singular values in real rectangular matrices arise naturally in both numerical simulation and theoretical analysis, with applications in areas such as statistical physics and optimization in deep learning. Deriving closed-form expressions beyond first order has remained a difficult problem within classical matrix analysis, and no general framework has been available. To address this gap, we present an operator-theoretic framework that extends Kato’s analytic perturbation theory from self-adjoint operators to real rectangular matr-

ces, thereby yielding general n -th order Fréchet derivatives of singular values. As a special case, we obtain a closed-form Kronecker-product representation of the singular-value Hessian, not previously found in the literature. This framework bridges abstract perturbation theory with matrix analysis and provides a systematic tool for higher-order spectral analysis.

3.1 Introduction

SINGULAR values lie at the core of modern matrix analysis, encapsulating key spectral information such as *operator norm*, *conditioning*, *effective rank*, and underpinning applications across numerical linear algebra, data science, control theory, and mathematical physics (Edelman and Rao, 2005; Yosida, 2012; Horn and Johnson, 2012; Tao, 2012). In random matrix theory, singular values govern limiting laws such as Marchenko–Pastur distributions (Marčenko and Pastur, 1967), edge fluctuations described by Tracy–Widom laws (Tracy and Widom, 1994), and fine-scale local statistics such as local eigenvalue spacings (Edelman and Rao, 2005). In physics and deep learning, higher-order derivatives of singular values are indispensable for rigorous analysis in stochastic dynamical settings, where systems are subject to noise and random perturbations (Oksendal, 2013).

For example, let $\Theta_t \in \mathbb{R}^{m \times n}$ be a continuous matrix with r non-zero singular values $\sigma_1, \sigma_2, \dots, \sigma_r$ with respect to time t . Assume that its dynamics are characterized by an adapted Itô process (Itô, 1951)

$$d\text{vec}(\Theta_t) = G_t dt + D_t dW_t, \quad (3.1)$$

where $\text{vec}(\cdot)$ denotes the vectorization operator, $G_t \in \mathbb{R}^{mn}$ is the *drift term*, $D_t \in \mathbb{R}^{mn \times mn}$ is the *diffusion coefficient*, and dW_t is a high-dimensional Wiener process in \mathbb{R}^{mn} . Let

$$\phi_t = \phi(\sigma_1, \sigma_2, \dots, \sigma_r)(t) \quad (3.2)$$

denote a spectral functional of the singular values of Θ_t , then applying Itô’s lemma shows that the rigorous analysis of the spectral dynamics of $d\phi_t$ requires the second-order derivatives of singular values (Oksendal, 2013). Such induced dynamics arise naturally in both physics and deep learning. In physics, the *von Neumann entropy* — a measure of the statistical uncertainty within a quantum system — is a spectral functional of singular val-

ues (Fano, 1957), and widely used in the study of quantum entanglement (Nielsen and Chuang, 2010). In deep learning, the Lipschitz continuity of neural networks is a spectral functional of the largest singular value (Róisín Luo et al., 2025a). For more general non-Gaussian drivers in stochastic dynamics, such as Lévy processes, higher-order derivatives of singular values are indispensable for rigorous analysis and for deriving sharp bounds (Applebaum, 2009).

Although first-order derivatives of singular values are well known in the literature (Stewart and Sun, 1990), explicit closed-form expressions for second- and higher-order derivatives are largely absent from the literature. A unified, highly procedural, and systematic framework for their derivation has been lacking, since direct approaches via matrix analysis are challenging due to the intricate interplay among local spectral structures (*e.g.*, spectral gaps), left and right singular subspaces, and the associated null spaces.

To bridge this gap, we present an operator-theoretic framework for deriving arbitrary higher-order derivatives of singular values in a highly procedural approach. Our approach treats matrices as bounded linear operators on Hilbert spaces and extends Kato’s analytic perturbation theory (Kato, 1995) beyond the self-adjoint setting. The key step is to embed a non-self-adjoint real rectangular matrix into a self-adjoint operator via the Jordan–Wielandt embedding (*i.e.*, Hermitian dilation trick) (Stewart and Sun, 1990; Shalit, 2021). We then analyze the asymptotic expansions of the resulting eigenvalues by extending Kato’s results in eigenvalue expansions, relate these eigenvalue expansions to Fréchet derivatives of singular values, and express the Fréchet derivative tensors with Kronecker-product representation.

3.1.1 Perturbation Theory

Classical perturbation theory has developed along several independent traditions. For example, **analytic operator-theoretic perturbation theory** (Rellich, 1969; Kato, 1995) treats holomorphic families of operators on Banach or Hilbert spaces, using resolvents, Riesz projectors, and contour integrals to prove the existence of analytic eigenvalue and eigenspace branches and to derive expansion formulas, including trace identities for eigenvalue clusters. **Matrix perturbation theory** (Stewart and Sun, 1990; Horn and Johnson, 2012) focuses on the finite-dimensional case and derives explicit perturbation formulas via algebraic tools such as characteristic polynomials, Schur forms, and Sylvester equations, typically without explicitly invoking the operator-theoretic machinery. **Rayleigh–Schrödinger perturbation theory** (Rayleigh, 2013; Schrödinger, 1926; Sakurai and Napoli, 2020) in quantum mechanics provides basis-dependent expansions in terms of ma-

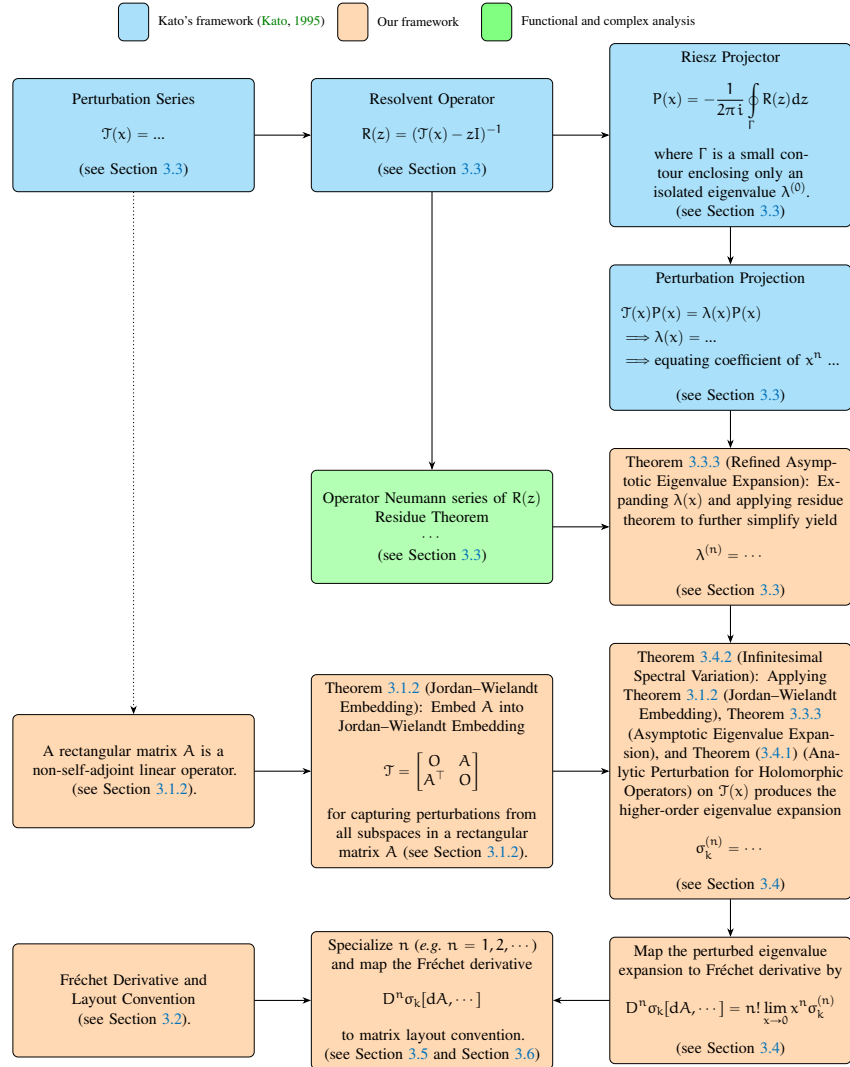


Figure 3.1: Theoretical Framework for Infinitesimal Spectral Variations. We employ Kato's analytic perturbation theory for self-adjoint operators (Kato, 1995). For a rectangular matrix A , we construct its Jordan–Wielandt embedding (Theorem 3.1.2), a block self-adjoint operator that encodes perturbations across all subspaces (*i.e.*, left-singular, right-singular, left-null, and right-null). Applying Kato's asymptotic eigenvalue expansions to this embedding, together with the residue theorem to simplify, yields an n -th order expansion of the singular values of A . This expansion is then related to Fréchet derivatives. Finally, by specializing and mapping into explicit matrix-layout conventions, we obtain a systematic procedure for deriving arbitrary-order singular-value derivatives of rectangular matrices.

trix elements and energy gaps; these coincide with the analytic expansions under discreteness and gap assumptions, but are often presented in physics as formal series rather than within Kato's framework. Despite their differences in tool and emphasis, these frameworks are mathematically consistent and recover the same perturbative corrections in overlapping regimes.

3.1.2 Schematic Overview

A schematic overview of the framework is illustrated in Figure 3.1. To apply Kato's framework for self-adjoint operators, we first embed a non-self-adjoint $A \in \mathbb{R}^{m \times n}$ (since $A \neq A^\top$) into a self-adjoint operator \mathcal{T} using the Jordan–Wielandt embedding (*i.e.*, Hermitian dilation) (Stewart and Sun, 1990; Edelman and Rao, 2005; Li and Li, 2005; Horn and Johnson, 2012; Shalit, 2021), taking:

$$\mathcal{T} := \begin{bmatrix} O & A \\ A^\top & O \end{bmatrix} \in \mathbb{R}^{(m+n) \times (m+n)}. \quad (3.3)$$

It is immediate that \mathcal{T} is self-adjoint, since:

$$\mathcal{T}^\top = \begin{bmatrix} O & A \\ A^\top & O \end{bmatrix}^\top = \begin{bmatrix} O & A \\ A^\top & O \end{bmatrix} = \mathcal{T}. \quad (3.4)$$

This embedding preserves the complete information regarding the spectrum of A . The spectrum of A is stated in Theorem 3.1.1 (Matrix Singular Value Decomposition (Full Form)), and the spectrum of \mathcal{T} relates to the spectral structure of A as stated in Theorem 3.1.2 (Spectrum of Jordan–Wielandt Embedding).

Theorem 3.1.1 (Matrix Singular Value Decomposition (Full Form)). *Let $A \in \mathbb{R}^{m \times n}$ be a real rectangular matrix. Then A admits a full singular value decomposition (SVD) (Horn and Johnson, 2012; Stewart and Sun, 1990) by:*

$$A = U \Sigma V^\top, \quad (3.5)$$

$$U = [U_r \ U_0] \in \mathbb{R}^{m \times m}, \quad V = [V_r \ V_0] \in \mathbb{R}^{n \times n}, \quad (3.6)$$

$$\Sigma = \begin{bmatrix} \sigma_1 & & & \\ & \sigma_2 & & \\ & & \ddots & \\ & & & \sigma_r \\ \hline & O_{(m-r) \times r} & & O_{(m-r) \times (n-r)} \end{bmatrix}, \quad (3.7)$$

where $\sigma_1 \geq \sigma_2 \geq \dots \geq \sigma_r > 0$ are the non-zero singular values, $U_r \in \mathbb{R}^{m \times r}$ and $V_r \in \mathbb{R}^{n \times r}$ contain the corresponding left and right singular vectors, and U_0 and V_0 span the left and right null spaces of A , respectively.

Theorem 3.1.2 (Spectrum of Jordan–Wielandt Embedding). *The singular values of $A \in \mathbb{R}^{m \times n}$ and the spectrum (i.e., eigenvalues) $\sigma(\mathcal{T})$ of its Jordan–Wielandt embedding :*

$$\mathcal{T} := \begin{bmatrix} O & A \\ A^\top & O \end{bmatrix} \in \mathbb{R}^{(m+n) \times (m+n)} \quad (3.8)$$

are directly related. If A admits a SVD as stated in Theorem 3.1.1, the singular values of A relates to the eigenvalues of \mathcal{T} by:

$$\mathcal{T} \left(\frac{1}{\sqrt{2}} \begin{bmatrix} u_i \\ v_i \end{bmatrix} \right) = \sigma_i \left(\frac{1}{\sqrt{2}} \begin{bmatrix} u_i \\ v_i \end{bmatrix} \right), \quad (3.9)$$

and:

$$\mathcal{T} \left(\frac{1}{\sqrt{2}} \begin{bmatrix} u_i \\ -v_i \end{bmatrix} \right) = -\sigma_i \left(\frac{1}{\sqrt{2}} \begin{bmatrix} u_i \\ -v_i \end{bmatrix} \right), \quad (3.10)$$

respectively, where the factor $\frac{1}{\sqrt{2}}$ ensures normalization and hence orthonormality of the eigenvectors. Thus, each singular value σ_i of A corresponds to a pair of eigenvalues:

$$\lambda_i^{(+)} = \sigma_i, \quad \lambda_i^{(-)} = -\sigma_i, \quad (3.11)$$

with eigenvectors constructed directly from the singular vector pair (u_i, v_i) . The null spaces are also preserved in this embedding:

$$\ker(\mathcal{T}) = \left\{ \begin{bmatrix} u_j \\ 0 \end{bmatrix} : u_j \in \ker(A^\top) \right\} \oplus \left\{ \begin{bmatrix} 0 \\ v_k \end{bmatrix} : v_k \in \ker(A) \right\}. \quad (3.12)$$

Remark 3.1.3. The use of the Jordan–Wielandt embedding to transfer results on Hermitian eigenvalues to singular values of rectangular matrices is well-known in the literature (Stewart and Sun, 1990; Li and Li, 2005; Calkin et al., 2022).

Next, starting from the eigenvalue expansion of reduced resolvent of operator \mathcal{T} and applying the residue theorem to simplify, we derive the asymptotic eigenvalue expansion of \mathcal{T} up to n -th order under holomorphic perturbations (Theorem 3.3.3). By relating the n -th order term of this expansion with the corresponding n -th order Fréchet derivative, we obtain explicit expressions for higher-order derivatives of singular values. Finally, we deploy the n -th order Fréchet derivative with matrix layout conventions. In particular, the first-order case ($n = 1$) recovers the well-known Jacobian of singular values; while the second-order case ($n = 2$) yields the singular-value Hessian with Kronecker-product representation, which has not appeared previously in the literature. By bridging the ab-

stract operator-theoretic expansions with matrices, our framework provides a toolkit for arbitrary-order singular-value analysis.

3.1.3 Contributions

This paper makes the following contributions:

1. **Spectral Variations in Rectangular Matrices.** We present an operator-theoretic framework for analyzing n -th order spectral variations in real rectangular matrices (see Figure 3.1). This framework provides a **systematic procedure** for deriving higher-order derivatives of singular values in real rectangular matrices.
2. **Singular-Value Hessian.** Specializing to $n = 2$ yields the second-order derivative (Hessian) of singular values, expressed in a Kronecker-product representation that, to the best of our knowledge, has not appeared previously in the literature. This result is particularly essential for analysis of **induced spectral stochastic dynamics**, where second-order derivatives arise naturally in Itô calculus for stochastic differential equations (SDEs) driven by Wiener processes.

3.2 Fréchet Derivative and Layout Convention

Deploying results from abstract operator theory in matrix settings requires explicit layout conventions, particularly for the representation of derivatives. Before commencing the theoretical analysis, this section introduces the conventions fundamental to our framework. Section 3.2.1 introduces matrix layout and the differentiability condition; Section 3.2.3 presents general Fréchet derivatives for matrix-to-matrix maps together with their tensor representations; and Section 3.2.4 specializes to Fréchet derivatives of matrix-to-scalar functionals and their vectorized Kronecker-product representation (Kolda and Bader, 2009).

3.2.1 Matrix and Spectral Decomposition

Let

$$A = \begin{bmatrix} A_{1,1} & A_{1,2} & \cdots & A_{1,n} \\ A_{2,1} & A_{2,2} & \cdots & A_{2,n} \\ \vdots & \vdots & \ddots & \vdots \\ A_{m,1} & A_{m,2} & \cdots & A_{m,n} \end{bmatrix} \in \mathbb{R}^{m \times n} \quad (3.13)$$

be a real rectangular matrix of rank $r = \text{rank}(A)$, where $A_{i,j}$ denotes its (i, j) -th entry. A admits a *full* SVD as stated in Theorem 3.1.1. Specially, the *reduced* or *truncated* SVD of A is given as:

$$A = \sum_{k=1}^r \sigma_k u_k v_k^\top, \quad (3.14)$$

where $r = \text{rank}(A)$, and u_k and v_k are the left and right singular vectors associated with singular value $\sigma_k > 0$.

Lemma 3.2.1 (Essential Matrix Identities). *Let $x \in \mathbb{R}$ be a scalar, and real matrices A , B , C and V be of such sizes that one can form their products. Then the following identities hold (Franklin, 2000; Horn and Johnson, 2012):*

1. $\text{vec}(x) = x$,
2. $\text{tr}(x) = x$,
3. $\text{vec}(BVA^\top) = (A \otimes B) \text{vec}(V)$,
4. $(A \otimes B)^\top = A^\top \otimes B^\top$,
5. $\text{tr}(ABC) = \text{tr}(CAB) = \text{tr}(BCA)$.

3.2.2 Differentiability Condition

To ensure the existence of higher-order differentiability of non-zero singular values and associated singular vectors, we further assume that the non-zero singular values of $A \in \mathbb{R}^{m \times n}$ are simple (*i.e.*, each non-zero singular value has multiplicity one), as stated in Assumption 3.2.2 (Simplicity Assumption of Non-Zero Singular Values). This *simplicity* assumption is essential for ensuring that non-zero singular value $\sigma_i > 0$ of A and associated singular vectors u_i and v_i depend smoothly on the entries of A , in fact yielding

$u_i, v_i, \sigma_i \in C^\infty$ (i.e. maps are infinitely continuously differentiable). Under this assumption, non-zero singular values and their associated singular vectors vary smoothly with perturbations of A .

Assumption 3.2.2 (Simplicity Assumption of Non-Zero Singular Values). We assume that the non-zero singular values of A are *simple*, i.e.,

$$\sigma_i \neq \sigma_j \quad \text{for all } i \neq j. \quad (3.15)$$

If this assumption fails, a non-zero singular value may have multiplicity greater than one; singular values then remain continuous but may fail to be differentiable at points of multiplicity, and the associated singular subspaces are well defined whereas individual singular vectors are not unique. In such settings, higher-order derivatives generally do not exist in the classical context, and analysis must instead be carried out in terms of spectral projectors or within the framework of subdifferential calculus (Clarke, 1990; Lewis and Sendov, 2005).

3.2.3 Matrix Fréchet Derivative as Multilinear Operator

We regard matrix Fréchet derivatives as multilinear operators (Yosida, 2012). A definition for general Fréchet differentiable real matrix-to-matrix maps and their tensor representation are in Definition 3.2.3 (α -Times Continuously Fréchet Differentiable Matrix Map). The existence and uniqueness of the Fréchet derivative are stated in Theorem 3.2.4 (Uniqueness of α -Times Fréchet Derivative (Yosida, 2012; Spivak, 2018)).

Definition 3.2.3 (α -Times Continuously Fréchet Differentiable Matrix Map). Let

$$F: \mathbb{R}^{m \times n} \rightarrow \mathbb{R}^{s \times t} \quad (3.16)$$

be α -times continuously Fréchet differentiable (i.e., $F \in C^\alpha$) (Yosida, 2012; Spivak, 2018; Horn and Johnson, 2012). The α -th Fréchet derivative of F is a multilinear map:

$$D^\alpha F: (\mathbb{R}^{m \times n})^\alpha \rightarrow \mathbb{R}^{s \times t}. \quad (3.17)$$

Writing $F_{i,j}$ for the (i,j) -th component of F and $A_{p,q}$ for the (p,q) -th entry of A , with:

$$1 \leq i \leq s, \quad 1 \leq j \leq t, \quad 1 \leq p \leq m, \quad 1 \leq q \leq n, \quad (3.18)$$

then the α -th derivative $D^\alpha F$ at matrix A is a tensor, defined by:

$$[D^\alpha F(A)]_{i,j;p_1q_1 \dots p_\alpha q_\alpha} = \frac{\partial^\alpha F_{i,j}(A)}{\partial A_{p_1q_1} \dots \partial A_{p_\alpha q_\alpha}} \in \mathbb{R}. \quad (3.19)$$

The action of tensor $D^\alpha F(A)$ on directions $H_1, \dots, H_\alpha \in \mathbb{R}^{m \times n}$ is obtained *component-wise* by contracting tensor $D^\alpha F(A)$ with the indices on H_1, \dots, H_α :

$$[D^\alpha F(A)[H_1, \dots, H_\alpha]]_{i,j} = \frac{\partial^\alpha F_{i,j}(A)}{\partial A_{p_1q_1} \dots \partial A_{p_\alpha q_\alpha}} (H_1)_{p_1q_1} \dots (H_\alpha)_{p_\alpha q_\alpha}. \quad (3.20)$$

Moreover, for $H \in \mathbb{R}^{m \times n}$, the F at A admits a multivariate Taylor expansion:

$$F(A + H) = \sum_{\beta=0}^{\alpha} \frac{1}{\beta!} D^\beta F(A) [\underbrace{H, \dots, H}_{\beta \text{ times}}] + o(\|H\|^\alpha), \quad (\|H\| \rightarrow 0), \quad (3.21)$$

where $\|\cdot\|$ is any norm on $\mathbb{R}^{m \times n}$ (e.g., the Frobenius norm).

Theorem 3.2.4 (Uniqueness of α -Times Fréchet Derivative (Yosida, 2012; Spivak, 2018)). *Suppose $F \in C^\alpha$ is differentiable up to order α . Then $D^\alpha F$ exists, is a symmetric α -linear map, and is unique. That is, there is no other α -linear operator satisfying the defining Taylor-remainder condition. This theorem ensures the uniqueness of the derivatives of singular values under the differentiability condition, as stated in Assumption 3.2.2 (Simplicity Assumption of Non-Zero Singular Values).*

3.2.4 Representation Convention for Matrix-Valued Functionals

We focus on the derivatives of singular values, which are matrix-valued functionals. To obtain matrix representations to facilitate concrete applications, we specialize the general matrix-to-matrix maps of Definition 3.2.3 to matrix-valued functionals. In general, the α -th Fréchet derivative is a higher-order tensor. To express such tensors in matrix form, we employ vectorization (with a **column-major convention**) together with the Kronecker-product representation (Kolda and Bader, 2009; Magnus and Neudecker, 2019), as established in Corollary 3.2.5 (Vectorized Kronecker-Product Representation of Fréchet Derivative). As complementary conventions, we also introduce explicit matrix layouts for the Jacobian in Section 3.2.4.1 (Representation Convention for Jacobian of Matrix-Valued Functional) and for the Hessian in Section 3.2.4.2 (Representation Convention for Hessian of Matrix-Valued Functional).

Corollary 3.2.5 (Vectorized Kronecker-Product Representation of Fréchet Derivative).

Let

$$f : \mathbb{R}^{m \times n} \rightarrow \mathbb{R} \quad (3.22)$$

be α -times continuously Fréchet differentiable (i.e., $f \in C^\alpha$). For directions $H_1, \dots, H_\alpha \in \mathbb{R}^{m \times n}$, the multilinear action $D^\alpha f$ at $A \in \mathbb{R}^{m \times n}$ is given by the Frobenius tensor inner product (Kolda and Bader, 2009; Magnus and Neudecker, 2019):

$$D^\alpha f(A)[H_1, \dots, H_\alpha] = \langle D^\alpha f(A), H_1 \otimes \dots \otimes H_\alpha \rangle \quad (3.23)$$

$$= \langle \text{vec}(D^\alpha f(A)), \text{vec}(H_1 \otimes \dots \otimes H_\alpha) \rangle \quad (3.24)$$

$$= \text{vec}(D^\alpha f(A))^\top \text{vec}(H_1 \otimes \dots \otimes H_\alpha), \quad (3.25)$$

where \otimes represents Kronecker product (i.e., tensor product) and:

$$\text{vec} : \mathbb{R}^{m \times n} \mapsto \mathbb{R}^{mn} \quad (3.26)$$

represents the vectorization operator with the **column-major convention** (Kolda and Bader, 2009).

This vectorization is particularly useful for representing arbitrary-order derivatives of matrix-valued functionals in matrix form.

3.2.4.1 Representation Convention for Jacobian of Matrix-Valued Functional

Representing the Jacobian of matrix-valued functionals in matrix form is standard in the literature (Horn and Johnson, 2012). For clarity, we introduce a matrix layout as a complementary representation for the Jacobian of matrix-valued functionals. Let

$$f : \mathbb{R}^{m \times n} \mapsto \mathbb{R} \quad (3.27)$$

be a first-order Fréchet differentiable functional. Then the differential of f admits:

$$df = Df(A)[dA] = \langle Df(A), dA \rangle = \left(\frac{\partial f}{\partial A} \right)^\top dA = \text{tr} \left[\left(\frac{\partial f}{\partial A} \right)^\top dA \right], \quad (3.28)$$

where $\frac{\partial f}{\partial A}$ and infinitesimal variation $dA \in \mathbb{R}^{m \times n}$ are piece-wisely defined as:

$$\frac{\partial f}{\partial A} = \begin{bmatrix} \frac{\partial f}{\partial A_{1,1}} & \frac{\partial f}{\partial A_{1,2}} & \cdots & \frac{\partial f}{\partial A_{1,n}} \\ \frac{\partial f}{\partial A_{2,1}} & \frac{\partial f}{\partial A_{2,2}} & \cdots & \frac{\partial f}{\partial A_{2,n}} \\ \vdots & \vdots & \ddots & \vdots \\ \frac{\partial f}{\partial A_{m,1}} & \frac{\partial f}{\partial A_{m,2}} & \cdots & \frac{\partial f}{\partial A_{m,n}} \end{bmatrix} \quad (3.29)$$

with **denominator layout convention**, and:

$$dA = \begin{bmatrix} dA_{1,1} & dA_{1,2} & \cdots & dA_{1,n} \\ dA_{2,1} & dA_{2,2} & \cdots & dA_{2,n} \\ \vdots & \vdots & \ddots & \vdots \\ dA_{m,1} & dA_{m,2} & \cdots & dA_{m,n} \end{bmatrix}. \quad (3.30)$$

3.2.4.2 Representation Convention for Hessian of Matrix-Valued Functional

The Hessian of a matrix-valued functional is naturally a higher-order tensor; for instance, it is a fourth-order tensor for matrix-valued functionals (Kolda and Bader, 2009). Let

$$f : \mathbb{R}^{m \times n} \rightarrow \mathbb{R} \quad (3.31)$$

be a twice Fréchet differentiable functional. Since

$$D^2 f = D(Df), \quad (3.32)$$

to obtain a matrix representation of $D^2 f$, we first consider the representation layout of the first-order derivative for a matrix-to-matrix map $F : \mathbb{R}^{m \times n} \rightarrow \mathbb{R}^{s \times t}$. We then apply vectorization together with this layout to express the second-order derivatives of matrix-valued functionals in matrix form.

Let

$$F : \mathbb{R}^{m \times n} \mapsto \mathbb{R}^{s \times t} \quad (3.33)$$

be a first-order Fréchet differentiable matrix-to-matrix map. Then there exists:

$$\frac{\partial \text{vec}(F)}{\partial \text{vec}(A)} \in \mathbb{R}^{p \times q} \quad p = mn \quad \text{and} \quad q = st, \quad (3.34)$$

piece-wisely defined as:

$$\frac{\partial \text{vec}(F)}{\partial \text{vec}(A)} = \begin{pmatrix} \frac{\partial \text{vec}(F)_1}{\partial \text{vec}(A)_1} & \frac{\partial \text{vec}(F)_2}{\partial \text{vec}(A)_1} & \dots & \frac{\partial \text{vec}(F)_q}{\partial \text{vec}(A)_1} \\ \frac{\partial \text{vec}(F)_1}{\partial \text{vec}(A)_2} & \frac{\partial \text{vec}(F)_2}{\partial \text{vec}(A)_2} & \dots & \frac{\partial \text{vec}(F)_q}{\partial \text{vec}(A)_2} \\ \vdots & \vdots & \ddots & \vdots \\ \frac{\partial \text{vec}(F)_1}{\partial \text{vec}(A)_p} & \frac{\partial \text{vec}(F)_2}{\partial \text{vec}(A)_p} & \dots & \frac{\partial \text{vec}(F)_q}{\partial \text{vec}(A)_p} \end{pmatrix} \quad (3.35)$$

by using **denominator layout convention** on $\text{vec}(F)$ and $\text{vec}(A)$ (Horn and Johnson, 2012). Then the Hessian of the matrix-valued functional f can be defined as:

$$\frac{\partial}{\partial \text{vec}(A)} \text{vec} \left(\frac{\partial f}{\partial A} \right) \quad (3.36)$$

with vectorized representation.

Relating Vectorized Representation to D^2f . We now relate this vectorized representation to D^2f . By Corollary 3.2.5 (Vectorized Kronecker-Product Representation of Fréchet Derivative), consider:

$$D^2f[dA, dA] = \langle D^2f, dA \otimes dA \rangle, \quad (3.37)$$

and use the following identities from Lemma 3.2.1 (Essential Matrix Identities):

$$1. \text{ vec}(x) = x,$$

$$2. \text{ vec}(BVA^\top) = (A \otimes B) \text{ vec}(V),$$

then it yields:

$$D^2f[dA, dA] = \langle D^2f, dA \otimes dA \rangle \quad (3.38)$$

$$= \text{vec}(D^2f)^\top \text{vec}(dA \otimes dA) \quad (3.39)$$

$$= \text{vec}(dA)^\top (D^2f)^\top \text{vec}(dA). \quad (3.40)$$

Relating

$$\frac{\partial}{\partial \text{vec}(A)} \text{vec} \left(\frac{\partial f}{\partial A} \right) \quad (3.41)$$

with D^2f yields:

$$D^2f = \left[\frac{\partial}{\partial \text{vec}(A)} \text{vec} \left(\frac{\partial f}{\partial A} \right) \right]^\top, \quad (3.42)$$

such that:

$$D^2f[dA, dA] = \text{vec}(dA)^\top \left[\frac{\partial}{\partial \text{vec}(A)} \text{vec} \left(\frac{\partial f}{\partial A} \right) \right] \text{vec}(dA). \quad (3.43)$$

3.3 Refined Asymptotic Eigenvalue Expansion

Kato's monograph (Kato, 1995) establishes the existence of asymptotic eigenvalue expansions and, in particular, provides a closed-form expression for the *weighted mean* of eigenvalue coefficients, as stated in Theorem 3.3.2 (Kato's Weighted Mean of Eigenvalue Expansions (Kato, 1995, Ch. II, §2.2)). Nevertheless, Kato's formulation is expressed with an infinite summation of contour integrals involving the perturbed resolvent and does not yield explicit, constructive formulas for the individual coefficients, which limits its direct applicability in our setting. Building on the analytic foundations laid by Kato, and by employing explicit Neumann expansions of resolvents together with the residue theorem, we refine this framework to derive an *explicit, closed-form formula for arbitrary-order eigenvalue coefficients* of holomorphic families of bounded self-adjoint operators. Our main result, Theorem 3.3.3 (Refined Closed-Form Asymptotic Expansion of Simple Isolated Eigenvalue in Self-Adjoint Operator), goes beyond Kato's weighted mean by furnishing a fully constructive representation of each eigenvalue coefficient. The overall scheme is illustrated in Figure 3.1.

Definition 3.3.1 (Space of Bounded Linear Operators). Let

$$\mathcal{L}(X) = \{ T : X \mapsto X \mid X \text{ is a Banach space and } T \text{ is a bounded linear operator} \} \quad (3.44)$$

be the Banach space of bounded linear operators.

Theorem 3.3.2 (Kato's Weighted Mean of Eigenvalue Expansions (Kato, 1995, Ch. II, §2.2)). *Let*

$$\mathcal{T}(x) = \mathcal{T}^{(0)} + \sum_{j=1}^{\infty} x^j \mathcal{T}^{(j)} \in \mathcal{L}(X) \quad (3.45)$$

be a holomorphic family of bounded operators on a Banach space X (Kato, 1995, Ch. II, §2.1, Eq (2.1)). Suppose $\lambda^{(0)}$ is an isolated eigenvalue of $\mathcal{T}^{(0)}$ of algebraic multiplicity m .

Let

$$R(z) = (\mathcal{T}(x) - zI)^{-1} \quad (3.46)$$

be the perturbed resolvent, let

$$P(x) = -\frac{1}{2\pi i} \oint_{\Gamma} R(z) dz, \quad (3.47)$$

be Riesz projector, and define

$$\hat{\mathcal{T}}^{(n)} = \sum_{p=1}^{\infty} (-1)^{p-1} \sum_{\substack{i_1 + \dots + i_p = n \\ i_j \geq 1}} \frac{1}{2\pi i} \oint_{\Gamma} R(z) \mathcal{T}^{(i_1)} R(z) \dots R(z) \mathcal{T}^{(i_p)} R(z) (z - \lambda^{(0)}) dz, \quad (3.48)$$

where Γ is a small contour enclosing only $\lambda^{(0)}$ and no other spectrum (Kato, 1995, Ch. II, §2.1, Eq (2.18)). Then the weighted mean of the perturbed eigenvalues is:

$$\hat{\lambda}(x) := \frac{1}{m} \operatorname{tr}(\mathcal{T}(x) P(x)), \quad (3.49)$$

admits the expansion

$$\hat{\lambda}(x) = \lambda^{(0)} + \sum_{n=1}^{\infty} x^n \hat{\lambda}^{(n)} \quad (3.50)$$

(Kato, 1995, Ch. II, §2.1, Eq (2.21)), and:

$$\hat{\lambda}^{(n)} = \frac{1}{m} \operatorname{tr}(\hat{\mathcal{T}}^{(n)}) \quad (3.51)$$

(Kato, 1995, Ch. II, §2.1, Eq (2.22)).

Sketch to Refine Kato's Result. Following Kato's analytic framework, we also begin with the perturbation series $\mathcal{T}(x)$ of a self-adjoint operator \mathcal{T} . Kato's monograph establishes eigenvalue expansions via contour integrals of the resolvent and provides a closed-form expression for the *weighted mean* of eigenvalues, but it does not supply explicit constructive formulas for the individual coefficients. Our approach departs at this point: we expand the resolvent explicitly through its Neumann series, apply the residue theorem on the contour integrals, and simplify the resulting expressions. This yields a closed-form asymptotic eigenvalue expansion for \mathcal{T} with computable coefficients. Unlike Kato's result,

our expansion is formulated in terms of the finite summation of the series of unperturbed resolvent, which enables systematic computation and, in particular, facilitates the subsequent derivation of singular-value Fréchet derivatives. As a special case, it also recovers the classical Rayleigh–Schrödinger corrections of quantum mechanics (Rayleigh, 2013; Schrödinger, 1926; Sakurai and Napolitano, 2020).

Theorem 3.3.3 (Refined Closed-Form Asymptotic Expansion of Simple Isolated Eigenvalue in Self-Adjoint Operator). *Let*

$$\mathcal{T}(x) = \mathcal{T}^{(0)} + \sum_{j=1}^{\infty} x^j \mathcal{T}^{(j)} \in \mathcal{L}(X) \quad (3.52)$$

be a holomorphic family of bounded operators on a Banach space X , where $\mathcal{T}^{(0)}$ denotes the unperturbed operator and $x \in \mathbb{C}$ is the perturbation parameter.

Unperturbed Reduced Resolvent. Define the unperturbed reduced resolvent (Kato, 1995; Yosida, 2012) of $\mathcal{T}^{(0)}$:

$$S^{(0)} = (\mathcal{T}^{(0)} - \lambda^{(0)} I)^{-1} (I - w^{(0)}(w^{(0)})^*), \quad (3.53)$$

where $\lambda^{(0)}$ is a simple eigenvalue of $\mathcal{T}^{(0)}$ and $w^{(0)}$ is the associated normalized eigenvector (i.e., $\|w^{(0)}\|_2 = 1$).

Theorem Claim. Then there exists a unique holomorphic branch $\lambda(x)$ of eigenvalues of $\mathcal{T}(x)$. It admits the power series:

$$\lambda(x) = \sum_{n=0}^{\infty} x^n \lambda^{(n)}, \quad (3.54)$$

and for each integer $n \geq 1$,

$$\lambda^{(n)} = \sum_{p=1}^n (-1)^{p-1} \sum_{\substack{i_1 + \dots + i_p = n \\ i_j \geq 1}} \langle w^{(0)}, \mathcal{T}^{(i_1)} S^{(0)} \mathcal{T}^{(i_2)} S^{(0)} \dots S^{(0)} \mathcal{T}^{(i_p)} w^{(0)} \rangle. \quad (3.55)$$

Proof 3.3.4. We begin by presenting a compact and explicit proof of Theorem 3.3.2 (Kato's Weighted Mean of Eigenvalue Expansions (Kato, 1995, Ch. II, §2.2)) in the case of a simple eigenvalue of a self-adjoint operator, which does not exist in Kato's monograph.

Since $\lambda^{(0)}$ is a simple eigenvalue of $\mathcal{T}^{(0)}$, analytic-perturbation theory ensures there exists a unique eigenvalue branch $\lambda(x)$. Let

$$R(z) = (\mathcal{T}(x) - zI)^{-1} \quad (3.56)$$

be the *resolvent* of operator $\mathcal{T}(x)$, which encapsulates the full spectral information of $\mathcal{T}(x)$, and let

$$S(z) = R(z)(I - P(x)) \quad (3.57)$$

be the associated reduced resolvent $S(z)$ (*i.e.*, the regular part of the resolvent), where $P(x)$ is the Riesz–Dunford contour integral (Dunford and Schwartz, 1988; Kato, 1995) is:

$$P(x) = -\frac{1}{2\pi i} \oint_{\Gamma} R(z) dz = -\frac{1}{2\pi i} \oint_{\Gamma} (\mathcal{T}(x) - zI)^{-1} dz, \quad (3.58)$$

where Γ is a small contour enclosing only $\lambda^{(0)}$ and no other spectrum. Hence the projection:

$$\mathcal{T}(x) P(x) = -\frac{1}{2\pi i} \oint_{\Gamma} [I + zR(z)] dz = \frac{1}{2\pi i} \oint_{\Gamma} -zR(z) dz = \lambda(x) P(x), \quad (3.59)$$

holds true since the resolvent $R(z)$ for a simple eigenvalue admits the Laurent expansion (Kato, 1995, Ch. I, §5.3, Eq (5.18))

$$R(z) = \frac{P(x)}{\lambda(x) - z} + S(z) + \hat{R}(z), \quad \hat{R}(z) = \sum_{n=1}^{\infty} (z - \lambda(x))^n (S(z))^{n+1}, \quad (3.60)$$

where $\hat{R}(z)$ is the analytic regular remainder of z , and the residue of $-zR(z)$ at $z = \lambda(x)$ is

$$\text{Res}_{z=\lambda(x)}(-zR(z)) = [z - \lambda(x)][-zR(z)]|_{z=\lambda(x)} = \lambda(x)P(x). \quad (3.61)$$

Contour Integral of Perturbed Eigenvalue Series $\lambda(x)$. Starting from the identity in Equation (3.59),

$$\mathcal{T}(x)P(x) = \lambda(x)P(x) \quad (3.62)$$

$$\implies \text{tr}(\mathcal{T}(x)P(x)) = \text{tr}(\lambda(x)P(x)) \quad (3.63)$$

$$= \text{tr}(\lambda(x)) \text{tr}(P(x)) \quad (3.64)$$

$$= \lambda(x) \quad (3.65)$$

$$\implies \lambda(x) - \lambda^{(0)} = \text{tr}(\mathcal{T}(x)P(x)) - \lambda^{(0)} \quad (3.66)$$

$$= \text{tr}(\mathcal{T}(x)P(x)) - \text{tr}(\lambda^{(0)}P(x)) \quad (3.67)$$

$$= \text{tr}\left((\mathcal{T}(x) - \lambda^{(0)}I)P(x)\right), \quad (3.68)$$

then substituting $P(x)$ from Equation (3.59) yields:

$$\lambda(x) - \lambda^{(0)} = \text{tr}\left((\mathcal{T}(x) - \lambda^{(0)}I)\left(-\frac{1}{2\pi i} \oint_{\Gamma} R(z) dz\right)\right) \quad (3.69)$$

$$= -\frac{1}{2\pi i} \oint_{\Gamma} \text{tr}((\mathcal{T}(x) - \lambda^{(0)}I)R(z)) dz. \quad (3.70)$$

Considering the resolvent identity:

$$(\mathcal{T}(x) - zI)R(z) = I \quad (3.71)$$

and:

$$(\mathcal{T}(x) - \lambda^{(0)}I)R(z) = (\mathcal{T}(x) - zI + zI - \lambda^{(0)}I)R(z) \quad (3.72)$$

$$= (\mathcal{T}(x) - zI + (z - \lambda^{(0)})I)R(z) \quad (3.73)$$

$$= (\mathcal{T}(x) - zI)R(z) + (z - \lambda^{(0)})R(z) \quad (3.74)$$

$$= I + (z - \lambda^{(0)})R(z), \quad (3.75)$$

it yields:

$$\lambda(x) - \lambda^{(0)} = -\frac{1}{2\pi i} \oint_{\Gamma} \text{tr}((T(x) - \lambda^{(0)}I)R(z)) dz \quad (3.76)$$

$$= -\frac{1}{2\pi i} \oint_{\Gamma} \text{tr}(I + (z - \lambda^{(0)})R(z)) dz \quad (3.77)$$

$$= -\frac{1}{2\pi i} \oint_{\Gamma} \text{tr}((z - \lambda^{(0)})R(z)) dz \quad (3.78)$$

$$= -\frac{1}{2\pi i} \oint_{\Gamma} \text{tr}((z - \lambda^{(0)})R(z)) \text{tr}(I) dz \quad (3.79)$$

$$= -\frac{1}{2\pi i} \oint_{\Gamma} \text{tr}((z - \lambda^{(0)})R(z)) \text{tr}(P^{(0)}) dz \quad (3.80)$$

$$= -\frac{1}{2\pi i} \oint_{\Gamma} \text{tr}((z - \lambda^{(0)})R(z)P^{(0)}) dz. \quad (3.81)$$

Resolvent Expansion. To expand the resolvent $R(z)$, define the unperturbed resolvent $R^{(0)}(z)$:

$$R^{(0)}(z) = (T^{(0)} - zI)^{-1}, \quad (3.82)$$

then this identity holds:

$$(T^{(0)} - zI)R^{(0)}(z) = I. \quad (3.83)$$

Note that:

$$T(x) - zI = T^{(0)} - zI + \sum_{j=1}^{\infty} x^j T^{(j)} \quad (3.84)$$

$$= T^{(0)} - zI + I \sum_{j=1}^{\infty} x^j T^{(j)} \quad (3.85)$$

$$= T^{(0)} - zI + (T^{(0)} - zI)R^{(0)}(z) \sum_{j=1}^{\infty} x^j T^{(j)} \quad (3.86)$$

$$= (T^{(0)} - zI) \left(I + R^{(0)}(z) \sum_{j=1}^{\infty} x^j T^{(j)} \right), \quad (3.87)$$

so that the operator Neumann series of $R(z)$ expands as:

$$R(z) = (\mathcal{T}(x) - zI)^{-1} \quad (3.88)$$

$$= \left[(\mathcal{T}^{(0)} - zI) \left(I + R^{(0)}(z) \sum_{j=1}^{\infty} x^j \mathcal{T}^{(j)} \right) \right]^{-1} \quad (3.89)$$

$$= \left(I + R^{(0)}(z) \sum_{j=1}^{\infty} x^j \mathcal{T}^{(j)} \right)^{-1} (\mathcal{T}^{(0)} - zI)^{-1} \quad (3.90)$$

$$= \left(I + R^{(0)}(z) \sum_{j=1}^{\infty} x^j \mathcal{T}^{(j)} \right)^{-1} R^{(0)}(z) \quad (3.91)$$

$$= \underbrace{\left(I - \left(-R^{(0)}(z) \sum_{j=1}^{\infty} x^j \mathcal{T}^{(j)} \right) \right)^{-1}}_{\text{Neumann series}} R^{(0)}(z) \quad (3.92)$$

$$= \sum_{k=0}^{\infty} (-1)^k \left(R^{(0)}(z) \sum_{j=1}^{\infty} x^j \mathcal{T}^{(j)} \right)^k R^{(0)}(z). \quad (3.93)$$

Asymptotic Eigenvalue Expansion. Expanding the term in Equation (3.93):

$$\left(R^{(0)}(z) \sum_{j=1}^{\infty} x^j \mathcal{T}^{(j)} \right)^k \quad (3.94)$$

yields:

$$\left(R^{(0)}(z) \sum_{j=1}^{\infty} x^j \mathcal{T}^{(j)} \right)^k = \sum_{i_1, \dots, i_k \geq 1} x^{i_1 + \dots + i_k} R^{(0)}(z) \mathcal{T}^{(i_1)} R^{(0)}(z) \dots R^{(0)}(z) \mathcal{T}^{(i_k)} \quad (3.95)$$

$$= \sum_{i_1, \dots, i_k \geq 1} x^{i_1 + \dots + i_k} R^{(0)}(z) R_{i_k}(z), \quad (3.96)$$

where $R_{i_k}(z)$ represents an operator composition series:

$$R_{i_k}(z) = \mathcal{T}^{(i_1)} R^{(0)}(z) \dots R^{(0)}(z) \mathcal{T}^{(i_k)}. \quad (3.97)$$

Substituting Equation (3.96) into Equation (3.93) yields:

$$R(z) = \sum_{k=0}^{\infty} (-1)^k \sum_{i_1, \dots, i_k \geq 1} x^{i_1 + \dots + i_k} R^{(0)}(z) R_{i_k}(z) R^{(0)}(z) \quad (3.98)$$

$$= \sum_{k=0}^{\infty} (-1)^k \sum_{i_1, \dots, i_k \geq 1} x^{i_1 + \dots + i_k} R^{(0)}(z) R_{i_k}(z) R^{(0)}(z). \quad (3.99)$$

Substituting Equation (3.99) into the contour integral for $\lambda(x) - \lambda^{(0)}$ in Equation (3.81):

$$\lambda(x) - \lambda^{(0)} = -\frac{1}{2\pi i} \oint_{\Gamma} \text{tr}((z - \lambda^{(0)}) R(z) P^{(0)}) dz, \quad (3.100)$$

yields:

$$\lambda^{(n)} = \sum_{k=0}^{\infty} (-1)^k \sum_{\substack{i_1 + \dots + i_k = n \\ i_j \geq 1}} -\frac{1}{2\pi i} \oint_{\Gamma} \text{tr}((z - \lambda^{(0)}) R^{(0)}(z) R_{i_k}(z) R^{(0)}(z) P^{(0)}) dz \quad (3.101)$$

$$= \sum_{k=0}^{\infty} (-1)^{k-1} \sum_{\substack{i_1 + \dots + i_k = n \\ i_j \geq 1}} \frac{1}{2\pi i} \oint_{\Gamma} \text{tr}((z - \lambda^{(0)}) R^{(0)}(z) R_{i_k}(z) R^{(0)}(z) P^{(0)}) dz, \quad (3.102)$$

which recovers Theorem 3.3.2 (Kato's Weighted Mean of Eigenvalue Expansions (Kato, 1995, Ch. II, §2.2)).

Contracting and Relabeling Indices. We refine Theorem 3.3.2 (Kato's Weighted Mean of Eigenvalue Expansions (Kato, 1995, Ch. II, §2.2)) further, with the aim of obtaining a constructive, computable and basis-dependent formulation. Note that only the multi-indices satisfying:

$$i_1 + \dots + i_k = n \quad (3.103)$$

contribute to the coefficient of x^n , and since the terms with:

$$k = 0 \quad \text{or} \quad k > n \quad (3.104)$$

for $n \geq 1$ vanish, we contract the summation to the admissible subset of indices. For clarity, we denote this contracted index set by $p \subseteq k$:

$$\lambda^{(n)} = \sum_{p=1}^n (-1)^{p-1} \sum_{\substack{i_1 + \dots + i_p = n \\ i_j \geq 1}} \frac{1}{2\pi i} \oint_{\Gamma} \text{tr}((z - \lambda^{(0)}) R^{(0)}(z) R_{i_p}(z) R^{(0)}(z) P^{(0)}) dz. \quad (3.105)$$

Applying Cauchy's Residue Theorem Applying Cauchy's residue theorem via Riesz–Dunford functional calculus (Dunford and Schwartz, 1988) for Equation (3.105) yields:

$$\lambda^{(n)} = \sum_{p=1}^n (-1)^{p-1} \sum_{\substack{i_1 + \dots + i_p = n \\ i_j \geq 1}} \text{Res}_{z=\lambda^{(0)}} \left[\text{tr} \left((z - \lambda^{(0)}) R^{(0)}(z) R_{i_p}(z) R^{(0)}(z) P^{(0)} \right) \right]. \quad (3.106)$$

Simplifying Residue. We now aim to compute the residue:

$$\text{Res}_{z=\lambda^{(0)}} \left[\text{tr} \left((z - \lambda^{(0)}) R^{(0)}(z) R_{i_p}(z) R^{(0)}(z) P^{(0)} \right) \right]. \quad (3.107)$$

Note that near $z = \lambda^{(0)}$, the Laurent expansion of the unperturbed resolvent $R^{(0)}(z)$ for a simple eigenvalue $\lambda^{(0)}$ admits (Kato, 1995, Ch. I, §5.3, Eq (5.18)):

$$R^{(0)}(z) = \frac{P^{(0)}}{\lambda^{(0)} - z} + S^{(0)} + \hat{R}^{(0)}(z), \quad \hat{R}^{(0)}(z) = \sum_{n=1}^{\infty} (z - \lambda^{(0)})^n (S^{(0)})^{n+1}, \quad (3.108)$$

where $P^{(0)} = w^{(0)}(w^{(0)})^*$, $S^{(0)} = R^{(0)}(z)(I - P^{(0)})$ is the unperturbed reduced resolvent of $R^{(0)}(z)$, and $\hat{R}^{(0)}(z)$ is the analytic regular remainder of z . Substitute $R^{(0)}(z)$ into the trace product:

$$\text{tr} \left((z - \lambda^{(0)}) R^{(0)}(z) R_{i_p}(z) R^{(0)}(z) P^{(0)} \right), \quad (3.109)$$

and consider that in the expanded trace product:

1. the terms $P^{(0)}S^{(0)} = S^{(0)}P^{(0)} = 0$ vanish,

2. the terms with higher-order poles vanish, since the denominators are constant operators.

Then only the term with simple pole survives:

$$\text{Res}_{z=\lambda^{(0)}} \left[\text{tr} \left((z - \lambda^{(0)}) R^{(0)}(z) R_{i_p}(z) R^{(0)}(z) P^{(0)} \right) \right] = \text{Res}_{z=\lambda^{(0)}} \left[\text{tr} \left((z - \lambda^{(0)}) \frac{P^{(0)} \mathcal{T}^{(i_1)} S^{(0)} \dots S^{(0)} \mathcal{T}^{(i_p)} P^{(0)}}{(\lambda^{(0)} - z)^2} P^{(0)} \right) \right] \quad (3.110)$$

$$= \text{Res}_{z=\lambda^{(0)}} \left[\text{tr} \left(\frac{P^{(0)} \mathcal{T}^{(i_1)} S^{(0)} \dots S^{(0)} \mathcal{T}^{(i_p)} P^{(0)}}{z - \lambda^{(0)}} P^{(0)} \right) \right] \quad (3.111)$$

$$= (z - \lambda^{(0)}) \text{tr} \left(\frac{P^{(0)} \mathcal{T}^{(i_1)} S^{(0)} \dots S^{(0)} \mathcal{T}^{(i_p)} P^{(0)}}{z - \lambda^{(0)}} P^{(0)} \right) |_{z \rightarrow \lambda^{(0)}} \quad (3.112)$$

$$= \text{tr} \left(P^{(0)} \mathcal{T}^{(i_1)} S^{(0)} \dots S^{(0)} \mathcal{T}^{(i_p)} P^{(0)} P^{(0)} \right) \quad (3.113)$$

$$= \text{tr} \left(\mathcal{T}^{(i_1)} S^{(0)} \dots S^{(0)} \mathcal{T}^{(i_p)} P^{(0)} P^{(0)} P^{(0)} \right) \quad (3.114)$$

$$= \text{tr} \left(\mathcal{T}^{(i_1)} S^{(0)} \dots S^{(0)} \mathcal{T}^{(i_p)} P^{(0)} \right), \quad (3.115)$$

since $P^{(0)} P^{(0)} = P^{(0)}$.

Producing Theorem Claim. Substituting the residue from Equation (3.115) into Equation (3.106) yields:

$$\lambda^{(n)} = \sum_{p=1}^n (-1)^{p-1} \sum_{\substack{i_1 + \dots + i_p = n \\ i_j \geq 1}} \text{tr} \left(\mathcal{T}^{(i_1)} S^{(0)} \dots S^{(0)} \mathcal{T}^{(i_p)} P^{(0)} \right) \quad (3.116)$$

$$= \sum_{p=1}^n (-1)^{p-1} \sum_{\substack{i_1 + \dots + i_p = n \\ i_j \geq 1}} \text{tr} \left(\mathcal{T}^{(i_1)} S^{(0)} \dots S^{(0)} \mathcal{T}^{(i_p)} w^{(0)} (w^{(0)})^* \right) \quad (3.117)$$

$$= \sum_{p=1}^n (-1)^{p-1} \sum_{\substack{i_1 + \dots + i_p = n \\ i_j \geq 1}} \text{tr} \left((w^{(0)})^* \mathcal{T}^{(i_1)} S^{(0)} \dots S^{(0)} \mathcal{T}^{(i_p)} w^{(0)} \right) \quad (3.118)$$

$$= \sum_{p=1}^n (-1)^{p-1} \sum_{\substack{i_1 + \dots + i_p = n \\ i_j \geq 1}} \langle w^{(0)}, \mathcal{T}^{(i_1)} S^{(0)} \mathcal{T}^{(i_2)} S^{(0)} \dots S^{(0)} \mathcal{T}^{(i_p)} w^{(0)} \rangle, \quad (3.119)$$

which is basis-dependent and expressed in terms of unperturbed reduced resolvent.

□

Remark 3.3.5. By refining Theorem 3.3.2 (Kato's Weighted Mean of Eigenvalue Expansions (Kato, 1995, Ch. II, §2.2)), Theorem 3.3.3 (Refined Closed-Form Asymptotic Expansion of Simple Isolated Eigenvalue in Self-Adjoint Operator) provides an *explicit, closed-form representation* of the coefficients $\lambda^{(n)}$ in the eigenvalue perturbation series. Classical analytic perturbation theory (Kato, 1995) guarantees the existence of such expansions and gives recursive characterizations of the coefficients, but does not furnish constructive closed forms. In contrast, our formulation expresses each $\lambda^{(n)}$ in terms of finitely

many operator products involving the perturbation operators $\mathcal{T}^{(j)}$ and the unperturbed reduced resolvent $S^{(0)}$, making the coefficients directly computable. As a validation, for $n = 1, 2, \dots$, the expansion specializes to the familiar Rayleigh–Schrödinger corrections of quantum mechanics (Rayleigh, 2013; Schrödinger, 1926; Sakurai and Napolitano, 2020).

3.4 Infinitesimal Higher-Order Spectral Variations

Guided by the scheme in Figure 3.1, and under Assumption 3.2.2 (Simplicity Assumption of Non-Zero Singular Values), we exploit the spectral correspondence between a rectangular matrix $A \in \mathbb{R}^{m \times n}$ and its Jordan–Wielandt embedding \mathcal{T} as established in Theorem 3.1.2 (Spectrum of Jordan–Wielandt Embedding). This allows us to derive arbitrary-order Fréchet derivatives of the singular values of A from the asymptotic eigenvalue expansions of \mathcal{T} . The argument proceeds by first establishing the correspondence between the perturbation series and Fréchet derivatives as stated in Theorem 3.4.1 (Analytic Perturbation for Holomorphic Operators), and then applying this relation to obtain higher-order derivatives of singular values as stated in Theorem 3.4.2 (Higher-Order Infinitesimal Spectral Variation).

Theorem 3.4.1 (Analytic Perturbation for Holomorphic Operators). *Let X be a Banach space and let $\mathcal{T}(x) : U \subset \mathbb{C} \rightarrow \mathcal{L}(X)$ be a holomorphic family — i.e., type (A) in the sense of Kato’s framework (Kato, 1995), defined in a neighborhood of 0 in the operator norm. Then \mathcal{T} is C^∞ in the Fréchet sense at 0 and admits the convergent operator–norm expansion:*

$$\mathcal{T}(x) = \sum_{n=0}^{\infty} \frac{x^n}{n!} D^n \mathcal{T}(0), \quad |x| < \rho, \quad (3.120)$$

where ρ is the distance from 0 to the boundary of U . In particular, if one writes the perturbation series as:

$$\mathcal{T}(x) = \mathcal{T}^{(0)} + \sum_{n=1}^{\infty} x^n \mathcal{T}^{(n)}, \quad (3.121)$$

then the coefficients agree with the Fréchet derivatives, namely:

$$\mathcal{T}^{(n)} = \frac{1}{n!} D^n \mathcal{T}(0), \quad n \geq 1. \quad (3.122)$$

Theorem 3.4.2 (Higher-Order Infinitesimal Spectral Variation). *Let*

$$A \in \mathbb{R}^{m \times n} \quad (3.123)$$

be a real rectangular matrix under Assumption 3.2.2 (Simplicity Assumption of Non-Zero Singular Values).

Matrix Perturbation Series. *Let*

$$A(x) = \sum_{k=0}^{\infty} x^k A^{(k)} \in \mathbb{R}^{m \times n} \quad (3.124)$$

be holomorphic perturbed operator near $x = 0$ with unperturbed matrix $A^{(0)} = A$.

The unperturbed matrix $A^{(0)}$ admits a full SVD:

$$A^{(0)} = U^{(0)} \Sigma^{(0)} (V^{(0)})^T, \quad (3.125)$$

as defined in Theorem 3.1.1 (Matrix Singular Value Decomposition (Full Form)), where ordered $r = \text{rank}(A)$ non-zero singular values are given, under Assumption 3.2.2 (Simplicity Assumption of Non-Zero Singular Values), as:

$$\sigma_1^{(0)} > \sigma_2^{(0)} > \dots > \sigma_r^{(0)} > 0, \quad (3.126)$$

$u_k^{(0)}$ and $v_k^{(0)}$ are singular vectors associated with singular value $\sigma_k^{(0)}$, and:

$$U^{(0)} \in \mathbb{R}^{m \times m}, \quad V^{(0)} \in \mathbb{R}^{n \times n} \quad (3.127)$$

are orthogonal matrices. For brevity, we also use $\sigma_i = \sigma_i^{(0)}$, $u_i = u_i^{(0)}$, and $v_i = v_i^{(0)}$.

Jordan–Wielandt Perturbation Series Embedding. *Using Theorem 3.1.2 (Spectrum of Jordan–Wielandt Embedding), we embed the perturbation series $A(x)$ into $\mathcal{T}(x)$ to construct a Jordan–Wielandt embedding:*

$$\mathcal{T}(x) = \begin{bmatrix} 0 & A(x) \\ A(x)^T & 0 \end{bmatrix}. \quad (3.128)$$

This embedding admits a perturbation series:

$$\mathcal{T}(x) = \sum_{j=0}^{\infty} x^j \mathcal{T}^{(j)} \quad (3.129)$$

at \mathbf{x} near zero, with the unperturbed operator:

$$\mathcal{T}^{(0)} = \begin{bmatrix} 0 & A^{(0)} \\ (A^{(0)})^\top & 0 \end{bmatrix}, \quad (3.130)$$

and the perturbations:

$$\mathcal{T}^{(j)} = \begin{bmatrix} 0 & A^{(j)} \\ (A^{(j)})^\top & 0 \end{bmatrix}, \quad j \geq 1. \quad (3.131)$$

The non-zero eigenvalues $\lambda_i^{(\pm 0)}$ of $\mathcal{T}^{(0)}$ are therefore:

$$\lambda_i^{(+0)} = +\sigma_i^{(0)}, \quad \lambda_i^{(-0)} = -\sigma_i^{(0)}, \quad \text{for } i = 1, \dots, r, \quad (3.132)$$

associated with eigenvectors:

$$w_i^{(+0)} = \frac{1}{\sqrt{2}} \begin{bmatrix} u_i^{(0)} \\ v_i^{(0)} \end{bmatrix}, \quad w_i^{(-0)} = \frac{1}{\sqrt{2}} \begin{bmatrix} u_i^{(0)} \\ -v_i^{(0)} \end{bmatrix}, \quad (3.133)$$

and null eigenvectors,

$$a_j^{(0)} = \begin{bmatrix} u_j^{(0)} \\ 0 \end{bmatrix}, \quad (\text{for } j = r+1, \dots, m), \quad (3.134)$$

and:

$$b_k^{(0)} = \begin{bmatrix} 0 \\ v_k^{(0)} \end{bmatrix}, \quad (\text{for } j = r+1, \dots, n). \quad (3.135)$$

Since $w_k^{(+0)}$ and $w_k^{(-0)}$ are eigenvalues of $\mathcal{T}^{(0)}$, hence the identities hold:

$$\mathcal{T}^{(0)} w_k^{(+0)} = \lambda_k^{(+0)} w_k^{(+0)} \implies \mathcal{T}^{(0)} w_k^{(+0)} = \sigma_k^{(0)} w_k^{(+0)}, \quad (3.136)$$

and:

$$\mathcal{T}^{(0)} w_k^{(-0)} = \lambda_k^{(-0)} w_k^{(-0)} \implies \mathcal{T}^{(0)} w_k^{(-0)} = -\sigma_k^{(0)} w_k^{(-0)}. \quad (3.137)$$

Unperturbed Reduced Resolvent in Embedding. By definition, the spectral expansion of the reduced resolvent operator associated with the eigenvalue $\lambda_k^{(+0)} = \sigma_k^{(0)}$ and associated eigenvector $w_k^{(+0)}$ of $\mathcal{T}(x)$ is given as:

$$S_k^{(0)} = \left(\mathcal{T} - \sigma_k^{(0)} I \right)^{-1} \left(I - P_k^{(0)} \right), \quad P_k^{(0)} = w_k^{(+0)} (w_k^{(+0)})^\top, \quad (3.138)$$

which admits the spectral expansion:

$$S_k^{(0)} = \sum_{i=1, i \neq k}^r \frac{w_i^{(+0)} (w_i^{(+0)})^\top}{\sigma_i^{(0)} - \sigma_k^{(0)}} + \sum_{i=1, i \neq k}^r \frac{w_i^{(-0)} (w_i^{(-0)})^\top}{-\sigma_i^{(0)} - \sigma_k^{(0)}} - \sum_{j=r+1}^m \frac{a_j^{(0)} (a_j^{(0)})^\top}{\sigma_k^{(0)}} - \sum_{j=r+1}^n \frac{b_j^{(0)} (b_j^{(0)})^\top}{\sigma_k^{(0)}}. \quad (3.139)$$

Theorem Claim. For each integer $n \geq 1$,

$$\sigma_k^{(n)} = \sum_{p=1}^n (-1)^{p-1} \sum_{\substack{i_1 + \dots + i_p = n \\ i_j \geq 1}} \langle w_k^{(+0)}, \mathcal{T}^{(i_1)} S_k^{(0)} \mathcal{T}^{(i_2)} \dots S_k^{(0)} \mathcal{T}^{(i_p)} w_k^{(+0)} \rangle. \quad (3.140)$$

By Theorem 3.4.1 (Analytic Perturbation for Holomorphic Operators), the Fréchet derivative of the singular value is unique and given by:

$$D^n \sigma_k [dA, \dots, dA] = n! \lim_{x \rightarrow 0} \left(x^n \sigma_k^{(n)} \right), \quad (3.141)$$

where:

$$dA = \lim_{x \rightarrow 0} x A^{(1)}. \quad (3.142)$$

Proof 3.4.3. By Theorem 3.3.3 (Refined Closed-Form Asymptotic Expansion of Simple Isolated Eigenvalue in Self-Adjoint Operator), one eigenvalue $\lambda_k(x)$ of $\mathcal{T}(x)$ admits an asymptotic expansion:

$$\lambda_k(x) = \sum_{n=0}^{\infty} x^n \lambda_k^{(n)}. \quad (3.143)$$

By Theorem 3.1.2 (Spectrum of Jordan–Wielandt Embedding), for $n \geq 1$, choosing a positive eigenvalue branch $\sigma_k^{(0)}$ yields the asymptotic singular-value expansion of $A(x)$:

$$\sigma_k^{(n)} = \sum_{p=1}^n (-1)^{p-1} \sum_{\substack{i_1 + \dots + i_p = n \\ i_j \geq 1}} \langle w_k^{(+0)}, \mathcal{T}^{(i_1)} S_k^{(0)} \mathcal{T}^{(i_2)} \dots S_k^{(0)} \mathcal{T}^{(i_p)} w_k^{(+0)} \rangle. \quad (3.144)$$

By Theorem 3.4.1 (Analytic Perturbation for Holomorphic Operators), $D^n \sigma_k$ admits:

$$D^n \sigma_k = n! \sigma_k^{(n)}, \quad (3.145)$$

and its action is given by:

$$D^n \sigma_k [dA, \dots, dA] = n! \lim_{x \rightarrow 0} x^n \sigma_k^{(n)}, \quad (3.146)$$

where

$$dA = \lim_{x \rightarrow 0} x A^{(1)}. \quad (3.147)$$

□

Remark 3.4.4. Thanks to Kato's perturbation theory for linear operators, our framework for deriving singular-value derivatives rests on a rigorous analytic foundation and provides a procedural and systematic methodology, resting on a rigorous foundation, and going beyond the *ad hoc* approaches commonly found in classical matrix analysis. In the latter, derivatives are typically obtained through differential identities or perturbation arguments without a fully rigorous treatment of differentiability. For instance, Horn and Johnson (2012) present differential identities for spectral functions, but these do not constitute a unified framework for higher-order derivatives.

3.5 Special Case ($n = 1$): Closed-Form Singular-Value Jacobian

We now show that Theorem 3.4.2 (Higher-Order Infinitesimal Spectral Variation) can recover the well-known singular-value Jacobian, stated in Lemma 3.5.1 (Stewart and Sun, 1990; Magnus and Neudecker, 2019).

Lemma 3.5.1 (Closed-Form Singular-Value Jacobian). *The Jacobian of a singular value is well-known in the literature (Stewart and Sun, 1990; Magnus and Neudecker, 2019) in the form:*

$$\frac{\partial \sigma_k}{\partial A} = u_k v_k^\top, \quad (3.148)$$

which immediately admits an equivalent result with Kronecker-product presentation:

$$D\sigma_k[dA] = (v_k \otimes u_k)^\top \text{vec}(dA). \quad (3.149)$$

Proof 3.5.2. We specialize $n = 1$ in Theorem 3.4.2 (Higher-Order Infinitesimal Spectral Variation) to recover this result.

Constructing dA . We construct a perturbation series on A :

$$A(x) = A + xA^{(1)}, \quad A^{(0)} = A, \quad (3.150)$$

so it yields:

$$dA = \lim_{x \rightarrow 0} xA^{(1)}. \quad (3.151)$$

Specializing $n = 1$. Specializing $n = 1$ in Theorem 3.4.2 (Higher-Order Infinitesimal Spectral Variation) yields:

$$\sigma_k^{(1)} = \langle w_k^{(+0)}, \mathcal{T}^{(1)} w_k^{(0)} \rangle. \quad (3.152)$$

Simplifying First-Order Term. Consider:

$$\mathcal{T}^{(1)} w_k^{(+0)} = \begin{bmatrix} 0 & A^{(1)} \\ (A^{(1)})^\top & 0 \end{bmatrix} \cdot \frac{1}{\sqrt{2}} \begin{bmatrix} u_k \\ v_k \end{bmatrix} = \frac{1}{\sqrt{2}} \begin{bmatrix} A^{(1)} v_k \\ (A^{(1)})^\top u_k \end{bmatrix} \quad (3.153)$$

$$\implies \langle w_k^{(+0)}, \mathcal{T}^{(1)} w_k^{(+0)} \rangle = \left(\frac{1}{\sqrt{2}} \begin{bmatrix} u_k \\ v_k \end{bmatrix} \right)^\top \cdot \frac{1}{\sqrt{2}} \begin{bmatrix} A^{(1)} v_k \\ (A^{(1)})^\top u_k \end{bmatrix} \quad (3.154)$$

$$\implies \langle w_k^{(+0)}, \mathcal{T}^{(1)} w_k^{(+0)} \rangle = \frac{1}{2} \left[u_k^\top A^{(1)} v_k + v_k^\top (A^{(1)})^\top u_k \right] \quad (3.155)$$

$$\implies \langle w_k^{(+0)}, \mathcal{T}^{(1)} w_k^{(+0)} \rangle = u_k^\top A^{(1)} v_k \quad (3.156)$$

$$\implies \sigma_k^{(1)} = u_k^\top A^{(1)} v_k. \quad (3.157)$$

Adjusting Layout Representation. By Theorem 3.4.1 (Analytic Perturbation for Holomorphic Operators), we have:

$$D\sigma_k[dA] = \sigma_k^{(1)}[dA] \quad (3.158)$$

$$= \lim_{x \rightarrow 0} \sigma_k^{(1)} x A^{(1)} \quad (3.159)$$

$$= \lim_{x \rightarrow 0} u_k^\top x A^{(1)} v_k \quad (3.160)$$

$$= u_k^\top dA v_k \in \mathbb{R}. \quad (3.161)$$

Using following identities from Lemma 3.2.1 (Essential Matrix Identities):

1. $\text{tr}(x) = x,$
2. $\text{vec}(BVA^\top) = (A \otimes B) \text{vec}(V),$
3. $(A \otimes B)^\top = A^\top \otimes B^\top,$
4. $\text{tr}(ABC) = \text{tr}(CAB) = \text{tr}(BCA),$

yields:

$$D\sigma_k[dA] = \text{tr}(u_k^\top dA v_k) \quad (3.162)$$

$$= \text{tr}(v_k u_k^\top dA) \quad (3.163)$$

$$= (v_k \otimes u_k)^\top \text{vec}(dA), \quad (3.164)$$

and:

$$\frac{\partial \sigma_k}{\partial A} = (D\sigma_k)^\top = u_k v_k^\top. \quad (3.165)$$

□

3.6 Special Case ($n = 2$): Closed-Form Singular-Value Hessian

Explicit closed-form expressions for the singular-value Hessian of rectangular matrices are, to the best of our knowledge, not available in the literature. Such a result is essential for applications in stochastic analysis, for example when applying Itô's lemma to stochastic differential equations (SDEs) or stochastic partial differential equations (SPDEs) driven

by Wiener processes (Oksendal, 2013). We now derive the singular-value Hessian for general real rectangular matrices, under Assumption 3.2.2 (Simplicity Assumption of Non-Zero Singular Values), as stated in Lemma 3.6.1 (Closed-Form Singular-Value Hessian), represented in the layout:

$$\text{vec}(dA)^\top \left(\frac{\partial}{\partial \text{vec}(A)} \text{vec} \left(\frac{\partial \sigma_k}{\partial A} \right) \right) \text{vec}(dA), \quad (3.166)$$

by specializing Theorem 3.4.2 (Higher-Order Infinitesimal Spectral Variation) to the case $n = 2$.

Lemma 3.6.1 (Closed-Form Singular-Value Hessian). *The Hessian of a singular value is given as:*

$$\frac{\partial}{\partial \text{vec}(A)} \text{vec} \left(\frac{\partial \sigma_k}{\partial A} \right) = \underbrace{\sum_{i \neq k, i \leq m} \frac{\sigma_k}{\sigma_k^2 - \sigma_i^2} (v_k \otimes u_i) (v_k \otimes u_i)^\top}_{\text{left}} + \quad (3.167)$$

$$\underbrace{\sum_{j \neq k, j \leq n} \frac{\sigma_k}{\sigma_k^2 - \sigma_j^2} (v_j \otimes u_k) (v_j \otimes u_k)^\top}_{\text{right}} + \quad (3.168)$$

$$\underbrace{\sum_{l \neq k, l \leq r} \frac{\sigma_l}{\sigma_k^2 - \sigma_l^2} \left[(v_k \otimes u_l) (v_l \otimes u_k)^\top + (v_l \otimes u_k) (v_k \otimes u_l)^\top \right]}_{\text{left-right interaction}} \quad (3.169)$$

with Kronecker-product representation.

Proof 3.6.2. We specialize $n = 2$ in Theorem 3.4.2 (Higher-Order Infinitesimal Spectral Variation) to derive this result.

Constructing dA . We construct a perturbation series on A :

$$A(x) = A + xA^{(1)}, \quad A^{(0)} = A, \quad (3.170)$$

so it yields:

$$dA = \lim_{x \rightarrow 0} xA^{(1)}. \quad (3.171)$$

Specializing $n = 2$. Specializing $n = 2$ in Theorem 3.4.2 (Higher-Order Infinitesimal Spectral Variation) yields:

$$\sigma_k^{(2)} = \sum_{p=1}^2 (-1)^{p-1} \sum_{\substack{i_1 + \dots + i_p = 2 \\ i_j \geq 1}} \langle w_k^{(+0)}, \mathcal{T}^{(i_1)} S_k^{(0)} \mathcal{T}^{(i_2)} \dots S_k^{(0)} \mathcal{T}^{(i_p)} w_k^{(+0)} \rangle \quad (3.172)$$

$$= \sigma_k^{(2,p=1)} + \sigma_k^{(2,p=2)} \quad (3.173)$$

where

$$\sigma_k^{(2,p=1)} := \langle w_k^{(+0)}, \mathcal{T}^{(2)} w_k^{(+0)} \rangle, \quad (3.174)$$

and

$$\sigma_k^{(2,p=2)} := -\langle w_k^{(+0)}, \mathcal{T}^{(1)} S_k^{(0)} \mathcal{T}^{(1)} w_k^{(+0)} \rangle. \quad (3.175)$$

Computing Term $\sigma_k^{(2,p=1)}$. We first compute the term with $p = 1$ ($\sigma_k^{(2,p=1)}$). By Theorem 3.4.2 (Higher-Order Infinitesimal Spectral Variation), we substitute:

$$\mathcal{T}^{(2)} = \begin{bmatrix} 0 & A^{(2)} \\ (A^{(2)})^\top & 0 \end{bmatrix} \quad \text{and} \quad w_k^{(+0)} = \frac{1}{\sqrt{2}} \begin{bmatrix} u_k \\ v_k \end{bmatrix} \quad (3.176)$$

into:

$$\mathcal{T}^{(2)} w_k^{(+0)}, \quad (3.177)$$

it yields:

$$\mathcal{T}^{(2)} w_k^{(+0)} = \begin{bmatrix} 0 & A^{(2)} \\ (A^{(2)})^\top & 0 \end{bmatrix} \cdot \frac{1}{\sqrt{2}} \begin{bmatrix} u_k \\ v_k \end{bmatrix} = \frac{1}{\sqrt{2}} \begin{bmatrix} A^{(2)} v_k \\ (A^{(2)})^\top u_k \end{bmatrix}. \quad (3.178)$$

Substituting

$$\mathcal{T}^{(2)} w_k^{(+0)} = \frac{1}{\sqrt{2}} \begin{bmatrix} A^{(2)} v_k \\ (A^{(2)})^\top u_k \end{bmatrix} \quad (3.179)$$

into:

$$\sigma_k^{(2,p=1)} = \langle w_k^{(+0)}, \mathcal{T}^{(2)} w_k^{(+0)} \rangle \quad (3.180)$$

yields:

$$\sigma_k^{(2,p=1)} = \langle w_k^{(+0)}, \mathcal{T}^{(2)} w_k^{(+0)} \rangle \quad (3.181)$$

$$= \frac{1}{2} \left[u_k^\top A^{(2)} v_k + (v_k)^\top (A^{(2)})^\top u_k \right] \quad (3.182)$$

$$= u_k^\top A^{(2)} v_k \quad (3.183)$$

In the construction of dA , there is:

$$A^{(2)} = O, \quad (3.184)$$

so that:

$$\sigma_k^{(2,p=1)} = u_k^\top A^{(2)} v_k = 0. \quad (3.185)$$

Sketch of Computing Term $\sigma_k^{(2,p=2)}$. We compute the term with $p = 2$:

$$\sigma_k^{(2,p=2)} = -\langle w_k^{(+0)}, \mathcal{T}^{(1)} S_k^{(0)} \mathcal{T}^{(1)} w_k^{(+0)} \rangle. \quad (3.186)$$

To simplify, we first compute:

$$S_k^{(0)} \mathcal{T}^{(1)} w_k^{(+0)}, \quad (3.187)$$

then substitute this result into Equation (3.186) to produce complete $\sigma_k^{(2,p=2)}$.

Computing Contributions in $S_k^{(0)} \mathcal{T}^{(1)} w_k^{(+0)}$ in $\sigma_k^{(2,p=2)}$. By Theorem 3.4.2 (Higher-Order Infinitesimal Spectral Variation), the unperturbed reduced resolvent is defined as:

$$S_k^{(0)} = \sum_{i=1, i \neq k}^r \frac{w_i^{(+0)} (w_i^{(+0)})^\top}{\sigma_i^{(0)} - \sigma_k^{(0)}} + \sum_{i=1, i \neq k}^r \frac{w_i^{(-0)} (w_i^{(-0)})^\top}{-\sigma_i^{(0)} - \sigma_k^{(0)}} - \sum_{j=r+1}^m \frac{a_j^{(0)} (a_j^{(0)})^\top}{\sigma_k^{(0)}} - \sum_{j=r+1}^n \frac{b_j^{(0)} (b_j^{(0)})^\top}{\sigma_k^{(0)}}. \quad (3.188)$$

By Theorem 3.4.2 (Higher-Order Infinitesimal Spectral Variation), substituting non-null eigenvectors of the unperturbed embedding $\mathcal{T}^{(0)}$:

$$w_i^{(+0)} = \frac{1}{\sqrt{2}} \begin{bmatrix} u_i \\ v_i \end{bmatrix}, \quad w_i^{(-0)} = \frac{1}{\sqrt{2}} \begin{bmatrix} u_i \\ -v_i \end{bmatrix}, \quad (3.189)$$

and null eigenvectors of the unperturbed embedding $\mathcal{T}^{(0)}$:

$$a_j^{(0)} = \begin{bmatrix} u_j \\ 0 \end{bmatrix}, \quad b_j^{(0)} = \begin{bmatrix} 0 \\ v_j \end{bmatrix}, \quad (3.190)$$

into $S_k^{(0)}$ yields:

$$S_k^{(0)} = \underbrace{\sum_{i=1, i \neq k}^r \frac{1}{2} \begin{bmatrix} u_i \\ v_i \end{bmatrix} \begin{bmatrix} u_i^\top & v_i^\top \end{bmatrix}}_{\text{positive eigenspaces}} + \underbrace{\sum_{i=1, i \neq k}^r \frac{1}{2} \begin{bmatrix} u_i \\ -v_i \end{bmatrix} \begin{bmatrix} u_i^\top & -v_i^\top \end{bmatrix}}_{\text{negative eigenspaces}} - \underbrace{\sum_{j=r+1}^m \frac{\begin{bmatrix} u_j \\ 0 \end{bmatrix} \begin{bmatrix} u_j^\top & 0 \end{bmatrix}}{\sigma_k^{(0)}}}_{\text{left-null eigenspaces}} - \underbrace{\sum_{j=r+1}^n \frac{\begin{bmatrix} 0 \\ v_j \end{bmatrix} \begin{bmatrix} 0 & v_j^\top \end{bmatrix}}{\sigma_k^{(0)}}}_{\text{right-null eigenspaces}}, \quad (3.191)$$

where:

1. **contributions in positive eigenspaces** ($S_k^{(+0)}$) represents the contribution in the subspaces associated with $w_i^{(+0)}$;
2. **contributions in negative eigenspaces** ($S_k^{(-0)}$) represents the contribution in the subspaces associated with $w_i^{(-0)}$;
3. **contributions in left-null eigenspaces** ($S_k^{(0,a)}$) represents the contribution in the subspaces associated with $a_j^{(0)}$;
4. **contributions in right-null eigenspaces** ($S_k^{(0,b)}$) represents the contribution in the subspaces associated with $b_j^{(0)}$.

Substituting $w_k^{(+0)}$ into:

$$S_k^{(0)} \mathcal{T}^{(1)} w_k^{(+0)} \quad (3.192)$$

yields:

$$S_k^{(0)} \mathcal{T}^{(1)} w_k^{(+0)} = S_k^{(0)} \mathcal{T}^{(1)} \frac{1}{\sqrt{2}} \begin{bmatrix} u_k \\ v_k \end{bmatrix} = S_k^{(0)} \frac{1}{\sqrt{2}} \begin{bmatrix} A^{(1)} v_k \\ (A^{(1)})^\top u_k \end{bmatrix}, \quad (3.193)$$

then apply the explicit $S_k^{(0)}$ on this result:

$$S_k^{(0)} \mathcal{T}^{(1)} w_k^{(+0)} = S_k^{(0)} \frac{1}{\sqrt{2}} \begin{bmatrix} A^{(1)} v_k \\ (A^{(1)})^\top u_k \end{bmatrix} = (S_k^{(+0)} + S_k^{(-0)} + S_k^{(0,a)} + S_k^{(0,b)}) \frac{1}{\sqrt{2}} \begin{bmatrix} A^{(1)} v_k \\ (A^{(1)})^\top u_k \end{bmatrix}, \quad (3.194)$$

and discuss the contributions in terms of subspaces:

1. Contributions in Positive Eigenspaces.

To compute

$$S_k^{(+0)} \frac{1}{\sqrt{2}} \begin{bmatrix} A^{(1)}v_k \\ (A^{(1)})^\top u_k \end{bmatrix} = \sum_{i=1, i \neq k}^r \frac{w_i^{(+0)}(w_i^{(+0)})^\top}{\sigma_i - \sigma_k} \frac{1}{\sqrt{2}} \begin{bmatrix} A^{(1)}v_k \\ (A^{(1)})^\top u_k \end{bmatrix}, \quad (3.195)$$

consider:

$$\begin{aligned} (w_i^{(+0)})^\top \cdot \frac{1}{\sqrt{2}} \begin{bmatrix} A^{(1)}v_k \\ (A^{(1)})^\top u_k \end{bmatrix} &= \frac{1}{\sqrt{2}} \begin{bmatrix} u_i^\top & v_i^\top \end{bmatrix} \cdot \frac{1}{\sqrt{2}} \begin{bmatrix} A^{(1)}v_k \\ (A^{(1)})^\top u_k \end{bmatrix} \\ &= \frac{1}{2} \left[u_i^\top A^{(1)}v_k + v_i^\top (A^{(1)})^\top u_k \right]. \end{aligned} \quad (3.196)$$

Note the identity:

$$v_i^\top (A^{(1)})^\top u_k = u_k^\top A^{(1)}v_i \in \mathbb{R}, \quad (3.197)$$

so that:

$$(w_i^{(+0)})^\top \cdot \frac{1}{\sqrt{2}} \begin{bmatrix} A^{(1)}v_k \\ (A^{(1)})^\top u_k \end{bmatrix} = \frac{1}{2} \left[u_i^\top A^{(1)}v_k + u_k^\top A^{(1)}v_i \right]. \quad (3.198)$$

Therefore the contributions in positive eigenspaces are given as:

$$S_k^{(+0)} \frac{1}{\sqrt{2}} \begin{bmatrix} A^{(1)}v_k \\ (A^{(1)})^\top u_k \end{bmatrix} = \sum_{i=1, i \neq k}^r \frac{w_i^{(+0)}(w_i^{(+0)})^\top}{\sigma_i - \sigma_k} \frac{1}{\sqrt{2}} \begin{bmatrix} A^{(1)}v_k \\ (A^{(1)})^\top u_k \end{bmatrix} \quad (3.199)$$

$$= \sum_{i=1, i \neq k}^r \frac{1}{\sqrt{2}} \cdot \frac{u_i^\top A^{(1)}v_k + u_k^\top A^{(1)}v_i}{2(\sigma_i - \sigma_k)} \begin{bmatrix} u_i \\ v_i \end{bmatrix}. \quad (3.200)$$

2. Contributions in Negative Eigenspaces.

To compute:

$$S_k^{(-0)} \frac{1}{\sqrt{2}} \begin{bmatrix} A^{(1)}v_k \\ (A^{(1)})^\top u_k \end{bmatrix} = \sum_{i=1, i \neq k}^r \frac{w_i^{(-0)}(w_i^{(-0)})^\top}{-\sigma_i - \sigma_k} \frac{1}{\sqrt{2}} \begin{bmatrix} A^{(1)}v_k \\ (A^{(1)})^\top u_k \end{bmatrix}, \quad (3.201)$$

consider:

$$\begin{aligned} (w_i^{(-0)})^\top \cdot \frac{1}{\sqrt{2}} \begin{bmatrix} A^{(1)}v_k \\ (A^{(1)})^\top u_k \end{bmatrix} &= \frac{1}{\sqrt{2}} \begin{bmatrix} u_i^\top & -v_i^\top \end{bmatrix} \cdot \frac{1}{\sqrt{2}} \begin{bmatrix} A^{(1)}v_k \\ (A^{(1)})^\top u_k \end{bmatrix} \\ &= \frac{1}{2} \left[u_i^\top A^{(1)}v_k - v_i^\top (A^{(1)})^\top u_k \right]. \end{aligned} \quad (3.202)$$

Note the identity:

$$v_i^\top (A^{(1)})^\top u_k = u_k^\top A^{(1)} v_i \in \mathbb{R} \quad (3.203)$$

so that:

$$(w_i^{(+0)})^\top \cdot \frac{1}{\sqrt{2}} \begin{bmatrix} A^{(1)} v_k \\ (A^{(1)})^\top u_k \end{bmatrix} = \frac{1}{2} \left[u_i^\top A^{(1)} v_k - u_k^\top A^{(1)} v_i \right] \quad (3.204)$$

$$= \frac{1}{\sqrt{2}} \cdot \frac{u_i^\top A^{(1)} v_k - u_k^\top A^{(1)} v_i}{2(-\sigma_i - \sigma_k)} \begin{bmatrix} u_i \\ -v_i \end{bmatrix}. \quad (3.205)$$

Therefore the contributions in negative eigenspaces are given as:

$$S_k^{(-0)} \frac{1}{\sqrt{2}} \begin{bmatrix} A^{(1)} v_k \\ (A^{(1)})^\top u_k \end{bmatrix} = \sum_{i=1, i \neq k}^r \frac{w_i^{(-0)} (w_i^{(-0)})^\top}{-\sigma_i - \sigma_k} \frac{1}{\sqrt{2}} \begin{bmatrix} A^{(1)} v_k \\ (A^{(1)})^\top u_k \end{bmatrix} \quad (3.206)$$

$$= \sum_{i=1, i \neq k}^r \frac{1}{\sqrt{2}} \cdot \frac{u_i^\top A^{(1)} v_k - u_k^\top A^{(1)} v_i}{2(-\sigma_i - \sigma_k)} \begin{bmatrix} u_i \\ -v_i \end{bmatrix}. \quad (3.207)$$

3. Contributions in Left-Null Eigenspaces.

To compute:

$$S_k^{(0,a)} \frac{1}{\sqrt{2}} \begin{bmatrix} A^{(1)} v_k \\ (A^{(1)})^\top u_k \end{bmatrix} = - \sum_{j=r+1}^m \frac{a_j^{(0)} (a_j^{(0)})^\top}{\sigma_k} \frac{1}{\sqrt{2}} \begin{bmatrix} A^{(1)} v_k \\ (A^{(1)})^\top u_k \end{bmatrix}, \quad (3.208)$$

consider:

$$\begin{aligned} (a_j^{(0)})^\top \cdot \frac{1}{\sqrt{2}} \begin{bmatrix} A^{(1)} v_k \\ (A^{(1)})^\top u_k \end{bmatrix} &= \frac{1}{\sqrt{2}} \begin{bmatrix} u_j^\top & 0 \end{bmatrix} \cdot \frac{1}{\sqrt{2}} \begin{bmatrix} A^{(1)} v_k \\ (A^{(1)})^\top u_k \end{bmatrix} \\ &= \frac{1}{2} u_j^\top A^{(1)} v_k. \end{aligned} \quad (3.209)$$

Therefore the contributions in left-null eigenspaces are given as:

$$S_k^{(0,a)} \frac{1}{\sqrt{2}} \begin{bmatrix} A^{(1)} v_k \\ (A^{(1)})^\top u_k \end{bmatrix} = - \sum_{j=r+1}^m \frac{a_j^{(0)} (a_j^{(0)})^\top}{\sigma_k} \frac{1}{\sqrt{2}} \begin{bmatrix} A^{(1)} v_k \\ (A^{(1)})^\top u_k \end{bmatrix} \quad (3.210)$$

$$= - \sum_{j=r+1}^m \frac{1}{\sqrt{2}} \cdot \frac{u_j^\top A^{(1)} v_k}{\sigma_k} \begin{bmatrix} u_j \\ 0 \end{bmatrix}. \quad (3.211)$$

4. Contributions in Right-Null Eigenspaces.

To compute:

$$S_k^{(0,b)} \frac{1}{\sqrt{2}} \begin{bmatrix} A^{(1)} v_k \\ (A^{(1)})^\top u_k \end{bmatrix} = - \sum_{j=r+1}^n \frac{b_j^{(0)} (b_j^{(0)})^\top}{\sigma_k} \frac{1}{\sqrt{2}} \begin{bmatrix} A^{(1)} v_k \\ (A^{(1)})^\top u_k \end{bmatrix}, \quad (3.212)$$

consider:

$$(b_j^{(0)})^\top \cdot \frac{1}{\sqrt{2}} \begin{bmatrix} A^{(1)} v_k \\ (A^{(1)})^\top u_k \end{bmatrix} = \frac{1}{\sqrt{2}} \begin{bmatrix} 0 & v_j^\top \end{bmatrix} \cdot \frac{1}{\sqrt{2}} \begin{bmatrix} A^{(1)} v_k \\ (A^{(1)})^\top u_k \end{bmatrix} = \frac{1}{2} v_j^\top (A^{(1)})^\top u_k \quad (3.213)$$

$$= \frac{1}{2} u_k^\top A^{(1)} v_j. \quad (3.214)$$

Therefore the contributions in right-null eigenspaces are given as:

$$S_k^{(0,b)} \frac{1}{\sqrt{2}} \begin{bmatrix} A^{(1)} v_k \\ (A^{(1)})^\top u_k \end{bmatrix} = - \sum_{j=r+1}^n \frac{b_j^{(0)} (b_j^{(0)})^\top}{\sigma_k} \frac{1}{\sqrt{2}} \begin{bmatrix} A^{(1)} v_k \\ (A^{(1)})^\top u_k \end{bmatrix} \quad (3.215)$$

$$= - \sum_{j=r+1}^n \frac{1}{\sqrt{2}} \cdot \frac{u_k^\top A^{(1)} v_j}{\sigma_k} \begin{bmatrix} 0 \\ v_j \end{bmatrix}. \quad (3.216)$$

Computing Inner-Product Contributions in $\langle w_k, \mathcal{T}^{(1)} S_k \mathcal{T}^{(1)} w_k \rangle$. We compute the inner-product contributions in $\langle w_k, \mathcal{T}^{(1)} S_k \mathcal{T}^{(1)} w_k \rangle$:

1. **Inner-Product Contributions in Positive Eigenspaces.** Consider:

$$Z^{(+0)} := \mathcal{T}^{(1)} S_k^{(+0)} \mathcal{T}^{(1)} w_k^{(+0)} \quad (3.217)$$

$$= \mathcal{T}^{(1)} \sum_{i=1, i \neq k}^r \frac{1}{\sqrt{2}} \cdot \frac{u_i^\top A^{(1)} v_k + u_k^\top A^{(1)} v_i}{2(\sigma_i - \sigma_k)} \begin{bmatrix} u_i \\ v_i \end{bmatrix} \quad (3.218)$$

$$= \sum_{i=1, i \neq k}^r \frac{1}{\sqrt{2}} \cdot \frac{u_i^\top A^{(1)} v_k + u_k^\top A^{(1)} v_i}{2(\sigma_i - \sigma_k)} \begin{bmatrix} A^{(1)} v_i \\ (A^{(1)})^\top u_i \end{bmatrix}, \quad (3.219)$$

so that:

$$\langle w_k, Z^{(+0)} \rangle = \sum_{i \neq k} \left(\frac{1}{\sqrt{2}} \begin{bmatrix} u_k \\ v_k \end{bmatrix} \right)^\top \frac{1}{\sqrt{2}} \cdot \frac{u_i^\top A^{(1)} v_k + u_k^\top A^{(1)} v_i}{2(\sigma_i - \sigma_k)} \begin{bmatrix} A^{(1)} v_i \\ (A^{(1)})^\top u_i \end{bmatrix} \quad (3.220)$$

$$= \sum_{i=1, i \neq k}^r \left(\frac{1}{\sqrt{2}} \right)^2 \cdot \frac{u_i^\top A^{(1)} v_k + u_k^\top A^{(1)} v_i}{2(\sigma_i - \sigma_k)} \cdot \left[u_k^\top A^{(1)} v_i + v_k^\top (A^{(1)})^\top u_i \right] \quad (3.221)$$

$$= \sum_{i=1, i \neq k}^r \frac{1}{4(\sigma_i - \sigma_k)} \left[u_i^\top A^{(1)} v_k + u_k^\top A^{(1)} v_i \right] \left[u_k^\top A^{(1)} v_i + u_i^\top A^{(1)} v_k \right] \quad (3.222)$$

$$= \sum_{i=1, i \neq k}^r \frac{1}{4(\sigma_i - \sigma_k)} \left[u_i^\top A^{(1)} v_k + u_k^\top A^{(1)} v_i \right]^2 \quad (3.223)$$

$$= \sum_{i=1, i \neq k}^r \frac{1}{4(\sigma_i - \sigma_k)} \left[\left[u_i^\top A^{(1)} v_k \right]^2 + 2u_i^\top A^{(1)} v_k u_k^\top A^{(1)} v_i + \left[u_k^\top A^{(1)} v_i \right]^2 \right]. \quad (3.224)$$

2. **Inner-Product Contributions in Negative Eigenspaces.** Consider:

$$Z^{(-0)} := \mathcal{T}^{(1)} S_k^{(-0)} \mathcal{T}^{(1)} w_k^{(+0)} \quad (3.225)$$

$$= \mathcal{T}^{(1)} \sum_{i=1, i \neq k}^r \frac{1}{\sqrt{2}} \cdot \frac{u_i^\top A^{(1)} v_k - u_k^\top A^{(1)} v_i}{2(-\sigma_i - \sigma_k)} \begin{bmatrix} u_i \\ -v_i \end{bmatrix} \quad (3.226)$$

$$= \sum_{i=1, i \neq k}^r \frac{1}{\sqrt{2}} \cdot \frac{u_i^\top A^{(1)} v_k - u_k^\top A^{(1)} v_i}{2(-\sigma_i - \sigma_k)} \begin{bmatrix} A^{(1)}(-v_i) \\ (A^{(1)})^\top u_i \end{bmatrix}, \quad (3.227)$$

so that:

$$\langle w_k, Z^{(-0)} \rangle = \sum_{i=1, i \neq k}^r \frac{1}{2} \cdot \frac{u_i^\top A^{(1)} v_k - u_k^\top A^{(1)} v_i}{2(-\sigma_i - \sigma_k)} \left[u_k^\top A^{(1)}(-v_i) + v_k^\top (A^{(1)})^\top u_i \right] \quad (3.228)$$

$$= \sum_{i=1, i \neq k}^r \frac{1}{4(-\sigma_i - \sigma_k)} \left[u_i^\top A^{(1)} v_k - u_k^\top A^{(1)} v_i \right] \left[-(u_k)^\top A^{(1)} v_i + u_i^\top A^{(1)} v_k \right] \quad (3.229)$$

$$= \sum_{i=1, i \neq k}^r \frac{1}{4(-\sigma_i - \sigma_k)} \left[u_i^\top A^{(1)} v_k - u_k^\top A^{(1)} v_i \right]^2 \quad (3.230)$$

$$= \sum_{i=1, i \neq k}^r \frac{1}{4(-\sigma_i - \sigma_k)} \left[\left[u_i^\top A^{(1)} v_k \right]^2 - 2u_i^\top A^{(1)} v_k u_k^\top A^{(1)} v_i + \left[u_k^\top A^{(1)} v_i \right]^2 \right]. \quad (3.231)$$

3. Inner-Product Contributions in Left-Null Eigenspaces.

Consider:

$$Z^{(0,a)} := \mathcal{T}^{(1)} S_k^{(0,a)} \mathcal{T}^{(1)} w_k^{(+0)} \quad (3.232)$$

$$= \mathcal{T}^{(1)} \sum_{j=r+1}^m \left(-\frac{1}{\sqrt{2}} \cdot \frac{u_j^\top A^{(1)} v_k}{\sigma_k} \begin{bmatrix} u_j \\ 0 \end{bmatrix} \right) \quad (3.233)$$

$$= \sum_{j=r+1}^m -\frac{1}{\sqrt{2}} \cdot \frac{u_j^\top A^{(1)} v_k}{\sigma_k} \begin{bmatrix} 0 \\ (A^{(1)})^\top u_j \end{bmatrix}, \quad (3.234)$$

so that:

$$\langle w_k, Z^{(0,a)} \rangle = \sum_{j=r+1}^m -\frac{1}{2} \cdot \frac{u_j^\top A^{(1)} v_k}{\sigma_k} \left[u_k^\top \cdot 0 + v_k^\top (A^{(1)})^\top u_j \right] \quad (3.235)$$

$$= \sum_{j=r+1}^m -\frac{1}{2} \cdot \frac{u_j^\top A^{(1)} v_k u_j^\top A^{(1)} v_k}{\sigma_k}. \quad (3.236)$$

4. Inner-Product Contributions in Right-Null Eigenspaces.

Consider:

$$Z^{(0,b)} := \mathcal{T}^{(1)} S_k^{(0,b)} \mathcal{T}^{(1)} w_k^{(+0)} \quad (3.237)$$

$$= \mathcal{T}^{(1)} \sum_{j=r+1}^n \left(-\frac{1}{\sqrt{2}} \cdot \frac{u_k^\top A^{(1)} v_j}{\sigma_k} \begin{bmatrix} 0 \\ v_j \end{bmatrix} \right) \quad (3.238)$$

$$= \sum_{j=r+1}^n -\frac{1}{\sqrt{2}} \cdot \frac{u_k^\top A^{(1)} v_j}{\sigma_k} \begin{bmatrix} A^{(1)} v_j \\ 0 \end{bmatrix}, \quad (3.239)$$

so that:

$$\langle w_k, Z^{(0,b)} \rangle = \sum_{j=r+1}^n -\frac{1}{2} \cdot \frac{u_k^\top A^{(1)} v_j}{\sigma_k} \left[u_k^\top A^{(1)} v_j + v_k^\top \cdot 0 \right] \quad (3.240)$$

$$= \sum_{j=r+1}^n -\frac{1}{2} \cdot \frac{[u_k^\top A^{(1)} v_j]^2}{\sigma_k}. \quad (3.241)$$

Combining Terms.

Since

$$\sigma_k^{(2,p=1)} = 0, \quad (3.242)$$

thus,

$$\sigma_k^{(2)} = \sigma_k^{(2,p=2)} \quad (3.243)$$

$$= - \left[\sum_{i=1, i \neq k}^r \frac{1}{4(\sigma_i - \sigma_k)} \left[[u_i^\top A^{(1)} v_k]^2 + 2u_i^\top A^{(1)} v_k u_k^\top A^{(1)} v_i + [u_k^\top A^{(1)} v_i]^2 \right] \right] \quad (3.244)$$

$$+ \sum_{i=1, i \neq k}^r \frac{1}{4(-\sigma_i - \sigma_k)} \left[[u_i^\top A^{(1)} v_k]^2 - 2u_i^\top A^{(1)} v_k u_k^\top A^{(1)} v_i + [u_k^\top A^{(1)} v_i]^2 \right] \quad (3.245)$$

$$- \sum_{j=r+1}^m \frac{1}{2\sigma_k} [u_j^\top A^{(1)} v_k]^2 - \sum_{j=r+1}^n \frac{1}{2\sigma_k} [u_k^\top A^{(1)} v_j]^2 \quad (3.246)$$

$$= - \left[\sum_{i=1, i \neq k}^r \frac{(\sigma_i + \sigma_k) - (\sigma_i - \sigma_k)}{4(\sigma_i^2 - \sigma_k^2)} \left[[u_i^\top A^{(1)} v_k]^2 + [u_k^\top A^{(1)} v_i]^2 \right] \right. \quad (3.247)$$

$$\left. + \frac{1}{2} \sum_{i=1, i \neq k}^r \frac{(\sigma_i + \sigma_k) + (\sigma_i - \sigma_k)}{\sigma_i^2 - \sigma_k^2} u_i^\top A^{(1)} v_k u_k^\top A^{(1)} v_i \right] \quad (3.248)$$

$$- \sum_{j=r+1}^m \frac{1}{2\sigma_k} [u_j^\top A^{(1)} v_k]^2 - \sum_{j=r+1}^n \frac{1}{2\sigma_k} [u_k^\top A^{(1)} v_j]^2 \quad (3.249)$$

$$= \frac{1}{2} \sum_{i=1, i \neq k}^r \frac{\sigma_k}{\sigma_k^2 - \sigma_i^2} [u_i^\top A^{(1)} v_k]^2 + \frac{1}{2} \sum_{i \neq k}^r \frac{\sigma_k}{\sigma_k^2 - \sigma_i^2} [u_k^\top A^{(1)} v_i]^2 \quad (3.250)$$

$$+ \frac{1}{2} \sum_{i=1, i \neq k}^r \frac{\sigma_i}{\sigma_k^2 - \sigma_i^2} u_i^\top A^{(1)} v_k u_k^\top A^{(1)} v_i + \frac{1}{2} \sum_{i=1}^r \frac{\sigma_i}{\sigma_k^2 - \sigma_i^2} u_i^\top A^{(1)} v_k u_k^\top A^{(1)} v_i \quad (3.251)$$

$$+ \frac{1}{2} \sum_{j=r+1}^m \frac{\sigma_k}{\sigma_k^2 - \sigma_j^2} [u_j^\top A^{(1)} v_k]^2 + \frac{1}{2} \sum_{j=r+1}^n \frac{\sigma_k}{\sigma_k^2 - \sigma_j^2} [u_k^\top A^{(1)} v_j]^2 \quad (3.252)$$

$$\underline{\text{combine indices}} \quad \frac{1}{2} \sum_{i \neq k} \frac{\sigma_k}{\sigma_k^2 - \sigma_i^2} [u_i^\top A^{(1)} v_k]^2 \quad (3.253)$$

$$+ \frac{1}{2} \sum_{i \neq k} \frac{\sigma_k}{\sigma_k^2 - \sigma_i^2} [u_k^\top A^{(1)} v_i]^2 \quad (3.254)$$

$$+ \frac{1}{2} \sum_{i=1}^r \frac{\sigma_i}{\sigma_i^2 - \sigma_k^2} u_i^\top A^{(1)} v_k u_k^\top A^{(1)} v_i \quad (3.255)$$

$$+ \frac{1}{2} \sum_{i=1}^r \frac{\sigma_i}{\sigma_i^2 - \sigma_k^2} u_k^\top A^{(1)} v_i u_i^\top A^{(1)} v_k. \quad (3.256)$$

Obtaining Kronecker-Product Representation. Use following identity from Lemma 3.2.1 (Essential Matrix Identities):

$$1. \quad \text{vec}(BVA^\top) = (A \otimes B) \text{vec}(V),$$

consider:

$$\lim_{x \rightarrow 0} x^2 \left[u_i^\top A^{(1)} v_k \right]^2 = \lim_{x \rightarrow 0} u_i^\top x A^{(1)} v_k u_i^\top x A^{(1)} v_k \quad (3.257)$$

$$= [u_i^\top dA v_k] [u_i^\top dA v_k] \quad (3.258)$$

$$= [v_k^\top dA u_i] [u_i^\top dA v_k] \quad (3.259)$$

$$= \text{vec}[v_k^\top dA u_i] \text{vec}[u_i^\top dA v_k] \quad (3.260)$$

$$= (u_i^\top \otimes v_k^\top) \text{vec}(dA) (v_k^\top \otimes u_i^\top) \text{vec}(dA) \quad (3.261)$$

$$= [(u_i^\top \otimes v_k^\top) \text{vec}(dA)]^\top [(v_k^\top \otimes u_i^\top) \text{vec}(dA)] \quad (3.262)$$

$$= \text{vec}(dA^\top) (v_k \otimes u_i) (v_k \otimes u_i)^\top \text{vec}(dA). \quad (3.263)$$

Similarly,

$$\lim_{x \rightarrow 0} x^2 \left[u_k^\top A^{(1)} v_i \right]^2 = \text{vec}(dA^\top) (v_i \otimes u_k) (v_i \otimes u_k)^\top \text{vec}(dA), \quad (3.264)$$

$$\lim_{x \rightarrow 0} x^2 u_i^\top A^{(1)} v_k u_k^\top A^{(1)} v_i = \lim_{x \rightarrow 0} u_i^\top x A^{(1)} v_k u_k^\top x A^{(1)} v_i \quad (3.265)$$

$$= \lim_{x \rightarrow 0} u_i^\top dA v_k u_k^\top dA v_i \quad (3.266)$$

$$= \text{vec}(dA^\top) (v_k \otimes u_i) (v_i \otimes u_k)^\top \text{vec}(dA), \quad (3.267)$$

and:

$$\lim_{x \rightarrow 0} x^2 u_k^\top A^{(1)} v_i u_i^\top A^{(1)} v_k = \lim_{x \rightarrow 0} u_k^\top x A^{(1)} v_i u_i^\top x A^{(1)} v_k \quad (3.268)$$

$$= \lim_{x \rightarrow 0} u_k^\top dA v_i u_i^\top dA v_k \quad (3.269)$$

$$= \text{vec}(dA^\top) (v_i \otimes u_k) (v_k \otimes u_i)^\top \text{vec}(dA). \quad (3.270)$$

Producing Lemma Claim. Hence,

$$D^2\sigma_k[dA, dA] = \text{vec}(dA)^\top \frac{\partial}{\partial \text{vec}(A)} \text{vec}\left(\frac{\partial \sigma_k}{\partial A}\right) \text{vec}(dA) \quad (3.271)$$

$$= 2 \lim_{x \rightarrow 0} x^2 \sigma_k^{(2)} \quad (3.272)$$

$$= \sum_{i \neq k} \frac{\sigma_k}{\sigma_k^2 - \sigma_i^2} \lim_{x \rightarrow 0} x^2 \left[u_i^\top A^{(1)} v_k \right]^2 \quad (3.273)$$

$$+ \sum_{i \neq k} \frac{\sigma_k}{\sigma_k^2 - \sigma_i^2} \lim_{x \rightarrow 0} x^2 \left[u_k^\top A^{(1)} v_i \right]^2 \quad (3.274)$$

$$+ \sum_{i=1}^r \frac{\sigma_i}{\sigma_i^2 - \sigma_k^2} \lim_{x \rightarrow 0} x^2 u_i^\top A^{(1)} v_k u_k^\top A^{(1)} v_i \quad (3.275)$$

$$+ \sum_{i=1}^r \frac{\sigma_i}{\sigma_i^2 - \sigma_k^2} \lim_{x \rightarrow 0} x^2 u_k^\top A^{(1)} v_i u_i^\top A^{(1)} v_k. \quad (3.276)$$

Re-labeling indices yields the claim:

$$D^2\sigma_k[dA, dA] = \text{vec}(dA)^\top \left[\underbrace{\sum_{i \neq k, i \leq r} \frac{\sigma_k}{\sigma_k^2 - \sigma_i^2} (v_k \otimes u_i) (v_k \otimes u_i)^\top}_{\text{left}} \right] \quad (3.277)$$

$$+ \underbrace{\sum_{j \neq k, j \leq n} \frac{\sigma_k}{\sigma_k^2 - \sigma_j^2} (v_j \otimes u_k) (v_j \otimes u_k)^\top}_{\text{right}} \quad (3.278)$$

$$+ \underbrace{\sum_{l \neq k, l \leq r} \frac{\sigma_l}{\sigma_k^2 - \sigma_l^2} \left[(v_k \otimes u_l) (v_l \otimes u_k)^\top + (v_l \otimes u_k) (v_k \otimes u_l)^\top \right]}_{\text{left-right interaction}} \right] \text{vec}(dA). \quad (3.279)$$

□

3.7 Numerical Experiments

We conduct numerical experiments to validate the correctness of the derived special cases $n = 1$ and $n = 2$. Matrix entries are sampled from $\mathcal{N}(0, 1)$ and $\mathcal{U}(0, 1)$, respectively,

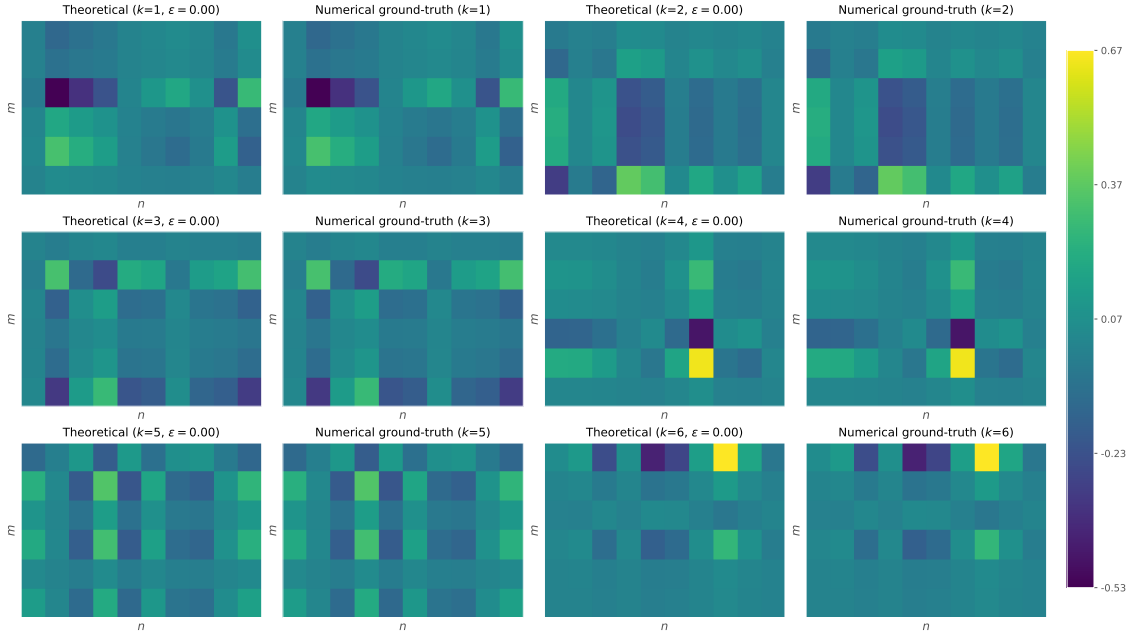
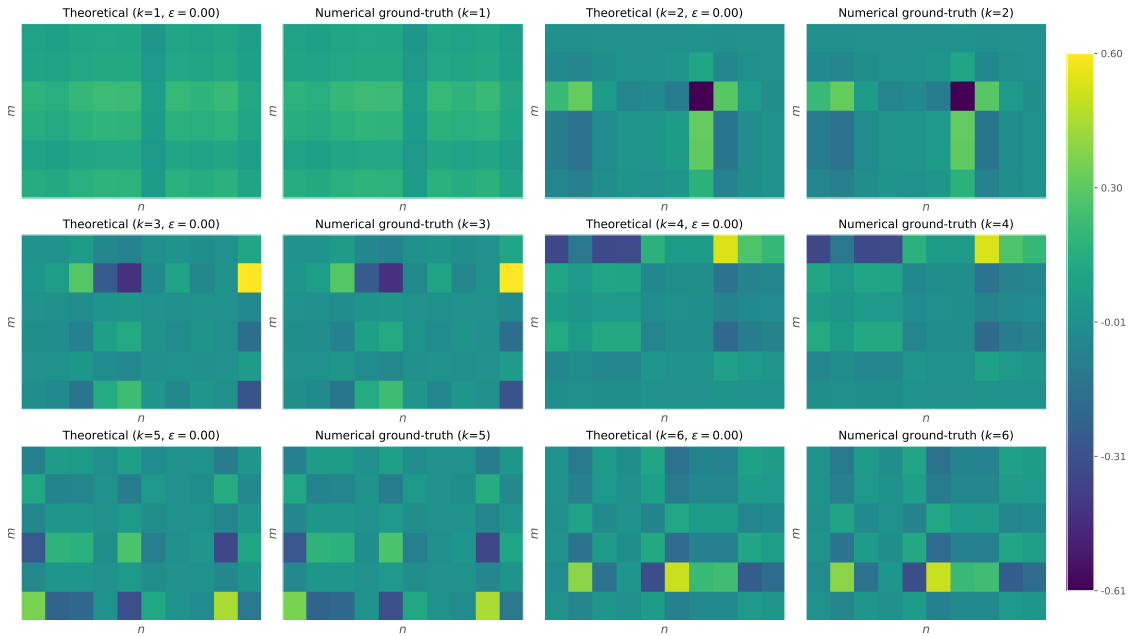
(a) Matrix entries i.i.d. from $\mathcal{N}(0, 1)$.(b) Matrix entries i.i.d. from $U[0, 1]$.

Figure 3.2: Numerical Experiments for Singular-Value Jacobian. This experiment compares the singular-value Jacobian derived from our framework with that obtained via PyTorch’s auto-differentiation. The error ϵ is measured as the ℓ_2 -norm between the theoretical and ground-truth results. The error is measured to be zero in these experiments, indicating no difference between the theoretical and ground-truth results.

for both $n = 1$ and $n = 2$. Ground truth is obtained numerically via PyTorch’s auto-differentiation framework (Paszke et al., 2019). The error ϵ is computed by the ℓ_2 -norm

$$\epsilon = \|\mathbf{R}_{\text{ours}} - \mathbf{R}_{\text{gt}}\|_2, \quad (3.280)$$

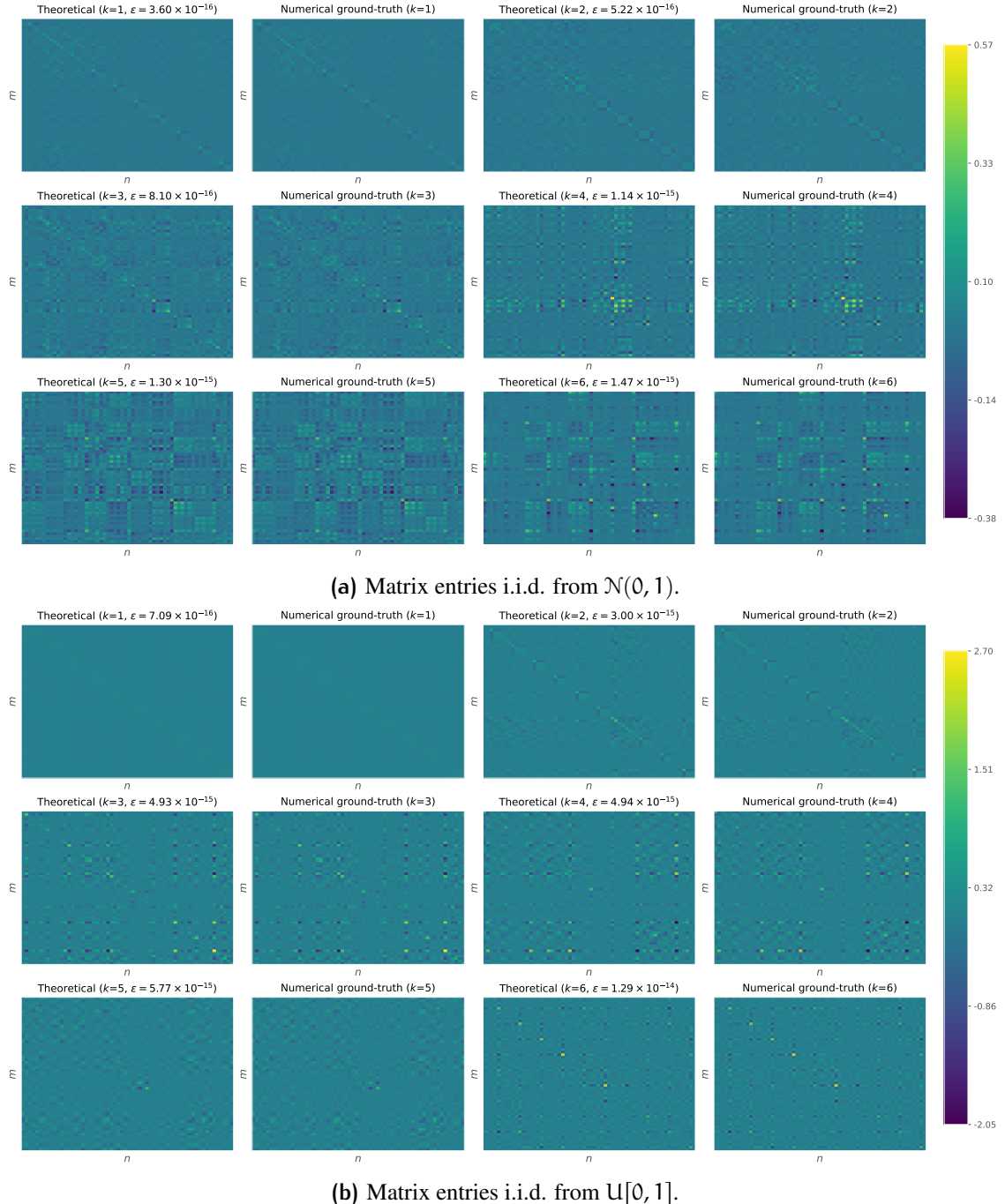


Figure 3.3: Numerical Experiments for Singular-Value Hessian. This experiment compares the singular-value Hessian derived from our framework with that obtained via PyTorch’s auto-differentiation. The error ϵ is measured as the ℓ_2 -norm between the theoretical and ground-truth results. The maximum error is measured to be less than 1.3×10^{-14} in these experiments, indicating the difference between the theoretical and ground-truth results is negligible.

where R_{ours} denotes the result from our theoretical computation and R_{gt} the ground truth from auto-differentiation. Singular values are indexed by $k = 1, 2, \dots, r$ in the reported

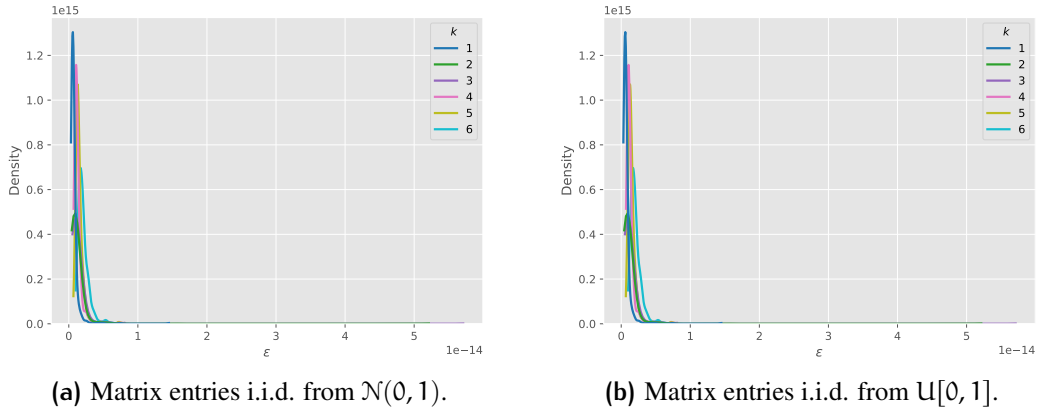


Figure 3.4: Errors for Singular-Value Hessian. Random matrix entries are sampled i.i.d. from $\mathcal{N}(0, 1)$ and $\mathcal{U}[0, 1]$, respectively. For each singular-value index $k = 1, 2, \dots, r$, the error ϵ is computed over 500 trials and visualized using an unnormalized histogram density. All reported errors are below 6×10^{-14} in these experiments.

results. To facilitate the visualization and computation, we choose the dimensions 6×10 in all experiments.

Reproducibility. The random seed is fixed to 1 for reproducibility. All experimental code is available at https://github.com/roisincrtai/highorder_spectral_variation_analysis.

Results of Singular-Value Jacobian. Figure 3.2 reports the results for the singular-value Jacobian. Matrix entries are sampled i.i.d. from $\mathcal{N}(0, 1)$ and $\mathcal{U}(0, 1)$, respectively. The derivative matrices are visualized using the *viridis* color map. For each singular-value index k , results are shown in pairs: the left panel gives the theoretical computation from Lemma 3.5.1, while the right panel shows the numerical ground truth obtained from PyTorch’s auto-differentiation framework. The reported errors are zero across all experiments.

Results of Singular-Value Hessian. Figure 3.3 reports the results for the singular-value Hessian. Matrix entries are sampled i.i.d. from $\mathcal{N}(0, 1)$ and $\mathcal{U}(0, 1)$, respectively. The derivative matrices are visualized using the *viridis* color map. For each singular-value index k , results are shown in pairs: the left panel gives the theoretical computation from Lemma 3.6.1, while the right panel shows the numerical ground truth obtained from PyTorch’s auto-differentiation framework. The observed errors between theoretical results and numerical ground-truth are on the order of 10^{-14} , confirming that they are numerically negligible.

3.8 Conclusion

By viewing matrices as compact linear operators and extending Kato's perturbation theory for self-adjoint operators, we present a unified operator-theoretic framework for obtaining closed-form, arbitrary-order derivatives of singular values in real rectangular matrices. In contrast to the *ad hoc* methods of classical matrix analysis, our approach is systematic and procedural, allowing the derivation of singular-value derivatives of any order. The key step is the Jordan–Wielandt embedding, which maps a real rectangular matrix, usually non-self-adjoint, to a self-adjoint operator, thereby encapsulating its complete spectral information. Based on Kato's framework, we establish a general framework for deriving higher-order singular-value derivatives. Specializing to first order ($n = 1$) recovers the classical singular-value Jacobian, while specializing to second order ($n = 2$) yields a Kronecker-product representation of the singular-value Hessian that, to the best of our knowledge, has not previously appeared in the literature. Beyond these cases, the framework extends to arbitrary order. Higher-order singular-value derivatives are indispensable for analyzing induced spectral dynamics in statistical physics and deep learning.

4

STOCHASTIC DYNAMIC ANALYSIS OF LIPSCHITZ CONTINUITY

Copyright Disclaimer. This chapter includes content adapted from the following article:

1. **Róisín Luo**, J. McDermott, C. Gagné, Q. Sun, and C. O’Riordan. **Optimization-Induced Dynamics of Lipschitz Continuity in Neural Networks**. Manuscript is under review at Journal of Machine Learning Research (JMLR), 2025a. URL <https://arxiv.org/abs/2506.18588>

Portions of the content are reused verbatim or with minor edits, in accordance with institutional guidelines and the policies of the relevant publishers. Permission from all co-authors has been obtained.

Authorship Statement. This chapter is the result of collaborative research. Contributions from the authors are stated as below:

- (i) Róisín Luo, affiliated with *University of Galway – Ireland* and *Irish National Centre for Research Training in AI*, made the primary contributions, including conceptualization, theoretical analysis, drafting, etc.
- (ii) Dr. James McDermott, affiliated with *University of Galway – Ireland* and *Irish National Centre for Research Training in AI*, provided supervision, contributed to the refinement of the manuscript, offered academic guidance, and critically reviewed the content.
- (iii) Dr. Christian Gagné, affiliated with *Université Laval – Canada, Canada – CIFAR AI Chair*, and *Mila – Québec AI Institute*, contributed to the refinement of the manuscript, offered academic guidance, and critically reviewed the content.
- (iv) Dr. Qiang Sun, affiliated with *University of Toronto - Canada*, and *MBZUAI – UAE*, contributed to the refinement of the manuscript, offered academic guidance, and critically reviewed the content.
- (v) Dr. Colm O’Riordan, affiliated with *University of Galway – Ireland* and *Irish National Centre for Research Training in AI*, provided supervision, contributed to the refinement of the manuscript, offered academic guidance, and critically reviewed the content.

I confirm that the contributions stated above accurately reflect the work I completed and the assistance provided by co-authors. All collaborators have reviewed, approved the manuscript to which they contributed, and consent to its inclusion in this thesis.

Guiding Research Question. This chapter addresses the secondary research question **(SRQ4) Stochastic Dynamic Analysis of Lipschitz Continuity**, in service of the primary research question — **(RQ2) Training Dynamics**. Building on the analytic operator-norm Hessian formulation introduced in the previous chapter, and incorporating high-dimensional stochastic differential equations (SDEs), this chapter establishes — to the best of our knowledge — the first theoretical framework for modeling the temporal evolution of Lipschitz continuity in neural networks during training. The proposed framework is validated through numerical experiments with a convolutional neural network trained on CIFAR-10 and CIFAR-100 with multiple regularization configurations. It also offers theoretical insights into neural network behaviors, including near convergence dynamics, the role of hyper-parameters, and the impact of noisy supervision.

Reproducibility. https://anonymous.4open.science/r/lipschitz_dynamics_reproducibility-4721

ABSTRACT

Lipschitz continuity characterizes the worst-case sensitivity of neural networks to small input perturbations; yet its dynamics (*i.e.* temporal evolution) during training remains under-explored. We present a rigorous mathematical framework to model the temporal evolution of Lipschitz continuity during training with stochastic gradient descent (SGD). This framework leverages a system of stochastic differential equations (SDEs) to capture both deterministic and stochastic forces. Our theoretical analysis identifies three principal factors driving the evolution: (i) the projection of gradient flows, induced by the optimization dynamics, onto the operator-norm Jacobian of parameter matrices; (ii) the projection of gradient noise, arising from the randomness in mini-batch sampling, onto the operator-norm Jacobian; and (iii) the projection of the gradient noise onto the operator-norm Hessian of parameter matrices. Furthermore, our theoretical framework sheds light on how noisy supervision, parameter initialization, batch size, and mini-batch sampling trajectories, among other factors, shape the evolution of the Lipschitz continuity of neural networks. Our experimental results demonstrate

strong agreement between the theoretical implications and the observed behaviors.

4.1 Introduction

RECENT advancements in deep learning have led to models that excel across a broad range of domains, from vision to language. Their vulnerability to input perturbations remains a significant challenge for establishing trustworthy learning systems (Szegedy et al., 2014; Goodfellow et al., 2015; Madry et al., 2018). Lipschitz continuity (Definition 4.1.1) measures the worst-case sensitivity of the output of a network to small input perturbations. Furthermore, several fundamental properties, including robustness to perturbation (Róisín Luo et al., 2024b) and generalization capability, are closely linked to network Lipschitz continuity (Shalev-Shwartz and Ben-David, 2014; Bartlett et al., 2017; Yin et al., 2019; Zhang et al., 2021). Networks with lower Lipschitz constants tend to be more resilient to input perturbations (*e.g.* adversarial perturbations) and exhibit improved generalization capabilities (Zhang et al., 2022; Fazlyab et al., 2023; Khromov and Singh, 2024).

Definition 4.1.1 (Globally K-Lipschitz Continuous (Yosida, 2012)). Let $f : X \mapsto Y$ be a function, where $X \subseteq \mathbb{R}^d$ and $Y \subseteq \mathbb{R}^c$. The function f is said to be *globally K-Lipschitz continuous* if there exists a constant $K > 0$ such that:

$$\|f(u) - f(v)\|_2 \leq K\|u - v\|_2, \quad \forall u, v \in X \quad (4.1)$$

upper-bounds the function f .

Gradient-based optimization methods, such as stochastic gradient descent (SGD) and its variants (Robbins and Monro, 1951; Hinton et al.; Kingma and Ba, 2017), are fundamental to training deep learning models by iteratively minimizing the loss function through parameter updates with gradients. The optimization dynamics in a neural network induce the corresponding dynamics of its Lipschitz continuity, which we refer to as **optimization-induced dynamics**. As illustrated in Figure 4.1, every optimization trajectory in the loss landscape induces a corresponding trajectory in the Lipschitz landscape. Although the dynamics (*i.e.* temporal evolution) of SGD has been extensively explored in the literature, including topics such as: (i) continuous-time/SDE modeling (Li et al., 2019b; Malladi et al., 2022; Welling and Teh, 2011; Zhu et al., 2019); (ii) edge-of-stability and implicit bias (Li et al., 2022b; Damian et al., 2023); (iii) convergence analysis (Li and Yuan, 2017); (iv) sharp versus flat minima and generalization (Keskar et al., 2017; Chaudhari et al.,

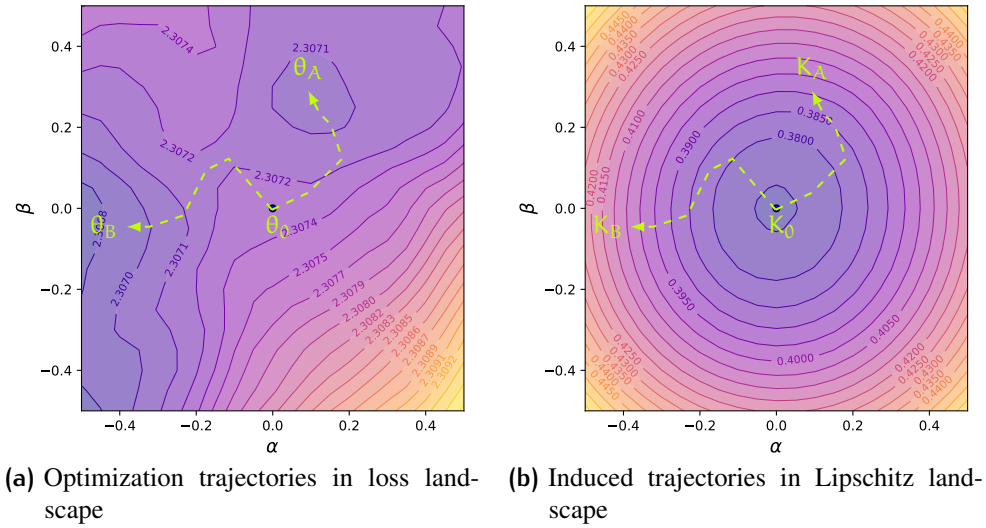


Figure 4.1: Optimization-induced dynamics. During the training, the network parameters, starting from Θ_0 , moves towards a solution Θ_A or Θ_B as shown in the loss landscape (a), driven by optimization process. Accordingly, this dynamics, driven by the optimization, induces the evolution of the network Lipschitz continuity, starting from K_0 to K_A or K_B , as shown in the Lipschitz landscape (b). The trajectories in the loss landscape (a) and the Lipschitz landscape (b) are visualized on the same parameter space α O β . The α and β are two randomly-chosen orthogonal directions in the parameter space.

2019; Zhang et al., 2021), a comprehensive understanding of how the Lipschitz constant evolves over time during training remains lacking.

This gap motivates us to establish a rigorous theoretical framework for modeling the dynamics of Lipschitz continuity, induced by optimization dynamics. Equipped with the toolkit from stochastic differential equations (SDEs) (Applebaum, 2009; Karatzas and Shreve, 2012; Oksendal, 2013) and operator perturbation theory (Kato, 1995; Róisín Luo et al., 2025c), we can rigorously analyze the evolution of the matrix operator norm (*i.e.* matrix Lipschitz constant), induced by the optimization process, within an SDE framework. Our framework can capture both the deterministic and stochastic forces driving the temporal evolution of Lipschitz constants. The effectiveness of our mathematical framework is empirically verified in Figure 4.2, where the theoretical implications derived using our framework (Theorem 4.6.7 and Theorem 4.6.8) are closely aligned with the observations. Furthermore, our theoretical framework sheds light on questions such as how batch size, parameter initialization, mini-batch sampling trajectories, label noise, etc., shape the Lipschitz continuity evolution during optimization.

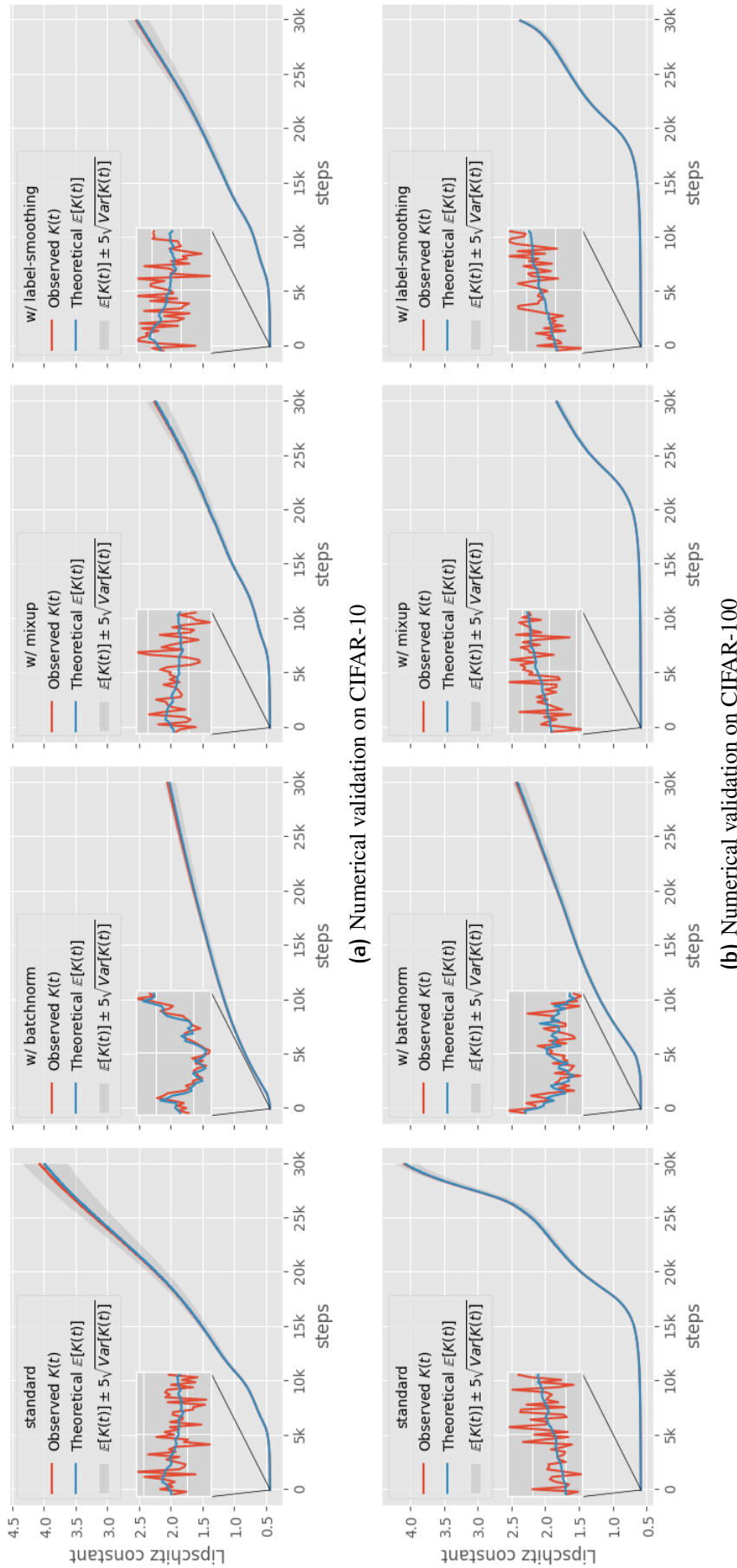


Figure 4.2: Numerical validation of our mathematical framework. The theoretical Lipschitz constants computed using our framework closely agree with empirical observations. To validate our framework, we train a five-layer ConvNet on CIFAR-10 and CIFAR-100 across multiple configurations for 30,000 steps (200 epochs). We collect the instance-wise gradients over time for all layers. Using Theorem 4.6.5, Theorem 4.6.6, Theorem 4.6.7 and Theorem 4.6.8, we are able to theoretically compute the predicted Lipschitz continuity. The inset plots zoom in on the first 50 steps, and demonstrate that the **trends of Lipschitz constants do not necessarily grow monotonically**. Results with more regularization configurations on CIFAR-10 are provided in Appendix 4.D.

4.1.1 Contributions

We highlight the key contributions below:

1. **Theoretical Framework** (Section 4.2-4.6). We present a rigorous mathematical framework that models the dynamics of Lipschitz continuity, leveraging an SDE system driven by Wiener processes. This SDE-based framework captures both deterministic and stochastic forces, providing a comprehensive understanding of the dynamics of Lipschitz continuity. To ensure practical applicability, we also develop a low-rank approximation method for modeling gradient noise in Section 4.4, enabling efficient computation of these dynamics.
2. **Principal Driving Forces** (Section 4.6.2-4.6.4). Our theoretical analysis (Theorem 4.6.7) identifies three principal forces governing the dynamics: (i) the projection of gradient flows, induced by the optimization dynamics, onto the operator-norm Jacobian of parameter matrices; (ii) the projection of gradient noise, arising from the randomness in mini-batch sampling, onto the operator-norm Jacobian; and (iii) the projection of the gradient noise onto the operator-norm Hessian of parameter matrices. In the evolution of Lipschitz continuity, forces (i) and (iii) act as deterministic forces, while force (ii) modulates the stochasticity of the dynamics.
3. **Framework Validation and Theoretical Implications** (Section 4.7-4.8). Firstly, we validate our theoretical framework under multiple configurations, including *batch normalization*, *dropout*, *weight decay*, *mixup*, *auto-augment*, *label smoothing* and *adversarial training*. Furthermore, we test the theoretical implications derived from our framework, as detailed in Section 4.8, including parameter initialization, noisy gradient regularization, uniform label corruption, batch size, and mini-batch sampling trajectories shape the evolution of Lipschitz continuity. The results show a strong agreement between the theoretical implications and observed behaviors.

4.2 Preliminaries

We define the notation used in our theoretical analysis. Let $f : \mathbb{R}^d \rightarrow \mathbb{R}^c$ be a function. For a time-dependent function g , we use g_k to denote its value at discrete time step k , and $g(t)$ for its value at continuous time t . For a random variable ξ , e.g., representing data sampling, gradient noise, Wiener process, and filtration (Oksendal, 2013), we consistently use subscripts, such as ξ_k or ξ_t , for brevity. A function written as $g^{(\ell)}$ indicates that g is

the ℓ -th layer of a neural network. We use I_n to denote an $n \times n$ identity matrix; $\mathbb{1}_n$ to denote an n -dimensional all-ones vector.

Mini-Batch Sampling. Let $\mathcal{D} := \{(x_i, y_i)\}_{i=1}^N \subseteq \mathcal{X} \times \mathcal{Y}$ denote a dataset consisting of N samples, where (x_i, y_i) represents the i -th data point and its corresponding target. Let $\xi_t := \{(x_{t_j}, y_{t_j})\}_{j=1}^M \subseteq \mathcal{X} \times \mathcal{Y}$ denote a mini-batch sampled from \mathcal{D} at time point t , where $M (M \ll N)$ is the size of the mini-batch. The sequence $\{\xi_i\}_{i=0}^t$ up to time t is referred to as a *sampling trajectory* from \mathcal{D} . The σ -algebra $\mathcal{F}_t = \sigma\{\xi_0, \xi_1, \dots, \xi_t\}$, defined on mini-batch sampling, is referred to as the *filtration* generated by the sampling trajectory $\{\xi_i\}_{i=0}^t$ (Oksendal, 2013). In stochastic analysis, \mathcal{F}_t represents that the information accumulates up to time t (*i.e.* history). Any history up to a time point t_k contains the history up to a time point t_l for all $t_k \geq t_l$, *i.e.* $\mathcal{F}_{t_l} \subseteq \mathcal{F}_{t_k}$.

Feed-Forward Network. Let $\theta^{(\ell)} \in \mathbb{R}^{m_\ell \times n_\ell}$ denote the parameter matrix of the ℓ -th layer of an L -layer feed-forward network. Let $\theta := \{\theta^{(1)}, \theta^{(2)}, \dots, \theta^{(L)}\} \in \Theta$ denote the collection of all L parameter matrices. Let $f_\theta : \mathbb{R}^d \mapsto \mathbb{R}^c$ represent a feed-forward network parameterized by θ . Let $\text{vec}(\theta^{(\ell)}) \in \mathbb{R}^{m_\ell n_\ell}$ denote the vectorized $\theta^{(\ell)}$ with *column-major convention* (Horn and Johnson, 2012).

Remark 4.2.1. The explicit use of the $\text{vec}(\cdot)$ operator is essential for rigorous spectral analysis of parameter matrices beyond the usual context of parameter updates in SGD optimization.

Instance and Population Loss. Let $\ell_f(\theta; x, y) : \Theta \times \mathcal{X} \times \mathcal{Y} \mapsto \mathbb{R}$ denote the instance loss for f_θ . Let $\mathcal{L}_f(\theta; \xi)$ denote the population loss over a mini-batch ξ :

$$\mathcal{L}_f(\theta; \xi) := \frac{1}{M} \sum_{x_i, y_i \in \xi} \ell_f(\theta; x_i, y_i).$$

Let $\mathcal{L}_f(\theta)$ denote the population loss over the dataset \mathcal{D} :

$$\mathcal{L}_f(\theta) := \mathbb{E}_{(x_i, y_i) \sim \mathcal{D}} [\ell_f(\theta; x_i, y_i)].$$

Unbiased Gradient Estimator. For brevity, we use:

$$\nabla^{(\ell)} \mathcal{L}_f(\theta) := \nabla_{\theta^{(\ell)}} \mathcal{L}_f(\theta), \quad \text{and} \quad \nabla \mathcal{L}_f(\theta) := \nabla_{\theta} \mathcal{L}_f(\theta),$$

to denote the gradient with respect to the ℓ -th layer parameter matrix, and the gradient with respect to the collective parameter matrices, respectively. Note that $\nabla \mathcal{L}_f(\theta; \xi)$ is an unbiased gradient estimator for $\nabla \mathcal{L}_f(\theta)$:

$$\mathbb{E} [\nabla \mathcal{L}_t(\theta; \xi)] = \mathbb{E} [\nabla \mathcal{L}_f(\theta)] = \mathbb{E} [\nabla \ell_f(\theta; x, y)].$$

4.3 Vectorized SDE for Continuous-Time SGD

SGD and its variants (*e.g.* Adam) (Robbins and Monro, 1951; Hinton et al.; Kingma and Ba, 2017) serve as cornerstone optimization algorithms widely used for training deep neural networks. Formally, at a time point k , the SGD-based update regarding the parameter $\theta_k^{(\ell)}$ with a mini-batch ξ_k can be formulated by:

$$\theta_{k+1}^{(\ell)} = \theta_k^{(\ell)} - \eta \nabla^{(\ell)} \mathcal{L}_f(\theta_k; \xi_k), \quad (4.2)$$

where η is the learning rate. Some studies (Mandt et al., 2015; Su et al., 2016; Mandt et al., 2017) view SGD as a deterministic process with a deterministic ordinary differential equation (ODE) as:

$$\frac{d\theta^{(\ell)}(t)}{dt} = -\nabla^{(\ell)} \mathcal{L}_f(\theta(t)),$$

where $t \approx k\eta$ and $dt \approx \eta \rightarrow 0$.

However, the inherent stochasticity in the population gradients $\nabla^{(\ell)} \mathcal{L}_f(\theta_k; \xi_k)$, arising from the randomness in mini-batch sampling ξ_k , is not accounted for by ODE methods. The *layer-wise batch gradient noise* (*i.e.* batch gradient fluctuations) (Welling and Teh, 2011; Keskar et al., 2017; Chaudhari et al., 2019; Zhang et al., 2021), defined as a positive semi-definite (PSD) matrix:

$$\Sigma_k^{(\ell)} := \text{Var} \left[\text{vec} \left(\nabla^{(\ell)} \mathcal{L}_f(\theta_k; \xi_k) \right) \right] = \frac{1}{M} \text{Var} \left[\text{vec} \left(\nabla^{(\ell)} \ell_f(\theta_k; x, y) \right) \right] \in \mathbb{R}^{m_\ell n_\ell \times m_\ell n_\ell}, \quad (4.3)$$

induced by mini-batch sampling, can influence the optimization trajectory. **It remains under-explored in the literature how such stochasticity affects the evolution of Lipschitz continuity of neural networks over time.**

Assumption 4.3.1 (Collective Gradient Noise Structure Assumption). For tractability, we assume that gradient-noise covariances between different layers are negligible. Equivalently, Σ_t has block-diagonal structure:

$$\Sigma_t = \text{diag}(\Sigma_t^{(1)}, \Sigma_t^{(2)}, \dots, \Sigma_t^{(L)}),$$

so that we model batch gradient noise on a per-layer basis only. This layer-wise approximation is common in large-scale SDE analyses, *e.g.* (Grosse and Martens, 2016; Malladi et al., 2022; Simsekli et al., 2019).

To address the limitations of ODE methods, SDE methods (Li and Yuan, 2017; Zhu et al., 2019; Chaudhari et al., 2019) extend ODE methods by accounting for gradient noise. SDE-based methods capture the stochasticity inherent in mini-batch updates and its effects on the optimization trajectory. The multivariate Central Limit Theorem (CLT) states that the population gradient estimator:

$$\nabla^{(\ell)} \mathcal{L}_f(\theta_k; \xi_k) = \frac{1}{M} \sum_{(x_i, y_i) \in \xi_k} \nabla^{(\ell)} \ell_f(\theta_k; x_i, y_i),$$

distributionally converges to a normal distribution in $\mathbb{R}^{m_\ell n_\ell}$:

$$\text{vec} \left(\nabla^{(\ell)} \mathcal{L}_f(\theta_k; \xi_k) \right) \xrightarrow{d} \mathcal{N} \left(\text{vec}(\nabla^{(\ell)} \mathcal{L}_f(\theta_k)), \Sigma_k^{(\ell)} \right),$$

as $M \rightarrow \infty$, where the samples (x_i, y_i) are *i.i.d.* Therefore, SGD can be modeled as an Itô process, which provides a more accurate representation of the dynamics by considering the continuous-time SDEs (Mandt et al., 2015, 2017).

Definition 4.3.2 (Vectorized SDE for Continuous-Time SGD). Under Assumption 4.3.1, and the assumption that $\nabla^{(\ell)} \mathcal{L}_f(\theta_t)$ and $\Sigma_t^{(\ell)}$ satisfy global Lipschitz and linear-growth conditions (Oksendal, 2013; Karatzas and Shreve, 2012), the SGD update for the parameter $\theta_t^{(\ell)}$ with a mini-batch ξ_t at time t can be formulated as a matrix-valued Itô's SDE by:

$$d\text{vec} \left(\theta^{(\ell)}(t) \right) = -\text{vec} \left[\nabla^{(\ell)} \mathcal{L}_f(\theta(t)) \right] dt + \sqrt{\eta} \left[\Sigma_t^{(\ell)} \right]^{\frac{1}{2}} dB_t^{(\ell)}, \quad (4.4)$$

where the batch gradient noise $\left[\Sigma_t^{(\ell)} \right]^{\frac{1}{2}} \in \mathbb{R}^{m_\ell n_\ell \times m_\ell n_\ell}$ satisfies:

$$\left(\Sigma_t^{(\ell)} \right)^{\frac{1}{2}} \left[\left(\Sigma_t^{(\ell)} \right)^{\frac{1}{2}} \right]^\top = \Sigma_t^{(\ell)}, \quad \text{and} \quad \mathbb{R}^{m_\ell n_\ell} \ni dB_t^{(\ell)} \sim \mathcal{N}(\mathbf{0}, \mathbf{I}_{m_\ell n_\ell} dt)$$

represents the infinitesimal increment of a Wiener process (standard Brownian motion) adapted to the filtration \mathcal{F}_t in $\mathbb{R}^{m_\ell n_\ell}$.

4.4 Estimating batch gradient noise

The covariance of gradient noise structure reflects how neurons interact with each other. Capturing the full structure of gradient noise for numerically analyzing the spectra of network parameters (Stewart and Sun, 1990; Horn and Johnson, 2012; Kato, 1995) is shaped by the stochasticity arising from mini batch sampling. However, modeling the full gradient noise covariance is computationally prohibitive: accurately estimating batch gradient noise requires sampling all gradient trajectories over the entire dataset, which leads to intractable storage and computational costs (Mandt et al., 2015; Li et al., 2019b).

SDE-based models often have strong assumptions regarding the structure of gradient noise. For example, in the literature (Welling and Teh, 2011; Mandt et al., 2017), the gradient noise is reduced into a constant scalar. Under this assumption, the SDE reduces to an Ornstein-Uhlenbeck process (Oksendal, 2013; Karatzas and Shreve, 2012). However, this simplification overlooks the covariance structures inherent in mini-batch sampling. To address this, some literature assume a diagonal structure for the gradient noise (Jastrz̄bski et al., 2019; Simsekli et al., 2020). While this approximation captures varying variances across parameters, it neglects potential correlations between them.

In practice, Mandt et al. compute the exact 2×2 covariance matrix for a low-dimensional logistic-regression problem; Zhu et al. estimate the full noise covariance — solely to extract its leading eigenpairs — in an MLP with several hundred parameters (Zhu et al., 2019). Nonetheless, these methods do not scale to modern deep networks, where the number of parameters can be on the order of millions. In the remaining part of this section, we aim to develop experiment-friendly method for tracking full structure of gradient noise.

4.4.1 Unbiased batch gradient noise estimator

To capture the complex interactions among neurons, we model the complete structure of the gradient noise. However, by Equation 4.3, the exact $\Sigma_t^{(\ell)}$ is given by at time point t:

$$\Sigma_t^{(\ell)} := \text{Var} \left[\text{vec} \left(\nabla^{(\ell)} \mathcal{L}_f(\theta_t; \xi_t) \right) \right] \quad (4.5)$$

$$= \frac{1}{M} \text{Var} \left[\text{vec} \left(\nabla^{(\ell)} \ell_f(\theta_k; x, y) \right) \right] \quad (4.6)$$

$$= \frac{1}{M} \mathbb{E} \left[\left\{ \text{vec} \left(\nabla^{(\ell)} \ell_f(\theta_k; x, y) \right) - \mathbb{E} \left[\text{vec} \left(\nabla^{(\ell)} \ell_f(\theta_k; x, y) \right) \right] \right\} \right. \\ \left. \left\{ \text{vec} \left(\nabla^{(\ell)} \ell_f(\theta_k; x, y) \right) - \mathbb{E} \left[\text{vec} \left(\nabla^{(\ell)} \ell_f(\theta_k; x, y) \right) \right] \right\}^\top \right], \quad (4.7)$$

which suggests that the $\Sigma_t^{(\ell)}$ requires the evaluation of

$$\text{vec} \left(\nabla^{(\ell)} \ell_f(\theta_k; x, y) \right) \quad \text{and} \quad \mathbb{E} \left[\text{vec} \left(\nabla^{(\ell)} \ell_f(\theta_k; x, y) \right) \right] \quad (4.8)$$

over the entire dataset for each time point t. Therefore, the computational cost of $\Sigma_t^{(\ell)}$ poses a challenge to the applicability of our framework. This computation remains highly demanding, even when using state-of-the-art GPUs. To overcome this, we develop a low-rank approximation method. We now seek to estimate $\Sigma_t^{(\ell)}$ without bias.

Proposition 4.4.1 (Unbiased Batch Gradient Noise Estimator). *Starting from Equation 4.3, the batch gradient noise at time t is approximately estimated from a batch ξ_t by:*

$$\Sigma_t^{(\ell)} \approx \frac{1}{M} \left[\frac{1}{M-1} \sum_{x_{t_i}, y_{t_i} \in \xi_t} \underbrace{\left\{ \text{vec} \left[\nabla^{(\ell)} \ell_f(\theta(t); x_{t_i}, y_{t_i}) - \nabla^{(\ell)} \mathcal{L}_f(\theta(t); \xi_t) \right] \right\}}_{(\Omega_{t_i}^{(\ell)})^\top} \right. \\ \left. \underbrace{\left\{ \text{vec} \left[\nabla^{(\ell)} \ell_f(\theta(t); x_{t_i}, y_{t_i}) - \nabla^{(\ell)} \mathcal{L}_f(\theta(t); \xi_t) \right] \right\}^\top}_{\Omega_{t_i}^{(\ell)}} \right] \\ = \frac{1}{M} \left(\frac{1}{\sqrt{M-1}} \begin{bmatrix} \Omega_{t_1}^{(\ell)} \\ \Omega_{t_2}^{(\ell)} \\ \vdots \\ \Omega_{t_M}^{(\ell)} \end{bmatrix} \right)^\top \left(\frac{1}{\sqrt{M-1}} \begin{bmatrix} \Omega_{t_1}^{(\ell)} \\ \Omega_{t_2}^{(\ell)} \\ \vdots \\ \Omega_{t_M}^{(\ell)} \end{bmatrix} \right) = \frac{1}{M} (\Omega_t^{(\ell)})^\top \Omega_t^{(\ell)}, \quad (4.9)$$

where $\Omega_{t_i}^{(\ell)}$ is the point-wise gradient fluctuation:

$$(\Omega_{t_i}^{(\ell)})^\top = \text{vec} \left[\nabla^{(\ell)} \ell_f(\theta(t); x_{t_i}, y_{t_i}) - \nabla^{(\ell)} \mathcal{L}_f(\theta(t); \xi_t) \right] \in \mathbb{R}^{m_\ell n_\ell},$$

and $\Omega_t^{(\ell)}$ is batch-wise gradient fluctuation:

$$\Omega_t^{(\ell)} = \frac{1}{\sqrt{M-1}} \begin{bmatrix} \Omega_{t_1}^{(\ell)} \\ \Omega_{t_2}^{(\ell)} \\ \vdots \\ \Omega_{t_M}^{(\ell)} \end{bmatrix} = \sqrt{\frac{1}{M-1}} \begin{pmatrix} \text{vec} \left[\nabla^{(\ell)} \ell_f(\theta(t); x_{t_1}, y_{t_1}) - \nabla^{(\ell)} \mathcal{L}_f(\theta(t); \xi_t) \right]^\top \\ \text{vec} \left[\nabla^{(\ell)} \ell_f(\theta(t); x_{t_2}, y_{t_2}) - \nabla^{(\ell)} \mathcal{L}_f(\theta(t); \xi_t) \right]^\top \\ \vdots \\ \text{vec} \left[\nabla^{(\ell)} \ell_f(\theta(t); x_{t_M}, y_{t_M}) - \nabla^{(\ell)} \mathcal{L}_f(\theta(t); \xi_t) \right]^\top \end{pmatrix}.$$

4.4.2 Estimating variance and covariance

To study the contributions of variances (diagonal elements) and covariances (off-diagonal elements) of gradient noise to the dynamics, we decompose the gradient noise into variance and covariance components using Proposition 4.4.2.

Proposition 4.4.2 (Diagonal and Off-Diagonal Elements of Batch Gradient Noise). *The diagonal variance $\Sigma_t^{(\ell)}|_{\text{var}}$ and the off-diagonal covariance $\Sigma_t^{(\ell)}|_{\text{cov}}$ are computed, respectively, by:*

$$\Sigma_t^{(\ell)}|_{\text{var}} \approx \frac{1}{M} (\Omega_t^{(\ell)} \odot \Omega_t^{(\ell)})^\top \mathbb{1}_M, \quad \text{and} \quad \Sigma_t^{(\ell)}|_{\text{cov}} \approx \Sigma_t^{(\ell)} - \Sigma_t^{(\ell)}|_{\text{var}},$$

where \odot denotes Hadamard product. Note that $\Sigma_t^{(\ell)}|_{\text{cov}}$ is not necessarily a PSD matrix.

Proof. Starting from Equation 4.9, this can be obtained by:

$$\begin{aligned} (\Sigma_t^{(\ell)}|_{\text{var}})_{i,i} &= (\Sigma_t^{(\ell)})_{i,i} \approx \frac{1}{M} ((\Omega_t^{(\ell)})^\top \Omega_t^{(\ell)})_{i,i} = \frac{1}{M} \sum_{j=1}^M ((\Omega_t^{(\ell)})^\top)_{i,j} \Omega_{j,i}^{(\ell)} \\ &= \frac{1}{M} \sum_{j=1}^M \Omega_{j,i}^{(\ell)} \Omega_{j,i}^{(\ell)} = \frac{1}{M} \sum_{j=1}^M (\Omega_t^{(\ell)} \odot \Omega_t^{(\ell)})_{j,i} = \frac{1}{M} \left((\Omega_t^{(\ell)} \odot \Omega_t^{(\ell)})^\top \mathbb{1}_M \right)_i. \end{aligned}$$

□

4.4.3 Computing square root

Direct computation of $(\Sigma_t^{(\ell)})^{1/2}$ by

$$(\Sigma_t^{(\ell)})^{1/2} \approx \left[\frac{1}{M} (\Omega_t^{(\ell)})^\top \Omega_t^{(\ell)} \right]^{1/2} \in \mathbb{R}^{m_\ell n_\ell \times m_\ell n_\ell}$$

is computationally infeasible for large parameter matrices. Note that

$$\frac{1}{M} \Omega_t^{(\ell)} (\Omega_t^{(\ell)})^\top \in \mathbb{R}^{M \times M}, \quad M \ll m_\ell n_\ell,$$

has low-rank structure and the same spectrum of $\Sigma_t^{(\ell)}$. We seek an efficient method by exploiting the low-rank SVD in $\frac{1}{M} \Omega_t^{(\ell)} (\Omega_t^{(\ell)})^\top$.

Proposition 4.4.3 (Square Root Approximation of Covariance Matrix). *Suppose $\Omega_t^{(\ell)}/\sqrt{M}$ admits SVD:*

$$\frac{\Omega_t^{(\ell)}}{\sqrt{M}} = \mathbf{U}_t^{(\ell)} (\Lambda_t^{(\ell)})^{1/2} (\mathbf{V}_t^{(\ell)})^\top,$$

where $\Lambda_t^{(\ell)}$ and $\mathbf{U}_t^{(\ell)}$ are the eigenvalues and eigenvectors of $\frac{1}{M} \Omega_t^{(\ell)} (\Omega_t^{(\ell)})^\top$. Then:

$$(\Sigma_t^{(\ell)})^{1/2} \approx \left[\frac{(\Omega_t^{(\ell)})^\top \mathbf{U}_t^{(\ell)}}{\sqrt{M}} \right] (\Lambda_t^{(\ell)})^{-1/2} \left[\frac{(\Omega_t^{(\ell)})^\top \mathbf{U}_t^{(\ell)}}{\sqrt{M}} \right]^\top.$$

Proof. Starting from Equation 4.9, this can be obtained by:

$$\begin{aligned} (\Sigma_t^{(\ell)})^{1/2} &\approx \left[\frac{1}{M} (\Omega_t^{(\ell)})^\top \Omega_t^{(\ell)} \right]^{1/2} = \left[\frac{(\Omega_t^{(\ell)})^\top \mathbf{U}_t^{(\ell)} (\mathbf{U}_t^{(\ell)})^\top \Omega_t^{(\ell)}}{\sqrt{M}} \right]^{1/2} \\ &= \left[\frac{(\Omega_t^{(\ell)})^\top \mathbf{U}_t^{(\ell)}}{\sqrt{M}} (\Lambda_t^{(\ell)})^{-1/2} (\Lambda_t^{(\ell)}) (\Lambda_t^{(\ell)})^{-1/2} \frac{(\mathbf{U}_t^{(\ell)})^\top \Omega_t^{(\ell)}}{\sqrt{M}} \right]^{1/2} \end{aligned} \quad (4.10)$$

Set:

$$\mathbf{P} = \frac{(\Omega_t^{(\ell)})^\top \mathbf{U}_t^{(\ell)}}{\sqrt{M}} (\Lambda_t^{(\ell)})^{-1/2},$$

and note:

$$\mathbf{P} = \frac{(\Omega_t^{(\ell)})^\top \mathbf{U}_t^{(\ell)}}{\sqrt{M}} (\Lambda_t^{(\ell)})^{-1/2} = \left[\mathbf{U}_t^{(\ell)} (\Lambda_t^{(\ell)})^{1/2} (\mathbf{V}_t^{(\ell)})^\top \right]^\top \mathbf{U}_t^{(\ell)} (\Lambda_t^{(\ell)})^{-1/2} = \mathbf{V}_t^{(\ell)}$$

is orthonormal.

Hence:

$$\begin{aligned}
 (\Sigma_t^{(\ell)})^{\frac{1}{2}} &\approx \left[\frac{(\Omega_t^{(\ell)})^\top \mathbf{U}_t^{(\ell)}}{\sqrt{M}} (\Lambda_t^{(\ell)})^{-\frac{1}{2}} (\Lambda_t^{(\ell)}) (\Lambda_t^{(\ell)})^{-\frac{1}{2}} \frac{(\mathbf{U}_t^{(\ell)})^\top \Omega_t^{(\ell)}}{\sqrt{M}} \right]^{\frac{1}{2}} \\
 &= \left[\frac{(\Omega_t^{(\ell)})^\top \mathbf{U}_t^{(\ell)}}{\sqrt{M}} (\Lambda_t^{(\ell)})^{-\frac{1}{2}} \right] (\Lambda_t^{(\ell)})^{\frac{1}{2}} \left[(\Lambda_t^{(\ell)})^{-\frac{1}{2}} \frac{(\mathbf{U}_t^{(\ell)})^\top \Omega_t^{(\ell)}}{\sqrt{M}} \right]^{\frac{1}{2}} \\
 &= \underbrace{\left[\frac{(\Omega_t^{(\ell)})^\top \mathbf{U}_t^{(\ell)}}{\sqrt{M}} (\Lambda_t^{(\ell)})^{-\frac{1}{2}} \right]}_{\mathbf{P}} (\Lambda_t^{(\ell)})^{\frac{1}{2}} \underbrace{\left[\frac{(\Omega_t^{(\ell)})^\top \mathbf{U}_t^{(\ell)}}{\sqrt{M}} (\Lambda_t^{(\ell)})^{-\frac{1}{2}} \right]}_{\mathbf{P}^\top}^\top \\
 &= \left[\frac{(\Omega_t^{(\ell)})^\top \mathbf{U}_t^{(\ell)}}{\sqrt{M}} \right] (\Lambda_t^{(\ell)})^{-\frac{1}{2}} \left[\frac{(\Omega_t^{(\ell)})^\top \mathbf{U}_t^{(\ell)}}{\sqrt{M}} \right]^\top.
 \end{aligned}$$

□

4.5 Temporal evolution of Lipschitz upper bound

Suppose that an L -layer feed-forward neural network f is the composition of L layers, each comprising a linear unit with an activation unit, expressed as:

$$f := (\rho^{(L)} \circ \phi^{(L)}) \circ \dots \circ (\rho^{(2)} \circ \phi^{(2)}) \circ (\rho^{(1)} \circ \phi^{(1)})$$

where $(\rho^{(\ell)} \circ \phi^{(\ell)})$ represents the ℓ -th layer consisting of the linear unit $\psi^{(\ell)}(\cdot)$ and the activation unit $\rho^{(\ell)}(\cdot)$. Let the Lipschitz constants of $\rho^{(\ell)}$ and $\phi^{(\ell)}$ be $A^{(\ell)}$ and $K^{(\ell)}$, respectively. The upper bound of the network Lipschitz constant of f then is the product of $A^{(\ell)}$ and $K^{(\ell)}$ across all layers, as shown in Proposition 4.5.1 (Miyato et al., 2018; Fazlyab et al., 2019; Virmaux and Scaman, 2018; Gouk et al., 2021; Virmaux and Scaman, 2018).

Proposition 4.5.1 (Lipschitz Continuity Bound in Feed-Forward Network). *Let $\hat{K}(t)$ be the Lipschitz constant of a feed-forward neural network f without skip connections. The network Lipschitz constant $\hat{K}(t)$ is upper-bounded by:*

$$\hat{K}(t) := \sup_{\forall u \neq v} \frac{\|f(u) - f(v)\|_2}{\|u - v\|_2} \leq K(t) := \prod_{l=1}^L A^{(l)} \cdot \prod_{l=1}^L K^{(l)}(t).$$

This upper bound is useful in robust certification and theoretical analysis of deep models with complex topologies (Fazlyab et al., 2019; Gouk et al., 2021; Virmaux and Scaman, 2018). We refer to $K(t)$ as Lipschitz continuity or Lipschitz constant for brevity.

Since most activation functions, such as ReLU, Leaky ReLU, Tanh, Sigmoid, etc, have 1-Lipschitz continuity (Virmaux and Scaman, 2018), we set $A^{(\ell)} = 1$ for brevity in theoretical analysis. Note that Proposition 4.5.1 does not take into account skip connections.

Proposition 4.5.2 (Operator Norm of Linear Unit). *Suppose the $\phi^{(\ell)}(t)$ is a linear unit with matrix multiplication or convolution:*

$$\phi^{(\ell)}(t)(z) := \theta^{(\ell)}(t)(z) + b^{(\ell)}(t), \quad (4.11)$$

where $\theta^{(\ell)}(t)$ and $b^{(\ell)}(t)$ are the ℓ -th layer parameter matrix and bias, respectively. Then, the operator norm of $\phi^{(\ell)}(t)$ (i.e. spectral norm) admits:

$$\|\phi^{(\ell)}(t)\|_{\text{op}} = \|\theta^{(\ell)}(t)\|_{\text{op}} = \sigma_1^{(\ell)}(t),$$

where $\sigma_1^{(\ell)}(t)$ is the largest singular value of $\theta^{(\ell)}(t)$ (Miyato et al., 2018; Sedghi et al., 2019).

Definition 4.5.3 (Stochastic Dynamical System of Lipschitz Continuity Bound). Collect:

1. Definition 4.3.2: Vectorized SDE for Continuous-Time SGD;
2. Proposition 4.5.1: Lipschitz Continuity Bound in Feed-Forward Network;
3. Proposition 4.5.2: Operator Norm of Linear Unit,

so that the dynamics of Lipschitz continuity bound for a feed-forward neural network is characterized by a system of SDEs:

$$\begin{cases} d\text{vec}(\theta^{(\ell)}(t)) = -\text{vec}\left[\nabla^{(\ell)} \mathcal{L}_f(\theta(t))\right] dt + \sqrt{\eta} \left[\Sigma_t^{(\ell)}\right]^{\frac{1}{2}} dB_t^{(\ell)} \\ K^{(\ell)}(t) = \|\theta^{(\ell)}(t)\|_{\text{op}} \\ Z(t) = \sum_{l=1}^L \log K^{(l)}(t) \\ K(t) = e^{Z(t)} \end{cases}$$

adapted to the filtration \mathcal{F}_t , where: (i) $K^{(\ell)}(t)$ governs the ℓ -th layer dynamics of Lipschitz continuity; (ii) $K(t)$ governs the network dynamics of Lipschitz continuity bound; and

(iii) $Z(t)$ is the logarithmic Lipschitz constant to facilitate theoretical deductions. **This stochastic dynamical system characterizes the dynamics of the Lipschitz continuity bound induced by the optimization dynamics.**

4.6 Theoretical analysis

Note that the equation system in Definition 4.5.3 is driven by a Wiener process, which consists of stochastic differential equations (SDEs), and is adapted to the filtration \mathcal{F}_t , with time-dependent parameters $\theta^{(l)}(t)$. We leverage Itô's Lemma (Itô, 1951; Oksendal, 2013) to analyze this SDE system. We aim to analyze the dynamics of $Z(t)$ and $K(t)$. The sketch for theoretical analysis is:

1. **Layer-Specific Dynamics** (Section 4.6.2). We derive the SDE for $dK_t^{(l)}$ by applying Itô's Lemma to the process $d\text{vec}[\theta^{(l)}(t)]$. This step establishes a direct connection between parameter-level updates driven by the optimization process and the layer-wise operator norm.
2. **Network-Specific Dynamics** (Section 4.6.3). Building on the layer-specific analysis, we derive the network-level SDE for $dZ(t)$ by applying Itô's Lemma to the processes $dK^{(l)}(t)$ across L layers. The process $Z(t)$ captures the logarithmic, network-level dynamics of Lipschitz continuity. Finally, we obtain the dynamics of $K(t)$ from $dZ(t)$ via Itô calculus.
3. **Statistical Characterization** (Section 4.6.4). We analyze the statistical properties of $Z(t)$ and $K(t)$, including their expectations and variances. These results provide insight into the asymptotic behavior of the system near convergence.

4.6.1 First- and second-order operator-norm derivatives

Stochastic spectral analysis regarding the parameter matrices requires the first-order and second-order derivatives of the largest singular values with respect to parameter matrices. The first-order operator-norm derivative is well-known in the literature (Róisín Luo et al., 2025c; Kato, 1995; Horn and Johnson, 2012; Magnus and Neudecker, 2019) (Lemma 4.6.2). The second-order operator-norm derivative can be derived through perturbation theory (Kato, 1995; Róisín Luo et al., 2025c). Lemma 4.6.3 is proved in the

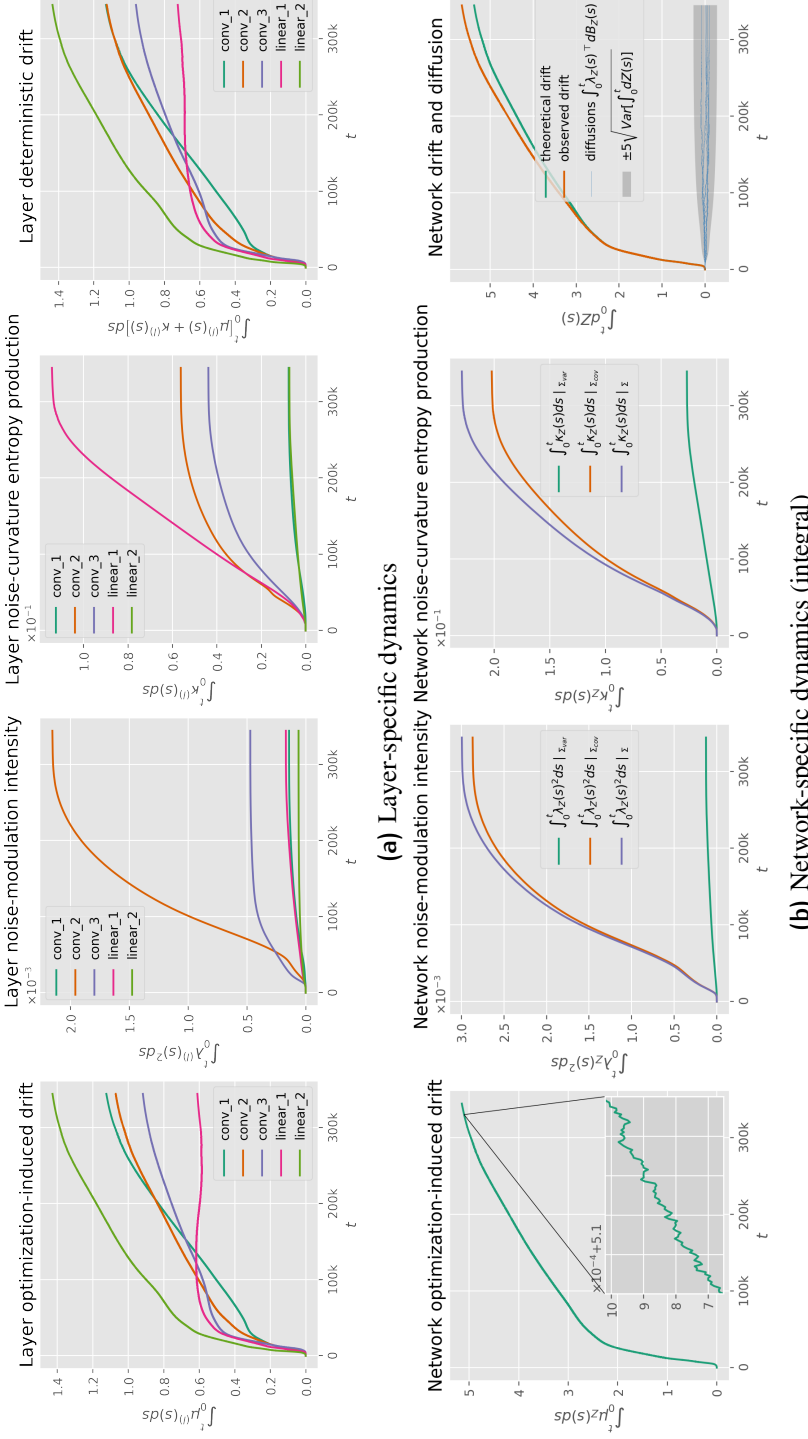


Figure 4.3: Dynamics near convergence. We profile both layer-specific and network-specific dynamics over 344,370 steps (1766 epochs) on CIFAR-10. At the end of training, the final training loss and test loss are 9.75×10^{-3} and 2.22, respectively; the final training accuracy and test accuracy are 0.99996 and 0.68540, respectively. To investigate how the variances (i.e. diagonal elements) and covariances (i.e. off-diagonal elements) of the gradient noise affect the dynamics, the dynamics are computed with respect to variances (Σ_{var}) and covariances (Σ_{cov}) respectively, using Theorem 4.6.6. The results indicate that: (i) the optimization-trajectory drift plays the primary role in shaping Lipschitz continuity over time; (ii) the covariances dominate the noise contributions; and (iii) the noise-curvature entropy production $\kappa_Z(t)$ remains significant near convergence, leading to a gradual and steady increase in Lipschitz continuity. The inset plot zooms in on 100 steps at $t = 330,000$. The moving averages are computed over a window of 500 steps.

literature ([Róisín Luo et al., 2025c](#)) based on perturbation theory for linear operators ([Kato, 1995](#)). Let $\Theta^{(\ell)}(t)$ admit a SVD:

$$\Theta_t^{(\ell)} = \sum_{i=1}^r \sigma_i^{(\ell)}(t) \mathbf{u}_i^{(\ell)}(t) \mathbf{v}_i^{(\ell)}(t)^\top, \quad \sigma_1^{(\ell)}(t) > \sigma_2^{(\ell)}(t) > \dots > \sigma_r^{(\ell)}(t), \quad r = \text{rank}(\Theta^{(\ell)}(t)),$$

under the Assumption 4.6.1.

Assumption 4.6.1 (Spectral Differentiability). We assume the singular values of parameter matrices are *simple*: $\sigma_i^{(\ell)} \neq \sigma_j^{(\ell)}$, for all $i \neq j$. This assumption guarantees $\sigma_i^{(\ell)}, \mathbf{u}_i^{(\ell)}, \mathbf{v}_i^{(\ell)} \in C^\infty$ (i.e. differentiable at arbitrary integer order) ([Kato, 1995](#)).

Lemma 4.6.2 (Operator-Norm Jacobian). *The operator-norm Jacobian of $\|\Theta^{(\ell)}(t)\|_{\text{op}}$ with respect to $\text{vec}[\Theta^{(\ell)}(t)]$ is given by:*

$$J_{\text{op}}^{(\ell)}(t) = \frac{\partial \|\Theta^{(\ell)}(t)\|_{\text{op}}}{\partial \text{vec}[\Theta^{(\ell)}(t)]} = \mathbf{v}_1^{(\ell)}(t) \otimes \mathbf{u}_1^{(\ell)}(t) \in \mathbb{R}^{m_\ell n_\ell},$$

where \otimes denotes Kronecker product (i.e. tensor product) ([Róisín Luo et al., 2025c; Kato, 1995; Horn and Johnson, 2012; Magnus and Neudecker, 2019](#)).

Lemma 4.6.3 (Operator-Norm Hessian ([Róisín Luo et al., 2025c](#))). *The operator-norm Hessian of $\|\Theta^{(\ell)}(t)\|_{\text{op}}$ with respect to $\text{vec}[\Theta^{(\ell)}(t)]$ is given by:*

$$\mathbf{H}_{\text{op}}^{(\ell)}(t) = \frac{\partial}{\partial \text{vec}[\Theta^{(\ell)}(t)]} \text{vec} \left[\frac{\partial \|\Theta^{(\ell)}(t)\|_{\text{op}}}{\partial \Theta^{(\ell)}(t)} \right] = \mathbf{H}_L^{(\ell)}(t) + \mathbf{H}_R^{(\ell)}(t) + \mathbf{H}_C^{(\ell)}(t) \in \mathbb{R}^{m_\ell n_\ell \times m_\ell n_\ell},$$

where:

$$\begin{aligned} \mathbf{e}_{i,j}^{(\ell)}(t) &:= \mathbf{v}_i^{(\ell)}(t) \otimes \mathbf{u}_j^{(\ell)}(t), \\ \mathbf{H}_L^{(\ell)}(t) &= \sum_{i \neq 1, i \leq m_\ell} \frac{\sigma_1^{(\ell)}(t)}{\sigma_1^{(\ell)}(t)^2 - \sigma_i^{(\ell)}(t)^2} \mathbf{e}_{1,i}^{(\ell)}(t) \otimes \mathbf{e}_{1,i}^{(\ell)}(t)^\top, \\ \mathbf{H}_R^{(\ell)}(t) &= \sum_{j \neq 1, j \leq n_\ell} \frac{\sigma_1^{(\ell)}(t)}{\sigma_1^{(\ell)}(t)^2 - \sigma_j^{(\ell)}(t)^2} \mathbf{e}_{j,1}^{(\ell)}(t) \otimes \mathbf{e}_{j,1}^{(\ell)}(t)^\top, \\ \mathbf{H}_C^{(\ell)}(t) &= \sum_{k \neq 1, k \leq r_\ell} \frac{\sigma_k^{(\ell)}(t)}{\sigma_1^{(\ell)}(t)^2 - \sigma_k^{(\ell)}(t)^2} \left[\mathbf{e}_{1,k}^{(\ell)}(t) \otimes \mathbf{e}_{k,1}^{(\ell)}(t)^\top + \mathbf{e}_{k,1}^{(\ell)}(t) \otimes \mathbf{e}_{1,k}^{(\ell)}(t)^\top \right], \end{aligned}$$

and $r_\ell = \text{rank}(\Theta^{(\ell)}(t))$.

Remark 4.6.4. Note that the function $\sigma_1^{(\ell)}(t) : \Theta^{(\ell)}(t) \mapsto \mathbb{R}$ is convex. Since the Hessian of a convex function is PSD, it follows that $\mathbf{H}_{\text{op}}^{(\ell)}(t)$ is PSD.

4.6.2 Layer-specific dynamics

Theorem 4.6.5 (Layer-Specific Dynamics). *The layer-specific dynamics of Lipschitz continuity is given by:*

$$\frac{dK^{(\ell)}(t)}{K^{(\ell)}(t)} = \left(\mu^{(\ell)}(t) + \kappa^{(\ell)}(t) \right) dt + \boldsymbol{\lambda}^{(\ell)}(t)^\top dB_t^{(\ell)}, \quad (4.12)$$

where $dB_t^{(\ell)} \sim \mathcal{N}(\mathbf{0}, \mathbf{I}_{m_\ell n_\ell} dt)$ represents the increment of a standard Wiener process in $\mathbb{R}^{m_\ell n_\ell}$, and:

$$\begin{aligned} \mu^{(\ell)}(t) &= \frac{1}{\sigma_1^{(\ell)}(t)} \left\langle \mathbf{J}_{\text{op}}^{(\ell)}(t), -\text{vec} \left[\nabla^{(\ell)} \mathcal{L}_f(\boldsymbol{\theta}(t)) \right] \right\rangle, \\ \boldsymbol{\lambda}^{(\ell)}(t) &= \frac{\sqrt{\eta}}{\sigma_1^{(\ell)}(t)} \left(\left[\boldsymbol{\Sigma}_t^{(\ell)} \right]^{\frac{1}{2}} \right)^\top \mathbf{J}_{\text{op}}^{(\ell)}(t), \quad \|\boldsymbol{\lambda}^{(\ell)}(t)\|_2^2 = \boldsymbol{\lambda}^{(\ell)}(t)^\top \boldsymbol{\lambda}^{(\ell)}(t) \geq 0, \\ \kappa^{(\ell)}(t) &= \frac{\eta}{2\sigma_1^{(\ell)}(t)} \left\langle \mathbf{H}_{\text{op}}^{(\ell)}(t), \boldsymbol{\Sigma}_t^{(\ell)} \right\rangle \geq 0, \end{aligned}$$

where we refer to:

1. $\mu^{(\ell)}(t)$ as **layer optimization-induced drift**, representing the contribution of the gradient flow $\nabla^{(\ell)} \mathcal{L}_f(\boldsymbol{\theta}(t))$ — induced by the optimization process — to the expectation of Lipschitz continuity. This term corresponds to the projection of the negative gradient expectation onto the principal subspace (i.e. largest singular value) of the parameter matrix, and acts as a deterministic drift in the evolution of the Lipschitz constant.
2. $\boldsymbol{\lambda}^{(\ell)}(t)$ as **layer diffusion-modulation intensity**, representing the contribution of the gradient noise $\boldsymbol{\Sigma}_t^{(\ell)}$ — arising from the randomness in mini-batch sampling — to the stochasticity of Lipschitz continuity. This term modulates the stochasticity of Lipschitz continuity and governs the uncertainty of temporal evolution.
3. $\kappa^{(\ell)}(t)$ as **layer noise-curvature entropy production**, representing the non-negative, irreversible contribution of the gradient noise $\boldsymbol{\Sigma}_t^{(\ell)}$ to the deterministic of Lipschitz continuity. Intuitively, the dynamical system bathes in the stochastic gradient fluctuations captured by $\boldsymbol{\Sigma}_t^{(\ell)}$, arising from mini-batch sampling. The stochastic fluctuations “dissipate” into the system via the curvature of the operator-norm landscape $\mathbf{H}_{\text{op}}^{(\ell)}(t)$, driving an irreversible increase in the Lipschitz constant and entropy.

Proof. Start with Definition 4.5.3:

$$\left\{ \begin{aligned} d\text{vec}(\boldsymbol{\theta}^{(\ell)}(t)) &= -\text{vec}[\nabla^{(\ell)} \mathcal{L}_f(\boldsymbol{\theta}(t))] dt + \sqrt{\eta} [\boldsymbol{\Sigma}_t^{(\ell)}]^{\frac{1}{2}} dB_t^{(\ell)} \end{aligned} \right. \quad (4.13)$$

$$K^{(\ell)}(t) = \|\boldsymbol{\theta}^{(\ell)}(t)\|_{\text{op}} = \sigma_1^{(\ell)}(t) \quad (4.14)$$

Using Lemma 4.6.2 and Lemma 4.6.3, we apply Itô's Lemma on Equation 4.14:

$$dK^{(\ell)}(t) = \underbrace{J_{\text{op}}^{(\ell)}(t)^{\top} d\text{vec}(\boldsymbol{\theta}^{(\ell)}(t))}_A + \underbrace{\frac{1}{2} \left(d\text{vec}(\boldsymbol{\theta}^{(\ell)}(t)) \right)^{\top} H_{\text{op}}^{(\ell)}(t) d\text{vec}(\boldsymbol{\theta}^{(\ell)}(t))}_B. \quad (4.15)$$

Compute A and B.

1. Substitute Equation 4.13 into A:

$$\begin{aligned} A &= J_{\text{op}}^{(\ell)}(t)^{\top} d\text{vec}(\boldsymbol{\theta}^{(\ell)}(t)) \\ &= J_{\text{op}}^{(\ell)}(t)^{\top} \left[-\text{vec}[\nabla^{(\ell)} \mathcal{L}_f(\boldsymbol{\theta}(t))] dt + \sqrt{\eta} [\boldsymbol{\Sigma}_t^{(\ell)}]^{\frac{1}{2}} dB_t^{(\ell)} \right] \\ &= \left\langle J_{\text{op}}^{(\ell)}(t), -\text{vec}[\nabla^{(\ell)} \mathcal{L}_f(\boldsymbol{\theta}(t))] \right\rangle dt + J_{\text{op}}^{(\ell)}(t)^{\top} \sqrt{\eta} [\boldsymbol{\Sigma}_t^{(\ell)}]^{\frac{1}{2}} dB_t^{(\ell)}. \end{aligned} \quad (4.16)$$

2. Use trace identity $\text{tr}(XYZ) = \text{tr}(YZX)$:

$$\begin{aligned} B &= \frac{1}{2} \left(d\text{vec}(\boldsymbol{\theta}^{(\ell)}(t)) \right)^{\top} H_{\text{op}}^{(\ell)}(t) d\text{vec}(\boldsymbol{\theta}^{(\ell)}(t)) \\ &= \frac{1}{2} \text{tr} \left[H_{\text{op}}^{(\ell)}(t) d\text{vec}(\boldsymbol{\theta}^{(\ell)}(t)) \left(d\text{vec}(\boldsymbol{\theta}^{(\ell)}(t)) \right)^{\top} \right]. \end{aligned}$$

Substituting Equation 4.13 into B, we obtain:

$$\begin{aligned} B &= \frac{1}{2} \text{tr} \left[H_{\text{op}}^{(\ell)}(t) d\text{vec}(\boldsymbol{\theta}^{(\ell)}(t)) \left(d\text{vec}(\boldsymbol{\theta}^{(\ell)}(t)) \right)^{\top} \right] \\ &= \frac{1}{2} \text{tr} \left[H_{\text{op}}^{(\ell)}(t) \eta [\boldsymbol{\Sigma}_t^{(\ell)}]^{\frac{1}{2}} \left\{ [\boldsymbol{\Sigma}_t^{(\ell)}]^{\frac{1}{2}} \right\}^{\top} dB_t^{(\ell)} (dB_t^{(\ell)})^{\top} \right] \\ &= \frac{1}{2} \eta \text{tr} \left[H_{\text{op}}^{(\ell)}(t) [\boldsymbol{\Sigma}_t^{(\ell)}]^{\frac{1}{2}} \left\{ [\boldsymbol{\Sigma}_t^{(\ell)}]^{\frac{1}{2}} \right\}^{\top} \right] dt \\ &= \frac{1}{2} \eta \text{tr} \left[H_{\text{op}}^{(\ell)}(t) \boldsymbol{\Sigma}_t^{(\ell)} \right] dt = \frac{1}{2} \eta \left\langle H_{\text{op}}^{(\ell)}(t), \boldsymbol{\Sigma}_t^{(\ell)} \right\rangle dt, \end{aligned} \quad (4.17)$$

by dropping higher-order infinitesimal terms, as $o((dt)^2) \rightarrow 0$ and $o(dt dB_t^{(\ell)}) \rightarrow 0$.

Combine A + B. Combine expanded A and B:

$$\frac{dK^{(\ell)}(t)}{K^{(\ell)}(t)} = \left[\underbrace{\frac{1}{\sigma_1^{(\ell)}(t)} \left\langle J_{op}^{(\ell)}(t), -\text{vec} \left[\nabla^{(\ell)} \mathcal{L}_f(\Theta(t)) \right] \right\rangle}_{\mu^{(\ell)}(t)} + \underbrace{\frac{\eta}{2\sigma_1^{(\ell)}(t)} \left\langle H_{op}^{(\ell)}(t), \Sigma_t^{(\ell)} \right\rangle}_{\kappa^{(\ell)}(t)} \right] dt + \underbrace{\frac{\sqrt{\eta}}{\sigma_1^{(\ell)}(t)} J_{op}^{(\ell)}(t)^\top \left[\Sigma_t^{(\ell)} \right]^{\frac{1}{2}} dB_t^{(\ell)}}_{\lambda^{(\ell)}(t)^\top}. \quad (4.18)$$

□

4.6.3 Network-specific dynamics

Theorem 4.6.6 (Logarithmic Network-Specific Dynamics). *The logarithmic, network-specific dynamics of Lipschitz continuity is given by:*

$$dZ(t) = \left(\mu_Z(t) + \kappa_Z(t) - \frac{1}{2} \lambda_Z(t)^2 \right) dt + \lambda_Z(t) dW_t, \quad (4.19)$$

where $dW_t \sim \mathcal{N}(0, dt)$ represents the increment of a standard Wiener process adapted to the filtration \mathcal{F}_t in \mathbb{R} by:

$$dW_t := \left[\sum_{\ell=1}^L \|\lambda^{(\ell)}(t)\|_2^2 \right]^{-\frac{1}{2}} \cdot \sum_{\ell=1}^L \lambda^{(\ell)}(t)^\top dB_t^{(\ell)} \sim \mathcal{N}(0, dt),$$

$$\mu_Z(t) = \sum_{\ell=1}^L \mu^{(\ell)}(t) \in \mathbb{R}, \quad \kappa_Z(t) = \sum_{\ell=1}^L \kappa^{(\ell)}(t) \in \mathbb{R}_+, \quad \lambda_Z(t) = \left[\sum_{\ell=1}^L \|\lambda^{(\ell)}(t)\|_2^2 \right]^{\frac{1}{2}} \in \mathbb{R}_+,$$

where we refer to: (i) $\mu_Z(t)$ as **network optimization-induced drift**; (ii) $\lambda_Z(t)$ as **network diffusion-modulation intensity**; and (iii) $\kappa_Z(t)$ as **network noise-curvature entropy production**, respectively.

Proof. Consider the differentials:

$$\frac{\partial Z(t)}{\partial K^{(\ell)}(t)} = \frac{1}{K^{(\ell)}(t)}, \quad \text{and} \quad \frac{\partial^2 Z(t)}{\partial K^{(\ell)}(t)^2} = -\frac{1}{K^{(\ell)}(t)^2}. \quad (4.20)$$

We apply Itô's Lemma on $dK^{(\ell)}$ across all layers to derive the dynamics of:

$$Z(t) = \sum_{l=1}^L \log K^{(l)}(t),$$

so that:

$$dZ(t) = d\left(\sum_{l=1}^L \log K^{(l)}(t)\right) = \sum_{l=1}^L \left(\underbrace{\frac{\partial Z(t)}{\partial K^{(l)}(t)} dK^{(l)}(t)}_C + \underbrace{\frac{1}{2} \frac{\partial^2 Z(t)}{\partial K^{(l)}(t)^2} (dK^{(l)}(t))^2}_D \right).$$

Derive C and D.

1. Derive C:

$$C = \frac{\partial Z(t)}{\partial K^{(\ell)}(t)} dK^{(\ell)}(t) = \frac{dK^{(\ell)}(t)}{K^{(\ell)}(t)} = \left(\mu^{(\ell)}(t) + \kappa^{(\ell)}(t) \right) dt + \lambda^{(\ell)}(t)^\top dB_t^{(\ell)}.$$

2. Derive D:

$$D = \frac{1}{2} \frac{\partial^2 Z(t)}{\partial K^{(\ell)}(t)^2} (dK^{(\ell)}(t))^2 = -\frac{1}{2K^{(\ell)}(t)^2} (dK^{(\ell)}(t))^2 = -\frac{1}{2} \|\lambda^{(\ell)}(t)\|_2^2 dt,$$

by dropping higher-order infinitesimal terms as $o((dt)^2) \rightarrow 0$ and $o(dt dB_t^{(\ell)}) \rightarrow 0$.

Combine C + D. Hence:

$$\begin{aligned} dZ(t) &= \left(\sum_{l=1}^L \mu^{(l)}(t) + \kappa^{(l)}(t) - \frac{1}{2} \|\lambda^{(l)}(t)\|_2^2 \right) dt + \sum_{l=1}^L \lambda^{(l)}(t)^\top dB_t^{(l)} \\ &= \left(\mu_Z(t) + \kappa_Z(t) - \frac{1}{2} \lambda_Z(t)^2 \right) dt + \lambda_Z(t) dW_t \end{aligned}$$

where $dW_t \sim \mathcal{N}(0, dt)$ represents the increment of a Wiener process in \mathbb{R} .

□

Theorem 4.6.7 (Integral-Form Dynamics of Lipschitz Continuity). *Using Itô's calculus, the integral-form dynamics of Lipschitz continuity is stated as:*

$$\begin{cases} Z(t) = Z(0) + \int_0^t \left[\mu_Z(s) + \kappa_Z(s) - \frac{1}{2} \lambda_Z(s)^2 \right] ds + \int_0^t \lambda_Z(s) dW_s \\ K(t) = \exp \{Z(t)\} \end{cases}$$

where $Z(0)$ is the initial value of $Z(t)$.

4.6.4 Statistical characterization

Theorem 4.6.8 (Statistics of Lipschitz Continuity). *Let $K(0)$ be the initial Lipschitz continuity bound, and hence $Z(0) = \log K(0)$. The expectation and variance of $K(t)$ are given as:*

$$\mathbb{E}[K(t)] = e^{\mathbb{E}[Z(t)] + \frac{1}{2} \text{Var}[Z(t)]} = K(0) \cdot e^{\int_0^t \mu_Z(s) ds} \cdot e^{\int_0^t \kappa_Z(s) ds} \quad (4.21)$$

$$\text{Var}[K(t)] = \mathbb{E}[K(t)]^2 \left(e^{\text{Var}[Z(t)]} - 1 \right) = \mathbb{E}[K(t)]^2 \left(e^{\int_0^t \lambda_Z(s)^2 ds} - 1 \right), \quad (4.22)$$

where:

$$\mathbb{E}[Z(t)] = Z(0) + \int_0^t \left[\mu_Z(s) + \kappa_Z(s) - \frac{1}{2} \lambda_Z(s)^2 \right] ds \quad (4.23)$$

$$\text{Var}[Z(t)] = \int_0^t \lambda_Z(s)^2 ds. \quad (4.24)$$

Remark 4.6.9. The expectation of Lipschitz continuity is dominated only by three factors:

- i **Parameter initialization** $K(0)$. The parameter initialization determines the network Lipschitz continuity. We discuss the details in Section 4.8.2.
- ii **Optimization-induced drift** $\mu_Z(t)$. The projection of gradient expectations on the operator-norm Jacobian, induced by optimization process, drive the evolution of Lipschitz continuity;
- iii **Noise-curvature entropy production** $\kappa_Z(t)$. The gradient fluctuations, arising from mini-batch sampling, has a deterministic, non-negative and irreversible increase in the Lipschitz continuity.

The uncertainty of Lipschitz continuity is determined by two factors:

- i **Lipschitz continuity expectation** $\mathbb{E}[K(t)]$. The uncertainty is proportional to the current Lipschitz constant bound. Larger Lipschitz constant bound leads to larger uncertainty of the evolution;
- ii **Diffusion-modulation intensity** $\lambda_Z(t)$. The projection of the gradient fluctuations on the operator-norm Jacobian modulates the diffusion process of Lipschitz continuity, hence dominates the uncertainty of the evolution.

Proof.

Lemma 4.6.10 (Moment-Generating Function of $Z(t)$). *Consider $Z(t)$:*

$$Z(t) \sim \mathcal{N}(\mathbb{E}[Z(t)], \text{Var}[Z(t)]), \quad (4.25)$$

then the MGF of $Z(t)$ is given as:

$$\mathbb{E}[e^{kZ(t)}] = e^{k\mathbb{E}[Z(t)] + \frac{1}{2}k^2 \text{Var}[Z(t)]}. \quad (4.26)$$

Set $k = 1$:

$$\mathbb{E}[K(t)] = \mathbb{E}[e^{Z(t)}] = e^{\mathbb{E}[Z(t)] + \frac{1}{2} \text{Var}[Z(t)]} = e^{Z(0) + \int_0^t [\mu_Z(s) + \kappa_Z(s)] ds}, \quad (4.27)$$

so that:

$$(\mathbb{E}[K(t)])^2 = (\mathbb{E}[e^{Z(t)}])^2 = e^{2\mathbb{E}[Z(t)] + \text{Var}[Z(t)]} = e^{2Z(0) + \int_0^t [2\mu_Z(s) + 2\kappa_Z(s)] ds}. \quad (4.28)$$

Set $k = 2$:

$$\mathbb{E}[K(t)^2] = \mathbb{E}[e^{2Z(t)}] = e^{2\mathbb{E}[Z(t)] + 2\text{Var}[Z(t)]}. \quad (4.29)$$

Hence:

$$\text{Var}[K(t)] = \mathbb{E}[K(t)^2] - (\mathbb{E}[K(t)])^2 = \mathbb{E}[K(t)]^2 (e^{\text{Var}[Z(t)]} - 1). \quad (4.30)$$

□

4.7 Framework validation

Experimental Settings. We conduct numerical experiments to validate our framework, using a five-layer ConvNet (details in Table 4.1 in the Appendix), optimized with SGD (without momentum). Experimental details are as follows:

1. **Datasets.** To validate the effectiveness of our framework across various datasets, the ConvNet is trained on CIFAR-10 and CIFAR-100 respectively, for 39,000 steps (200 epochs) with a learning rate of 10^{-3} and a batch size of 256.
2. **Regularizers.** To validate the effectiveness of our framework under various regularization configurations (see Table 4.3 in Appendix), the ConvNet is trained with multiple regularizers, including *batch normalization*, *mixup*, and *label smoothing*. Additional results with *dropout*, *weight decay*, *auto-augment*, and *adversarial training* are presented in the Appendix.

Experimental Results. Figure 4.2a presents the results on CIFAR-10, and Figure 4.2b shows the corresponding results on CIFAR-100. These experiments demonstrate that our mathematical framework closely captures the dynamics of Lipschitz continuity across a range of regularizers.

4.8 Theoretical implications

Our theoretical framework provides a unified perspective for analyzing and interpreting the evolution of Lipschitz continuity in neural networks. Specifically, it enables us to answer the following questions:

1. Section 4.8.1: **Key factors.** What are the key factors governing the temporal evolution of Lipschitz continuity during training?
2. Section 4.8.2: **Parameter initialization.** How does parameter initialization affect the temporal evolution of Lipschitz continuity?
3. Section 4.8.3: **Unbounded growth near convergence.** What dynamics emerge as the network approaches convergence, particularly in the regime where the training loss approaches zero?
4. Section 4.8.4: **Noisy gradient regularization.** How does gradient noise regulate the temporal evolution of Lipschitz continuity?

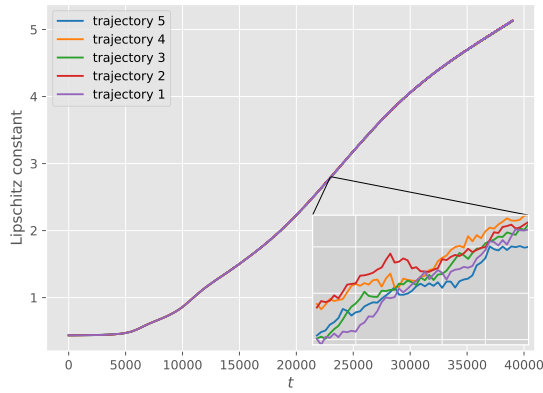


Figure 4.4: Predicted effect of the trajectory in mini-batch sampling on Lipschitz continuity. The inset plot zooms in on 50 steps at $t = 23000$.

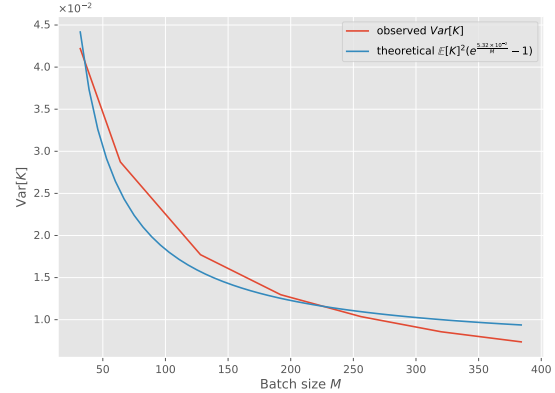


Figure 4.5: Predicted effect of batch size on the variance of Lipschitz continuity.

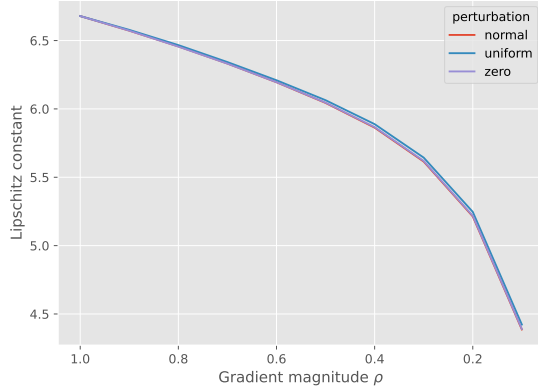


Figure 4.6: Predicted effect of gradient magnitude and perturbation.

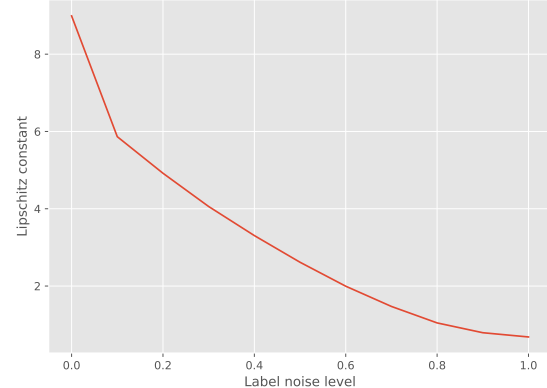


Figure 4.7: Predicted effect of uniform label corruption.

5. Section 4.8.5: **Uniform label corruption.** How does uniform label corruption implicitly regularize the dynamics of Lipschitz continuity?
6. Section 4.8.6: **Batch size.** What role does batch size play in shaping the temporal evolution of Lipschitz continuity?
7. Section 4.8.7: **Mini-batch sampling trajectory.** What impact does mini-batch sampling have on the temporal evolution of Lipschitz continuity?

4.8.1 Key factors driving dynamics

Principal driving factors. Theorem 4.6.5 and Theorem 4.6.6 identify four principal factors driving the evolution of Lipschitz continuity at both the layer and network levels:

- (i) **Gradient-principal-direction alignment.** The alignment between the gradient expectations and the principal directions of parameter matrices determines *optimization-induced drift* the $\mu_Z(t)$. As shown in Figure 4.3, this force dominates the drift of the Lipschitz continuity (see Theorem 4.6.5 and Theorem 4.6.6).
- (ii) **Directional gradient noise.** The directional projection of gradient fluctuations, arising from mini-batch sampling, on the principal directions of parameter matrices determines the *diffusion-modulation intensity* $\lambda_Z(t)$ arises from. As shown in Figure 4.3, this factor modulates the diffusion of the Lipschitz continuity.
- (iii) **Deterministic effect of gradient noise.** The interaction between the gradient fluctuations, arising from mini-batch sampling, and the operator-norm curvatures determines the *noise-curvature entropy production* $\kappa_Z(t)$. Our theoretical framework suggests that this term gives a deterministic, non-negative, and irreversible increase contributing to the drift of the dynamics.
- (iv) **Gradient noise amplification effect.** Lemma 4.6.3 and Theorem 4.6.5 suggest that the inverted principal spectral gaps in parameter matrices, defined as $\left[\sigma_1^{(\ell)}(t)^2 - \sigma_j^{(\ell)}(t)^2 \right]^{-1}$, for all $j \neq 1$, can amplify the gradient noise. Thus smaller spectral gaps amplifies gradient noise, contributing to larger *noise-curvature entropy production* $\kappa_Z(t)$.

4.8.2 Parameter initialization

According to Theorem 4.6.8, the network initialization $K(0)$ affects both the expectation and uncertainty of Lipschitz continuity in the evolution. Suppose that the entries of a parameter $\theta^{(\ell)} \in \mathbb{R}^{m_\ell \times n_\ell}$ are sampled from $\mathcal{N}(0, s_\ell^2)$. According to the Tracy-Widom limiting distribution (Tracy and Widom, 1994; Tao, 2012), the largest singular value limit is $\sigma_1^\ell \rightarrow (\sqrt{m_\ell} + \sqrt{n_\ell}) \cdot s_\ell$, if $m_\ell \cdot n_\ell$ is sufficiently large. For a network with L layers,

$$K(0) \rightarrow \prod_{\ell=1}^L (\sqrt{m_\ell} + \sqrt{n_\ell}) \cdot s_\ell,$$

hence a larger network has a larger Lipschitz continuity. For the case of Kaiming initialization, $s_\ell = \sqrt{2/n_\ell}$ (He et al., 2015).

4.8.3 Unbounded growth near-convergence

Suppose a negative-log-likelihood loss:

$$\ell_f(\theta(t); x, y) = -\log p_{\theta(t)}(y | x)$$

near convergence:

$$\ell_f(\theta(t); x, y) \rightarrow 0.$$

Under Assumption 4.3.1, the Fisher information matrix (FIM) of $p_{\theta(t)}(y | x)$ with respect to parameters $\theta^{(\ell)}(t)$ (Martens, 2020) is defined as

$$\mathbf{F}^{(\ell)}(t) := \mathbb{E} \left[\text{vec} \left[\nabla^{(\ell)} p_{\theta(t)}(y | x) \right] \text{vec} \left[\nabla^{(\ell)} p_{\theta(t)}(y | x) \right]^\top \right] \approx M \cdot \boldsymbol{\Sigma}_t^{(\ell)},$$

as $\ell_f(\theta; x, y) \rightarrow 0$, where M is the batch size (Mandt et al., 2017; Li et al., 2022b; Martens, 2020). This will serve as a foundation for our later theoretical analysis of the near-convergence dynamics.

Proposition 4.8.1 (Unbounded Growth Near-Convergence). *Consider the terms in the dynamics (Theorem 4.6.5):*

$$\begin{aligned} \mu^{(\ell)}(t) &= \frac{1}{\sigma_1^{(\ell)}(t)} \left\langle \mathbf{J}_{\text{op}}^{(\ell)}(t), -\text{vec} \left[\nabla^{(\ell)} \mathcal{L}_f(\theta(t)) \right] \right\rangle \approx 0, \\ \lambda^{(\ell)}(t) &= \frac{\sqrt{\eta}}{\sigma_1^{(\ell)}(t)} \left(\left[\boldsymbol{\Sigma}_t^{(\ell)} \right]^{\frac{1}{2}} \right)^\top \mathbf{J}_{\text{op}}^{(\ell)}(t) \approx \frac{\sqrt{\eta}}{\sigma_1^{(\ell)}(t)} \left(\left[\frac{1}{M} \mathbf{F}^{(\ell)}(t) \right]^{\frac{1}{2}} \right)^\top \mathbf{J}_{\text{op}}^{(\ell)}(t) \rightarrow 0, \\ \kappa^{(\ell)}(t) &= \frac{\eta}{2\sigma_1^{(\ell)}(t)} \left\langle \mathbf{H}_{\text{op}}^{(\ell)}(t), \boldsymbol{\Sigma}_t^{(\ell)} \right\rangle \approx \frac{\eta}{2\sigma_1^{(\ell)}(t)} \frac{1}{M} \left\langle \mathbf{H}_{\text{op}}^{(\ell)}(t), \mathbf{F}^{(\ell)}(t) \right\rangle > 0, \end{aligned}$$

so that Lipschitz continuity is not bounded in expectation:

$$\lim_{t \rightarrow \infty} \mathbb{E} [K(t)] = \lim_{t \rightarrow \infty} e^{Z(0) + \int_0^t [\mu_Z(s) + \kappa_Z(s)] ds} = \lim_{t \rightarrow \infty} e^{Z(0) + \int_0^t \kappa_Z(s) ds} \rightarrow \infty,$$

and uncertainty:

$$\lim_{t \rightarrow \infty} \text{Var} [K(t)] = \lim_{t \rightarrow \infty} \mathbb{E} [K(t)]^2 \left(e^{\text{Var}[Z(t)]} - 1 \right) \rightarrow \infty,$$

as $t \rightarrow \infty$. This result demonstrates that the Lipschitz continuity bound monotonically increases as optimization progresses. This phenomenon has been noted in literature (Miyato et al., 2018; Bartlett et al., 2017; Sedghi et al., 2019; Gamba et al., 2023).

Experimental Results. We extend the training of the five-layer ConvNet on CIFAR-10 without regularization to 344,370 steps (1766 epochs) for observing the long range dynamics near convergence. Figure 4.3a shows the layer-specific dynamics; Figure 4.3b shows the network-specific dynamics. The observations are as follows:

- (i) **Unbounded growth.** We train the network for up to 344,370 steps, near convergence. The gradual increase driven by $\kappa_Z(t)$ persists throughout the training, with no observable indication of stopping, suggesting that the dynamics do not admit a finite-time steady state.
- (ii) **Non-negligible contribution of gradient noise.** Although the magnitude of $\kappa_Z(t)$ is typically one order smaller than that of $\mu_Z(t)$ in our experiments, its cumulative effect on the growth of Lipschitz continuity near-convergence is non-negligible and persists throughout training.
- (iii) **Four Phases.** We observe that $\kappa_Z(t)$ exhibits four distinct phases: (i) phase 1 — a rapid initial increase at the beginning of training, (ii) phase 2 — large fluctuations prior to overfitting, (iii) phase 3 — a steady decline, and (iv) phase 4 — convergence to a non-negative constant.

4.8.4 Noisy gradient regularization

Prior work shows that injecting noise into gradients during training can improve robustness (Welling and Teh, 2011) and help escape local minima (Neelakantan et al., 2015). Our theoretical framework elucidates the mechanism by which gradient noise serves as a regularizer for Lipschitz continuity. Consider a loss ℓ_* with noisy supervision consists of a signal loss ℓ_f and a noisy loss ℓ_n :

$$\ell_*(\theta; x, y) = \sqrt{\rho} \cdot \ell_f(\theta; x, y) + \sqrt{1 - \rho} \cdot \ell_n(\theta; x, y), \quad (4.31)$$

where $\rho \in [0, 1]$. The corresponding batch loss is:

$$\nabla^{(\ell)} \mathcal{L}_*(\theta; \xi) = \sqrt{\rho} \cdot \nabla^{(\ell)} \mathcal{L}_f(\theta; \xi) + \sqrt{1 - \rho} \cdot \nabla^{(\ell)} \mathcal{L}_n(\theta; \xi), \quad (4.32)$$

and the gradient noise covariance is:

$$\Sigma^{(\ell),*} = \rho \cdot \Sigma^{(\ell),f} + (1 - \rho) \cdot \Sigma^{(\ell),n}. \quad (4.33)$$

If the noise is sampled from $\mathcal{N}(0, \sigma^2)$, $\Sigma^{(\ell),n} = \sigma^2 \mathbf{I}$, the dynamics has the changes:

$$\mu_*^{(\ell)}(t) = \sqrt{\rho} \mu^{(\ell)}(t),$$

and

$$\kappa_*^{(\ell)}(t) = \rho \cdot \kappa^{(\ell)}(t) + (1 - \rho) \cdot \frac{\eta}{2\sigma_1^{(\ell)}(t)} \underbrace{\left\langle \mathbf{H}_{\text{op}}^{(\ell)}(t), \sigma^2 \mathbf{I} \right\rangle}_{\text{variance is negligible}} \approx \rho \cdot \kappa^{(\ell)}(t).$$

The variance contribution from $\mathbf{H}_{\text{op}}^{(\ell)}(t)$ is neglected, as experimental results indicate it is negligible (see Figure 4.3). According to Theorem 4.6.8, by ignoring $\lambda_Z(t)$, we have:

$$\mathbb{E} [K(t)] \approx e^{Z(0) + \int_0^t \sqrt{\rho} \cdot \mu_Z(s) ds + \int_0^t \rho \cdot \kappa_Z(s) ds} = K(0) \left[e^{\int_0^t \mu_Z(s) ds} \right]^{\sqrt{\rho}} \left[e^{\int_0^t \kappa_Z(s) ds} \right]^\rho. \quad (4.34)$$

Although the integrals $\int_0^t \mu_Z(s) ds$ and $\int_0^t \kappa_Z(s) ds$ are unlikely to be computed — without the structural information of the noisy supervision regarding Equation (4.31), (4.32) and (4.33), it provides insight how gradient magnitude affects the evolution of Lipschitz continuity bound. This result shows higher gradient magnitude leads larger Lipschitz continuity bound. This framework can be used to analyze the uniform label corruption (see Section 4.8.5).

Experimental Results. We train a MLP (see Table 4.2) on the MNIST with a batch size of 128 and a learning rate of 0.01, using SGD without momentum. During training, the gradients are scaled by $\sqrt{\rho}$, and additive noise is injected sampled from: (i) a Gaussian distribution $\mathcal{N}(0, 1)$; (ii) a uniform distribution $U[-0.5, 0.5]$; and (iii) zero noise, scaled by $\sqrt{1 - \rho}$. As shown in Figure 4.6, the Lipschitz constant decreases monotonically as ρ decreases.

4.8.5 Uniform label corruption

Suppose a classifier is trained with a negative-log-likelihood loss function $\ell_f(\theta; x, y) := -\log p_\theta(y|x)$. Further suppose that the label corruption probability is $\epsilon \in [0, 1]$ with a uniform distribution $U(\mathcal{Y})$, while the label remains intact with a probability $1 - \epsilon$. There-

fore the gradient with label corruption can be expressed as (Natarajan et al., 2013; Patrini et al., 2017; Ghosh et al., 2017):

$$\begin{aligned} \mathbb{E} \left[\nabla^{(\ell)} \ell_f(\theta; x, y) \right] &:= (1 - \epsilon) \cdot \mathbb{E}_{x,y} \left[\nabla^{(\ell)} [-\log p_\theta(y|x)] \right] \\ &\quad + \epsilon \cdot \mathbb{E}_x \left[\nabla^{(\ell)} \frac{1}{|\mathcal{Y}|} \sum_{\tilde{y} \sim U(\mathcal{Y})} [-\log p_\theta(\tilde{y}|x)] \right], \end{aligned}$$

where $\tilde{y} \sim U(\mathcal{Y})$. The literature on this topic (Natarajan et al., 2013; Ghosh et al., 2017) assumes that the loss component with label noise contributes only a constant, hence zero gradient:

$$\langle J_{op}^{(\ell)}(t), \text{vec} \left[-\nabla^{(\ell)} \mathbb{E}_{x,\tilde{y}} [-\log p_\theta(\tilde{y}|x)] \right] \rangle \rightarrow 0.$$

According to Equation 4.31, we can treat the label noise as ℓ_n . By using Equation 4.34, note $\rho = (1 - \epsilon)^2$, then we have:

$$\mathbb{E} [K'(t)] \approx K(0) \cdot \left[e^{\int_0^t \mu_Z(s) ds} \right]^{1-\epsilon} \cdot \left[e^{\int_0^t \kappa_Z(s) ds} \right]^{(1-\epsilon)^2}.$$

Experimental Results. We train a MLP (see Table 4.2) on the MNIST with a batch size of 128 and a learning rate of 0.01, using SGD without momentum. We inject uniform label noise into the dataset with a level from 0 to 1. As shown in Figure 4.7, the Lipschitz constant decreases monotonically as label noise level increases.

4.8.6 Batch size

Suppose that the batch size M in mini-batch sampling affects only the gradient noise $\Sigma(t)$, and does not affect the expectations of gradients $\nabla \mathcal{L}_f(\theta)$. Therefore, the batch size M affects only the diffusion term (Theorem 4.6.8). We analyze the effect of mini-batch size.

Proposition 4.8.2 (Uncertainty Under Large Batch). *Let the batch size be M and sufficiently large, then:*

$$\text{Var}[K(t)] \approx \mathbb{E}[K(t)]^2 \frac{C}{M},$$

where C is a constant given as:

$$C = \int_0^t \sum_{l=1}^L \frac{\eta}{\sigma_1^{(l)}(t)^2} J_{op}^{(l)}(t) \text{Var} \left[\text{vec} \left(\nabla^{(l)} \ell_f(\theta(t); x, y) \right) \right] J_{op}^{(l)}(t)^\top ds$$

Proof. Substitute Equation 4.3 into Theorem 4.6.8:

$$\begin{aligned} \text{Var}[Z(t)] &= \int_0^t \lambda_Z(s)^2 ds = \int_0^t \sum_{l=1}^L \|\lambda^{(l)}(s)\|_2^2 ds = \int_0^t \sum_{l=1}^L \frac{\eta}{\sigma_1^{(l)}(t)^2} J_{op}^{(l)}(t) \Sigma^{(l)}(t) J_{op}^{(l)}(t)^\top ds \\ &= \int_0^t \sum_{l=1}^L \frac{\eta}{\sigma_1^{(l)}(t)^2} J_{op}^{(l)}(t) \frac{1}{M} \text{Var} \left[\text{vec} \left(\nabla^{(l)} \ell_f(\theta(t); x, y) \right) \right] J_{op}^{(l)}(t)^\top ds \\ &= \underbrace{\frac{1}{M} \int_0^t \sum_{l=1}^L \frac{\eta}{\sigma_1^{(l)}(t)^2} J_{op}^{(l)}(t) \text{Var} \left[\text{vec} \left(\nabla^{(l)} \ell_f(\theta(t); x, y) \right) \right] J_{op}^{(l)}(t)^\top ds}_{\text{a constant}} = \frac{1}{M} C. \end{aligned}$$

Hence:

$$\text{Var}[K(t)] = \mathbb{E}[K(t)]^2 \left(e^{\text{Var}[Z(t)]} - 1 \right) = \mathbb{E}[K(t)]^2 \left(e^{\frac{C}{M}} - 1 \right).$$

Suppose $M \rightarrow \infty$:

$$\text{Var}[K(t)] = \mathbb{E}[K(t)]^2 \left(e^{\frac{C}{M}} - 1 \right) \approx \mathbb{E}[K(t)]^2 \left(1 + \frac{C}{M} - 1 \right) = \mathbb{E}[K(t)]^2 \frac{C}{M} \asymp \frac{1}{M}.$$

□

Experimental Results. We train the five-layer ConvNet (Table 4.1 in the Appendix), optimized with SGD without momentum. The batch size is varied from 32 to 384 in increments of 32, and each configuration is trained for 39,000 steps. During training, we profile and collect the dynamics to compute the uncertainty of Lipschitz continuity $\text{Var}[K(t)]$. As shown in Figure 4.5, the observed effect of batch size aligns closely with the theoretical prediction in Proposition 4.8.2.

4.8.7 Mini-batch sampling trajectory

According to Proposition 4.8.2, if the batch size is sufficiently large, the effect from various mini-batch sampling trajectories can be neglected since:

$$\text{Var}[K(t)] \approx \mathbb{E}[K(t)]^2 \frac{C}{M} \rightarrow 0,$$

as batch size M is sufficiently large.

Experimental Results. We train the five-layer ConvNet (Table 4.1 in the Appendix), optimized with SGD without momentum. The parameter initialization random seed is fixed to 1, while the random seed for mini-batch sampling is varied from 1 to 5. As shown in Figure 4.4, the sampling trajectories have a negligible effect on the evolution of Lipschitz continuity.

4.9 Limitations and future work

While our mathematical framework shows strong agreement with empirical results, it has several limitations:

1. **Layer-wise noise assumption.** The simplification in Assumption 4.3.1 neglects inter-layer interactions among neurons; this may pose as a challenge for studying large models.
2. **Distributional assumption.** We assume that the gradient noise follows a time-state-dependent normal distribution varying smoothly. However, this assumption may not hold for small batch sizes, where the noise distribution can deviate significantly from Gaussian.
3. **Continuous–discrete error.** Our framework models gradient dynamics in continuous time, whereas SGD operates in discrete steps. This discrepancy may introduce non-negligible errors, particularly when modeling long-range dynamics.

4.10 Conclusions

We present a mathematical framework that models the dynamics of Lipschitz continuity in neural networks through a system of SDEs. This theoretical framework not only identifies

the key factors governing the evolution of Lipschitz continuity, but also provides insight into how it is implicitly regularized during training. Beyond its analytical value, the framework offers a foundation for future research and development. Our experiments further validate the effectiveness of the proposed framework and the predicted effects of the theoretical implications.

4.A Appendix

4.B Network configuration

Function Block	# of Layer	Module
Block #1	1	nn.Conv2d(3, 32, kernel_size=3, padding=1)
	2	nn.ReLU()
	3	nn.MaxPool2d(kernel_size=2, stride=2)
Block #2	4	nn.Conv2d(32, 64, kernel_size=3, padding=1)
	5 (*)	nn.Dropout(p=0.2)
	6	nn.ReLU()
	7	nn.MaxPool2d(kernel_size=2, stride=2)
Block #3	8	nn.Conv2d(64, 128, kernel_size=3, padding=1, stride=2)
	9 (*)	nn.Dropout(p=0.2)
	10 (*)	nn.BatchNorm2d(128, track_running_stats=False)
	11	nn.ReLU()
Classifier	12	nn.Linear(128 * 4 * 4, 256)
	13	nn.ReLU()
	14 (*)	nn.Dropout(p=0.3)
	15	nn.Linear(256, num_classes)

Table 4.1: ConvNet configuration. The layer marked as ‘(*)’ is configurable with respect to experimental needs. There are five parameterized layers (*i.e.* # 1, # 4, # 8, # 12 and # 15).

# of Layer	Module
1	nn.Linear(28*28, 512)
2	nn.ReLU()
3	nn.Linear(512, 256)
4	nn.ReLU()
5	nn.Linear(256, 10)

Table 4.2: MLP configuration. There are three parameterized layers (*i.e.* # 1, # 3, and # 5).

4.C Regularization configuration

Regularization	Configuration
mixup	$\alpha = 0.4$
label smoothing	$\epsilon = 0.1$
adversarial training w/ FGSM	$\epsilon = 0.03$
weight-decay	$\lambda = 0.001$
auto-augment	AutoAugment(policy=AutoAugmentPolicy.CIFAR10) AutoAugment(policy=AutoAugmentPolicy.CIFAR100)

Table 4.3: Regularization configuration.

4.D Full validation experiment

Results of full validation experiments are shown as in Figure 4.8.

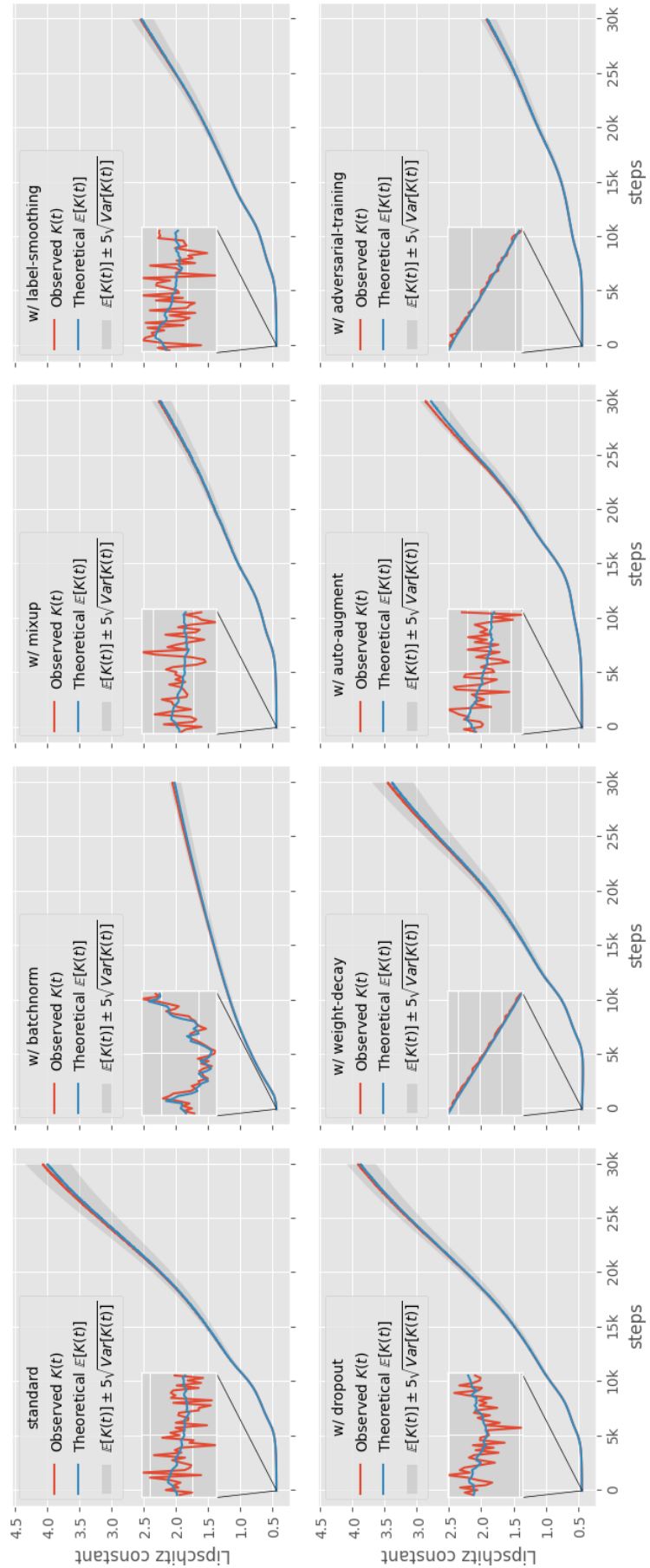


Figure 4.8: Full numerical validation of our mathematical framework on CIFAR-10.

5

FOURIER ANALYSIS OF LIPSCHITZ CONTINUITY

Guiding Research Question. This chapter explores the relationship between frequency-domain features, robustness, and Lipschitz continuity. It addresses the secondary research question (**SRQ5**) **Fourier Analysis of Lipschitz Continuity**, in service of the primary research question — (**RQ3**) **Modulation of Frequency Signal Propagation**. Using tools from Fourier analysis, information theory, and Shapley value theory, the chapter first establishes a frequency-domain upper bound on the Lipschitz continuity of neural networks. It then analyzes how input-space frequency perturbations are modulated by this bound. As a direct corollary, it is shown that the variational mutual information induced by frequency perturbations is bounded above by spectral contributions to Lipschitz continuity. As a complement to the theory, empirical studies are also presented to support the connection between frequency-domain perturbations and Lipschitz continuity during training.

Notes. Theoretical claims appear in the main text only when supported by numerical experiments, while purely theoretical analyses are compiled in the appendix. This chapter also serves as a conceptual transition to the next chapter, which interprets global robustness of image classifiers using Shapley value theory to quantify the effects of frequency-domain perturbations.

Reproducibility. https://anonymous.4open.science/r/lipschitz_fourier_analysis-DCF2/

ABSTRACT

Lipschitz continuity plays a central role in understanding the robustness and generalization of neural networks. In this work, we investigate how Lipschitz properties interact with the frequency structure of data. We begin with a theoretical analysis, showing that the global Lipschitz constant can be decomposed as an integral over frequency-specific contributions, revealing how Lipschitz continuity modulates frequency signal propagation. We further demonstrate that perturbing input frequen-

cies leads to bounded changes in mutual information, where the bounds are determined by local spectral Lipschitz coefficients. Complementing this, we provide an empirical analysis that examines the relationship between frequency structures and Lipschitz continuity. Our experiments show that training on high-frequency signals results in larger Lipschitz constants and sharper loss landscapes. These findings bridge the gap between frequency-domain analysis and learning dynamics, offering new tools to interpret model behavior through spectral properties.

5.1 Introduction

LIPSCHITZ continuity in neural networks refers to a constraint on the network’s function, ensuring that the output changes at a bounded rate with respect to input changes. Mathematically, a function $f : \mathbb{R}^m \mapsto \mathbb{R}^n$ is K -Lipschitz continuous if there exists a constant L (the Lipschitz constant) such that

$$\|f(u) - f(v)\| \leq K\|u - v\|, \quad (5.1)$$

for all inputs $\forall u, v$. In neural networks, this property governs multiple fundamental properties such as robustness to small input changes and generalization to unseen data (Cisse et al., 2017).

Lipschitz continuity also governs frequency feature propagation in neural networks, a phenomenon closely tied to **spectral bias** (Rahaman et al., 2019). Spectral bias refers to the tendency of neural networks to learn low-frequency components of a target function more quickly and effectively than high-frequency components (Rahaman et al., 2019; Xu et al., 2020; Róisín Luo et al., 2024b).

Content Organization. We present two complementary investigations: one theoretical and one empirical. The content is organized as follows:

1. Section 5.3 (Fourier Analysis) provides a theoretical analysis of the role of Lipschitz continuity using Fourier analysis. We show that the variational mutual information gap under frequency perturbations is locally upper-bounded by the contribution of the spectral Lipschitz constant.
2. Section 5.4 (Empirical Study) presents an empirical analysis of the relationship between Lipschitz continuity and the frequency structure of training data. Our ex-

periments demonstrate that networks trained on high-frequency data tend to exhibit larger Lipschitz constants and sharper loss landscapes, which in turn lead to reduced robustness and generalization performance.

5.2 Preliminaries

Lebesgue Measure. The *Lebesgue measure* μ on \mathbb{R}^d is a complete, translation-invariant measure defined on the σ -algebra of Lebesgue-measurable subsets of \mathbb{R}^d . It extends the intuitive notions of length (in \mathbb{R}), area (in \mathbb{R}^2), and volume (in \mathbb{R}^3) to arbitrary dimension and to more general sets than those handled by the Riemann integral. Formally, for any box (*i.e.*, product of intervals) $I = \prod_{i=1}^d [a_i, b_i] \subseteq \mathbb{R}^d$, the Lebesgue measure is defined as:

$$\mu(I) := \prod_{i=1}^d (b_i - a_i). \quad (5.2)$$

Key Properties. The Lebesgue measure satisfies the following key properties:

- **Non-negativity.** $\mu(E) \geq 0$ for all measurable sets $E \subseteq \mathbb{R}^d$.
- **Countable additivity.** If $\{E_n\}_{n=1}^{\infty}$ is a countable collection of pairwise disjoint measurable sets, then

$$\mu\left(\bigcup_{n=1}^{\infty} E_n\right) = \sum_{n=1}^{\infty} \mu(E_n). \quad (5.3)$$

- **Translation invariance.** For any measurable set $E \subseteq \mathbb{R}^d$ and any vector $x \in \mathbb{R}^d$, we have

$$\mu(E + x) = \mu(E), \quad (5.4)$$

where $E + x := \{y + x : y \in E\}$.

Lebesgue Measurable. A set $E \subseteq \mathbb{R}^d$ is *Lebesgue measurable* if for every $\varepsilon > 0$, there exists an open set $O \supseteq E$ such that

$$\mu(O \setminus E) < \varepsilon. \quad (5.5)$$

Lebesgue Integral. Let $f : \mathbb{R}^d \rightarrow \mathbb{R}$ be a Lebesgue-measurable function. The Lebesgue integral of f with respect to the Lebesgue measure μ is defined by first considering non-negative functions, where

$$\int_{\mathbb{R}^d} f \, d\mu := \sup \left\{ \int_{\mathbb{R}^d} s \, d\mu : 0 \leq s \leq f, s \text{ simple} \right\}, \quad (5.6)$$

and each simple function takes the form $s(x) = \sum_{i=1}^n a_i \cdot \mathbf{1}_{E_i}(x)$ for $a_i \geq 0$ and measurable sets E_i . For a general function f , we write $f = f^+ - f^-$ with $f^+ := \max(f, 0)$ and $f^- := \max(-f, 0)$, and define the integral as

$$\int_{\mathbb{R}^d} f \, d\mu := \int_{\mathbb{R}^d} f^+ \, d\mu - \int_{\mathbb{R}^d} f^- \, d\mu. \quad (5.7)$$

Inequalities in Function Spaces L^p . Minkowski's inequality states that for $1 \leq p \leq \infty$ and functions $f, g \in L^p(\mathbb{R}^d)$, the norm satisfies

$$\|f + g\|_p \leq \|f\|_p + \|g\|_p, \quad (5.8)$$

ensuring the triangle inequality in L^p .

Hölder's inequality, for $1 \leq p, q \leq \infty$ with $\frac{1}{p} + \frac{1}{q} = 1$, asserts that for $f \in L^p(\mathbb{R}^d)$ and $g \in L^q(\mathbb{R}^d)$,

$$\int |fg| \, d\mu \leq \|f\|_p \|g\|_q. \quad (5.9)$$

Cauchy-Schwarz inequality, a special case of Hölder's inequality, of when $p = q = 2$, yields

$$\int |fg| \, d\mu \leq \left(\int |f|^2 \, d\mu \right)^{1/2} \left(\int |g|^2 \, d\mu \right)^{1/2}. \quad (5.10)$$

Fourier Representation of Function. Let $f \in L^1(\mathbb{R}^d)$, the space of Lebesgue integrable functions. The *Fourier transform* of f is defined as

$$\hat{f}(\zeta) := \int_{\mathbb{R}^d} f(x) e^{-2\pi i \langle \zeta, x \rangle} \, dx, \quad (5.11)$$

where $\zeta \in \mathbb{R}^d$ is the frequency variable. The *inverse Fourier transform* recovers f from its frequency representation when $\hat{f} \in L^1(\mathbb{R}^d)$:

$$f(x) = \int_{\mathbb{R}^d} \hat{f}(\zeta) e^{2\pi i \langle \zeta, x \rangle} d\zeta. \quad (5.12)$$

Parseval's Identity. If additionally $f \in L^1(\mathbb{R}^d) \cap L^2(\mathbb{R}^d)$ (i.e., absolutely integrable and square-integrable with respect to the Lebesgue measure), then $\hat{f} \in L^2(\mathbb{R}^d)$ and Parseval's identity holds:

$$\int_{\mathbb{R}^d} |f(x)|^2 dx = \int_{\mathbb{R}^d} |\hat{f}(\zeta)|^2 d\zeta. \quad (5.13)$$

Directional Fourier Representation. The **Fourier series** of a real-valued, integrable, and periodic function $f : \mathbb{R} \mapsto \mathbb{R}$ with period T , its Fourier series spans a set of **discrete Fourier bases**:

$$f(x) = a_0 + \sum_{n=1}^{\infty} \left(a_n \cos \left(\frac{2\pi n}{T} x \right) + b_n \sin \left(\frac{2\pi n}{T} x \right) \right), \quad (5.14)$$

where the Fourier coefficients are:

$$a_0 = \frac{1}{T} \int_0^T f(x) dx, \quad (5.15)$$

$$a_n = \frac{2}{T} \int_0^T f(x) \cos \left(\frac{2\pi n}{T} x \right) dx, \quad (5.16)$$

$$b_n = \frac{2}{T} \int_0^T f(x) \sin \left(\frac{2\pi n}{T} x \right) dx. \quad (5.17)$$

In contrast, the Fourier representation of a function on \mathbb{R}^d spans an **infinite continuum of frequency components** across \mathbb{R}^d . For visualization and analysis, it is often useful to examine the behavior of the transform along a fixed direction in frequency space, reducing the high-dimensional spectrum to a one-dimensional slice. Let $f \in L^1(\mathbb{R}^d)$ and fix a direction $\zeta_0 \in \mathbb{R}^d$ with $\|\zeta_0\| = 1$. The *directional Fourier transform* of f along ζ_0 is defined for $t \in \mathbb{R}$ as:

$$\hat{f}_{\zeta_0}(t) := \int_{\mathbb{R}^d} f(x) e^{-2\pi i \langle t\zeta_0, x \rangle} dx, \quad (5.18)$$

which equals the restriction of the full Fourier transform \hat{f} to the line $\zeta = t\zeta_0$, i.e., $\hat{f}_{\zeta_0}(t) = \hat{f}(t\zeta_0)$.

It is notable that the directional Fourier transform $\hat{f}_{\zeta_0}(t)$ captures the frequency content of f along a fixed direction ζ_0 , but in general, $f(x)$ cannot be fully recovered from $\hat{f}_{\zeta_0}(t)$ alone. Full reconstruction requires that f be supported on, or constant along, hyperplanes orthogonal to ζ_0 , thereby reducing the problem to a one-dimensional setting.

5.3 Fourier Analysis

This section develops a Fourier representation of the Lipschitz continuity bound, establishing a theoretical framework that expresses the Lipschitz constant as an integral over local spectral contributions. We further demonstrate that the variational mutual information gap resulting from the removal of a frequency component is directly controlled by these spectral terms. Together, these results provide a principled connection between frequency-domain signal propagation and Lipschitz continuity.

5.3.1 Fourier Representation of Lipschitz Continuity Bound

Theorem 5.3.1 (Spectral Bound of Lipschitz Continuity). *Let $f : \mathbb{R}^d \rightarrow \mathbb{R}$ be a differentiable function that is K_f -Lipschitz continuous, with Fourier transform $\hat{f}(\zeta) \in L^1(\mathbb{R}^d)$:*

$$\int_{\mathbb{R}^d} |\hat{f}(\zeta)| d\zeta < \infty, \quad (5.19)$$

the space of Lebesgue absolutely integrable functions. Then the Lipschitz constant of f satisfies:

$$K_f := \sup_{x \in \mathbb{R}^d} \|\nabla f(x)\|_2 \leq \int_{\mathbb{R}^d} 2\pi \|\zeta\|_2 |\hat{f}(\zeta)| d\zeta, \quad (5.20)$$

*where $\zeta \in \mathbb{R}^d$ denotes the frequency variable, and $\|\cdot\|_2$ is the Euclidean norm. Furthermore, define the **spectral Lipschitz contribution** at frequency ζ as:*

$$K_\zeta := 2\pi \|\zeta\|_2 |\hat{f}(\zeta)|. \quad (5.21)$$

Then:

$$K_f \leq \int_{\mathbb{R}^d} K_\zeta d\zeta. \quad (5.22)$$

Proof. Since f is differentiable and $\hat{f} \in L^1(\mathbb{R}^d)$, the Fourier transform of f is defined as:

$$\hat{f}(\zeta) = \int_{\mathbb{R}^d} f(x) e^{-2\pi i \langle \zeta, x \rangle} dx, \quad (5.23)$$

where dx denotes the Lebesgue measure on \mathbb{R}^d , and $\langle \cdot, \cdot \rangle$ is the standard inner product.

By the Fourier inversion theorem (Stein and Shakarchi, 2011), since $\hat{f} \in L^1(\mathbb{R}^d)$, we have:

$$f(x) = \int_{\mathbb{R}^d} \hat{f}(\zeta) e^{2\pi i \langle \zeta, x \rangle} d\zeta, \quad (5.24)$$

where $d\zeta$ is the Lebesgue measure on \mathbb{R}^d .

Since f is differentiable, we compute the gradient by interchanging differentiation and integration, which is justified by the dominated convergence theorem and the integrability of \hat{f} (Rudin, 1987):

$$\begin{aligned} \nabla_x f(x) &= \nabla_x \int_{\mathbb{R}^d} \hat{f}(\zeta) e^{2\pi i \langle \zeta, x \rangle} d\zeta \\ &= \int_{\mathbb{R}^d} \hat{f}(\zeta) \nabla_x \left(e^{2\pi i \langle \zeta, x \rangle} \right) d\zeta \\ &= \int_{\mathbb{R}^d} \hat{f}(\zeta) \cdot 2\pi i \zeta e^{2\pi i \langle \zeta, x \rangle} d\zeta. \end{aligned} \quad (5.25)$$

Thus, the Fourier transform of the gradient is $\widehat{\nabla f}(\zeta) = 2\pi i \zeta \hat{f}(\zeta)$.

To bound the Lipschitz constant, note that since f is differentiable and K_f -Lipschitz:

$$K_f = \sup_{x \in \mathbb{R}^d} \|\nabla_x f(x)\|_2, \quad (5.26)$$

we estimate:

$$\begin{aligned} \|\nabla_x f(x)\|_2 &= \left\| \int_{\mathbb{R}^d} 2\pi i \zeta \hat{f}(\zeta) e^{2\pi i \langle \zeta, x \rangle} d\zeta \right\|_2 \\ &\leq \int_{\mathbb{R}^d} \|2\pi i \zeta \hat{f}(\zeta) e^{2\pi i \langle \zeta, x \rangle}\|_2 d\zeta \\ &= \int_{\mathbb{R}^d} |2\pi i| \|\zeta\|_2 |\hat{f}(\zeta)| \cdot |e^{2\pi i \langle \zeta, x \rangle}| d\zeta \\ &= \int_{\mathbb{R}^d} 2\pi \|\zeta\|_2 |\hat{f}(\zeta)| d\zeta, \end{aligned} \quad (5.27)$$

since $|e^{2\pi i \langle \zeta, x \rangle}| = 1$ and $|i| = 1$. The integral converges because $\hat{f} \in L^1(\mathbb{R}^d)$.

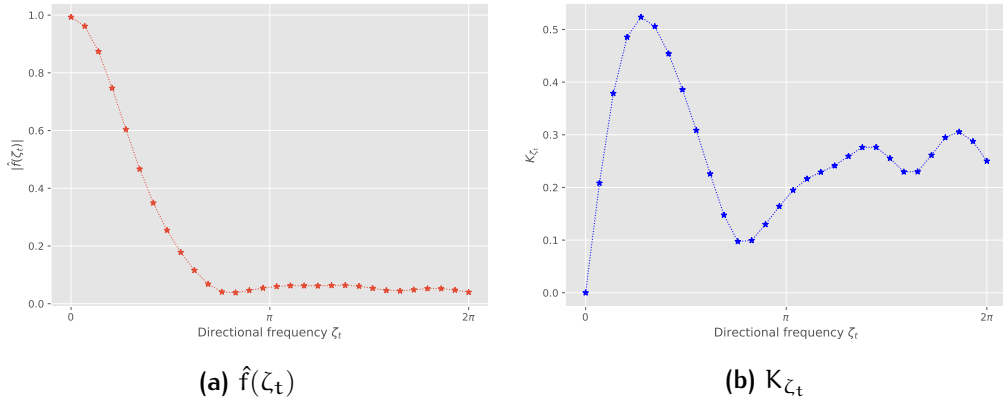


Figure 5.1: Directional frequency analysis of a three-layer MLP (Table 5.1). The directional frequency vector is chosen as the principal direction of the training set. We visualize $|\hat{f}(\zeta_t)|$ and K_{ζ_t} along the principal component direction $\zeta_t := \frac{t}{2\pi} \cdot \zeta$, with $t \in [0, 2\pi]$.

Define the spectral Lipschitz contribution as:

$$K_\zeta = 2\pi \|\zeta\|_2 |\hat{f}(\zeta)|, \quad (5.28)$$

then:

$$K_f = \sup_{x \in \mathbb{R}^d} \|\nabla_x f(x)\|_2 \leq \int_{\mathbb{R}^d} K_\zeta d\zeta. \quad (5.29)$$

□

5.3.1.1 Experiment of Directional Frequency Response

Figure 5.1 presents results from an experiment using a three-layer MLP trained on MNIST. The $f(x) : x \rightarrow [0, 1]$ is defined as the predicted probability for the true label. The \hat{f} is normalized by $1/N$ where N is the number of samples. We visualize $|\hat{f}(\zeta_t)|$ and the corresponding spectral Lipschitz contribution K_{ζ_t} along a chosen frequency direction of the form $\zeta_t := \frac{t}{2\pi} \zeta$, where ζ is the principal component direction of the training data. Frequency t is normalized over the interval $[0, 2\pi]$, enabling a directional analysis of the learned function's frequency response and its contribution to the Lipschitz bound. The MLP model, detailed in Table 5.1, is trained for 10 epochs using the Adam optimizer with a learning rate of 0.001.

Function Block	Layer #	Module
Input Layer	1	nn.Linear(768, 200)
	2	nn.ReLU()
Hidden Layer #1	3	nn.Linear(200, 200)
	4	nn.ReLU()
Output Layer	5	nn.Linear(200, 10)
	6	nn.LogSoftmax(dim=1)

Table 5.1: MLP configuration used in the directional frequency response experiment.

Remark 5.3.2. The term $|\hat{f}(\zeta)|$ represents the amplitude of f at frequency ζ in the frequency domain. This theorem implies that the Lipschitz constant K_f is controlled by the weighted contribution of all frequencies, with higher frequencies (large $\|\zeta\|_2$) amplifying the effect of $|\hat{f}(\zeta)|$. For neural networks modeled by f , large $|\hat{f}(\zeta)|$ at high frequencies indicates sensitivity to rapid changes, leading to a larger K_f and potentially less robust behavior.

5.3.1.2 Numerical Validation – Synthesized Function

We now demonstrate the validity of Theorem 5.3.1 using synthesized functions, as illustrated in Figure 5.2. Specifically, we construct a *multi-sine* function defined as:

$$f(x) = \sum_{n=1}^N a_n \sin(2\pi\omega_n x), \quad (5.30)$$

where $N = 10$, $x \in [-5, 5]$ is sampled at 50,000 evenly spaced points, and the amplitudes a_n and frequencies ω_n are independently drawn from uniform distributions: $a_n \sim \mathcal{U}[0.1, 1]$ and $\omega_n \sim \mathcal{U}[0.1, 5]$. The corresponding Fourier transform of this function admits:

$$\hat{f}(\zeta) = \sum_{n=1}^N \frac{a_n}{2i} [\delta(\zeta - \omega_n) - \delta(\zeta + \omega_n)], \quad (5.31)$$

where $\delta(\cdot)$ represents the Dirac delta distribution.

Using Theorem 5.3.1, we compute the theoretical spectral bound of the Lipschitz constant of f across three independent trials with random seeds 1, 2, and 3, respectively. The results consistently confirm that the theorem accurately bounds the Lipschitz continuity of the synthesized function.

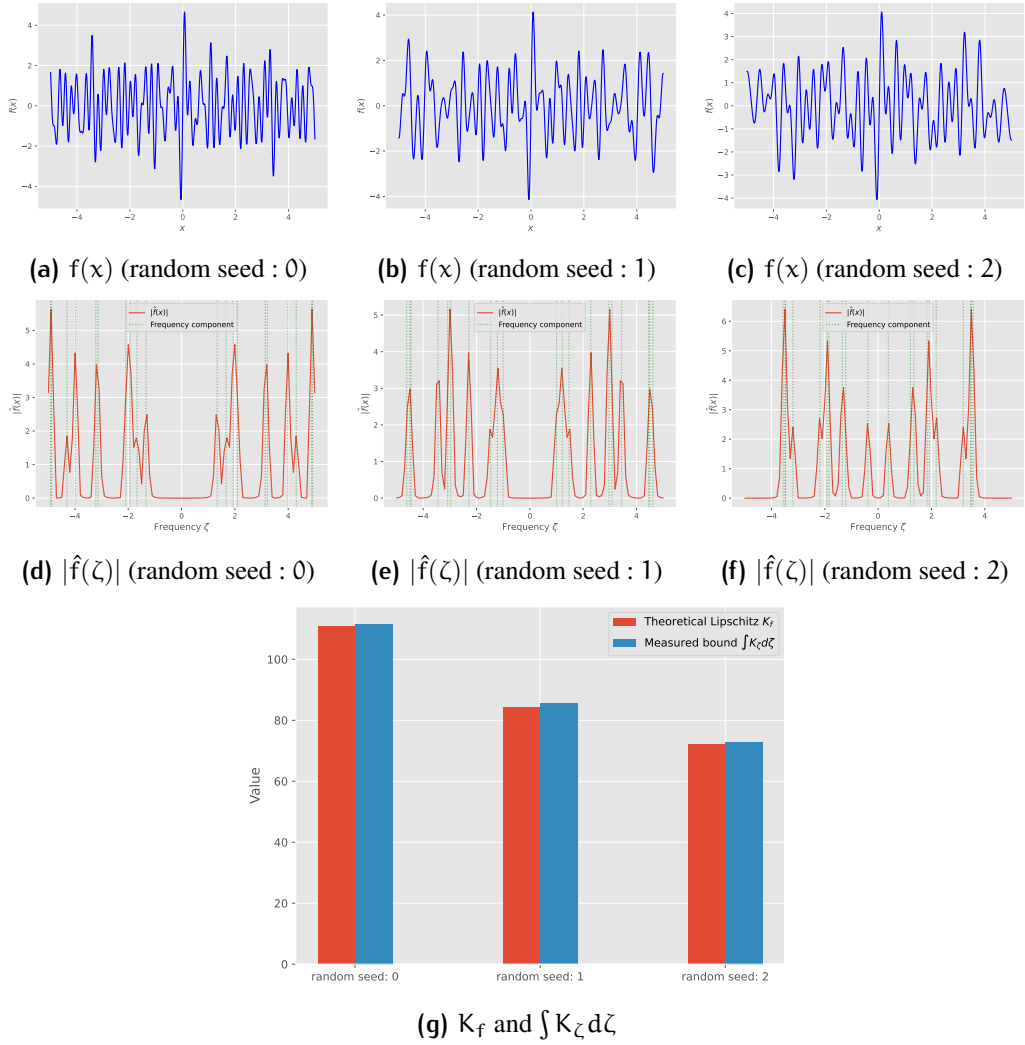


Figure 5.2: Spectral bound of Lipschitz continuity with synthesized functions. (a)–(c): Three functions $f(x)$ generated using different random seeds, each as a sum of sinusoidal components with randomly sampled frequencies and amplitudes. (d)–(f): Fourier transforms $\hat{f}(\zeta)$ of $f(x)$. (g): Comparison between the theoretical Lipschitz constant $K_f = \sup_x \|\nabla f(x)\|_2$ and the theoretical spectral bound $\int K_\zeta d\zeta$ computed using Theorem 5.3.1. The close agreement across trials numerically validates the proposed spectral decomposition of Lipschitz continuity bound.

5.3.1.3 Numerical Validation – Well-Defined Example

We now show that Theorem 5.3.1 holds true with a well-defined example.

Proposition 5.3.3. Suppose $f : \mathbb{R}^2 \rightarrow \mathbb{R}$ is given by:

$$f(x) = e^{-\alpha(x_1^2 + x_2^2)}, \quad (5.32)$$

where $a > 0$. Then f is smooth and globally defined. The $f(x) = e^{-a(x_1^2 + x_2^2)}$ has a Lipschitz constant:

$$K_f = \sqrt{\frac{2a}{e}}, \quad (5.33)$$

spectral Lipschitz contribution:

$$K_\zeta = \frac{2\pi^2}{a} \|\zeta\|_2 e^{-\frac{\pi^2}{a} \|\zeta\|_2^2}, \quad (5.34)$$

and spectral bound:

$$\int K_\zeta = \int_{\mathbb{R}^2} K_\zeta d\zeta = \sqrt{a}. \quad (5.35)$$

Proof. True Lipschitz constant. Set $r = \sqrt{x_1^2 + x_2^2}$. The gradient is:

$$\nabla f(x) = \begin{bmatrix} -2ax_1 e^{-ar^2} \\ -2ax_2 e^{-ar^2} \end{bmatrix} \quad (5.36)$$

and its norm is:

$$g(r) := \|\nabla f(x)\|_2 = 2ae^{-ar^2}. \quad (5.37)$$

Maximizing $g(r)$ over $r \geq 0$, we find:

$$g'(r) = 2ae^{-ar^2}(1 - 2ar^2) = 0 \quad \Rightarrow \quad r = \frac{1}{\sqrt{2a}}. \quad (5.38)$$

Hence,

$$K_f := \sup_x \|\nabla f(x)\|_2 = g\left(\frac{1}{\sqrt{2a}}\right) = \sqrt{\frac{2a}{e}}. \quad (5.39)$$

Derive Fourier transform. The Fourier transform is:

$$\hat{f}(\zeta) = \int_{\mathbb{R}^2} e^{-a(x_1^2 + x_2^2)} e^{-2\pi i(\zeta_1 x_1 + \zeta_2 x_2)} dx_1 dx_2 = \left(\int_{-\infty}^{\infty} e^{-ax_1^2 - 2\pi i \zeta_1 x_1} dx_1 \right)^2. \quad (5.40)$$

Note the square:

$$-ax_1^2 - 2\pi i \zeta_1 x_1 = -a \left(x_1 + \frac{\pi i \zeta_1}{a} \right)^2 + \frac{\pi^2 \zeta_1^2}{a}, \quad (5.41)$$

$$\int_{-\infty}^{\infty} e^{-a(x_1 + \frac{\pi i \zeta_1}{a})^2 + \frac{\pi^2 \zeta_1^2}{a}} dx_1 = e^{-\frac{\pi^2 \zeta_1^2}{a}} \sqrt{\frac{\pi}{a}}, \quad (5.42)$$

$$\hat{f}(\zeta) = \frac{\pi}{a} e^{-\frac{\pi^2(\zeta_1^2 + \zeta_2^2)}{a}}. \quad (5.43)$$

Verify that $\hat{f} \in L^1(\mathbb{R}^2)$ is absolute integrable with respect to Lebesgue measure:

$$\int_{\mathbb{R}^2} |\hat{f}(\zeta)| d\zeta = \int_{\mathbb{R}^2} \frac{\pi}{a} e^{-\frac{\pi^2(\zeta_1^2 + \zeta_2^2)}{a}} d\zeta = 1 < \infty. \quad (5.44)$$

Spectral bound. By Theorem 5.3.1, define the point-wise spectral contribution:

$$K_\zeta = 2\pi \|\zeta\|_2 |\hat{f}(\zeta)| = \frac{2\pi^2}{a} \|\zeta\|_2 e^{-\frac{\pi^2}{a} \|\zeta\|_2^2}. \quad (5.45)$$

Applying polar coordinates in frequency-domain \mathbb{R}^2 :

$$\begin{cases} \zeta_1 = r \cos \theta \\ \zeta_2 = r \sin \theta \end{cases}, \quad (5.46)$$

hence:

$$\int_{\mathbb{R}^2} K_\zeta d\zeta = \int_0^{2\pi} \int_0^\infty \frac{2\pi^2}{a} r \cdot r e^{-\frac{\pi^2}{a} r^2} dr d\theta = \frac{2\pi^2}{a} \cdot 2\pi \int_0^\infty r^2 e^{-\frac{\pi^2}{a} r^2} dr. \quad (5.47)$$

Use the standard integral:

$$\int_0^\infty r^2 e^{-cr^2} dr = \frac{1}{2} \cdot \frac{\sqrt{\pi}}{2c^{3/2}} = \frac{\sqrt{\pi}}{4c^{3/2}}. \quad (5.48)$$

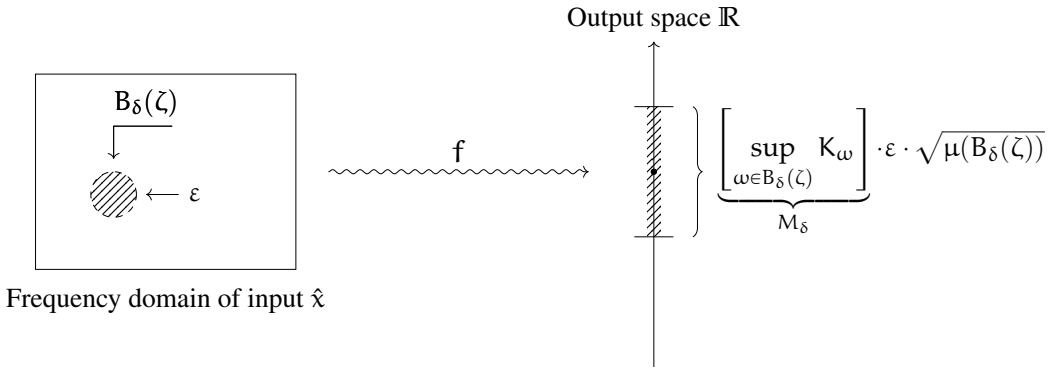


Figure 5.3: Lemma 5.3.4: **Spectral-Band Perturbation Bound** states that the output change due to a perturbation at a frequency point ζ , within the ball $B_\delta(\zeta)$ of energy ϵ in the frequency domain of the input space, is proportionally bounded above by the supremum M_δ of the spectral Lipschitz contribution at that frequency ball.

Apply with $c = \frac{\pi^2}{a}$:

$$\int_0^\infty r^2 e^{-\frac{\pi^2}{a} r^2} dr = \frac{\sqrt{\pi}}{4} \left(\frac{a}{\pi^2} \right)^{3/2}. \quad (5.49)$$

Therefore:

$$\int_{\mathbb{R}^2} K_\zeta d\zeta = \frac{2\pi^2}{a} \cdot 2\pi \cdot \frac{\sqrt{\pi}}{4} \left(\frac{a}{\pi^2} \right)^{3/2} = \sqrt{\pi a}. \quad (5.50)$$

Results. We compare K_f with its spectral bound:

$$K_f = \sqrt{\frac{2a}{e}} \leq \sqrt{\pi a} \iff \frac{2}{\pi e} \leq 1, \quad (5.51)$$

which always holds. Hence, the spectral Lipschitz bound

$$K_f \leq \int_{\mathbb{R}^2} K_\zeta d\zeta \quad (5.52)$$

is valid for all $a > 0$.

□

5.3.2 Small Frequency Perturbation in Input Spaces

Lemma 5.3.4 (Spectral-Band Perturbation Bound). *Let $f : \mathbb{R}^d \rightarrow \mathbb{R}$ be a continuously differentiable function with Fourier transform $\hat{f} \in L^1(\mathbb{R}^d) \cap L^2(\mathbb{R}^d)$, and assume*

$$\int_{\mathbb{R}^d} 2\pi\|\omega\| \cdot |\hat{f}(\omega)| d\omega < \infty. \quad (5.53)$$

Fix $\zeta \in \mathbb{R}^d$ and $\delta > 0$, and define the frequency ball $B_\delta(\zeta) := \{\omega \in \mathbb{R}^d : \|\omega - \zeta\| \leq \delta\}$. Let $x^{(-\zeta)}$ be the signal obtained by removing the frequency ball $B_\delta(\zeta)$ from the Fourier transform of x , and define

$$\Delta x := x - x^{(-\zeta)}, \quad \|\Delta x\|_2 = \varepsilon. \quad (5.54)$$

Define the local spectral Lipschitz bound

$$M_\delta := \sup_{\omega \in B_\delta(\zeta)} 2\pi\|\omega\| \cdot |\hat{f}(\omega)|, \quad (5.55)$$

and let $\mu(B_\delta(\zeta))$ denote the Lebesgue measure of the frequency ball.

Then the output perturbation satisfies

$$\sup_x |f(x) - f(x^{(-\zeta)})| \lesssim M_\delta \cdot \varepsilon \cdot \sqrt{\mu(B_\delta(\zeta))}. \quad (5.56)$$

Proof. By the Fourier inversion formula,

$$f(x) = \int_{\mathbb{R}^d} \hat{f}(\omega) e^{2\pi i \langle \omega, x \rangle} d\omega. \quad (5.57)$$

Differentiating under the integral gives

$$\nabla f(x) = \int_{\mathbb{R}^d} 2\pi i \omega \hat{f}(\omega) e^{2\pi i \langle \omega, x \rangle} d\omega, \quad (5.58)$$

so the Fourier transform of ∇f is

$$\widehat{\nabla f}(\omega) = 2\pi i \omega \hat{f}(\omega), \quad \|\widehat{\nabla f}(\omega)\| = 2\pi\|\omega\| \cdot |\hat{f}(\omega)|. \quad (5.59)$$

By a Taylor expansion,

$$f(x) = f(x^{(-\zeta)}) + \langle \nabla f(\tilde{x}), \Delta x \rangle + o(\|\Delta x\|_2^2), \quad (5.60)$$

for some \tilde{x} on the line segment between x and $x^{(-\zeta)}$.

By Parseval's identity (Stein and Shakarchi, 2011), the inner product is preserved in frequency domain:

$$\langle \nabla f(\tilde{x}), \Delta x \rangle = \int_{\mathbb{R}^d} \langle \widehat{\nabla f}(\omega)^*, \widehat{\Delta x}(\omega) \rangle d\omega. \quad (5.61)$$

Since $\widehat{\Delta x}$ is supported on $B_\delta(\zeta)$, applying Hölder's inequality, the integral reduces to

$$|\langle \nabla f(\tilde{x}), \Delta x \rangle| = \left| \int_{\mathbb{R}^d} \langle \widehat{\nabla f}(\omega)^*, \widehat{\Delta x}(\omega) \rangle d\omega \right| \leq \int_{B_\delta(\zeta)} \|\widehat{\nabla f}(\omega)\|_2 \cdot \|\widehat{\Delta x}(\omega)\|_2 d\omega. \quad (5.62)$$

Using Cauchy–Schwarz:

$$\int_{B_\delta(\zeta)} |\widehat{\Delta x}(\omega)| d\omega \leq \|\widehat{\Delta x}\|_2 \cdot \sqrt{\mu(B_\delta(\zeta))} = \varepsilon \cdot \sqrt{\mu(B_\delta(\zeta))}. \quad (5.63)$$

Therefore,

$$|f(x) - f(x^{(-\zeta)})| \lesssim M_\delta \cdot \varepsilon \cdot \sqrt{\mu(B_\delta(\zeta))}, \quad (5.64)$$

uniformly in x , as claimed. \square

Remark 5.3.5. An illustration is provided in Figure 5.3. This result establishes a connection between input-space frequency perturbation at frequency ζ and the Fourier representation of the function f at the same frequency. It highlights how localized spectral properties of f govern its sensitivity to frequency-specific perturbations in the input.

5.3.2.1 Numerical Validation – Well-Defined Example

To verify Lemma 5.3.4, we use the function $f(x) = e^{-\alpha(x_1^2 + x_2^2)}$, where $\alpha > 0$, defined on \mathbb{R}^2 . We first compute the direct perturbation supremum $\sup_x |f(x) - f(x^{(-\zeta)})|$, where $x^{(-\zeta)}$ is the signal with frequencies in the ball $B_\delta(\zeta) = \{\omega \in \mathbb{R}^2 : \|\omega - \zeta\|_2 \leq \delta\}$ removed, and $\|\Delta x\|_2 = \|x - x^{(-\zeta)}\|_2 = \varepsilon$. We then compute the theoretical bound $M_\delta \cdot \varepsilon \cdot \sqrt{\mu(B_\delta(\zeta))}$, where $M_\delta = \sup_{\omega \in B_\delta(\zeta)} 2\pi\|\omega\|_2 \cdot |\hat{f}(\omega)|$, and compare to confirm the lemma holds.

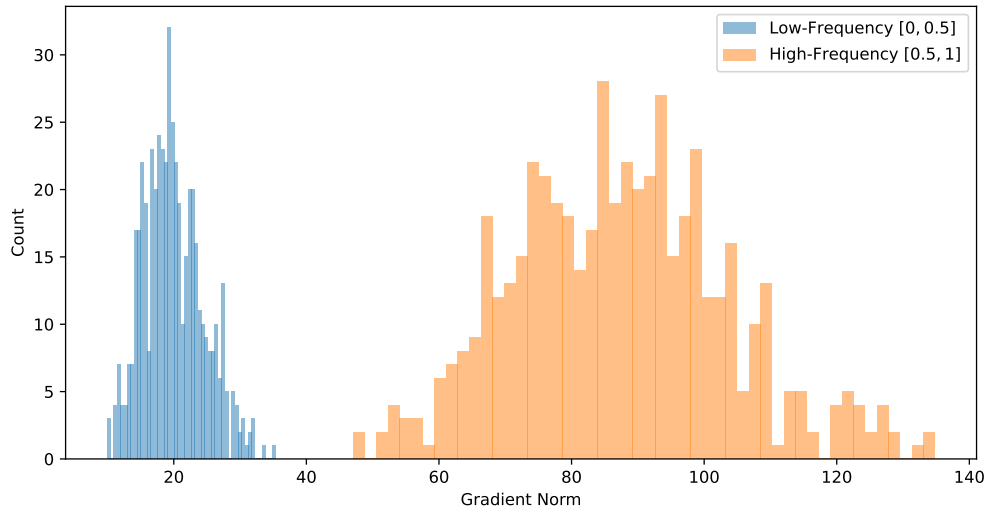


Figure 5.4: We train a ConvNet (see Table 5.2) on three versions of the CIFAR-10 dataset. The low-frequency dataset is obtained by applying a low-pass filter with cutoff frequency 0.5, while the high-frequency dataset is obtained using a high-pass filter with the same cutoff. The ConvNet is trained separately on each dataset. We then compute and visualize the ℓ_2 norms of the input gradients. Theoretically, larger gradient norms correspond to larger Lipschitz constants. The results show that models trained on higher-frequency data tend to exhibit larger Lipschitz constants.

Function perturbation supremum. Use the Fourier representation of $f(x)$:

$$f(x) - f(x^{(-\zeta)}) = \int_{B_\delta(\zeta)} \hat{f}(\omega) \left(e^{2\pi i \langle \omega, x \rangle} - e^{2\pi i \langle \omega, x^{(-\zeta)} \rangle} \right) d\omega \quad (5.65)$$

$$= \int_{B_\delta(\zeta)} \hat{f}(\omega) \left(e^{2\pi i \langle \omega, x \rangle} - e^{2\pi i \langle \omega, x - \Delta x \rangle} \right) d\omega \quad (5.66)$$

$$= \int_{B_\delta(\zeta)} \hat{f}(\omega) e^{2\pi i \langle \omega, x \rangle} \left(1 - e^{2\pi i \langle \omega, -\Delta x \rangle} \right) d\omega \quad (5.67)$$

$$= \int_{B_\delta(\zeta)} \hat{f}(\omega) e^{2\pi i \langle \omega, x \rangle} \left(1 - e^{-2\pi i \langle \omega, \Delta x \rangle} \right) d\omega. \quad (5.68)$$

Suppose $\|\Delta x\|_2$ is a small perturbation:

$$\langle \omega, \Delta x \rangle \rightarrow 0, \quad (5.69)$$

then:

$$\left| 1 - e^{-2\pi i \langle \omega, \Delta x \rangle} \right| = |1 - \cos(-2\pi \langle \omega, \Delta x \rangle) - i \sin(-2\pi \langle \omega, \Delta x \rangle)| \quad (5.70)$$

$$\approx |\sin(-2\pi \langle \omega, \Delta x \rangle)| \quad (5.71)$$

$$\approx 2\pi \|\omega\|_2 \varepsilon. \quad (5.72)$$

Since:

$$\hat{f}(\omega) = \frac{\pi}{a} e^{-\frac{\pi^2}{a} \|\omega\|_2^2}, \quad (5.73)$$

hence:

$$|f(x) - f(x^{(-\zeta)})| \leq \frac{2\pi^2 \varepsilon}{a} \int_{B_\delta(\zeta)} \|\omega\|_2 e^{-\frac{\pi^2}{a} \|\omega\|_2^2} d\omega. \quad (5.74)$$

For small δ , $\|\omega\|_2 \approx \|\zeta\|_2$, so:

$$\sup_x |f(x) - f(x^{(-\zeta)})| \approx \frac{2\pi^2 \varepsilon}{a} \|\zeta\|_2 e^{-\frac{\pi^2}{a} \|\zeta\|_2^2} \cdot \pi \delta^2 = \frac{2\pi^3 \delta^2 \varepsilon}{a} \|\zeta\|_2 e^{-\frac{\pi^2}{a} \|\zeta\|_2^2}. \quad (5.75)$$

Theoretical bound. The bound is:

$$M_\delta \cdot \varepsilon \cdot \sqrt{\mu(B_\delta(\zeta))}, \quad (5.76)$$

where:

$$M_\delta = \sup_{\omega \in B_\delta(\zeta)} \frac{2\pi^2}{a} \|\omega\|_2 e^{-\frac{\pi^2}{a} \|\omega\|_2^2}, \quad \mu(B_\delta(\zeta)) = \pi \delta^2. \quad (5.77)$$

For small δ , $M_\delta \approx \frac{2\pi^2}{a} \|\zeta\|_2 e^{-\frac{\pi^2}{a} \|\zeta\|_2^2}$, and $\sqrt{\mu(B_\delta(\zeta))} = \sqrt{\pi} \delta$. Thus:

$$M_\delta \cdot \varepsilon \cdot \sqrt{\mu(B_\delta(\zeta))} \approx \frac{2\pi^2}{a} \|\zeta\|_2 e^{-\frac{\pi^2}{a} \|\zeta\|_2^2} \cdot \varepsilon \cdot \sqrt{\pi} \delta = \frac{2\pi^{5/2} \delta \varepsilon}{a} \|\zeta\|_2 e^{-\frac{\pi^2}{a} \|\zeta\|_2^2}. \quad (5.78)$$

Comparison. Compare:

$$\frac{\sup_x |f(x) - f(x^{(-\zeta)})|}{M_\delta \cdot \varepsilon \cdot \sqrt{\mu(B_\delta(\zeta))}} \approx \frac{\frac{2\pi^3 \delta^2 \varepsilon}{a} \|\zeta\|_2 e^{-\frac{\pi^2}{a} \|\zeta\|_2^2}}{\frac{2\pi^{5/2} \delta \varepsilon}{a} \|\zeta\|_2 e^{-\frac{\pi^2}{a} \|\zeta\|_2^2}} = \frac{\pi^3 \delta^2}{\pi^{5/2} \delta} = \sqrt{\pi} \delta \leq 1, \quad (5.79)$$

subject to:

$$\sqrt{\pi} \delta < 1 \iff \delta < \frac{1}{\sqrt{\pi}} \approx 0.56418 \dots . \quad (5.80)$$

This shows that the Lemma 5.3.4 holds true if the frequency perturbation band is sufficiently small.

5.3.3 Variational Mutual Information Gap in Image Classifiers

Corollary 5.3.6 (Spectral Lipschitz Contribution Bounds Variational Mutual Information Gap). *Let (X, Y) be a classification dataset with a joint distribution $P_{X,Y}$. Let $P(Y)$ be the prior distribution of labels. Let $Q(y|x) : x \mapsto [0, 1]$ be a probabilistic classifier. Let $Y = \{1, \dots, k\}$ be the label set. The variational mutual information of the classifier is defined as:*

$$I(Q(y|x); Y) = \mathbb{E}_{x,y} \left[\log \frac{Q(y|x)}{P(y)} \right] \quad (5.81)$$

where $(x, y) \sim P_{X,Y}$ sampled the dataset $P_{X,Y}$.

The absolute variational mutual information gap ΔI_ζ perturbed by removing frequency ζ is approximately bounded above by:

$$|\Delta I_\zeta| := \left| I(Q(y|x); Y) - I(Q(y|x^{(-\zeta)}); Y) \right| \lesssim M_\delta \cdot \varepsilon \cdot \sqrt{\mu(B_\delta(\zeta))}, \quad (5.82)$$

where ε is the perturbed magnitude and $B_\delta(\zeta)$ is a frequency ball.

Proof. By definition:

$$|\Delta I_\zeta| = \left| \mathbb{E}_{x,y} \left[\log \frac{Q(y|x)}{Q(y|x^{(-\zeta)})} + \log \frac{P(y)}{P(y)} \right] \right| \quad (5.83)$$

$$\leq \mathbb{E}_{x,y} \left[\left| \log \frac{Q(y|x)}{Q(y|x^{(-\zeta)})} + \log \frac{P(y)}{P(y)} \right| \right] \quad (5.84)$$

$$= \mathbb{E}_{x,y} \left[\left| \log Q(y|x) - \log Q(y|x^{(-\zeta)}) \right| \right]. \quad (5.85)$$

Set:

$$f(x) = \log Q(y|x) \quad \text{and} \quad f(x^{(-\zeta)}) = \log Q(y|x^{(-\zeta)}), \quad (5.86)$$

then use Lemma 5.3.4:

$$|\Delta I_\zeta| = \mathbb{E}_{x,y} \left[\left| f(x) - f(x^{(-\zeta)}) \right| \right] \quad (5.87)$$

$$\leq \sup_{x,y} \left| f(x) - f(x^{(-\zeta)}) \right| \quad (5.88)$$

$$\leq M_\delta \cdot \varepsilon \cdot \sqrt{\mu(B_\delta(\zeta))} + o(\varepsilon^2) \quad (5.89)$$

$$\lesssim M_\delta \cdot \varepsilon \cdot \sqrt{\mu(B_\delta(\zeta))}. \quad (5.90)$$

□

Remark 5.3.7. This result shows that the variational mutual information perturbation due to frequency perturbation is bounded below locally by $2\pi\varepsilon \cdot \|\zeta\| \cdot |\hat{f}(\zeta)|$ and proportional to frequency 2-norm.

5.4 Empirical Study

Experimental Setting. We use a convolutional neural network (ConvNet), shown in Table 5.2, consisting of three convolutional layers, followed by an adaptive average pooling layer and two fully connected layers serving as the classifier. We construct frequency CIFAR10 datasets by applying a low-passing filters, varying the cutoff frequencies from 0.1 to 1.0 with step size 0.1. For reproducibility, we fix random seeds to 42. We use learning rate 0.001, batch size 128 and SGD optimizer.

Function Block	# of Layer	Module
Block #1	1	<code>nn.Conv2d(3, 64, kernel_size=3, stride=2)</code>
	2	<code>nn.ReLU()</code>
Block #2	3	<code>nn.Conv2d(64, 128, kernel_size=3, stride=2)</code>
	4	<code>nn.ReLU()</code>
Block #3	5	<code>nn.Conv2d(128, 256, kernel_size=3, stride=2)</code>
	6	<code>nn.ReLU()</code>
	7	<code>nn.AdaptiveAvgPool2d(output_size = 1)</code>
Classifier	8	<code>nn.Linear(256, 100)</code>
	9	<code>nn.ReLU()</code>
	10	<code>nn.Linear(100, 10)</code>

Table 5.2: ConvNet configuration for the experiments exploring the connection between frequency signal propagation and Lipschitz continuity.

5.4.1 Role of High-Frequency Components

Theorem 5.3.1 states that the spectral Lipschitz contribution K_ζ at frequency ζ is: contribution term:

$$K_\zeta = 2\pi \cdot \|\zeta\| \cdot |\hat{f}(\zeta)|. \quad (5.91)$$

This implies that if a network f is sensitive to high-frequency components — *i.e.*, $|\hat{f}(\zeta)|$ is large for large $\|\zeta\|$ — then these components contribute more strongly to the overall

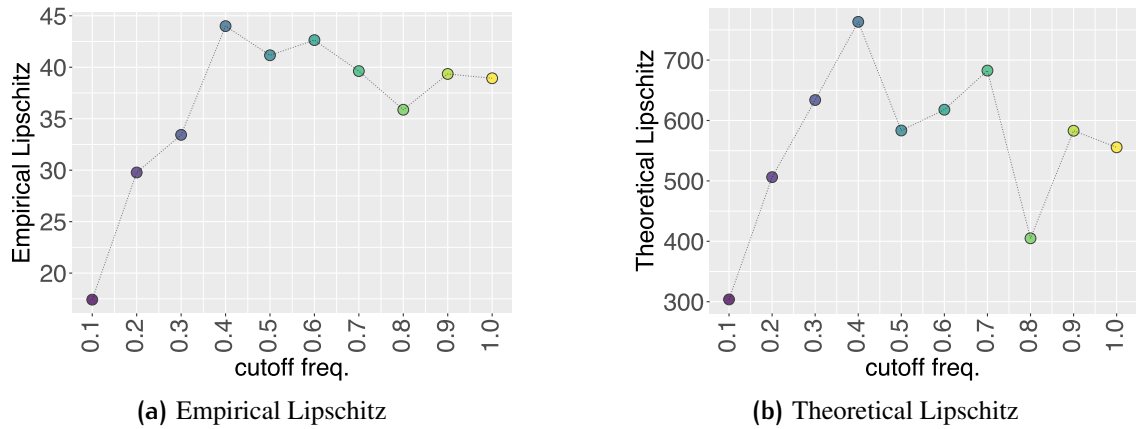


Figure 5.5: Empirical and theoretical Lipschitz constants with respect to frequency signals in training data. The results show that models trained on datasets with stronger high-frequency components associate with larger Lipschitz constants.

Lipschitz constant K_f . The frequency 2-norm $\|\zeta\|$ further amplifies the contribution term. This impacts neural network training, as shown in Figure 5.4, where a network trained on a low-frequency-only dataset displays lower gradient norms, while one trained on a high-frequency-only dataset exhibits higher gradient norms.

To comprehensively study the impact of high-frequency components on Lipschitz continuity, we conduct experiments in which a low-pass frequency-domain filter is applied to the CIFAR-10 dataset. We vary the normalized cutoff frequency from 0.1 to 1.0 in increments of 0.1, producing a series of progressively low-pass filtered datasets. For each filtered dataset, we train a ConvNet (see Table 5.2).

Figure 5.5 reports both the empirical Lipschitz constants and the corresponding theoretical upper bounds. The empirical Lipschitz constant is estimated as

$$\max_{x \in \hat{X}} \|\nabla f(x)\|_2, \quad (5.92)$$

using a validation set \hat{X} containing 500 samples. The theoretical upper bound is computed as

$$\prod_{\ell=1}^L \sigma_1^{(\ell)}, \quad (5.93)$$

where $\sigma_1^{(\ell)}$ denotes the largest singular value of the weight matrix in the ℓ -th layer. The results show a clear correlation: models trained on datasets with stronger high-frequency components associate with larger Lipschitz constants.

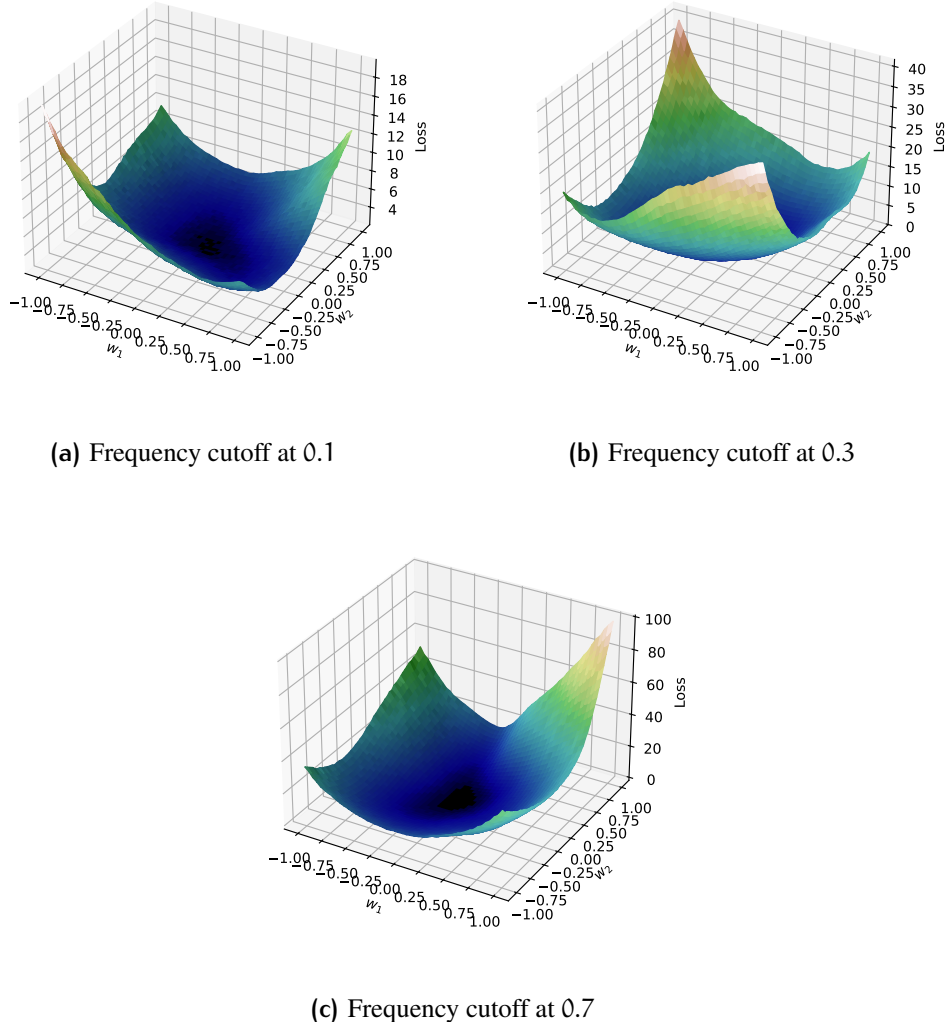


Figure 5.6: Frequency Signals in Training Data Shape Loss Landscape Flatness of a ConvNet on CIFAR-10 (Table 5.2). Training with high-frequency signals not only increases the Lipschitz constant but also sharpens the loss landscape. The cutoff frequencies are normalized into $[0, 1]$.

Remark 5.4.1. The actual Lipschitz constant K lies between the empirical Lipschitz constant:

$$\max_{x \in \hat{X}} \|\nabla f(x)\|_2, \quad (5.94)$$

and the upper bound:

$$\prod_{\ell=1}^L \sigma_1^{(\ell)}, \quad (5.95)$$

such that:

$$\max_{x \in \hat{X}} \|\nabla f(x)\|_2 \leq K \leq \prod_{\ell=1}^L \sigma_1^{(\ell)}. \quad (5.96)$$

Figure 5.5 shows a correlation between the empirical Lipschitz constant and the upper bound.

5.4.2 Flatness of Loss Landscape

High-frequency components affect not only the Lipschitz constant but also the geometric properties of the loss landscape. As shown in Figure 5.6, networks trained on data with stronger high-frequency components tend to exhibit sharper loss landscapes, while those trained on data with weaker high-frequency content result in smoother, flatter landscapes.

5.5 Conclusions

This work establishes a theoretical and empirical connection between Lipschitz continuity and the frequency structure of data in neural networks. We introduced a spectral decomposition of the Lipschitz constant, showing that it can be expressed as an integral over frequency-local contributions. We further demonstrated that the impact of frequency perturbations on mutual information is bounded by these local spectral Lipschitz coefficients, linking spectral sensitivity to robustness. Empirically, we showed that networks trained on high-frequency data tend to exhibit larger Lipschitz constants and sharper loss landscapes. Lipschitz constants directly quantify how strongly a model amplifies input perturbations; consequently, larger Lipschitz constants are associated with reduced robustness and weaker generalization. In contrast, low-frequency training data lead to smoother models with better stability. Together, our results offer a unified spectral perspective on how frequency content shapes learning dynamics and model robustness, providing both theoretical insight and practical guidance for frequency-aware model design.

6

INTERPRETING GLOBAL ROBUSTNESS

Copyright Disclaimer. This chapter includes content adapted from the following article:

1. **Róisín Luo**, J. McDermott, and C. O’Riordan. **Interpreting Global Perturbation Robustness of Image Models using Axiomatic Spectral Importance Decomposition**. *Transactions on Machine Learning Research (TMLR)*, 2024b. ISSN 2835-8856. URL <https://arxiv.org/abs/2408.01139>. Presented at The Thirteenth International Conference on Learning Representations (ICLR 2025), Singapore

Portions of the content are reused verbatim or with minor edits, in accordance with institutional guidelines and the policies of the relevant publishers. Permission from all co-authors has been obtained.

Guiding Research Question. This chapter addresses the secondary research question — **(SRQ6) Interpreting Global Robustness**, in service of the primary research question — **(RQ3) Modulation of Frequency Signal Propagation**. Building on the theoretical analysis and empirical study from the previous chapter, it presents a method for interpreting the global robustness of image models to input perturbations. The results further support and extend the theoretical and empirical insights established in the previous chapter.

Reproducibility. https://anonymous.4open.science/r/lipschitz_dynamics_reproducibility-4721

ABSTRACT

Perturbation robustness evaluates the vulnerabilities of models, arising from a variety of perturbations, such as data corruptions and adversarial attacks. Understanding the mechanisms of perturbation robustness is critical for global interpretability. We present a model-agnostic, global mechanistic interpretability method to interpret the perturbation robustness of image models. This research is motivated by two key aspects.

First, previous global interpretability works, in tandem with robustness benchmarks, *e.g.* mean corruption error (mCE), are not designed to directly interpret the mechanisms of perturbation robustness within image models. Second, we notice that the spectral signal-to-noise ratios (SNR) of perturbed natural images exponentially decay over the frequency. This power-law-like decay implies that: Low-frequency signals are generally more robust than high-frequency signals — yet high classification accuracy can not be achieved by low-frequency signals alone. By applying Shapley value theory, our method axiomatically quantifies the predictive powers of robust features and non-robust features within an information theory framework. Our method, dubbed as **I-ASIDE** (**I**mage **A**xiomatic **S**pectral **I**mportance **D**ecomposition **E**xplanation), provides a unique insight into model robustness mechanisms. We conduct extensive experiments over a variety of vision models pre-trained on ImageNet, including both convolutional neural networks (*e.g.* *AlexNet*, *VGG*, *GoogLeNet/Inception-v1*, *Inception-v3*, *ResNet*, *SqueezeNet*, *RegNet*, *MnasNet*, *MobileNet*, *EfficientNet*, etc.) and vision transformers (*e.g.* *ViT*, *Swin Transformer*, and *MaxViT*), to show that **I-ASIDE** can not only **measure** the perturbation robustness but also **provide interpretations** of its mechanisms.

6.1 Introduction

IMAGE modeling with deep neural networks has achieved great success (Li et al., 2021). Yet, deep neural networks are known to be vulnerable to perturbations. For example, the perturbations may arise from corruptions and adversarial attacks (Goodfellow et al., 2015; Hendrycks and Dietterich, 2019; Szegedy et al., 2014), etc. Perturbation robustness, henceforth referred to as robustness, characterizes a crucial intrinsic property of models (Hendrycks and Dietterich, 2019; Bai et al., 2021; Goodfellow et al., 2015).

Robustness mechanisms refer to the mechanisms which lead to robustness in models. The study of robustness mechanisms aims to answer the question ‘**why some models are more robust than others**’ (Bereska and Gavves, 2024). The causes within this question can arise from multifarious aspects, including architecture designs (Zhou et al., 2022), data annotations, training methods (Pang et al., 2021), inferences, etc. For example, noisy labels can arise from data annotations (Frenay and Verleysen, 2014; Natarajan et al., 2013);

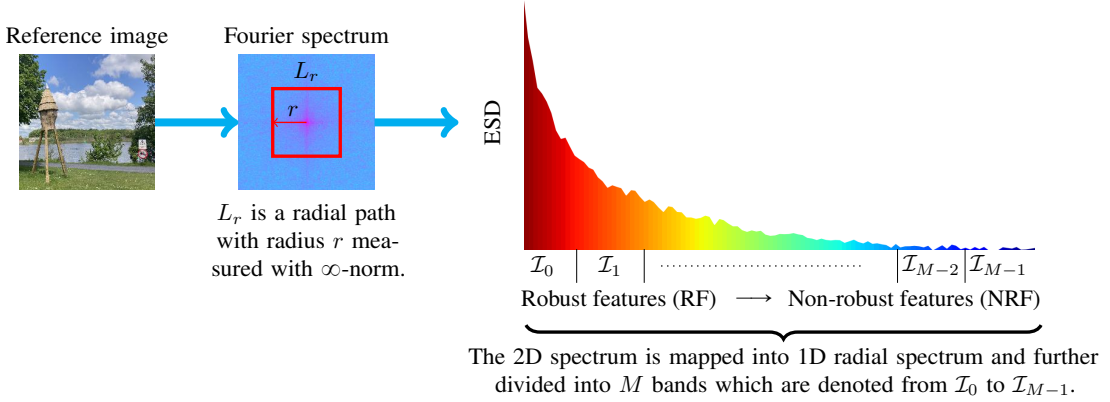


Figure 6.1: Power-law-like energy spectral density (ESD) distribution of natural images over the frequency. The signal spectrum is divided into M bands (from I_0 to I_{M-1}). Each spectral band is a robustness band.

adversarial attacks often take place in inferences. This research provides a unified view regarding the mechanisms of image model robustness on spectra. We only focus on global interpretation of robustness mechanisms of image models by examining the robustness globally on an entire dataset. Our method is primarily motivated by two key aspects, as detailed below.

Despite the substantial advances in previous global interpretability works (Covert et al., 2020; Kolek et al., 2022), in tandem with the wide adoption of empirical robustness benchmarks (Hendrycks and Dietterich, 2019), these methods are not designed to provide global interpretations regarding model robustness. For example, SAGE (Covert et al., 2020), a global interpretability work, can attribute the decisive pixel features in model's decision-makings. Yet, the importance of decisive pixel features fails to interpret the global robustness. Although the robustness of image models can be quantified by mean corruption errors (mCE) (Hendrycks and Dietterich, 2019) or the distances in feature spaces between clean and perturbed image pairs (Zheng et al., 2016), these scalar metrics often fall short in interpreting the underlying ‘why’ question. This gap prompts us to provide global mechanistic interpretations of perturbation robustness.

Motivation also arises from the robustness characterization of the spectral signals within natural images. Images can be represented as spectral signals (Körner, 2014). The signal-to-noise ratios (SNR) of spectral signals can be used to characterize the signal robustness with respect to perturbations. Our later empirical study, as illustrated in Figure 6.2, suggests that the spectral SNRs of perturbed natural images decay over the frequency with a power-law-like distribution. We refer to the *spectral SNR* as the ratio of the point-wise

energy spectral density (ESD) (Stoica et al., 2005) of spectral signal to noise (*i.e.* perturbation):

$$\text{SNR}(r) := \frac{\text{ESD}_r(x)}{\text{ESD}_r(\Delta x)} \quad (6.1)$$

where r is a radial frequency point, x is an image, Δx is the perturbation, $\text{ESD}_r(\cdot)$ gives the point-wise energy density at r . The $\text{ESD}_r(\cdot)$ is defined as:

$$\text{ESD}_r(x) := \frac{1}{|L_r|} \cdot \sum_{(u,v) \in L_r} |\mathcal{F}(x)(u,v)|^2 \quad (6.2)$$

where L_r denotes a circle as illustrated in Figure 6.1, $|L_r|$ denotes the circumference of L_r , and $\mathcal{F}(x)$ denotes the 2D Discrete Fourier Transform (DFT) of x . Readers can further refer to more details in Appendix 6.B.1.

Why do the spectral SNRs of some corruptions and adversarial attacks exhibit a power-law-like decay over the frequency? We surmise that the ESDs of many perturbations are often not power-law-like, while the ESDs of natural images are power-law-like empirically, as shown in Figure 6.1. For example, the spatial perturbation drawn from $\mathcal{N}(0, \sigma^2)$ (*i.e.* white noise) has a constant ESD: $\text{ESD}_r(\Delta x) = \sigma^2$. In Figure 6.2, we characterize the spectral SNR distributions of perturbed images. We set the energy of perturbations to 10% of the energy of the clean image for a fair comparison. The perturbation sources include corruptions (Hendrycks and Dietterich, 2019) and adversarial attacks (Szegedy et al., 2014; Tsipras et al., 2019). We notice that the SNR distributions are also power-law-like over the frequency. We refer to *spectral signals* as *spectral features* or simply as *features* if without ambiguity. This power-law-like SNR decay suggests an empirical feature robustness prior: **Low-frequency features are robust features (RFs) while high-frequency features are non-robust features (NRFs)**. The experiments in Figure 6.3 demonstrate that models trained with low-frequency signals exhibit higher robustness compared to the models trained with high-frequency signals. This also echoes with our earlier claim “low-frequency signals are generally more robust than high-frequency signals — yet high classification accuracy can not be achieved by low-frequency signals alone”.

Contributions. By applying the Shapley value theory framework (Roth, 1988), we are able to assess the predictive powers of RFs and NRFs. Further leveraging a specifically designed characteristic function of the Shapley value theory framework, the predictive powers are assessed on the basis of their information gains. **I-ASIDE** uses information

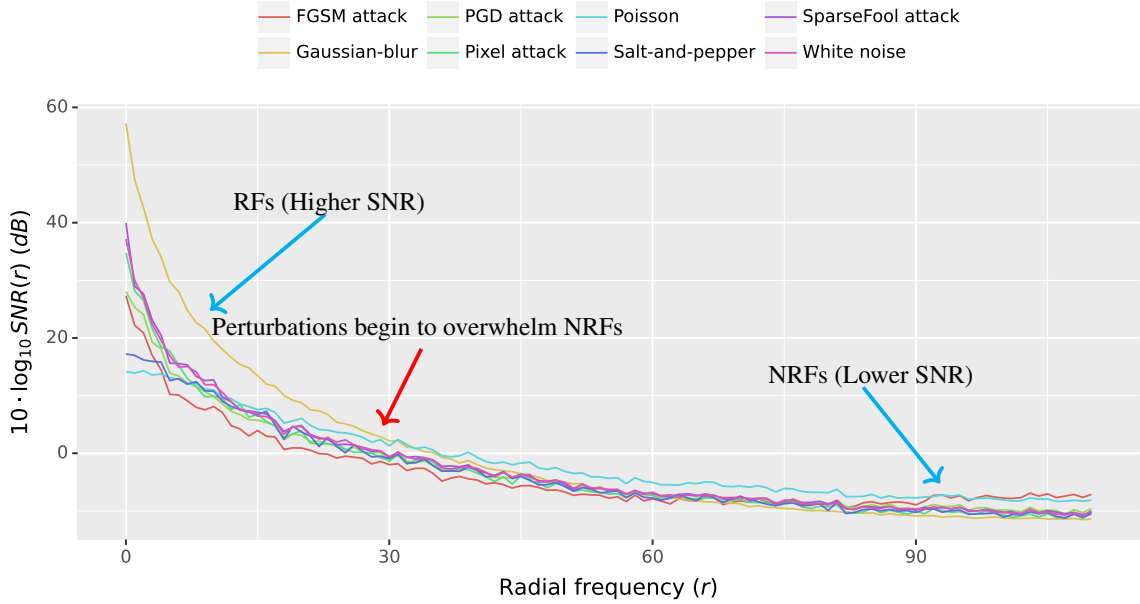


Figure 6.2: Spectral SNR characterization with respect to multiple corruptions and adversarial attacks. The corruptions include: white noise, Poisson noise, Salt-and-pepper noise, and Gaussian blur. The adversarial attacks include: FGSM (Goodfellow et al., 2015), PGD (Madry et al., 2018), SparseFool (Modas et al., 2019) and Pixel (Pomponi et al., 2022). We set the perturbation energy to 10% of the energy of the reference image. The results are shown in decibels (dB) for better visualization. The dB below zero indicates that the perturbations overwhelm the spectral features.

theory within the Shapley value theory framework, for interpreting robustness mechanisms, as detailed in Section 6.3. We claim our major contributions as:

- We propose a model-agnostic, global interpretability method, for interpreting robustness mechanisms of image models, through the lens of the predictive powers of robust features and non-robust features;
- We analyze the robustness mechanisms of image models within information theory on spectra;
- We showcase a case study that **I-ASIDE** has the potential to interpret how supervision noise levels affect model robustness.

6.2 Notations

Image classifier. The primary task of an image classifier is to predict the probability distributions over discrete classes for given images. We use $Q(y|x; \theta) : (x, y) \mapsto [0, 1]$ to

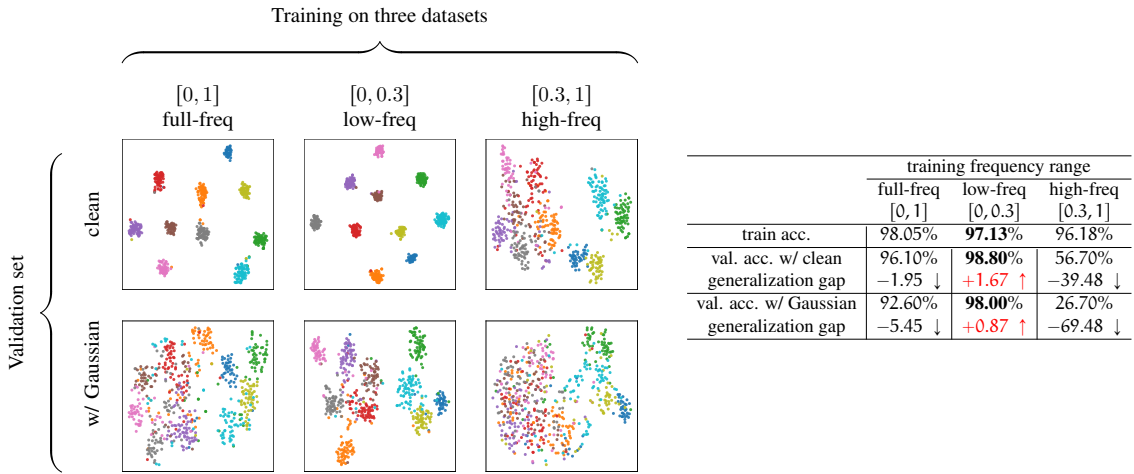


Figure 6.3: Understanding the role of spectral signals. We train a *resnet18* on three datasets derived from *STL10* (Coates et al., 2011): $[0, 1]$ contains full-frequency signals; $[0, 0.3]$ only contains low-frequency signals with a cut-off frequency by 0.3; and $[0.3, 1]$ only contains the high-frequency signal with a cut-off frequency by 0.3. In the derived datasets, the filtered high or low frequency signals are randomly replaced by the high or low frequency signals sampled from the full-frequency train set. We visualize the embeddings in the left figure with respect to clean samples and perturbed samples with Gaussian noise ($\sigma = 0.1$). The samples are from the validation set. The accuracy on both the train and validation sets is provided in the right table. We also provide generalization gaps, measured by the differences between validation accuracy and train accuracy (*i.e.* $\text{acc}_{\text{val}} - \text{acc}_{\text{train}}$). We have noted in that: (1) both high-frequency and low-frequency signals contain sufficient discriminative information to achieve high training accuracy; (2) high-frequency signals alone are not robust signals because they fail to generalize well from train to validation; (3) overall, low-frequency signals are more robust signals because models trained alone with them generalize better and exhibit higher robustness. We summarize these empirical observations into Assumption 6.3.8.

denote a classifier in the form of conditional probability. The Q predicts the probability that an image x is of class y . The θ are the parameters. For brevity, we ignore the parameter θ . For example, we denote $Q(y|x; \theta)$ as $Q(y|x)$.

Dataset and annotation. We use a tuple $\langle \mathcal{X}, \mathcal{Y} \rangle$ to denote an image classification dataset, where \mathcal{X} is the image set and \mathcal{Y} is the label set. We use $|\mathcal{Y}|$ to denote the number of classes (*i.e.* the cardinality of set \mathcal{Y}). The annotation task of image classification datasets is to assign each image with a discrete class probability distribution. We use $P(y|x)$ to denote the ground-truth probability that an image x is assigned as a class y . We use $P(x)$ to denote the probability of x in set \mathcal{X} . We use $P(y)$ to denote the probability of y in set \mathcal{Y} . In class-balanced datasets, $P(y) = \frac{1}{|\mathcal{Y}|}$.

6.3 Method

High-level overview. We apply Shapley value theory for axiomatically assigning credits to spectral bands. Within this framework, the specially devised characteristic function measures the information gains of spectral bands. **I-ASIDE** interprets robustness mechanisms using this axiomatic framework with the information theory.

Problem formulation. Quantifying the predictive powers of features can be viewed as a *value* decomposition problem. In this research, the *value* is the information quantity that a features contribute to decisions. Specifically, the *value* is in the form of the log-likelihood expectation of predictions (*i.e.* the negative cross-entropy loss). The *value* decomposition aims to assign each robustness band a predictive power such that: (1) The sums of the predictive powers are equal to the *value*, and (2) the assigned predictive powers should reflect their importance in the decisions. In the coalitional game theory, this decomposition scheme is known as an *axiomatic fairness division problem* (Roth, 1988; Klamler, 2010). The fairness division must satisfy four axioms: *efficiency*, *symmetry*, *linearity* and *dummy player* (Roth, 1988). We refer to the *axiomatic fairness division* as *axiomatic decomposition*. Of the scheme, the axioms guarantee *uniqueness* and *fairness* (Aumann and Maschler, 1985; Aumann and Dombb, 2015; Roth, 1988). The property *fairness* refers to the principle ‘*equal treatment of equals*’ (Navarro, 2019). Shapley value theory is the unique solution satisfying the above axioms. However, the theory merely provides an abstract framework. To employ, we have to instantiate two abstracts: (1) players and coalitions, and (2) characteristic function.

Abstract (1): players and coalitions. The spectral bands are dubbed as *spectral players*. A subset of the spectral player set is dubbed as a *spectral coalition*. The details are as shown in Section 6.3.1. The M spectral players can forge 2^M spectral coalitions. We represent the presences and absences of the spectral players as the pass-bands and stop-bands in a multi-band-pass digital signal filter (Oppenheim, 1978), as shown in Section 6.3.2.

Abstract (2): characteristic function. The characteristic function is designed to measure the contributions that the coalitions contribute in decisions. The contributions of the 2^M coalitions are then combined to compute their marginal contributions in decisions. We specially design the characteristic function, as shown in Section 6.3.3 and Appendix 6.B.3, to measure the information gains. Figure 6.4 shows the framework of applying the Shapley value theory. Figure 6.5 shows the block diagram of the spectral coalition filtering. Figure 6.6 shows an example of 2^M spectral coalitions.

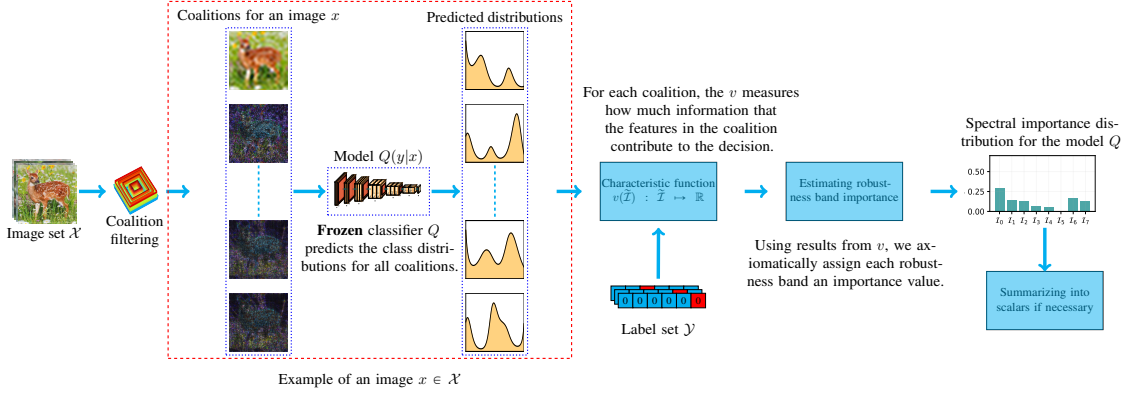


Figure 6.4: Framework of applying Shapley value theory. Spectral coalition filtering creates spectral coalitions over \mathcal{X} . Each coalition contains a unique combination of spectral signals, in which some spectral bands are present and others are absent. The coalitions are fed into a classifier Q . For each coalition, Q outputs the predictions. The characteristic function v then uses the predictions to estimate the contributions of the features present in the coalitions. The results from v are combined to compute the marginal contributions of spectral bands — *i.e.* the spectral importance distribution of Q .

We organize the implementation details of instantiating the aforementioned two abstracts from three aspects: (1) formulating a spectral coalitional game, (2) the implementation of spectral coalitions and (3) the design of the characteristic function.

6.3.1 Spectral coalitional game

Spectral player. We use \mathcal{I}_i (where $i \in [M] := \{0, 1, \dots, M-1\}$) to denote the i -th spectral player. The \mathcal{I}_0 contains the most robust features and the \mathcal{I}_{M-1} contains the most non-robust features. The M spectral players constitute a player set $\mathcal{I} := \{\mathcal{I}_i\}_{i=0}^{M-1}$. Figure 6.15 in Appendix 6.C.1 shows two partition schemes to partition spectral bands (ℓ_∞ and ℓ_2). We empirically choose ℓ_∞ .

Spectral coalition. A subset $\tilde{\mathcal{I}} \subseteq \mathcal{I}$ is referred to as the *spectral coalition*. The player set \mathcal{I} is often referred to as the *grand coalition*.

Characteristic function. A characteristic function $v(\tilde{\mathcal{I}}) : \tilde{\mathcal{I}} \mapsto \mathbb{R}$ measures the contribution for a given coalition and satisfies $v(\emptyset) = 0$. In this research, the contribution of $\tilde{\mathcal{I}}$ is measured in the form of the log-likelihood expectation of the predictions by the Q , in which the input images only contain the signals present in the $\tilde{\mathcal{I}}$. We show that this design of v theoretically measures how much information the Q uses from the features in the $\tilde{\mathcal{I}}$ for decisions.

Shapley value. A spectral coalitional game (\mathcal{J}, v) is defined on a spectral player set \mathcal{J} equipped with a characteristic function v . The weighted marginal contribution of a spectral player \mathcal{J}_i over all possible coalitions is referred to as the Shapley value of the spectral player \mathcal{J}_i . We use $\psi_i(\mathcal{J}, v)$ to represent the Shapley value of the player \mathcal{J}_i . The Shapley value $\psi_i(\mathcal{J}, v)$ is uniquely given by:

$$\psi_i(\mathcal{J}, v) = \sum_{\tilde{\mathcal{J}} \subseteq \mathcal{J} \setminus \mathcal{J}_i} \frac{1}{M} \binom{M-1}{|\tilde{\mathcal{J}}|}^{-1} \{v(\tilde{\mathcal{J}} \cup \{\mathcal{J}_i\}) - v(\tilde{\mathcal{J}})\} \quad (6.3)$$

where $\frac{1}{M} \binom{M-1}{|\tilde{\mathcal{J}}|}^{-1}$ gives the weight of the player \mathcal{J}_i presenting in the coalition $\tilde{\mathcal{J}}$.

Spectral importance distribution (SID). We use $\Psi(v) := (\psi_i)_{i \in [M]} \in \mathbb{R}^M$ to denote the collection of $\psi_i(\mathcal{J}, v)$ over all players. We min-max normalize $\Psi(v)$ by taking $\bar{\Psi}(v) = \frac{\Psi(v) - \min \Psi(v)}{\|\Psi(v) - \min \Psi(v)\|_1}$. The reason for normalizing the SIDs is that we want to scalarize the SIDs for numerical comparisons. The $\bar{\Psi}(v)$ is referred to as *spectral importance distribution*. Figure 6.7 shows examples of the spectral importance distributions of trained and un-trained models.

Spectral robustness score (SRS). We can also summarize spectral importance distributions into scalar values. We refer to the summarized scalar values as *spectral robustness scores*. We use $S(v) : v \mapsto [0, 1]$ to denote the summarizing function.

6.3.2 Spectral coalition filtering

We represent the *presences* and *absences* of the spectral players through the signal *pass-bands* and *stop-bands* using a multi-band-pass digital signal filtering (Oppenheim, 1978), as shown in Figure 6.5. For example, the example spectral coalition $\{\mathcal{J}_0, \mathcal{J}_2\}$ signifies the signals present only in \mathcal{J}_0 and \mathcal{J}_2 . With the spectral coalition filtering, we are able to evaluate the contributions of the combinations of various spectral features. Figure 6.6 shows an example of 2^M spectral coalitions.

To implement the presences and absences of spectral signals, we define a mask map $\mathbb{T}(\tilde{\mathcal{J}}) : \tilde{\mathcal{J}} \mapsto \{0, 1\}^{M \times N}$ on 2D spectrum, where $\tilde{\mathcal{J}}$ is a spectral coalition and $M \times N$ denotes 2D image dimensions. The mask map is point-wisely defined as:

$$\mathbb{T}(\tilde{\mathcal{J}})(m, n) = \begin{cases} 1, & \text{if the frequency point } (m, n) \text{ is present in coalition } \tilde{\mathcal{J}}, \\ 0, & \text{otherwise} \end{cases} \quad (6.4)$$

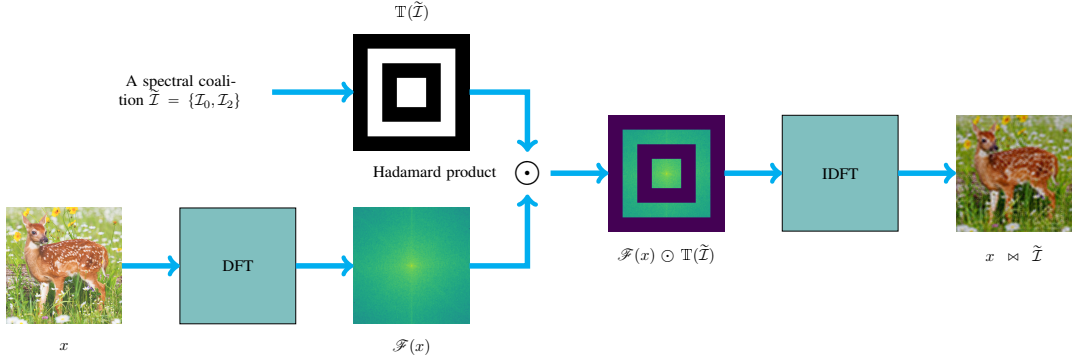


Figure 6.5: Spectral coalition filtering. In this example, the mask map $\mathbb{T}(\tilde{\mathcal{I}})$ (i.e. transfer function) only allows to pass the signals present in the spectral coalition $\{\mathcal{I}_0, \mathcal{I}_2\}$. The M is 4 and the absences are assigned to zeros. The images after spectral coalition filtering ($x \bowtie \tilde{\mathcal{I}}$) are then fed into frozen classifiers to assess the contributions of spectral coalitions. The binary operation notation \bowtie denotes coalition filtering given by Definition 6.3.1. The notation \odot denotes Hadamard product.

where $(m, n) \in [M] \times [N]$. In the digital signal processing literature, this mask map is known as a *transfer function* (Oppenheim, 1978). In the 2D mask map, the frequency points are ‘1’ in pass-bands (presences) and ‘0’ in stop-bands (absences). The process of spectral coalition filtering with the mask map for a given spectral coalition $\tilde{\mathcal{I}}$ is shown as in Figure 6.5.

We apply the transfer function $\mathbb{T}(\tilde{\mathcal{I}})$ on the spectra of images with element-wise product (i.e. Hadamard product (Horn, 1990)). Let \mathcal{F} be the Discrete Fourier transform (DFT) operator and \mathcal{F}^{-1} be the inverse DFT (IDFT) operator (Oppenheim, 1978). Readers can further refer to Appendix 6.B.1.

Definition 6.3.1 (Spectral coalition filtering). We define a binary operator ‘ \bowtie ’ to represent the signal filtering by:

$$x \bowtie \tilde{\mathcal{I}} := \mathcal{F}^{-1} \left[\underbrace{\mathcal{F}(x) \odot \mathbb{T}(\tilde{\mathcal{I}})}_{\text{Spectral presence}} + \underbrace{\mathbf{b} \odot (\mathbb{1} - \mathbb{T}(\tilde{\mathcal{I}}))}_{\text{Spectral absence}} \right] \quad (6.5)$$

where ‘ \odot ’ denotes Hadamard product (i.e. element-wise product), $\mathbb{1} \in \mathbb{R}^{M \times N}$ denotes an all-ones matrix and $\mathbf{b} \in \mathbb{C}^{M \times N}$ represents the assignments of the absences of spectral players. In the context of attribution analysis, \mathbf{b} is often referred as the baseline. In our implementation, we empirically set $\mathbf{b} = \mathbf{0}$.

Remark 6.3.2 (Absence baseline). Formally, in the context of attribution analysis, the term ‘baseline’ defines the absence assignments of players (Sundararajan et al., 2017; Shrikumar et al., 2017; Binder et al., 2016). For example, if we use ‘zeros’ to represent

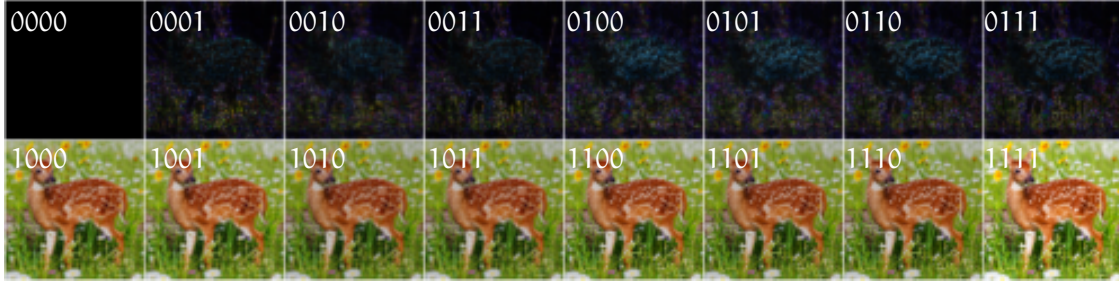


Figure 6.6: An example of a complete 2^M spectral coalitions. This example shows 16 spectral coalitions with $M = 4$. Each coalition provides various information relevant to decisions. Each image is a coalition. Each coalition contains a unique spectral signal combination. We use binary code to index these coalitions. The ‘1’ in the i -th position indicates the presence of the i -th player. For example, 1001 indicates the presences of two spectral players (\mathcal{I}_0 and \mathcal{I}_3) in the coalition.

the absence of players, the ‘zeros’ are dubbed as the ‘baseline’ in the attribution analysis. We have discussed multiple baselines in Appendix 6.B.2.

Definition 6.3.3 (Spectral coalition filtering over set). Accordingly, we define the filtering over a set \mathcal{X} as:

$$\mathcal{X} \bowtie \tilde{\mathcal{I}} := \{x \bowtie \tilde{\mathcal{I}} | x \in \mathcal{X}\}. \quad (6.6)$$

6.3.3 Characteristic function design

The characteristic function is needed in order to measure the contributions of the features in $\tilde{\mathcal{I}}$. We define the characteristic function as the gains of the negative cross-entropy loss values between feature presences and absences.

Definition 6.3.4 (Characteristic function). The characteristic function $v(\tilde{\mathcal{I}}) : \tilde{\mathcal{I}} \mapsto \mathbb{R}$ is defined as:

$$\begin{aligned} v(\tilde{\mathcal{I}}) &:= \mathbb{E}_{x \sim \mathcal{X}} \sum_{y \in \mathcal{Y}} \left\{ \underbrace{P(y|x) \cdot \log Q(y|x \bowtie \tilde{\mathcal{I}})}_{\text{Feature presence}} - \underbrace{P(y|x) \cdot \log Q(y|x \bowtie \emptyset)}_{\text{Absence baseline}} \right\} \\ &= \mathbb{E}_{x \sim \mathcal{X}} \sum_{y \in \mathcal{Y}} P(y|x) \cdot \log Q(y|x \bowtie \tilde{\mathcal{I}}) - C \end{aligned} \quad (6.7)$$

where the constant term $C := \mathbb{E}_{x \sim \mathcal{X}} \sum_{y \in \mathcal{Y}} P(y|x) \cdot \log Q(y|x \bowtie \emptyset)$ is used to fulfil $v(\emptyset) = 0$.

We refer to the C as the *Dummy player constant*.

Remark 6.3.5. If the labels are one-hot, then (6.7) is simplified into:

$$v(\tilde{\mathcal{I}}) := \mathbb{E}_{x,y \sim \langle \mathcal{X}, \mathcal{Y} \rangle} \log Q(y|x \bowtie \tilde{\mathcal{I}}) - C \quad (6.8)$$

$$\text{and } C := \mathbb{E}_{x,y \sim \langle \mathcal{X}, \mathcal{Y} \rangle} \log Q(y|x \bowtie \emptyset).$$

Linking to information theory. The relationship between information theory and the characteristic function in the form of negative log-likelihood of Bayes classifiers has been discussed in the literature (Covert et al., 2020; Aas et al., 2021; Lundberg and Lee, 2017). Following on from their discussions, we show that the v in (6.7) profoundly links to information theory in terms of spectral signals. The maximal information of features relevant to labels in $\tilde{\mathcal{I}}$ is the mutual information $\mathbb{I}(\mathcal{X} \bowtie \tilde{\mathcal{I}}, \mathcal{Y})$. A classifier Q can merely utilize a proportion of the information. Theorem 6.3.6 states an information quantity identity regarding the $\mathbb{I}(\mathcal{X} \bowtie \tilde{\mathcal{I}}, \mathcal{Y})$ and the v . The term $D_{KL}[P||Q]$ measures the point-wise (*i.e.* for an image x) KL-divergence between the predictions and ground-truth labels. On the basis of the information quantity identity, the v can be interpreted as the information gains between the presences and absences of the features, which the Q utilizes in decisions from the $\tilde{\mathcal{I}}$. By enumerating all coalitions, the information gains are then combined to compute the marginal information gains of features in decisions via (6.3).

Theorem 6.3.6 (Spectral coalition information identity). *The information quantity relationship is given as:*

$$\mathbb{I}(\mathcal{X} \bowtie \tilde{\mathcal{I}}, \mathcal{Y}) \equiv \mathbb{E}_{x \in \mathcal{X} \bowtie \tilde{\mathcal{I}}} D_{KL}[P(y|x) || Q(y|x)] + H(\mathcal{Y}) + v(\tilde{\mathcal{I}}) + C \quad (6.9)$$

where v is defined in (6.7) and $H(\mathcal{Y})$ is the Shannon entropy of the label set \mathcal{Y} . The proof is provided in Appendix 6.B.3.

6.3.4 Spectral robustness score (SRS)

Although we are firstly interested in using the spectral importance distributions (SID) for robustness interpretations, they can also be summarized into scalar scores for purposes such as numerical comparisons, and later correlation studies.

Assumption 6.3.7 (Spectral uniformity assumption of random decisions). The second row in Figure 6.7 shows the SIDs from various models with randomized weights. We randomize the model weights with *Kaiming* initialization (He et al., 2015). The measured SIDs exhibit spectral uniformity. This suggests: **Un-trained models do not have**

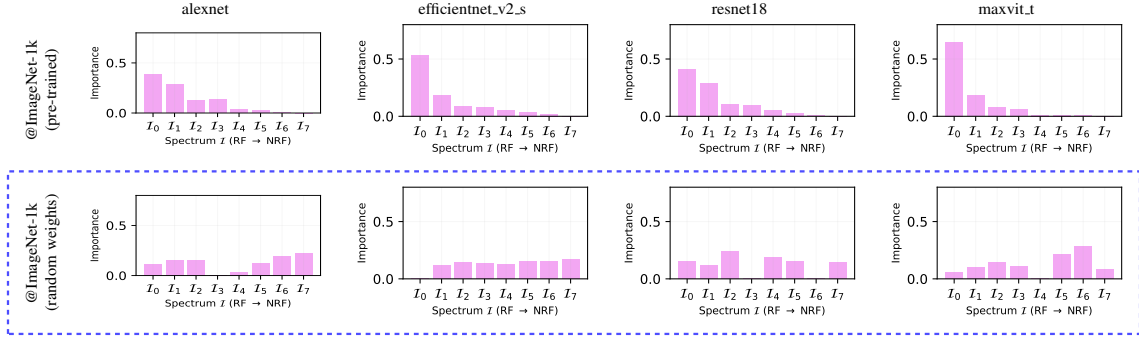


Figure 6.7: Spectral importance distributions (SIDs) of trained models and un-trained models.

The experimental models are pre-trained on *ImageNet*. We also include the models with random weights as a control marked by the blue box. We have noticed that: (1) The spectral importance distributions of trained models exhibit non-uniformity, and (2) the spectral importance distributions of un-trained models exhibit uniformity. We summarize these empirical observations as Assumption 6.3.7.

spectral preferences. We refer to ‘the models with randomized parameters’ as random decisions. Therefore, we assume that the SIDs of random decisions are uniform: $\frac{1}{M}$.

Assumption 6.3.8 (Robustness prior). We assume: **Higher utilization of robust features in decisions implies robust models.** This is further substantiated by the experiments in Figure 6.3. To reflect this robustness prior, we empirically design a series $\beta := (\beta^0, \beta^1, \dots, \beta^{M-1})^\top$ where $\beta \in (0, 1)$ as the summing weights of SIDs. Empirically, we choose $\beta = 0.75$ because this choice achieves the best correlation with model robustness.

Summarizing with weighted sum. Let $\Psi(v)$ be the measured spectral importance distribution (SID). Set $\bar{\Psi}(v) = \frac{\Psi(v) - \min \Psi(v)}{\|\Psi(v) - \min \Psi(v)\|_1}$ with min-max normalization. The weighted sum of the $\Psi(v)$ with the weights β is given by:

$$\left| \beta^\top \bar{\Psi}(v) - \beta^\top \frac{1}{M} \right| \quad (6.10)$$

where $\beta^\top \frac{1}{M}$ is served as a random decision baseline. Let $S(v) : v \mapsto [0, 1]$ be the normalized result in (6.10). The $S(v)$ is given by:

$$S(v) := \frac{\left| \beta^\top \bar{\Psi}(v) - \beta^\top \frac{1}{M} \right|}{\sup_{\bar{\Psi}} \left| \beta^\top \bar{\Psi}(v) - \beta^\top \frac{1}{M} \right|} = \left| \frac{\bar{\beta}^\top \bar{\Psi}(v) - \eta}{1 - \eta} \right| \quad (6.11)$$

where $\beta \in (0, 1)$, $\bar{\beta} = \frac{\beta}{\|\beta\|_2}$ and $\eta = \frac{1}{M} \|\beta\|_1$. Readers can refer to Appendix 6.C.2 for the simplification deduction.

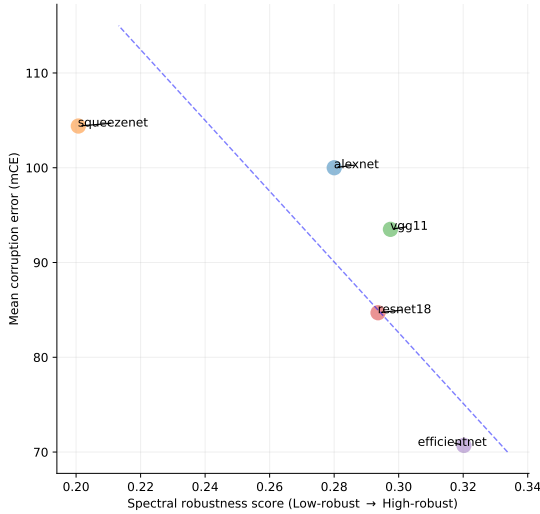


Figure 6.8: The spectral robustness scores (SRS), measured with I-ASIDE, correlate to the mean corruption errors (mCE) in the literature (Hendrycks and Dietterich, 2019).

6.4 Experiments

We design experiments to show the dual functionality of **I-ASIDE**, which can not only **measure** robustness and but also **interpret** robustness. We organize the experiments in three categories:

- Section 6.4.1: Correlation to a variety of robustness metrics;
- Section 6.4.2: Studying architectural robustness;
- Section 6.4.3: A case study interpreting how supervision noise levels affect model robustness.

Section 6.4.1 shows that the scores obtained with **I-ASIDE** correlate with the model robustness scores measured with other methods. Section 6.4.2 and Section 6.4.3 show that **I-ASIDE** is able to interpret robustness by examining SIDs.

Reproducibility. We choose $M = 8$ and 200 samples to conduct experiments. We choose 200 samples because the experiments in Appendix 6.C.3. The experiment shows that: **A small amount of examples are sufficiently representative for spectral signals.**

6.4.1 Correlation to robustness metrics

Definition 6.4.1 (Mean prediction error). In our experiments, we measure model perturbation robustness with mean prediction errors (mPE) besides the mean corruption errors

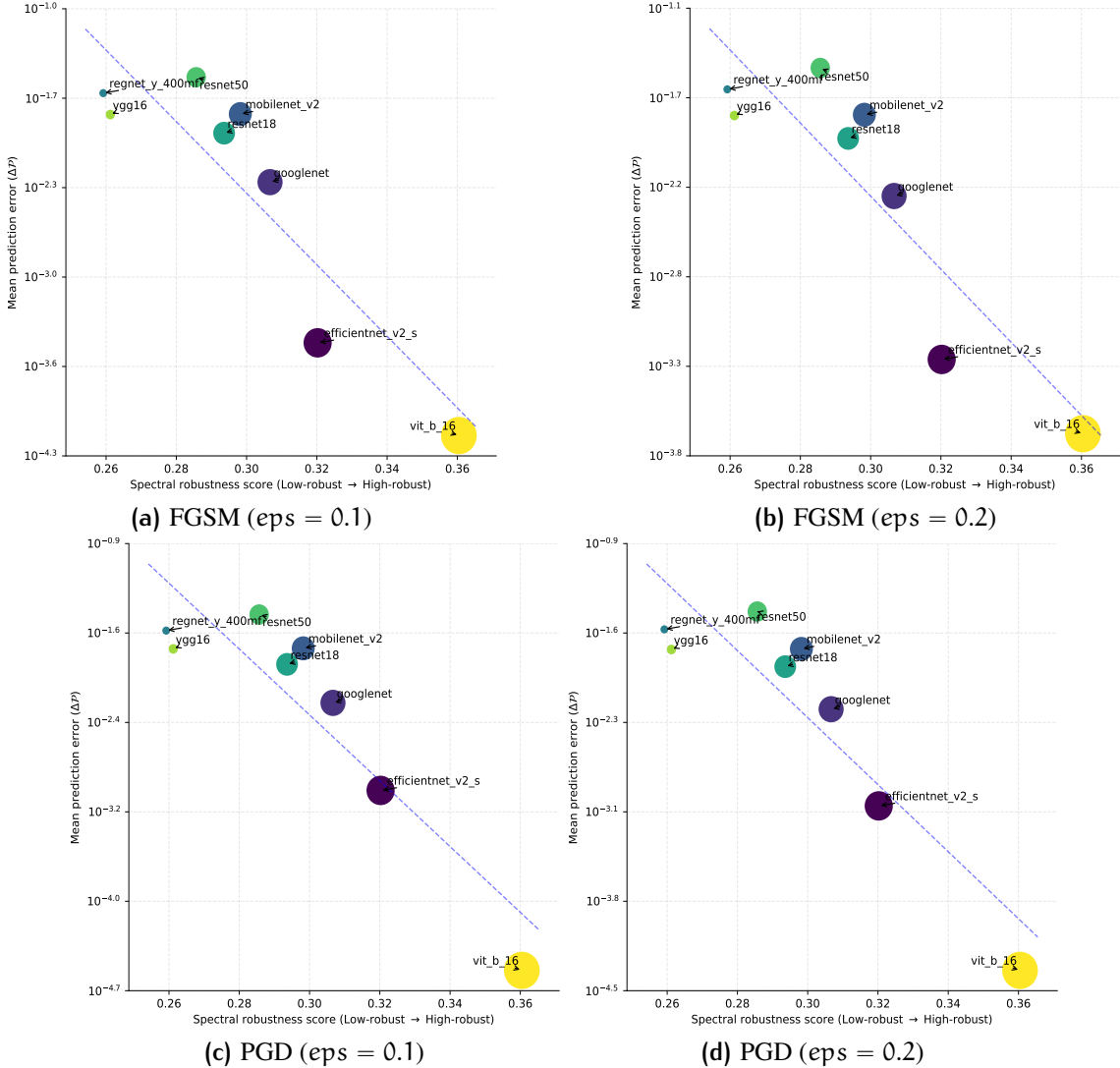


Figure 6.9: The spectral robustness scores (SRS), measured with I-ASIDE, correlate with the mean prediction errors (mPE) in adversarial attacks. The circle sizes in (b) are proportional to the SRS.

(mCE). Let x be some clean image and x^* be the perturbed image. For a classifier Q , we define the mean prediction error (mPE) as:

$$\Delta P := \mathbb{E}_{x,y \sim \langle \mathcal{X}, \mathcal{Y} \rangle} |Q(y|x) - Q(y|x^*)|. \quad (6.12)$$

We demonstrate that **I-ASIDE** is able to measure model robustness. The experiments are broken down into three aspects: (1) correlation to mCE scores, (2) correlation to adversarial robustness, and (3) correlation to corruption robustness.

Correlation to mCE scores. Figure 6.8 shows the correlation between spectral robustness scores (SRS) and the mean corruption errors (mCE). The mCE scores are taken

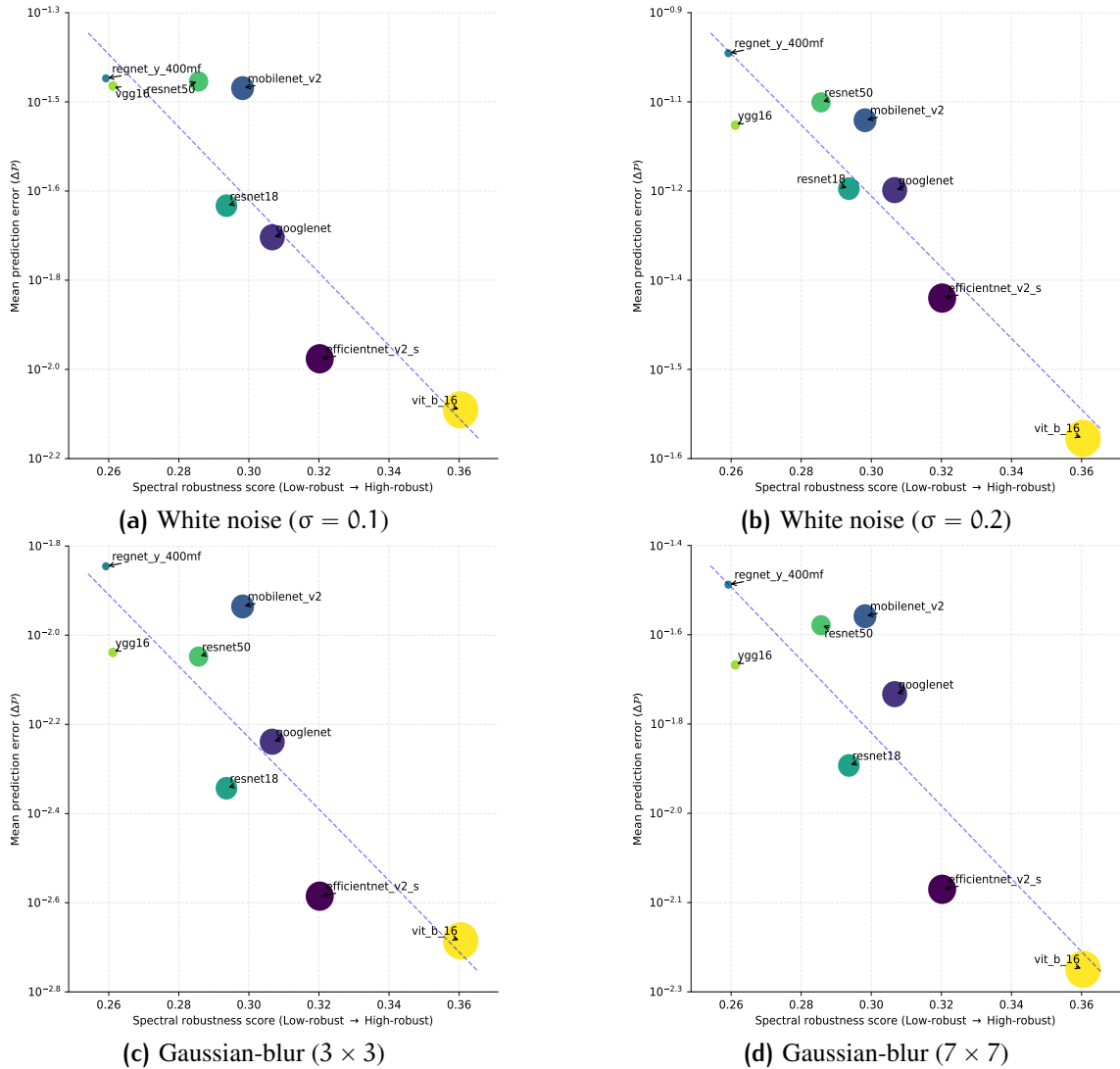


Figure 6.10: The spectral robustness scores (SRS), measured with I-ASIDE, correlate to the mean prediction errors (mPE) in corruptions. The circle sizes in (b) are proportional to the SRS.

from the literature (Hendrycks and Dietterich, 2019). The mCE scores are measured on a corrupted *ImageNet* which is known as *ImageNet-C* in the literature (Hendrycks and Dietterich, 2019). The *ImageNet-C* includes 75 common visual corruptions with five levels of severity in each corruption. This correlation suggests that the results measured with I-ASIDE correlate with the results measured with robustness metric mCE.

Correlation to adversarial robustness. Figure 6.9 shows the correlation between the correlation between spectral robustness scores (SRS) and the mean prediction errors (mPE) of the adversarial attacks with FGSM and PGD. We vary the eps from 0.1 to 0.2. The results show that our scores correlate with the mean prediction errors in various eps settings. This suggests that the results measured by our method correlate with adversarial robustness.

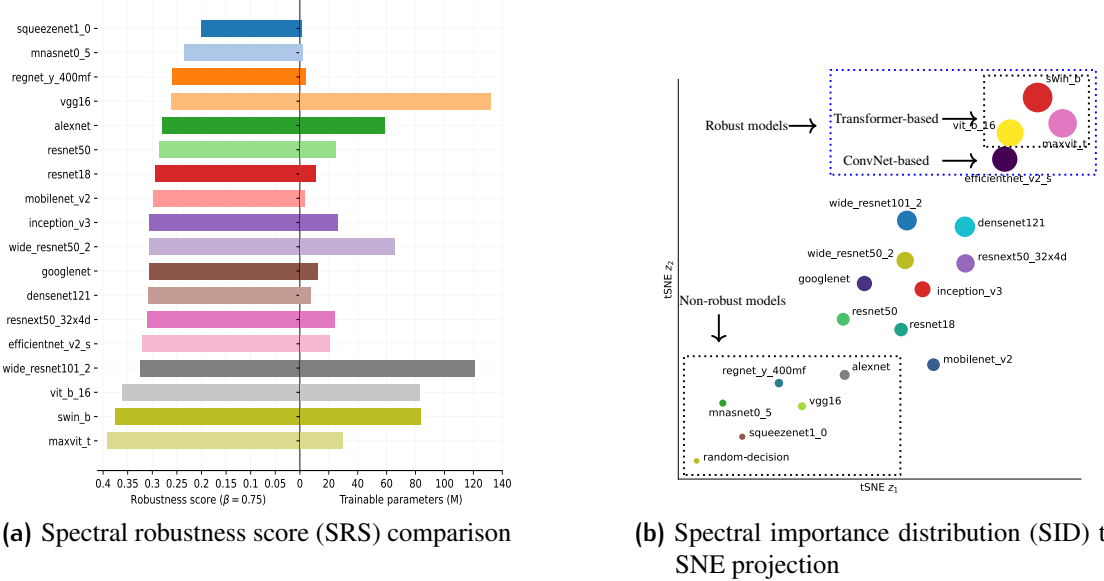


Figure 6.11: How do architectural elements affect robustness? The left figure is to answer: “Does model parameter size play a role on robustness?”. The right figure, a t-SNE projection of SIDs, is to answer: “Are vision transformers more robust than convolutional neural networks?”. For the two questions, the answers suggested by using **I-ASIDE** are yes. But the story is more complicated, we have provided a brief discussion regarding this case study within Section 6.4.2. We also have noted that *efficientnet* surprisingly exhibits comparable perturbation robustness as the architectures in Transformer family. All experimental models are pre-trained on *ImageNet*. The circle sizes in (b) are proportional to SRS.

Correlation to corruption robustness. Figure 6.10 shows the correlation between the correlation between spectral robustness scores (SRS) and the mean prediction errors (mPE) of the corruptions with white noise and Gaussian blurring. We vary the σ of white noise from 0.1 to 0.2. We vary the Gaussian blurring kernel sizes from 3×3 to 7×7 . The results show that our scores correlate with the mean prediction errors in all cases. This suggests that the results measured by our method can reflect the corruption robustness.

6.4.2 Studying architectural robustness

I-ASIDE is able to answer questions such as:

- Does model parameter size play a role in robustness?
- Are vision transformers more robust than convolutional neural networks (ConvNets)?

Does model parameter size play a role in robustness? Figure 6.11 (a) shows parameter counts do not correlate with model robustness. Thus, **the tendency of a model to use**

robust features is not determined by parameter counts alone. We would like to carry out further investigation in future work.

Are vision transformers more robust than ConvNets? Figure 6.11 (b) shows a t-SNE projection of the spectral importance distributions of a variety of models. The results show that vision transformers form a cluster (*swin_b*, *maxvit_t* and *vit_b_16*) and outperform ConvNets in terms of robustness. This results correlate with the recent robustness research in the literature (Paul and Chen, 2022; Zhou et al., 2022; Shao et al., 2022). The interpretation is that: **Vision transformers tend to use more robust features than ConvNets.**

Discussion. Vision transformers generally outperform ConvNets; nevertheless, state-of-the-art ConvNets, *e.g.* *efficientnet* (Tan and Le, 2019), can achieve comparable robustness performance (*e.g.* by error rates on benchmark datasets) (Li and Xu, 2023). The literature (Devaguptapu et al., 2021) affirms that *efficientnet* is more robust than most ConvNets. But, why *efficientnet* is unique? The *efficientnet* introduces an innovative concept in that the network sizes can be controlled by scaling the width, depth, and resolution with a compound coefficient (Tan and Le, 2019). The base architecture is then searched with neural architecture searching (NAS) (Elsken et al., 2019) instead of hand-crafted design. The NAS optimization objective is to maximize the network accuracy subject to arbitrary image resolutions. The searching implicitly encourages that the network structure of *efficientnet* uses more robust features. This is because: **The low-frequency signals in various resolutions are robust signals while high-frequency signals are not.** The second column in Figure 6.7 shows the SID of *efficientnet* pre-trained on *ImageNet*. The SID shows that *efficientnet_v2_s* uses more robust features than *alexnet* and *resnet18*.

6.4.3 Interpreting how supervision noise levels affect model robustness

The previous robustness benchmarks with mean corruption errors (mCE) are not able to answer the long-standing question: **“How and why label noise levels affect robustness?”**. We demonstrate that **I-ASIDE** is able to answer this question.

Learning with noisy labels. Supervision signals refer to the prior knowledge provided by labels (Sucholutsky et al., 2023; Zhang et al., 2020; Xiao et al., 2021). There is a substantial line of previous research on the question of “how supervision noise affects robustness” (Gou et al., 2021; Frenay and Verleysen, 2014; Lukasik et al., 2020). This question is not completely answered yet. For example, Flatow and Penner add uniform

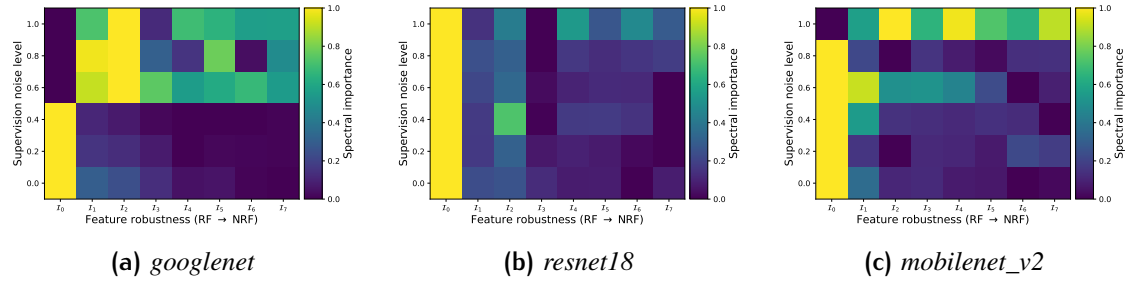


Figure 6.12: How do models respond to label noise? Our results show that models trained with higher label noise levels tend to use spectral signals uniformly, *i.e.* without a preference for robust (low-frequency) features.

label noise into *CIFAR-10* and study its impact on model robustness (Flatow and Penner, 2017). Their results show that classification test accuracy decreases as the training label noise level increases. However, empirical studies like this are not able to answer the underlying ‘why’ question.

Noisy-label dataset. We derive noisy-label datasets from a clean *Caltech101*. We randomly assign a proportion of labels with a uniform distribution over label classes to create a noisy-label dataset. We refer to the randomly assigned proportion as supervision noise level. We vary the noise level from 0.2 to 1.0 to derive five training datasets.

Experiment. We train three models (*googlenet*, *resnet18* and *mobilenet_v2*) over the clean and the five noisy-label datasets for 120 epochs respectively. We then measure their SIDs. The results are visualized in Figure 6.12 with heat maps. The results show that there is a pattern across the above three models in that: **The SIDs are more uniform with higher supervision noise levels.** The interpretation regarding the learning dynamics with the presence of label noise is that: **Models tend to use more non-robust features in the presence of higher label noise within training set.**

6.5 Related work

We further conduct a literature investigation from three research lines: (1) global interpretability, (2) model robustness, and (3) frequency-domain research. This literature study shows that **I-ASIDE** provides unique insights in these research lines.

Global interpretability. Global interpretability summarizes the decision behaviours of models from a holistic view. In contrast, local interpretability merely provides explanations on the basis of instances (Sundararajan et al., 2017; Smilkov et al., 2017; Selvaraju et al., 2017; Zhou et al., 2016; Ribeiro et al., 2016; Lundberg and Lee, 2017; Lakkaraju

et al., 2019; Shrikumar et al., 2017). There are four major research lines in image models: (1) feature visualization, (2) network dissection, (3) concept-based method, and (4) feature importance.

Feature visualization seeks the ideal inputs for specific neurons or classes by maximizing activations (Nguyen et al., 2019; Zeiler et al., 2010; Nguyen et al., 2016). This method provides intuitions regarding the question: “What inputs maximize the activations of specific neurons or classes?”. Network dissection aims to connect the functions of network units (*e.g. channels or layers*) with specific concepts (*e.g. eyes or ears*) (Bau et al., 2017). Concept-based methods understand the decisions by answering the question “how do models use a set of given concepts in decisions?” (Kim et al., 2018; Ghorbani et al., 2019; Koh et al., 2020). For example, TCAV explains model decisions by evaluating the importance of a given set of concepts (*e.g. the textures dotted, striped and zigzagged*) for a given class (*e.g. the class zebra*) (Kim et al., 2018).

Global input feature importance analysis, often by using Shapley value theory framework, attempts to answer the question: “How do input features contribute to predictions?” (Lundberg and Lee, 2017; Ribeiro et al., 2016; Sundararajan et al., 2017; Covert et al., 2020). However, there are few works falling in the scope of global interpretability with feature importance analysis. A related work, SAGE, applying the Shapley value theory framework, globally assigns spatial input features with importance values for interpreting spatial feature contributions (Covert et al., 2020).

Although the aforementioned global interpretability methods provide insights into understanding decisions inside black-box models, they do not provide interpretations regarding robustness mechanisms. Our work fundamentally differs from them in that: We provide interpretations regarding robustness mechanisms. We attempt to answer the fundamental question: “Why some models are more robust than others?”.

Model robustness. Model robustness refers to the prediction sensitivity of models to perturbations. The perturbations can perturb in spaces such as the input space and the parameter space (Hendrycks and Dietterich, 2019). In this research, we focus on the perturbations within the input space. The perturbations can stem from sources such as adversarial attacks (Szegedy et al., 2014; Goodfellow et al., 2015), corruptions (Hendrycks and Dietterich, 2019), outliers (Hendrycks et al., 2019) and supervision signal noise (Hendrycks et al., 2018).

Model robustness is often assessed using scalar metrics (Hendrycks and Dietterich, 2019; Krizhevsky et al., 2012; Taori et al., 2020). For example, robustness can be measured by the distances between clean and perturbed pairs in feature spaces (Zheng et al., 2016).

Hendrycks and Dietterich benchmark the corruption robustness with mean corruption errors (mCE) over a set of corrupted datasets like *ImageNet-C* (Hendrycks and Dietterich, 2019), using AlexNet (Hendrycks and Dietterich, 2019) as a normalization baseline.

Despite their widespread adoption in previous literature, these scalar metrics lack the ability to provide detailed insights into the robustness mechanisms. Our work not only serves as a robustness metric but also offers mechanistic interpretations, answering the “why” question behind model robustness. This dual functionality distinguishes our approach, providing a deeper understanding of the mechanisms.

Frequency-domain research. Neural networks are non-linear parameterized signal processing filters. Investigating how neural networks respond to input signals in the frequency-domain can provide a unique insight into understanding its functions. Xu et al. delve into the learning dynamics of neural networks in the frequency-domain (Xu et al., 2020, 2019b). They present their findings as ‘F-Principle’. Their work suggests that the learning behaviors of neural networks exhibit spectral non-uniformity: Neural networks fit low-frequency components first, then high-frequency components.

In a related study, Tsuzuku and Sato show that convolutional neural networks have spectral non-uniformity with respect to Fourier bases (Tsuzuku and Sato, 2019). Later, Wang et al. connect model generalization behaviors and image spectrum (Wang et al., 2020). They argue that: (1) The supervision signals provided by humans use more low-frequency signals in images and (2) models trained on it tend to use more low-frequency signals. Our showcase experiment in Figure 6.12 provides the interpretations regarding their empirical findings.

In the interpretability research line within the frequency-domain, Kolek et al. propose ‘CartoonX’ based on the rate-distortion explanation (RDE) framework (Macdonald et al., 2019). The RDE framework identifies decision-critical features by partially obfuscating the features. They refer to ‘the prediction errors between clean inputs and the partially obfuscated inputs’ as distortions. CartoonX pinpoints the decision-critical features within wavelet domain to answer the query: “What features are crucial for decisions?” (Kolek et al., 2022). Our work differs from CartoonX in that: (1) Our method aims to interpret model robustness mechanisms while CartoonX does not, (2) our method is a global interpretability method while CartoonX is a local interpretability method, (3) our method analyzes within an information theory framework while CartoonX uses RDE framework, and (4) our method uses Fourier bases while CartoonX uses wavelet bases.

6.6 Limitations

I-ASIDE provides a unique insight into the perturbation robustness mechanisms. Yet, our method has two major limitations: (1) The spectral perspective can merely reflect one aspect of the holistic view of model robustness, and (2) the SID resolutions are low.

Limitation (1). For example, carefully crafted malicious adversarial perturbations on low-frequency components can fool neural networks (Luo et al., 2022). Luo et al. demonstrate that attacking low-frequency signals can fool neural networks, resulting in attacks which are imperceptible to humans. This further implies the complexity of this research topic.

Limitation (2). The computation cost is imposed by $\mathcal{O}(2^M)$. Fortunately, we do not need high SID resolution to analyze the model robustness problem. For example, a choice with $M = 8$ is sufficient to interpret robustness mechanisms (as we have shown) while the computational cost remains reasonable.

6.7 Conclusions

On the solid ground provided by information theory and coalitional game theory, we present an axiomatic method to interpret model robustness mechanisms, by leveraging the power-law-like decay of SNRs over the frequency. Our method addresses the limitation that scalar metrics fail to interpret robustness mechanisms. We carry out extensive experiments over a variety of architectures. The SIDs, when scalarized, can largely reproduce the results found with previous methods, but addresses their failures to answer the underlying ‘why’ questions. Our method goes beyond them with the dual functionality in that: **I-ASIDE** can not only measure the robustness but also interpret its mechanisms. Our work provides a unique insight into the robustness mechanisms of image classifiers.

6.A Appendix

6.B Fairness division axioms

Symmetry axiom: Let $\tilde{\mathcal{I}} \in 2^{\mathcal{I}}$ be some spectral player coalition. For $\forall \mathcal{I}_i, \mathcal{I}_j \in \mathcal{I} \wedge \mathcal{I}_i, \mathcal{I}_j \notin \tilde{\mathcal{I}}$, the statement $v(\tilde{\mathcal{I}} \cup \{\mathcal{I}_i\}) = v(\tilde{\mathcal{I}} \cup \{\mathcal{I}_j\})$ implies $\psi_i(\mathcal{I}, v) = \psi_j(\mathcal{I}, v)$. This axiom restates the statement ‘*equal treatment of equals*’ principle mathematically. This axiom states that the ‘names’ of players should have no effect on the ‘treatments’ by the characteristic function in coalition games (Roth, 1988).

Linearity axiom: Let u and v be two characteristic functions. Let (\mathcal{I}, u) and (\mathcal{I}, v) be two coalition games. Let $(u + v)(\tilde{\mathcal{I}}) := u(\tilde{\mathcal{I}}) + v(\tilde{\mathcal{I}})$ where $\tilde{\mathcal{I}} \in 2^{\mathcal{I}}$. The divisions of the new coalition game $(\mathcal{I}, u + v)$ should satisfy: $\psi_i(\mathcal{I}, u + v) = \psi_i(\mathcal{I}, u) + \psi_i(\mathcal{I}, v)$. This axiom is also known as ‘*additivity axiom*’ and guarantees the uniqueness of the solution of dividing payoffs among players (Roth, 1988).

Efficiency axiom: This axiom states that the sum of the divisions of all players must be summed to the worth of the player set (the grand coalition): $\sum_{i=0}^{M-1} \psi_i(\mathcal{I}, v) = v(\mathcal{I})$.

Dummy player axiom: A dummy player (null player) \mathcal{I}_* is the player who has no contribution such that: $\psi_*(\mathcal{I}, v) = 0$ and $v(\tilde{\mathcal{I}} \cup \{\mathcal{I}_*\}) \equiv v(\tilde{\mathcal{I}})$ for $\forall \mathcal{I}_* \notin \tilde{\mathcal{I}} \wedge \mathcal{I}_* \subseteq \mathcal{I}$.

Remark 6.B.1. In the literature (Roth, 1988), the *efficiency axiom* and the *dummy player axiom* are also combined and relabeled as *carrier axiom*.

6.B.1 Spectral signal-to-noise ratio (SNR)

Discrete Fourier Transform. The notion ‘frequency’ measures how ‘fast’ the outputs can change with respect to inputs. High frequency implies that small variations in inputs can cause large changes in outputs. In terms of images, the ‘inputs’ are the pixel spatial locations while the ‘outputs’ are the pixel values.

Let $x : (i, j) \mapsto \mathbb{R}$ be some 2D image with dimension $M \times N$ which sends every location (i, j) to some real pixel value where $(i, j) \in [M] \times [N]$. Let $\mathcal{F} : \mathbb{R}^2 \mapsto \mathbb{C}^2$ be some DFT functional operator. The DFT of x is given by:

$$\mathcal{F}(x)(u, v) = \sum_{j=0}^{N-1} \sum_{i=0}^{M-1} x(i, j) e^{-2\pi(\frac{u}{M}i + \frac{v}{N}j)}. \quad (6.13)$$

Point-wise energy spectral density (ESD). The ESD measures the energy quantity at a frequency. To simplify discussions, we use *radial frequency*, which is defined as the radius r with respect to zero frequency point (*i.e.* the frequency center). The energy is defined as the square of the frequency magnitude according to Parseval’s Power Theorem.

Let L_r be a circle with radius r on the spectrum of image x , as illustrated in Figure 6.1. The r is referred to as radial frequency. The point-wise ESD function is given by:

$$\text{ESD}_r(x) := \frac{1}{|L_r|} \cdot \sum_{(u, v) \in L_r} |\mathcal{F}(x)(u, v)|^2 \quad (6.14)$$

where (u, v) is the spatial frequency point and $|L_r|$ is the circumference of L_r .

Spectral signal-to-noise ratio (SNR). The SNR can quantify signal robustness. We define the spectral SNR at radius frequency r as:

$$\text{SNR}(r) := \frac{\text{ESD}_r(x)}{\text{ESD}_r(\Delta x)} \quad (6.15)$$

where Δx is some perturbation. We have characterized the SNRs of some corruptions and adversarial attacks in Figure 6.2.

6.B.2 Absence assignment scheme

There exist multiple choices for the assignments of the absences of spectral layers in coalition filtering design: (1) Assigning to constant zeros (Zeroing), (2) assigning to complex Gaussian noise (Complex Gaussian) and (3) assigning to the corresponding frequency components randomly sampled from other images at the same dataset (Replacement).

Zeroing. The \mathbf{b} in (6.5) is set to zeros.

Complex Gaussian. The \mathbf{b} in (6.5) is sampled from a *i.i.d.* complex Gaussian distribution: $\mathcal{N}(\mu, \frac{\sigma^2}{2}) + i\mathcal{N}(\mu, \frac{\sigma^2}{2})$.

Replacement. The \mathbf{b} in (6.5) is set to: $\mathbf{b} = \mathcal{F}(\mathbf{x}^*)$ (where $\mathbf{x}^* \sim \mathcal{X}$ is a randomly sampled image from some set \mathcal{X}).

In our implementation, we simply choose ‘zeroing’: $\mathbf{b} = \mathbf{0}$. Figure 6.13 shows the filtered image examples by using the above three strategies and also show the examples of measured spectral importance distributions. Empirically, the three strategies have rather similar performance. In this research, we do not unfold the discussions regarding the masking strategy choices.

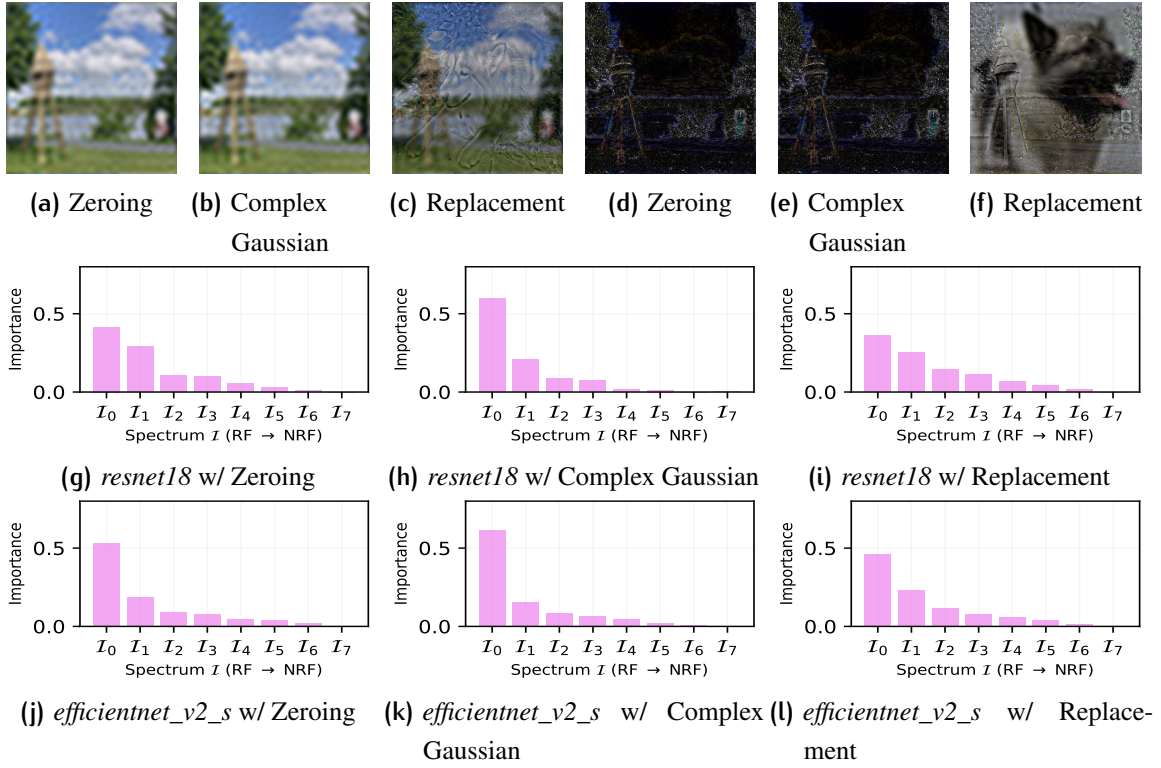


Figure 6.13: Three absence assignment strategies: (1) Assigning the spectral absences with constant zeros (Zeroing), (2) assigning the spectral absences with Gaussian noise (Complex Gaussian) and (3) randomly sampling spectral components from the same image datasets (Replacement). The standard complex Gaussian distribution is given by: $\mathcal{N}(0, \frac{1}{2}) + i\mathcal{N}(0, \frac{1}{2})$. The figures (a), (b) and (c) show the coalition filtering results with the spectral coalition: $\{J_0\}$. The figures (d), (e) and (f) show the coalition filtering results with the spectral coalition: $\{J_1, J_2, J_3, J_4, J_5, J_6, J_7\}$. The figures (g) to (l) show the examples of the measured spectral importance distributions of a *resnet18* and a *efficientnet_v2_s* (both are pre-trained on *ImageNet*) with the three assignment strategies.

6.B.3 Proof for Spectral Coalition Information Identity Theorem

Proof for Spectral Coalition Information Identity. Suppose the probability measures $P(x)$, $P(x, y)$, $P(y|x)$, and $Q(y|x)$ are absolutely continuous with respect to x on domain $\mathcal{X} \bowtie \tilde{\mathcal{I}}$.

$$\mathbb{I}(\mathcal{X} \bowtie \tilde{\mathcal{I}}, \mathcal{Y}) = \int_{\mathcal{X} \bowtie \tilde{\mathcal{I}}} \sum_{y \in \mathcal{Y}} P(x, y) \cdot \log \frac{P(x, y)}{P(x) \cdot P(y)} dx \quad (6.16)$$

$$= \int_{\mathcal{X} \bowtie \tilde{\mathcal{I}}} \sum_{y \in \mathcal{Y}} P(x, y) \cdot \log \left(\frac{P(y|x) \cdot P(x)}{P(y) \cdot P(x)} \cdot \frac{Q(y|x)}{Q(y|x)} \right) dx \quad (6.17)$$

$$= \int_{\mathcal{X} \bowtie \tilde{\mathcal{I}}} \sum_{y \in \mathcal{Y}} P(x, y) \cdot \log \left(\frac{P(y|x)}{Q(y|x)} \cdot \frac{1}{P(y)} \cdot Q(y|x) \right) dx \quad (6.18)$$

$$= \int_{\mathcal{X} \bowtie \tilde{\mathcal{I}}} P(x) \left(\sum_{y \in \mathcal{Y}} P(y|x) \cdot \log \frac{P(y|x)}{Q(y|x)} \right) dx \quad (6.19)$$

$$- \sum_{y \in \mathcal{Y}} \left(\int_{\mathcal{X} \bowtie \tilde{\mathcal{I}}} P(x, y) dx \right) \log P(y) \quad (6.20)$$

$$+ \int_{\mathcal{X} \bowtie \tilde{\mathcal{I}}} \sum_{y \in \mathcal{Y}} P(x, y) \cdot \log Q(y|x) dx \quad (6.21)$$

$$= \mathbb{E}_{x \in \mathcal{X} \bowtie \tilde{\mathcal{I}}} \underbrace{\text{KL}(P(y|x) || Q(y|x))}_{\text{point-wise}} + H(\mathcal{Y}) + \int_{\mathcal{X} \bowtie \tilde{\mathcal{I}}} P(x) \left(\sum_{y \in \mathcal{Y}} P(y|x) \cdot \log Q(y|x) \right) dx \quad (6.22)$$

$$= \mathbb{E}_{x \in \mathcal{X} \bowtie \tilde{\mathcal{I}}} \underbrace{\text{KL}(P(y|x) || Q(y|x))}_{\text{point-wise}} + H(\mathcal{Y}) + \mathbb{E}_{x \in \mathcal{X} \bowtie \tilde{\mathcal{I}}} \sum_{y \in \mathcal{Y}} P(y|x) \cdot \log Q(y|x) \quad (6.23)$$

$$= \mathbb{E}_{x \in \mathcal{X} \bowtie \tilde{\mathcal{I}}} \underbrace{\text{KL}(P(y|x) || Q(y|x))}_{\text{point-wise}} + H(\mathcal{Y}) + v(\tilde{\mathcal{I}}) + C \quad (6.24)$$

where $H(\mathcal{Y})$ is the Shannon entropy of the label set \mathcal{Y} .

□

6.C Information quantity relationship in spectral coalitions

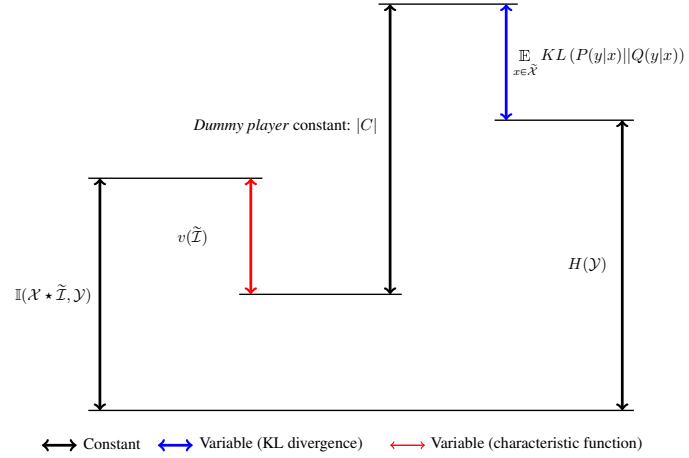


Figure 6.14: Information quantity relationship. This shows the theoretical information quantity relationship between what the characteristic function v measures and the mutual information $I(X \bowtie \tilde{\mathcal{I}}, \mathcal{Y})$. For a given coalition $\tilde{\mathcal{I}}$, a dataset $\langle \mathcal{X}, \mathcal{Y} \rangle$ and a classifier Q , the v measures how much information the classifier Q utilizes in decisions. The measured results are then used to compute the marginal contributions of features.

6.C.1 Partitioning spectrum with ℓ_∞ ball over ℓ_2 ball

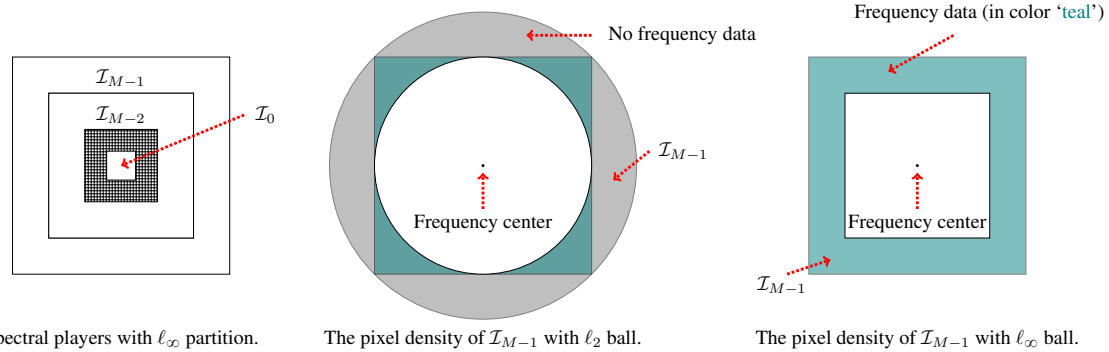


Figure 6.15: Two spectral band partitioning schemes. This shows the motivation we choose ℓ_∞ ball over ℓ_2 ball in partitioning the frequency domain into the M bands (i.e., M ‘spectral players’) over 2D Fourier spectrum. The frequency data density of the spectral players with ℓ_∞ remains a constant. However, the frequency data density of the spectral players with ℓ_2 is not a constant since some frequency components do not present. This motivates us to empirically choose ℓ_∞ metric to form spectral players in implementation.

6.C.2 Normalizing summarized SIDs

We normalize the above result and set:

$$S(v) := \frac{\left| \beta^T \bar{\Psi}(v) - \frac{\|\beta\|_1}{M} \right|}{\sup \left| \beta^T \bar{\Psi}(v) - \frac{\|\beta\|_1}{M} \right|} \quad (6.25)$$

$$= \frac{\left| \beta^T \bar{\Psi}(v) - \frac{\|\beta\|_1}{M} \right|}{\sup \left| \|\beta\|_2 \cdot \|\bar{\Psi}(v)\|_2 - \frac{\|\beta\|_1}{M} \right|} \quad (6.26)$$

$$= \frac{\left| \beta^T \bar{\Psi}(v) - \frac{\|\beta\|_1}{M} \right|}{\left| \|\beta\|_2 - \frac{\|\beta\|_1}{M} \right|} \quad (6.27)$$

$$= \left| \frac{\bar{\beta}^T \bar{\Psi}(v) - \frac{1}{M} \frac{\|\beta\|_1}{\|\beta\|_2}}{1 - \frac{1}{M} \frac{\|\beta\|_1}{\|\beta\|_2}} \right|. \quad (6.28)$$

where $\bar{\beta} = \frac{\beta}{\|\beta\|_2}$ and $\sup \left| \beta^T \bar{\Psi}(v) - \frac{\|\beta\|_1}{M} \right|$ is derived by:

$$\sup \left| \beta^T \bar{\Psi}(v) - \frac{\|\beta\|_1}{M} \right| = \left| \sup \beta^T \bar{\Psi}(v) - \frac{\|\beta\|_1}{M} \right| \quad (6.29)$$

$$= \left| \sup \|\beta\|_2 \cdot \|\bar{\Psi}(v)\|_2 - \frac{\|\beta\|_1}{M} \right| \quad \text{s.t. } \|\bar{\Psi}(v)\|_1 = 1 \quad (6.30)$$

$$= \left| \|\beta\|_2 - \frac{\|\beta\|_1}{M} \right| \quad \text{since } \|\bar{\Psi}(v)\|_2^2 \leq \|\bar{\Psi}(v)\|_1^2. \quad (6.31)$$

Set $\eta = \frac{1}{M} \frac{\|\beta\|_1}{\|\beta\|_2}$:

$$S(v) = \left| \frac{\bar{\beta}^T \bar{\Psi}(v) - \eta}{1 - \eta} \right|. \quad (6.32)$$

□

6.C.3 How many samples are sufficient?

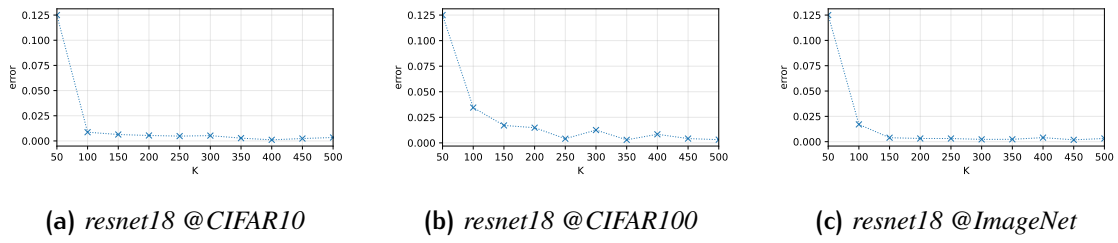


Figure 6.16: Convergence of relative estimation errors converge with respect to the numbers of samples K. The errors are measured by: $\frac{1}{M} \|\Psi^{(i+1)}(v) - \Psi^{(i)}(v)\|_1$ where $\Psi^{(i)}(v)$ denotes the i-th measured spectral importance distribution with respect to characteristic function v . The experiments are conducted on *CIFAR10*, *CIFAR100* and *ImageNet* with *resnet18*.

Error bound analysis. Let K be the number of the samples of some baseline dataset. Let:

$$\Delta v(\tilde{\mathcal{J}}, \mathcal{J}_i) := v(\tilde{\mathcal{J}} \cup \{\mathcal{J}_i\}) - v(\tilde{\mathcal{J}}) \quad (6.33)$$

and

$$\Delta v(\mathcal{J}_i) := (\Delta v(\tilde{\mathcal{J}}, \mathcal{J}_i))_{\tilde{\mathcal{J}} \subseteq \mathcal{J}} \quad (6.34)$$

and

$$W := \left(\frac{1}{M} \binom{M-1}{|\tilde{\mathcal{J}}|}^{-1} \right)_{\tilde{\mathcal{J}} \subseteq \mathcal{J}}. \quad (6.35)$$

Hence:

$$\psi_i(\mathcal{J}, v) = W^T \Delta v(\mathcal{J}_i) \quad (6.36)$$

where $\|W\|_1 \equiv 1$ since W is a probability distribution. Let $\bar{\psi}_i, \Delta\bar{v}(\mathcal{J}_i)$ and $\Delta\bar{v}(\tilde{\mathcal{J}}, \mathcal{J}_i)$ be estimations with K samples using Monte Carlo sampling. The error bound with ℓ_1 norm is given by:

$$\epsilon \stackrel{\text{def}}{=} \sup_i \|\bar{\psi}_i(\mathcal{J}, v) - \psi_i(\mathcal{J}, v)\|_1 = \sup_i \|W^T \Delta\bar{v}(\mathcal{J}_i) - W^T \Delta v(\mathcal{J}_i)\|_1 \quad (6.37)$$

$$\leq \sup_i \|W\|_1 \cdot \|\Delta\bar{v}(\mathcal{J}_i) - \Delta v(\mathcal{J}_i)\|_\infty \quad (\text{Hölder's inequality}) \quad (6.38)$$

$$= \sup_i \left\| \sum_{\tilde{\mathcal{J}} \subseteq \mathcal{J} \setminus \mathcal{J}_i} (\Delta\bar{v}(\tilde{\mathcal{J}}, \mathcal{J}_i) - \Delta v(\tilde{\mathcal{J}}, \mathcal{J}_i)) \right\|_\infty \quad (6.39)$$

$$\leq \sup_i 2^{M-1} \cdot \sup_{\tilde{\mathcal{J}}} \|\Delta\bar{v}(\tilde{\mathcal{J}}, \mathcal{J}_i) - \Delta v(\tilde{\mathcal{J}}, \mathcal{J}_i)\|_\infty \quad (6.40)$$

$$= \sup_i 2^{M-1} \cdot \sup_{\tilde{\mathcal{J}}} \|\Delta\bar{v}(\tilde{\mathcal{J}}, \mathcal{J}_i) - \Delta v(\tilde{\mathcal{J}}, \mathcal{J}_i)\|_1 \quad (6.41)$$

$$\leq 2^{M-1} \cdot \left\{ \frac{\text{Var}(\Delta\bar{v})}{K} \right\}^{\frac{1}{2}} \quad (6.42)$$

where $\text{Var}(\Delta\bar{v})$ gives the upper bound of the variance of $\Delta\bar{v}(\tilde{\mathcal{J}}, \mathcal{J}_i)$.

7 | FUTURE WORK

7.1 Introduction

THIS thesis has emphasized a theoretical understanding of the principles of Lipschitz continuity in neural networks. Building upon the foundations laid herein, we outline several promising directions for further exploration, including ongoing research currently in preparation as well as avenues for future investigation.

7.2 Spectral-gap regularization

A linear unit, parameterized by θ , *i.e.*, a fully connected layer or convolutional operation, represents an input z into $\text{rank}(\theta)$ orthogonal subspaces:

$$\theta z = \sum_{i=1}^{\text{rank}(\theta)} \sigma_i u_i v_i^\top, \quad (7.1)$$

where σ_i , u_i , and v_i denote the i -th singular value, left-singular vector, and right-singular vector, respectively. The *spectral gap* between σ_i and σ_j is defined as:

$$|\sigma_i - \sigma_j|. \quad (7.2)$$

One theoretical insight gained from Chapters 3–4 is that smaller spectral gaps amplify the influence of stochastic noise. This observation motivates the introduction of a regularization term:

$$|\sigma_{\max} - \sigma_{\min}|, \quad (7.3)$$

which has the following effects:

- a **smaller gap** encourages whitening of the subspaces by distributing features more evenly across all subspaces. This helps mitigate overfitting to dominant features and promotes fair feature learning;

- a **larger gap** may improve training stability but can also increase the Lipschitz constant, potentially reducing robustness.

7.3 Spectrum-gradient alignment

The stochastic dynamics of Lipschitz continuity, as presented in Chapter 4, reveal that the alignment between the gradient of the loss with respect to parameters and the principal direction of the parameter matrix governs the deterministic component in the evolution of the Lipschitz constant. Specifically, this alignment is captured by:

$$\mu^{(\ell)}(t) = \frac{1}{\sigma_1^{(\ell)}(t)} \left\langle \mathbf{J}_{\text{op}}^{(\ell)}(t), -\text{vec} \left[\nabla^{(\ell)} \mathcal{L}_f(\boldsymbol{\theta}(t)) \right] \right\rangle, \quad (7.4)$$

where $\sigma_1^{(\ell)}(t)$ is the largest singular value and $\mathbf{J}_{\text{op}}^{(\ell)}(t)$ denotes the principal direction of the parameter matrix at layer ℓ and time t .

Motivated by this insight, we propose a regularization term that explicitly controls this alignment through:

$$\left| \left\langle \mathbf{J}_{\text{op}}^{(\ell)}(t), -\text{vec} \left[\nabla^{(\ell)} \mathcal{L}_f(\boldsymbol{\theta}(t)) \right] \right\rangle \right|, \quad (7.5)$$

which has the following implications:

- a **higher alignment** promotes an increase in the Lipschitz constant during training, thereby reducing robustness;
- a **lower alignment** suppresses the growth of the Lipschitz constant, leading to improved robustness.

7.4 Conclusions

This chapter has outlined several promising avenues for future research inspired by the theoretical and empirical findings of this thesis. In continual learning, a deeper understanding of the dynamics of pretraining knowledge retention in LLMs may guide the development of novel optimization methods. In spectral analysis, regularization based on spectral-gaps and spectrum-gradient alignment offers a principled approach for improving both robustness and generalization.

8 | CONCLUSIONS

THIS thesis advances a principled understanding of the **principles of Lipschitz continuity in neural networks** from a **complementary dichotomy of perspectives**: an **internal** perspective — focusing on the temporal evolution of Lipschitz continuity in neural networks during training (*i.e.*, **Training Dynamics**); and an **external** perspective — investigating how Lipschitz continuity modulates the behavior of neural networks with respect to features in the input data, particularly its role in governing frequency signal propagation (*i.e.*, **Modulation of Frequency Signal Propagation**).

The inquiry thus is guided by three primary research questions (RQs) framed within a structured approach: (RQ1) **State of Knowledge** — what is the state of knowledge of Lipschitz continuity in deep learning? (RQ2) **Training Dynamics** — how does Lipschitz continuity of neural networks evolve over time during training? (RQ3) **Modulation of Frequency Signal Propagation** — how does Lipschitz continuity modulate the frequency signal propagation in neural networks, and how does this help us understand the global robustness of image models? Each primary research question gives rise to a set of secondary research questions (SRQs), addressed across one or two dedicated chapters. The research was conducted cumulatively during the Ph.D. training. This thesis compiles and presents a selection of research articles — either published or under review as of the submission date — into a **self-contained, modular, coherent, monograph-style** presentation format, all centered on the principles of Lipschitz continuity in neural networks.

In response to these research questions, in Chapter 2, this thesis first consolidates the existing state of knowledge of Lipschitz continuity in deep learning through a comprehensive literature review. In Chapter 3–4, it then develops a stochastic dynamic framework for analyzing Lipschitz continuity during training by drawing on tools from operator theory, perturbation analysis, and high-dimensional stochastic differential equations (SDEs). Finally, in Chapter 5, it conducts a Fourier-theoretic analysis to examine how Lipschitz continuity governs the modulation of frequency-domain signals in neural networks. Additionally, in Chapter 6, the thesis introduces an interpretability perspective by linking frequency-domain perturbations to global robustness through the underpinning lens of Lipschitz continuity. In doing so, it establishes a mathematically rigorous and conceptually unified understanding of Lipschitz continuity in deep learning, moving beyond the prevailing static and regularization-focused views in the literature.

8.1 Research Summary

(RQ1) State of Knowledge. (RQ1) gives rise to two secondary research questions: (SRQ1) **Theoretical Foundations** — what are the theoretical foundations of Lipschitz continuity in deep learning? (SRQ2) **Regularization Mechanism** — how does Lipschitz continuity serve as a regularization mechanism for improving robustness and generalization capabilities in deep learning?

Contributions of Addressing (SRQ1) and (SRQ2). To address (SRQ1) and (SRQ2), Chapter 2 presents a comprehensive literature review that synthesizes theoretical foundations, estimation methods, regularization approaches, and certifiable robustness. This chapter consolidates existing knowledge of Lipschitz continuity in deep learning, and provides a background for the research.

(RQ2) Training Dynamics. (RQ2) gives rise to two secondary research questions: (SRQ3) **Parameter Space Perturbation** — how do the spectral properties (*i.e.*, singular values) of parameter matrices change in training? (SRQ4) **Stochastic Dynamic Analysis of Lipschitz Continuity** — how does Lipschitz continuity evolve over time during training in neural networks?

Contributions of Addressing (SRQ3). To address (SRQ3), Chapter 3 develops an operator-theoretic framework for analyzing spectral variations in parameter matrices during optimization, enabling stochastic analysis of their spectral properties. As a direct corollary, this framework yields an explicit analytic formulation of the operator-norm Hessian of rectangular matrices.

Contributions of Addressing (SRQ4). To address (SRQ4), building on the foundations laid in Chapter 3, Chapter 4 establishes a rigorous theoretical framework for analyzing the dynamics of Lipschitz continuity using a system of stochastic differential equations (SDEs), applying Itô’s lemma to derive analytical expressions for the temporal evolution of Lipschitz bounds. These results reveal three fundamental driving factors governing the dynamics of Lipschitz continuity in neural networks:

- (i) the projection of gradient flows, induced by the optimization dynamics, onto the operator-norm Jacobian of parameter matrices;
- (ii) the projection of gradient noise, arising from the randomness in mini-batch sampling, onto the operator-norm Jacobian;

- (iii) the projection of the gradient noise onto the operator-norm Hessian of parameter matrices.

The theoretical framework is validated through numerical experiments with multiple regularization configurations. Furthermore, our theoretical framework sheds light on how noisy supervision, parameter initialization, batch size, and mini-batch sampling trajectories, among other factors, shape the evolution of the Lipschitz continuity of neural networks. To the best of our knowledge, it is the first theoretical framework rigorously analyzing the temporal evolution of Lipschitz continuity of neural networks during training.

(RQ3) Modulation of Frequency Signal Propagation. (RQ3) gives rise to two secondary research questions: (SRQ5) **Fourier Analysis of Lipschitz Continuity** — how does Lipschitz continuity modulate frequency signal propagation in image models? (SRQ6) **Interpreting Global Robustness** — how can global robustness be explained through the lens of spectral bias in Lipschitz continuity?

Contributions of Addressing (SRQ5). To address (SRQ5), Chapter 5 presents a Fourier-theoretic analysis of Lipschitz continuity, drawing on tools from harmonic analysis, information theory, and Shapley value theory, supported by analytical derivations and verification examples. To complement the theoretical findings, we also provide empirical studies investigating the relationship between Lipschitz continuity and frequency-domain features.

The analysis begins with a spectral decomposition of the Lipschitz continuity bound, revealing a **spectral bias: high-frequency components contribute disproportionately to the Lipschitz constant**, amplified by the frequency ℓ_2 -norm. This result is consistent with empirical observations, showing that high-frequency signals tend to increase the Lipschitz constants of neural networks during training.

Furthermore, we derive a frequency-domain perturbation bound, showing that the functional perturbation caused by frequency-domain input perturbation is approximately bounded above by the spectral contribution of the Lipschitz continuity decomposition. As a direct corollary, we demonstrate that the variational mutual information between classifier outputs and labels — under frequency-domain input perturbations — is also upper bounded by this spectral contribution. **These results reveals how Lipschitz continuity modulates feature propagation in the frequency domain.**

Contributions of Addressing (SRQ6). To address (SRQ6), Chapter 6, building on the theoretical framework developed in Chapter 5, proposes a method for quantifying

the global robustness of image classifiers. This method leverages Shapley value theory to measure the predictive importance of frequency components in input signals.

The empirical results reveal that the importance of frequency components — quantified via Shapley values — aligns with model sensitivity under a variety of perturbation sources, including corruptions and adversarial attacks. These correlations support the hypothesis that certain frequency bands disproportionately influence predictive robustness. Together, these findings reinforce the theoretical results and demonstrate that frequency-domain analysis offers a principled and interpretable approach for evaluating the global robustness of deep learning models.

8.2 Closing Remarks

In conclusion, this thesis establishes both theoretical and empirical foundations for understanding the **principles of Lipschitz continuity** in neural networks. Guided by three primary research questions, it advances our understanding of how Lipschitz continuity evolves over time during training, how it modulates frequency signal propagation, and how it can be used to interpret the global robustness of deep learning models.

BIBLIOGRAPHY

K. Aas, M. Jullum, and A. Løland. Explaining individual predictions when features are dependent: More accurate approximations to Shapley values. *Artificial Intelligence*, 298(C), Sept. 2021. ISSN 0004-3702. doi: 10.1016/j.artint.2021.103502. URL <https://doi.org/10.1016/j.artint.2021.103502>.

P.-A. Absil, R. Mahony, and R. Sepulchre. *Optimization Algorithms on Matrix Manifolds*. Princeton University Press, USA, 2007. ISBN 0691132984.

F. Amerehi and P. Healy. Label augmentation for neural networks robustness. In V. Lomonaco, S. Melacci, T. Tuytelaars, S. Chandar, and R. Pascanu, editors, *Proceedings of The 3rd Conference on Lifelong Learning Agents*, volume 274 of *Proceedings of Machine Learning Research*, pages 620–640. PMLR, 29 Jul–01 Aug 2025. URL <https://proceedings.mlr.press/v274/amerehi25a.html>.

C. Anil, J. Lucas, and R. Grosse. Sorting out Lipschitz function approximation. In K. Chaudhuri and R. Salakhutdinov, editors, *Proceedings of the 36th International Conference on Machine Learning*, volume 97 of *Proceedings of Machine Learning Research*, pages 291–301. PMLR, 09–15 Jun 2019. URL <https://proceedings.mlr.press/v97/anill19a.html>.

R. Anil, S. Borgeaud, J.-B. Alayrac, J. Yu, R. Soricut, J. Schalkwyk, A. M. Dai, A. Hauth, K. Millican, D. Silver, M. Johnson, I. Antonoglou, J. Schrittwieser, A. Glaese, J. Chen, E. Pitler, T. Lillicrap, A. Lazaridou, O. Firat, J. Molloy, M. Isard, P. R. Barham, T. Hennigan, B. Lee, F. Viola, M. Reynolds, Y. Xu, R. Doherty, E. Collins, C. Meyer, E. Rutherford, E. Moreira, K. Ayoub, M. Goel, J. Krawczyk, C. Du, E. Chi, H.-T. Cheng, E. Ni, P. Shah, P. Kane, B. Chan, M. Faruqui, A. Severyn, H. Lin, Y. Li, Y. Cheng, A. Ittycheriah, M. Mahdieh, M. Chen, P. Sun, D. Tran, S. Bagri, B. Lakshminarayanan, J. Liu, A. Orban, F. Güra, H. Zhou, X. Song, A. Boffy, H. Ganapathy, S. Zheng, H. Choe, Ágoston Weisz, T. Zhu, Y. Lu, S. Gopal, J. Kahn, M. Kula, J. Pittman, R. Shah, E. Taropa, M. A. Merey, M. Baeuml, Z. Chen, L. E. Shafey, Y. Zhang, O. Sercinoglu, G. Tucker, E. Piqueras, M. Krikun, I. Barr, N. Savinov, I. Danihelka, B. Roelofs, A. White, A. Andreassen, T. von Glehn, L. Yagati, M. Kazemi, L. Gonzalez, M. Khalman, J. Sygnowski, A. Frechette, C. Smith, L. Culp, L. Proleev, Y. Luan, X. Chen, J. Lottes, N. Schucher, F. Lebron, A. Rrustemi, N. Clay, P. Crone, T. Kociský, J. Zhao, B. Perz, D. Yu, H. Howard, A. Bloniarz, J. W. Rae, H. Lu, L. Sifre,

M. Maggioni, F. Alcober, D. Garrette, M. Barnes, S. Thakoor, J. Austin, G. Barth-Maron, W. Wong, R. Joshi, R. Chaabouni, D. Fatiha, A. Ahuja, G. S. Tomar, E. Senter, M. Chadwick, I. Kornakov, N. Attaluri, I. Iturraté, R. Liu, Y. Li, S. Cogan, J. Chen, C. Jia, C. Gu, Q. Zhang, J. Grimstad, A. J. Hartman, X. Garcia, T. S. Pillai, J. Devlin, M. Laskin, D. de Las Casas, D. Valter, C. Tao, L. Blanco, A. P. Badia, D. Reitter, M. Chen, J. Brennan, C. Rivera, S. Brin, S. Iqbal, G. Surita, J. Labanowski, A. Rao, S. Winkler, E. Parisotto, Y. Gu, K. Olszewska, R. Addanki, A. Miech, A. Louis, D. Teplyashin, G. Brown, E. Catt, J. Balaguer, J. Xiang, P. Wang, Z. Ashwood, A. Briukhov, A. Webson, S. Ganapathy, S. Sanghavi, A. Kannan, M.-W. Chang, A. Stjerngren, J. Djolonga, Y. Sun, A. Bapna, M. Aitchison, P. Pejman, H. Michalewski, T. Yu, C. Wang, J. Love, J. Ahn, D. Bloxwich, K. Han, P. Humphreys, T. Sellam, J. Bradbury, V. Godbole, S. Samangooei, B. Damoc, A. Kaskasoli, S. M. R. Arnold, V. Vasudevan, S. Agrawal, J. Riesa, D. Lepikhin, R. Tanburn, S. Srinivasan, H. Lim, S. Hodkinson, P. Shyam, J. Ferret, S. Hand, A. Garg, T. L. Paine, J. Li, Y. Li, M. Giang, A. Neitz, Z. Abbas, S. York, M. Reid, E. Cole, A. Chowdhery, D. Das, D. Rogozínska, V. Nikolaev, P. Sprechmann, Z. Nado, L. Zilka, F. Prost, L. He, M. Monteiro, G. Mishra, C. Welty, J. Newlan, D. Jia, M. Allamanis, C. H. Hu, R. de Liedekerke, J. Gilmer, C. Saroufim, S. Rijhwani, S. Hou, D. Shrivastava, A. Baddepudi, A. Goldin, A. Ozturk, A. Cassirer, Y. Xu, D. Sohn, D. Sachan, R. K. Amplayo, C. Swanson, D. Petrova, S. Narayan, A. Guez, S. Brahma, J. Landon, M. Patel, R. Zhao, K. Vil-lela, L. Wang, W. Jia, M. Rahtz, M. Giménez, L. Yeung, J. Keeling, P. Georgiev, D. Mincu, B. Wu, S. Haykal, R. Saputro, K. Vodrahalli, J. Qin, Z. Cankara, A. Sharma, N. Fernando, W. Hawkins, B. Neyshabur, S. Kim, A. Hutter, P. Agrawal, A. Castro-Ros, G. van den Driessche, T. Wang, F. Yang, S. yiin Chang, P. Komarek, R. McIl-roy, M. Lučić, G. Zhang, W. Farhan, M. Sharman, P. Natsev, P. Michel, Y. Bansal, S. Qiao, K. Cao, S. Shakeri, C. Butterfield, J. Chung, P. K. Rubenstein, S. Agrawal, A. Mensch, K. Soparkar, K. Lenc, T. Chung, A. Pope, L. Maggiore, J. Kay, P. Jhakra, S. Wang, J. Maynez, M. Phuong, T. Tobin, A. Tacchetti, M. Trebacz, K. Robinson, Y. Katariya, S. Riedel, P. Bailey, K. Xiao, N. Ghelani, L. Aroyo, A. Slone, N. Housby, X. Xiong, Z. Yang, E. Gribovskaya, J. Adler, M. Wirth, L. Lee, M. Li, T. Kagohara, J. Pavagadhi, S. Bridgers, A. Bortsova, S. Ghemawat, Z. Ahmed, T. Liu, R. Powell, V. Bolina, M. Iinuma, P. Zablotskaia, J. Besley, D.-W. Chung, T. Dozat, R. Co-manescu, X. Si, J. Greer, G. Su, M. Polacek, R. L. Kaufman, S. Tokumine, H. Hu, E. Buchatskaya, Y. Miao, M. Elhawaty, A. Siddhant, N. Tomasev, J. Xing, C. Greer, H. Miller, S. Ashraf, A. Roy, Z. Zhang, A. Ma, A. Filos, M. Besta, R. Blevins, T. Kli-menko, C.-K. Yeh, S. Changpinyo, J. Mu, O. Chang, M. Pajarskas, C. Muir, V. Cohen, C. L. Lan, K. Haridasan, A. Marathe, S. Hansen, S. Douglas, R. Samuel, M. Wang, S. Austin, C. Lan, J. Jiang, J. Chiu, J. A. Lorenzo, L. L. Sjösund, S. Cevey, Z. Gle-

icher, T. Avrahami, A. Boral, H. Srinivasan, V. Selo, R. May, K. Aisopos, L. Hussenot, L. B. Soares, K. Baumli, M. B. Chang, A. Recasens, B. Caine, A. Pritzel, F. Pavetic, F. Pardo, A. Gergely, J. Frye, V. Ramasesh, D. Horgan, K. Badola, N. Kassner, S. Roy, E. Dyer, V. C. Campos, A. Tomala, Y. Tang, D. E. Badawy, E. White, B. Mustafa, O. Lang, A. Jindal, S. Vikram, Z. Gong, S. Caelles, R. Hemsley, G. Thornton, F. Feng, W. Stokowiec, C. Zheng, P. Thacker, Çağlar Ünlü, Z. Zhang, M. Saleh, J. Svensson, M. Bileshi, P. Patil, A. Anand, R. Ring, K. Tsihlas, A. Vezer, M. Selvi, T. Shevlane, M. Rodriguez, T. Kwiatkowski, S. Daruki, K. Rong, A. Dafoe, N. FitzGerald, K. GuLemberg, M. Khan, L. A. Hendricks, M. Pellat, V. Feinberg, J. Cobon-Kerr, T. Sainath, M. Rauh, S. H. Hashemi, R. Ives, Y. Hasson, E. Noland, Y. Cao, N. Byrd, L. Hou, Q. Wang, T. Sottiaux, M. Paganini, J.-B. Lespiau, A. Moufarek, S. Hassan, K. Shivakumar, J. van Amersfoort, A. Mandhane, P. Joshi, A. Goyal, M. Tung, A. Brock, H. Sheahan, V. Misra, C. Li, N. Rakićević, M. Dehghani, F. Liu, S. Mittal, J. Oh, S. Noury, E. Sezener, F. Huot, M. Lamm, N. D. Cao, C. Chen, S. Mudgal, R. Stella, K. Brooks, G. Vasudevan, C. Liu, M. Chain, N. Melinkeri, A. Cohen, V. Wang, K. Seymore, S. Zubkov, R. Goel, S. Yue, S. Krishnakumaran, B. Albert, N. Hurley, M. Sano, A. Mohananey, J. Joughin, E. Filonov, T. Kępa, Y. Eldawy, J. Lim, R. Rishi, S. Badiezadegan, T. Bos, J. Chang, S. Jain, S. G. S. Padmanabhan, S. Puttagunta, K. Krishna, L. Baker, N. Kalb, V. Bedapudi, A. Kurzrok, S. Lei, A. Yu, O. Litvin, X. Zhou, Z. Wu, S. Sobell, A. Siciliano, A. Papir, R. Neale, J. Bragagnolo, T. Toor, T. Chen, V. Anklin, F. Wang, R. Feng, M. Gholami, K. Ling, L. Liu, J. Walter, H. Moghaddam, A. Kishore, J. Adamek, T. Mercado, J. Mallinson, S. Wandekar, S. Cagle, E. Ofek, G. Garrido, C. Lombriser, M. Mukha, B. Sun, H. R. Mohammad, J. Matak, Y. Qian, V. Peswani, P. Janus, Q. Yuan, L. Schelin, O. David, A. Garg, Y. He, O. Duzhyi, A. Älgmyr, T. Lottaz, Q. Li, V. Yadav, L. Xu, A. Chinien, R. Shivanna, A. Chuklin, J. Li, C. Spadine, T. Wolfe, K. Mohamed, S. Das, Z. Dai, K. He, D. von Dincklage, S. Upadhyay, A. Maurya, L. Chi, S. Krause, K. Salama, P. G. Rabinovitch, P. K. R. M, A. Selvan, M. Dektarev, G. Ghiasi, E. Guven, H. Gupta, B. Liu, D. Sharma, I. H. Shtacher, S. Paul, O. Akerlund, F.-X. Aubet, T. Huang, C. Zhu, E. Zhu, E. Teixeira, M. Fritze, F. Bertolini, L.-E. Marinescu, M. Bölle, D. Paulus, K. Gupta, T. Latkar, M. Chang, J. Sanders, R. Wilson, X. Wu, Y.-X. Tan, L. N. Thiet, T. Doshi, S. Lall, S. Mishra, W. Chen, T. Luong, S. Benjamin, J. Lee, E. Andrejczuk, D. Rabiej, V. Ranjan, K. Styrc, P. Yin, J. Simon, M. R. Harriott, M. Bansal, A. Robsky, G. Bacon, D. Greene, D. Mirylenka, C. Zhou, O. Sarvana, A. Goyal, S. Andermatt, P. Siegler, B. Horn, A. Israel, F. Pongetti, C.-W. L. Chen, M. Selvatici, P. Silva, K. Wang, J. Tolins, K. Guu, R. Yoge, X. Cai, A. Agostini, M. Shah, H. Nguyen, N. O. Donnaile, S. Pereira, L. Friso, A. Stambler, A. Kurzrok, C. Kuang, Y. Romanikhin, M. Geller, Z. Yan, K. Jang, C.-C. Lee, W. Fica, E. Malmi, Q. Tan, D. Banica, D. Balle, R. Pham, Y. Huang,

D. Avram, H. Shi, J. Singh, C. Hidey, N. Ahuja, P. Saxena, D. Dooley, S. P. Potharaju, E. O'Neill, A. Gokulchandran, R. Foley, K. Zhao, M. Dusenberry, Y. Liu, P. Mehta, R. Kotikalapudi, C. Safranek-Shrader, A. Goodman, J. Kessinger, E. Globen, P. Kolhar, C. Gorgolewski, A. Ibrahim, Y. Song, A. Eichenbaum, T. Brovelli, S. Potluri, P. Lahoti, C. Baetu, A. Ghorbani, C. Chen, A. Crawford, S. Pal, M. Sridhar, P. Gurita, A. Mujika, I. Petrovski, P.-L. Cedoz, C. Li, S. Chen, N. D. Santo, S. Goyal, J. Punjabi, K. Kappagantu, C. Kwak, P. LV, S. Velury, H. Choudhury, J. Hall, P. Shah, R. Figueira, M. Thomas, M. Lu, T. Zhou, C. Kumar, T. Jurdi, S. Chikkerur, Y. Ma, A. Yu, S. Kwak, V. Ähdel, S. Rajayogam, T. Choma, F. Liu, A. Barua, C. Ji, J. H. Park, V. Hellendoorn, A. Bailey, T. Bilal, H. Zhou, M. Khatir, C. Sutton, W. Rzadkowski, F. Macintosh, R. Vij, K. Shagin, P. Medina, C. Liang, J. Zhou, P. Shah, Y. Bi, A. Dankovics, S. Banga, S. Lehmann, M. Bredesen, Z. Lin, J. E. Hoffmann, J. Lai, R. Chung, K. Yang, N. Balani, A. Bražinskas, A. Sozanschi, M. Hayes, H. F. Alcalde, P. Makarov, W. Chen, A. Stella, L. Snijders, M. Mandl, A. Kärrman, P. Nowak, X. Wu, A. Dyck, K. Vaidyanathan, R. R, J. Mallet, M. Rudominer, E. Johnston, S. Mittal, A. Udathu, J. Christensen, V. Verma, Z. Irving, A. Santucci, G. Elsayed, E. Davoodi, M. Georgiev, I. Tenney, N. Hua, G. Cideron, E. Leurent, M. Alnahlawi, I. Georgescu, N. Wei, I. Zheng, D. Scandinaro, H. Jiang, J. Snoek, M. Sundararajan, X. Wang, Z. Ontiveros, I. Karo, J. Cole, V. Rajashekhar, L. Tumeh, E. Ben-David, R. Jain, J. Uesato, R. Datta, O. Bunyan, S. Wu, J. Zhang, P. Stanczyk, Y. Zhang, D. Steiner, S. Naskar, M. Azzam, M. Johnson, A. Paszke, C.-C. Chiu, J. S. Elias, A. Mohiuddin, F. Muhammad, J. Miao, A. Lee, N. Vieillard, J. Park, J. Zhang, J. Stanway, D. Garmon, A. Karmarkar, Z. Dong, J. Lee, A. Kumar, L. Zhou, J. Evens, W. Isaac, G. Irving, E. Loper, M. Fink, I. Arkatkar, N. Chen, I. Shafran, I. Petrychenko, Z. Chen, J. Jia, A. Levskaya, Z. Zhu, P. Grabowski, Y. Mao, A. Magni, K. Yao, J. Snaider, N. Casagrande, E. Palmer, P. Suganthan, A. Castaño, I. Giannoumis, W. Kim, M. Rybiński, A. Sreevatsa, J. Prendki, D. Soergel, A. Goedekemeyer, W. Gierke, M. Jafari, M. Gaba, J. Wiesner, D. G. Wright, Y. Wei, H. Vashisht, Y. Kulizhskaya, J. Hoover, M. Le, L. Li, C. Iwuanyanwu, L. Liu, K. Ramirez, A. Khorlin, A. Cui, T. LIN, M. Wu, R. Aguilar, K. Pallo, A. Chakladar, G. Perng, E. A. Abellan, M. Zhang, I. Dasgupta, N. Kushman, I. Penchev, A. Repina, X. Wu, T. van der Weide, P. Ponnappalli, C. Kaplan, J. Sims, S. Li, O. Dousse, F. Yang, J. Piper, N. Ie, R. Pasumarthi, N. Lintz, A. Vijayakumar, D. Andor, P. Valenzuela, M. Lui, C. Paduraru, D. Peng, K. Lee, S. Zhang, S. Greene, D. D. Nguyen, P. Kurylowicz, C. Hardin, L. Dixon, L. Janzer, K. Choo, Z. Feng, B. Zhang, A. Singhal, D. Du, D. McKinnon, N. Antropova, T. Bolukbasi, O. Keller, D. Reid, D. Finchelstein, M. A. Raad, R. Crocker, P. Hawkins, R. Dadashi, C. Gaffney, K. Franko, A. Bulanova, R. Leblond, S. Chung, H. Askham, L. C. Cobo, K. Xu, F. Fischer, J. Xu, C. Sorokin, C. Alberti, C.-C. Lin, C. Evans, A. Dimitriev, H. Forbes,

D. Banarse, Z. Tung, M. Omernick, C. Bishop, R. Sterneck, R. Jain, J. Xia, E. Amid, F. Piccinno, X. Wang, P. Banzal, D. J. Mankowitz, A. Polozov, V. Krakovna, S. Brown, M. Bateni, D. Duan, V. Firoiu, M. Thotakuri, T. Natan, M. Geist, S. tan Girgin, H. Li, J. Ye, O. Roval, R. Tojo, M. Kwong, J. Lee-Thorp, C. Yew, D. Sinopalnikov, S. Ramos, J. Mellor, A. Sharma, K. Wu, D. Miller, N. Sonnerat, D. Vnukov, R. Greig, J. Beattie, E. Caveness, L. Bai, J. Eisenschlos, A. Korchemniy, T. Tsai, M. Jasarevic, W. Kong, P. Dao, Z. Zheng, F. Liu, F. Yang, R. Zhu, T. H. Teh, J. Sanmiya, E. Gladchenko, N. Trdin, D. Toyama, E. Rosen, S. Tavakkol, L. Xue, C. Elkind, O. Woodman, J. Carpenter, G. Papamakarios, R. Kemp, S. Kafle, T. Grunina, R. Sinha, A. Talbert, D. Wu, D. Owusu-Afriyie, C. Du, C. Thornton, J. Pont-Tuset, P. Narayana, J. Li, S. Fatehi, J. Wieting, O. Ajmeri, B. Uria, Y. Ko, L. Knight, A. Héliou, N. Niu, S. Gu, C. Pang, Y. Li, N. Levine, A. Stolovich, R. Santamaria-Fernandez, S. Goenka, W. Yustalim, R. Strudel, A. Elqursh, C. Deck, H. Lee, Z. Li, K. Levin, R. Hoffmann, D. Holtmann-Rice, O. Bachem, S. Arora, C. Koh, S. H. Yeganeh, S. Pöder, M. Tariq, Y. Sun, L. Ionita, M. Seyedhosseini, P. Tafti, Z. Liu, A. Gulati, J. Liu, X. Ye, B. Chrzaszcz, L. Wang, N. Sethi, T. Li, B. Brown, S. Singh, W. Fan, A. Parisi, J. Stanton, V. Koverkathu, C. A. Choquette-Choo, Y. Li, T. Lu, A. Ittycheriah, P. Shroff, M. Varadarajan, S. Bahargam, R. Willoughby, D. Gaddy, G. Desjardins, M. Cornero, B. Robenek, B. Mittal, B. Albrecht, A. Shenoy, F. Moiseev, H. Jacobsson, A. Ghaffarkhah, M. Rivière, A. Walton, C. Crepy, A. Parrish, Z. Zhou, C. Farabet, C. Radebaugh, P. Srinivasan, C. van der Salm, A. Fidjeland, S. Scellato, E. Latorre-Chimoto, H. Klimczak-Plucińska, D. Bridson, D. de Cesare, T. Hudson, P. Mendolicchio, L. Walker, A. Morris, M. Mauger, A. Guseynov, A. Reid, S. Odoom, L. Loher, V. Cotruta, M. Yenugula, D. Grewe, A. Petrushkina, T. Duerig, A. Sanchez, S. Yadlowsky, A. Shen, A. Globerson, L. Webb, S. Dua, D. Li, S. Bhupatiraju, D. Hurt, H. Qureshi, A. Agarwal, T. Shani, M. Eyal, A. Khare, S. R. Belle, L. Wang, C. Tekur, M. S. Kale, J. Wei, R. Sang, B. Saeta, T. Liechty, Y. Sun, Y. Zhao, S. Lee, P. Nayak, D. Fritz, M. R. Vuyyuru, J. Aslanides, N. Vyas, M. Wicke, X. Ma, E. Eltyshev, N. Martin, H. Cate, J. Manyika, K. Amiri, Y. Kim, X. Xiong, K. Kang, F. Luisier, N. Tripuraneni, D. Madras, M. Guo, A. Waters, O. Wang, J. Ainslie, J. Baldridge, H. Zhang, G. Pruthi, J. Bauer, F. Yang, R. Mansour, J. Gelman, Y. Xu, G. Polovets, J. Liu, H. Cai, W. Chen, X. Sheng, E. Xue, S. Ozair, C. Angermueller, X. Li, A. Sinha, W. Wang, J. Wiesinger, E. Koukoumidis, Y. Tian, A. Iyer, M. Gurumurthy, M. Goldenson, P. Shah, M. Blake, H. Yu, A. Urbanowicz, J. Palomaki, C. Fernando, K. Durden, H. Mehta, N. Momchev, E. Rahimtoroghi, M. Georgaki, A. Raul, S. Ruder, M. Redshaw, J. Lee, D. Zhou, K. Jalan, D. Li, B. Hechtman, P. Schuh, M. Nasr, K. Milan, V. Mikulik, J. Franco, T. Green, N. Nguyen, J. Kelley, A. Mahendru, A. Hu, J. Howland, B. Vargas, J. Hui, K. Bansal, V. Rao, R. Ghiya, E. Wang, K. Ye, J. M. Sarr, M. M. Preston, M. Elish, S. Li, A. Kaku,

J. Gupta, I. Pasupat, D.-C. Juan, M. Someswar, T. M., X. Chen, A. Amini, A. Fabrikant, E. Chu, X. Dong, A. Muthal, S. Buthpitiya, S. Jauhari, N. Hua, U. Khandelwal, A. Hitron, J. Ren, L. Rinaldi, S. Drath, A. Dabush, N.-J. Jiang, H. Godhia, U. Sachs, A. Chen, Y. Fan, H. Taitelbaum, H. Noga, Z. Dai, J. Wang, C. Liang, J. Hamer, C.-S. Ferng, C. Elkind, A. Atias, P. Lee, V. Listík, M. Carlen, J. van de Kerkhof, M. Pikus, K. Zaher, P. Müller, S. Zykova, R. Stefanec, V. Gatsko, C. Hirnschall, A. Sethi, X. F. Xu, C. Ahuja, B. Tsai, A. Stefanou, B. Feng, K. Dhandhania, M. Katyal, A. Gupta, A. Parulekar, D. Pitta, J. Zhao, V. Bhatia, Y. Bhavnani, O. Alhadlaq, X. Li, P. Danenberg, D. Tu, A. Pine, V. Filippova, A. Ghosh, B. Limonchik, B. Urala, C. K. Lanka, D. Clive, Y. Sun, E. Li, H. Wu, K. Hongtongsak, I. Li, K. Thakkar, K. Omarov, K. Majmundar, M. Alverson, M. Kucharski, M. Patel, M. Jain, M. Zabelin, P. Pelagatti, R. Kohli, S. Kumar, J. Kim, S. Sankar, V. Shah, L. Ramachandruni, X. Zeng, B. Bariach, L. Weidinger, T. Vu, A. Andreev, A. He, K. Hui, S. Kashem, A. Subramanya, S. Hsiao, D. Hassabis, K. Kavukcuoglu, A. Sadovsky, Q. Le, T. Strohman, Y. Wu, S. Petrov, J. Dean, and O. Vinyals. Gemini: A family of highly capable multimodal models, 2025. URL <https://arxiv.org/abs/2312.11805>.

D. Applebaum. *Lévy Processes and Stochastic Calculus*. Cambridge Studies in Advanced Mathematics. Cambridge University Press, 2nd edition, 2009.

M. Arjovsky, A. Shah, and Y. Bengio. Unitary evolution recurrent neural networks. In M. F. Balcan and K. Q. Weinberger, editors, *Proceedings of The 33rd International Conference on Machine Learning*, volume 48 of *Proceedings of Machine Learning Research*, pages 1120–1128, New York, New York, USA, 20–22 Jun 2016. PMLR. URL <https://proceedings.mlr.press/v48/arjovsky16.html>.

M. Arjovsky, S. Chintala, and L. Bottou. Wasserstein generative adversarial networks. In D. Precup and Y. W. Teh, editors, *Proceedings of the 34th International Conference on Machine Learning*, volume 70 of *Proceedings of Machine Learning Research*, pages 214–223. PMLR, 06–11 Aug 2017. URL <https://proceedings.mlr.press/v70/arjovsky17a.html>.

R. J. Aumann and M. Maschler. Game theoretic analysis of a bankruptcy problem from the Talmud. *Journal of economic theory*, 36(2):195–213, 1985.

Y. Aumann and Y. Dombb. The efficiency of fair division with connected pieces. *ACM Transactions on Economics and Computation (TEAC)*, 3(4):1–16, 2015.

L. J. Ba, J. R. Kiros, and G. E. Hinton. Layer normalization. 2016. URL <http://arxiv.org/abs/1607.06450>.

T. Bai, J. Luo, J. Zhao, B. Wen, and Q. Wang. Recent advances in adversarial training for adversarial robustness. In Z.-H. Zhou, editor, *Proceedings of the Thirtieth International Joint Conference on Artificial Intelligence, IJCAI-21*, pages 4312–4321. International Joint Conferences on Artificial Intelligence Organization, 8 2021. doi: 10.24963/ijcai.2021/591. URL <https://doi.org/10.24963/ijcai.2021/591>. Survey Track.

N. Bansal, X. Chen, and Z. Wang. Can we gain more from orthogonality regularizations in training deep CNNs? In *Proceedings of the 32nd International Conference on Neural Information Processing Systems*, NIPS’18, page 4266–4276, Red Hook, NY, USA, 2018. Curran Associates Inc.

P. L. Bartlett, D. J. Foster, and M. Telgarsky. Spectrally-normalized margin bounds for neural networks. In *Proceedings of the 31st International Conference on Neural Information Processing Systems*, NIPS’17, page 6241–6250, Red Hook, NY, USA, 2017. Curran Associates Inc. ISBN 9781510860964.

D. Bau, B. Zhou, A. Khosla, A. Oliva, and A. Torralba. Network dissection: Quantifying interpretability of deep visual representations. In *Proceedings of the IEEE conference on computer vision and pattern recognition*, pages 6541–6549, 2017.

J. Behrmann, W. Grathwohl, R. T. Q. Chen, D. Duvenaud, and J.-H. Jacobsen. Invertible residual networks. In K. Chaudhuri and R. Salakhutdinov, editors, *Proceedings of the 36th International Conference on Machine Learning*, volume 97 of *Proceedings of Machine Learning Research*, pages 573–582. PMLR, 09–15 Jun 2019. URL <https://proceedings.mlr.press/v97/behrmann19a.html>.

L. Bereska and S. Gavves. Mechanistic interpretability for AI safety — A review. *Transactions on Machine Learning Research*, 2024. ISSN 2835-8856. URL <https://openreview.net/forum?id=ePUVetPKu6>. Survey Certification, Expert Certification.

A. Binder, G. Montavon, S. Lapuschkin, K.-R. Müller, and W. Samek. Layer-wise relevance propagation for neural networks with local renormalization layers. In *Artificial Neural Networks and Machine Learning—ICANN 2016: 25th International Conference on Artificial Neural Networks, Barcelona, Spain, September 6-9, 2016, Proceedings, Part II 25*, pages 63–71. Springer, 2016.

Å. Björck and C. Bowie. An iterative algorithm for computing the best estimate of an orthogonal matrix. *SIAM Journal on Numerical Analysis*, 8(2):358–364, 1971. doi: 10.1137/0708036. URL <https://doi.org/10.1137/0708036>.

S. Boyd, J. Duchi, M. Pilanci, and L. Vandenberghe. Notes for EE364b: Subgradients. Stanford University, 2022. URL https://stanford.edu/class/ee364b/lectures/subgradients_notes.pdf. Lecture notes for Spring 2021–22; Accessed on January 2nd 2026.

T. Brown, B. Mann, N. Ryder, M. Subbiah, J. D. Kaplan, P. Dhariwal, A. Neelakantan, P. Shyam, G. Sastry, A. Askell, et al. Language models are few-shot learners. *Advances in neural information processing systems*, 33:1877–1901, 2020.

N. J. Calkin, E. Y. S. Chan, R. M. Corless, D. J. Jeffrey, and P. W. Lawrence. A fractal eigenvector. *The American Mathematical Monthly*, 129(6):503–523, 2022.

N. Carlini and D. Wagner. Towards evaluating the robustness of neural networks. In *IEEE Symposium on Security and Privacy (SP)*, pages 39–57. IEEE, 2017.

V. Castin, P. Ablin, and G. Peyré. How smooth is attention? In *Proceedings of the 41st International Conference on Machine Learning*, ICML’24. JMLR, 2024.

A. Cayley. Sur quelques propriétés des déterminants gauches. *Journal für die reine und angewandte Mathematik*, 1846.

P. Chaudhari, A. Choromanska, S. Soatto, Y. LeCun, C. Baldassi, C. Borgs, J. Chayes, L. Sagun, and R. Zecchina. Entropy-SGD: Biasing gradient descent into wide valleys. *Journal of Statistical Mechanics: Theory and Experiment*, 2019(12):124018, 2019.

L. Chen and R. Ng. On the marriage of L_p -norms and edit distance. In *Proceedings of the Thirtieth International Conference on Very Large Data Bases - Volume 30*, VLDB ’04, page 792–803. VLDB Endowment, 2004. ISBN 0120884690.

R. T. Q. Chen, J. Behrmann, D. K. Duvenaud, and J.-H. Jacobsen. Residual flows for invertible generative modeling. In H. Wallach, H. Larochelle, A. Beygelzimer, F. d’Alché-Buc, E. Fox, and R. Garnett, editors, *Advances in Neural Information Processing Systems*, volume 32. Curran Associates, Inc., 2019. URL https://proceedings.neurips.cc/paper_files/paper/2019/file/5d0d5594d24f0f955548f0fc0ff83d10-Paper.pdf.

T. Chen, S. Kornblith, M. Norouzi, and G. Hinton. A simple framework for contrastive learning of visual representations. In *Proceedings of the 37th International Conference on Machine Learning*, pages 1597–1607. PMLR, 2020.

A. Chernodub and D. Nowicki. Norm-preserving orthogonal permutation linear unit activation functions (OPLU), 2017. URL <https://arxiv.org/abs/1604.02313>.

A. Chowdhery, S. Narang, J. Devlin, M. Bosma, G. Mishra, A. Roberts, P. Barham, H. W. Chung, C. Sutton, S. Gehrmann, P. Schuh, K. Shi, S. Tsvyashchenko, J. Maynez, A. Rao, P. Barnes, Y. Tay, N. Shazeer, V. Prabhakaran, E. Reif, N. Du, B. Hutchinson, R. Pope, J. Bradbury, J. Austin, M. Isard, G. Gur-Ari, P. Yin, T. Duke, A. Levskaya, S. Ghemawat, S. Dev, H. Michalewski, X. Garcia, V. Misra, K. Robinson, L. Fedus, D. Zhou, D. Ippolito, D. Luan, H. Lim, B. Zoph, A. Spiridonov, R. Sepassi, D. Dohan, S. Agrawal, M. Omernick, A. M. Dai, T. S. Pillai, M. Pellat, A. Lewkowycz, E. Moreira, R. Child, O. Polozov, K. Lee, Z. Zhou, X. Wang, B. Saeta, M. Diaz, O. Firat, M. Catasta, J. Wei, K. Meier-Hellstern, D. Eck, J. Dean, S. Petrov, and N. Fiedel. PaLM: Scaling language modeling with pathways. *Journal of Machine Learning Research*, 24(240):1–113, 2023. URL <http://jmlr.org/papers/v24/22-1144.html>.

M. Cisse, P. Bojanowski, E. Grave, Y. Dauphin, and N. Usunier. Parseval networks: improving robustness to adversarial examples. In *Proceedings of the 34th International Conference on Machine Learning - Volume 70*, ICML’17, page 854–863. PMLR, 2017.

F. H. Clarke. Generalized gradients and applications. *Transactions of the American Mathematical Society*, 205:247–262, 1975.

F. H. Clarke. *Optimization and Nonsmooth Analysis*, volume 5 of *Classics in Applied Mathematics*. SIAM, Philadelphia, PA, second edition, 1990.

D. Clevert, T. Unterthiner, and S. Hochreiter. Fast and accurate deep network learning by exponential linear units (ELUs). In Y. Bengio and Y. LeCun, editors, *4th International Conference on Learning Representations, ICLR 2016, San Juan, Puerto Rico, May 2-4, 2016, Conference Track Proceedings*, 2016. URL <http://arxiv.org/abs/1511.07289>.

A. Coates, A. Ng, and H. Lee. An analysis of single-layer networks in unsupervised feature learning. In *Proceedings of the fourteenth international conference on artificial intelligence and statistics*, pages 215–223. JMLR Workshop and Conference Proceedings, 2011.

I. C. Covert, S. Lundberg, and S.-I. Lee. Understanding global feature contributions with additive importance measures. In *Proceedings of the 34th International Conference on Neural Information Processing Systems*, NIPS ’20, Red Hook, NY, USA, 2020. Curran Associates Inc. ISBN 9781713829546.

G. Cybenko. Approximation by superpositions of a sigmoidal function. *Mathematics of Control, Signals and Systems*, 2(4):303–314, 1989. doi: 10.1007/BF02551274. URL <https://doi.org/10.1007/BF02551274>.

A. Damian, E. Nichani, and J. D. Lee. Self-stabilization: The implicit bias of gradient descent at the edge of stability. In *The Eleventh International Conference on Learning Representations*, 2023. URL <https://openreview.net/forum?id=nhKHA59gXz>.

DeepSeek-AI, D. Guo, D. Yang, H. Zhang, J. Song, R. Zhang, R. Xu, Q. Zhu, S. Ma, P. Wang, X. Bi, X. Zhang, X. Yu, Y. Wu, Z. F. Wu, Z. Gou, Z. Shao, Z. Li, Z. Gao, A. Liu, B. Xue, B. Wang, B. Wu, B. Feng, C. Lu, C. Zhao, C. Deng, C. Zhang, C. Ruan, D. Dai, D. Chen, D. Ji, E. Li, F. Lin, F. Dai, F. Luo, G. Hao, G. Chen, G. Li, H. Zhang, H. Bao, H. Xu, H. Wang, H. Ding, H. Xin, H. Gao, H. Qu, H. Li, J. Guo, J. Li, J. Wang, J. Chen, J. Yuan, J. Qiu, J. Li, J. L. Cai, J. Ni, J. Liang, J. Chen, K. Dong, K. Hu, K. Gao, K. Guan, K. Huang, K. Yu, L. Wang, L. Zhang, L. Zhao, L. Wang, L. Zhang, L. Xu, L. Xia, M. Zhang, M. Tang, M. Li, M. Wang, M. Li, N. Tian, P. Huang, P. Zhang, Q. Wang, Q. Chen, Q. Du, R. Ge, R. Zhang, R. Pan, R. Wang, R. J. Chen, R. L. Jin, R. Chen, S. Lu, S. Zhou, S. Chen, S. Ye, S. Wang, S. Yu, S. Zhou, S. Pan, S. S. Li, S. Zhou, S. Wu, S. Ye, T. Yun, T. Pei, T. Sun, T. Wang, W. Zeng, W. Zhao, W. Liu, W. Liang, W. Gao, W. Yu, W. Zhang, W. L. Xiao, W. An, X. Liu, X. Wang, X. Chen, X. Nie, X. Cheng, X. Liu, X. Xie, X. Liu, X. Yang, X. Li, X. Su, X. Lin, X. Q. Li, X. Jin, X. Shen, X. Chen, X. Sun, X. Wang, X. Song, X. Zhou, X. Wang, X. Shan, Y. K. Li, Y. Q. Wang, Y. X. Wei, Y. Zhang, Y. Xu, Y. Li, Y. Zhao, Y. Sun, Y. Wang, Y. Yu, Y. Zhang, Y. Shi, Y. Xiong, Y. He, Y. Piao, Y. Wang, Y. Tan, Y. Ma, Y. Liu, Y. Guo, Y. Ou, Y. Wang, Y. Gong, Y. Zou, Y. He, Y. Xiong, Y. Luo, Y. You, Y. Liu, Y. Zhou, Y. X. Zhu, Y. Xu, Y. Huang, Y. Li, Y. Zheng, Y. Zhu, Y. Ma, Y. Tang, Y. Zha, Y. Yan, Z. Z. Ren, Z. Ren, Z. Sha, Z. Fu, Z. Xu, Z. Xie, Z. Zhang, Z. Hao, Z. Ma, Z. Yan, Z. Wu, Z. Gu, Z. Zhu, Z. Liu, Z. Li, Z. Xie, Z. Song, Z. Pan, Z. Huang, Z. Xu, Z. Zhang, and Z. Zhang. Deepseek-r1: Incentivizing reasoning capability in LLMs via reinforcement learning, 2025. URL <https://arxiv.org/abs/2501.12948>.

C. Devaguptapu, D. Agarwal, G. Mittal, P. Gopalani, and V. N. Balasubramanian. On adversarial robustness: A neural architecture search perspective. In *Proceedings of the IEEE/CVF International Conference on Computer Vision*, pages 152–161, 2021.

J. Devlin, M.-W. Chang, K. Lee, and K. Toutanova. BERT: Pre-training of deep bidirectional transformers for language understanding. In *Proceedings of the 2019 Conference of the North American Chapter of the Association for Computational Linguistics (NAACL)*, pages 4171–4186, 2019.

L. Dinh, J. Sohl-Dickstein, and S. Bengio. Density estimation using real NVP. In *International Conference on Learning Representations*, 2017. URL <https://openreview.net/forum?id=HkpbnH91x>.

A. Dosovitskiy, L. Beyer, A. Kolesnikov, D. Weissenborn, X. Zhai, T. Unterthiner, M. Dehghani, M. Minderer, G. Heigold, S. Gelly, J. Uszkoreit, and N. Houlsby. An image is worth 16x16 words: Transformers for image recognition at scale. In *International Conference on Learning Representations (ICLR)*, 2021. arXiv:2010.11929.

C. Dugas, Y. Bengio, F. Bélisle, C. Nadeau, and R. Garcia. Incorporating second-order functional knowledge for better option pricing. In T. Leen, T. Dietterich, and V. Tresp, editors, *Advances in Neural Information Processing Systems*, volume 13. MIT Press, 2000.

N. Dunford and J. T. Schwartz. *Linear operators, part 1: general theory*. John Wiley & Sons, 1988.

A. Edelman and N. R. Rao. Random matrix theory. *Acta numerica*, 14:233–297, 2005.

T. Elsken, J. H. Metzen, and F. Hutter. Neural architecture search: A survey. *Journal of Machine Learning Research*, 20(55):1–21, 2019. URL <http://jmlr.org/papers/v20/18-598.html>.

European Commission. Ethics guidelines for trustworthy AI, 2019.

European Parliament and Council. Regulation (EU) 2024/1689 of the european parliament and of the council on harmonised rules on artificial intelligence (AI Act), 2024.

U. Fano. Description of states in quantum mechanics by density matrix and operator techniques. *Reviews of modern physics*, 29(1):74, 1957.

M. Fazlyab, A. Robey, H. Hassani, M. Morari, and G. Pappas. Efficient and accurate estimation of Lipschitz constants for deep neural networks. In H. Wallach, H. Larochelle, A. Beygelzimer, F. d'Alché-Buc, E. Fox, and R. Garnett, editors, *Advances in Neural Information Processing Systems*, volume 32. Curran Associates, Inc., 2019.

M. Fazlyab, T. Entesari, A. Roy, and R. Chellappa. Certified robustness via dynamic margin maximization and improved Lipschitz regularization. In *Thirty-seventh Conference on Neural Information Processing Systems*, 2023. URL <https://openreview.net/forum?id=LDhhi8HBO3>.

D. Flatow and D. Penner. On the robustness of convnets to training on noisy labels. *Technical report, Stanford University*, 2017.

J. N. Franklin. *Matrix theory*. Courier Corporation, 2000.

B. Frenay and M. Verleysen. Classification in the presence of label noise: A survey. *IEEE Transactions on Neural Networks and Learning Systems*, 25(5):845–869, 2014. doi: 10.1109/TNNLS.2013.2292894.

M. Gamba, H. Azizpour, and M. Bjorkman. On the Lipschitz constant of deep networks and double descent. In *34th British Machine Vision Conference 2023, BMVC 2023, Aberdeen, UK, November 20-24, 2023*. BMVA, 2023. URL <https://papers.bmvc2023.org/0871.pdf>.

A. Ghorbani, J. Wexler, J. Y. Zou, and B. Kim. Towards automatic concept-based explanations. In H. M. Wallach, H. Larochelle, A. Beygelzimer, F. d’Alché-Buc, E. B. Fox, and R. Garnett, editors, *Advances in Neural Information Processing Systems 32: Annual Conference on Neural Information Processing Systems 2019, NeurIPS 2019, December 8-14, 2019, Vancouver, BC, Canada*, pages 9273–9282, 2019.

A. Ghosh, H. Kumar, and P. S. Sastry. Robust loss functions under label noise for deep neural networks. In *Proceedings of the AAAI conference on artificial intelligence*, volume 31, 2017.

N. Golowich, A. Rakhlin, and O. Shamir. Size-independent sample complexity of neural networks. In S. Bubeck, V. Perchet, and P. Rigollet, editors, *Proceedings of the 31st Conference On Learning Theory*, volume 75 of *Proceedings of Machine Learning Research*, pages 297–299. PMLR, 06–09 Jul 2018. URL <https://proceedings.mlr.press/v75/golowich18a.html>.

G. H. Golub and C. F. Van Loan. *Matrix computations*. JHU press, 2013.

A. Gonon, N. Brisebarre, E. Riccietti, and R. Gribonval. A rescaling-invariant Lipschitz bound based on path-metrics for modern ReLU network parameterizations. In *Forty-second International Conference on Machine Learning*, 2025. URL <https://openreview.net/forum?id=T8VLY1KuOz>.

I. Goodfellow, J. Pouget-Abadie, M. Mirza, B. Xu, D. Warde-Farley, S. Ozair, A. Courville, and Y. Bengio. Generative adversarial nets. In *Advances in Neural Information Processing Systems (NeurIPS)*, pages 2672–2680, 2014.

I. Goodfellow, Y. Bengio, and A. Courville. *Deep learning*. MIT Press, 2016.

I. J. Goodfellow, J. Shlens, and C. Szegedy. Explaining and harnessing adversarial examples. In Y. Bengio and Y. LeCun, editors, *3rd International Conference on Learning Representations, ICLR 2015, San Diego, CA, USA, May 7-9, 2015, Conference Track Proceedings*, 2015. URL <http://arxiv.org/abs/1412.6572>.

J. Gou, B. Yu, S. J. Maybank, and D. Tao. Knowledge distillation: A survey. *International Journal of Computer Vision*, 129(6):1789–1819, 2021.

H. Gouk, E. Frank, B. Pfahringer, and M. J. Cree. Regularisation of neural networks by enforcing Lipschitz continuity. *Machine Learning*, 110:393–416, 2021.

R. Grosse and J. Martens. A Kronecker–factored approximate Fisher matrix for convolution layers. In *International Conference on Machine Learning*, pages 573–582. PMLR, 2016.

I. Gulrajani, F. Ahmed, M. Arjovsky, V. Dumoulin, and A. C. Courville. Improved training of Wasserstein GANs. In I. Guyon, U. V. Luxburg, S. Bengio, H. Wallach, R. Fergus, S. Vishwanathan, and R. Garnett, editors, *Advances in Neural Information Processing Systems*, volume 30. Curran Associates, Inc., 2017.

K. He, X. Zhang, S. Ren, and J. Sun. Delving deep into rectifiers: Surpassing human-level performance on ImageNet classification. In *Proceedings of the IEEE international conference on computer vision*, pages 1026–1034, 2015.

K. He, X. Zhang, S. Ren, and J. Sun. Deep residual learning for image recognition. In *Proceedings of the IEEE conference on computer vision and pattern recognition*, pages 770–778, 2016.

M. Hein and M. Andriushchenko. Formal guarantees on the robustness of a classifier against adversarial manipulation. *Advances in neural information processing systems*, 30, 2017.

D. Hendrycks and T. Dietterich. Benchmarking neural network robustness to common corruptions and perturbations. In *International Conference on Learning Representations*, 2019. URL <https://openreview.net/forum?id=HJz6tiCqYm>.

D. Hendrycks and K. Gimpel. Gaussian error linear units (GELUs). 2016. URL <https://arxiv.org/abs/1606.08415>.

D. Hendrycks, M. Mazeika, D. Wilson, and K. Gimpel. Using trusted data to train deep networks on labels corrupted by severe noise. In S. Bengio, H. Wallach, H. Larochelle, K. Grauman, N. Cesa-Bianchi, and R. Garnett, editors, *Advances in Neural Information Processing Systems*, volume 31. Curran Associates, Inc., 2018.

D. Hendrycks, M. Mazeika, and T. Dietterich. Deep anomaly detection with outlier exposure. In *International Conference on Learning Representations*, 2019. URL <https://openreview.net/forum?id=HyxCxhRcY7>.

D. Hendrycks, S. Basart, N. Mu, S. Kadavath, F. Wang, E. Dorundo, R. Desai, T. Zhu, S. Parajuli, M. Guo, et al. The many faces of robustness: A critical analysis of out-of-distribution generalization. In *Proceedings of the IEEE/CVF international conference on computer vision*, pages 8340–8349, 2021.

G. Hinton, N. Srivastava, and K. Swersky. Neural networks for machine learning lecture (6a): Overview of mini-batch gradient descent. URL https://www.cs.toronto.edu/~tijmen/csc321/slides/lecture_slides_lec6.pdf.

G. E. Hinton and R. R. Salakhutdinov. Reducing the dimensionality of data with neural networks. *Science*, 313(5786):504–507, 2006.

J. Ho, A. Jain, and P. Abbeel. Denoising diffusion probabilistic models. In H. Larochelle, M. Ranzato, R. Hadsell, M. Balcan, and H. Lin, editors, *Advances in Neural Information Processing Systems*, volume 33, pages 6840–6851. Curran Associates, Inc., 2020. URL https://proceedings.neurips.cc/paper_files/paper/2020/file/4c5bcfec8584af0d967f1ab10179ca4b-Paper.pdf.

S. Hochreiter and J. Schmidhuber. Long short-term memory. *Neural Computation*, 9(8):1735–1780, 1997. doi: 10.1162/neco.1997.9.8.1735.

R. A. Horn. The Hadamard product. In *Proc. Symp. Appl. Math*, volume 40, pages 87–169, 1990.

R. A. Horn and C. R. Johnson. *Matrix analysis*. Cambridge University Press, 2012.

X. Hu, R. Zheng, J. Wang, C. H. Leung, Q. Wu, and X. Xie. SpecFormer: Guarding vision transformer robustness via maximum singular value penalization. In *European Conference on Computer Vision*, pages 345–362. Springer, 2024.

L. Huang, X. Liu, B. Lang, A. W. Yu, Y. Wang, and B. Li. Orthogonal weight normalization: solution to optimization over multiple dependent Stiefel manifolds in deep neural networks. In *Proceedings of the Thirty-Second AAAI Conference on Artificial Intelligence and Thirtieth Innovative Applications of Artificial Intelligence Conference and Eighth AAAI Symposium on Educational Advances in Artificial Intelligence*, AAAI’18/IAAI’18/EAAI’18. AAAI Press, 2018. ISBN 978-1-57735-800-8.

A. Ilyas, S. Santurkar, D. Tsipras, L. Engstrom, B. Tran, and A. Madry. Adversarial examples are not bugs, they are features. *Advances in neural information processing systems*, 32, 2019.

K. Itô. *On stochastic differential equations*. Number 4. American Mathematical Soc., 1951.

A. K. Jain. *Fundamentals of digital image processing*. Englewood Cliffs, NJ: Prentice Hall, 1989.

S. Jastrzębski, Z. Kenton, N. Ballas, A. Fischer, Y. Bengio, and A. Storkey. On the relation between the sharpest directions of DNN loss and the SGD step length. In *International Conference on Learning Representations*, 2019. URL <https://openreview.net/forum?id=SkgEaj05t7>.

M. Jordan and A. G. Dimakis. Exactly computing the local Lipschitz constant of ReLU networks. In *International Conference on Machine Learning (ICML)*, pages 4985–4994. PMLR, 2020. URL <https://arxiv.org/abs/2002.11572>.

I. Karatzas and S. Shreve. *Brownian motion and stochastic calculus*, volume 113. Springer Science & Business Media, 2012.

T. Kato. *Perturbation theory for linear operators*. Springer, 1995.

N. S. Keskar, D. Mudigere, J. Nocedal, M. Smelyanskiy, and P. T. P. Tang. On large-batch training for deep learning: Generalization gap and sharp minima. In *International Conference on Learning Representations*, 2017. URL <https://openreview.net/forum?id=H1oyR1Ygg>.

G. Khromov and S. P. Singh. Some fundamental aspects about Lipschitz continuity of neural networks. In *The Twelfth International Conference on Learning Representations*, 2024. URL <https://openreview.net/forum?id=5jWsW08zUh>.

B. Kim, M. Wattenberg, J. Gilmer, C. Cai, J. Wexler, F. Viegas, and R. sayres. Interpretability beyond feature attribution: Quantitative testing with concept activation vectors (TCAV). In J. Dy and A. Krause, editors, *Proceedings of the 35th International Conference on Machine Learning*, volume 80 of *Proceedings of Machine Learning Research*, pages 2668–2677. PMLR, 10–15 Jul 2018. URL <https://proceedings.mlr.press/v80/kim18d.html>.

H. Kim, G. Papamakarios, and A. Mnih. The Lipschitz constant of self-attention. In M. Meila and T. Zhang, editors, *Proceedings of the 38th International Conference on Machine Learning*, volume 139 of *Proceedings of Machine Learning Research*, pages 5562–5571. PMLR, 18–24 Jul 2021. URL <https://proceedings.mlr.press/v139/kim21i.html>.

D. P. Kingma and J. Ba. Adam: A method for stochastic optimization, 2017. URL <https://arxiv.org/abs/1412.6980>.

T. N. Kipf and M. Welling. Semi-supervised classification with graph convolutional networks. In *International Conference on Learning Representations*, 2017. URL <https://openreview.net/forum?id=SJU4ayYgl>.

C. Klamler. Fair division. *Handbook of group decision and negotiation*, pages 183–202, 2010.

P. W. Koh, T. Nguyen, Y. S. Tang, S. Mussmann, E. Pierson, B. Kim, and P. Liang. Concept bottleneck models. In *International Conference on Machine Learning*, pages 5338–5348. PMLR, 2020.

T. G. Kolda and B. W. Bader. Tensor decompositions and applications. *SIAM review*, 51(3):455–500, 2009.

S. Kolek, D. A. Nguyen, R. Levie, J. Bruna, and G. Kutyniok. Cartoon explanations of image classifiers. In *European Conference on Computer Vision*, pages 443–458. Springer, 2022.

T. W. Körner. *Fourier analysis*. Cambridge University Press, 2014. ISBN 9781107049949.

A. Krizhevsky, I. Sutskever, and G. E. Hinton. ImageNet classification with deep convolutional neural networks. *Advances in neural information processing systems*, 25, 2012.

H. Lakkaraju, E. Kamar, R. Caruana, and J. Leskovec. Faithful and customizable explanations of black box models. In *Proceedings of the 2019 AAAI/ACM Conference on AI, Ethics, and Society*, pages 131–138, 2019.

V. I. Levenshtein. Binary codes capable of correcting deletions, insertions, and reversals. *Soviet Physics Doklady*, 10:707–710, 1966.

A. S. Lewis and H. S. Sendov. Nonsmooth analysis of singular values. Part I: Theory. *Set-Valued Analysis*, 13(3):213–241, 2005.

M. Lezcano-Casado and D. Martínez-Rubio. Cheap orthogonal constraints in neural networks: A simple parametrization of the orthogonal and unitary group. In K. Chaudhuri and R. Salakhutdinov, editors, *Proceedings of the 36th International Conference on Machine Learning*, volume 97 of *Proceedings of Machine Learning Research*, pages 3794–3803. PMLR, 09–15 Jun 2019. URL <https://proceedings.mlr.press/v97/lezcano-casado19a.html>.

C.-K. Li and R.-C. Li. A note on eigenvalues of perturbed Hermitian matrices. *Linear algebra and its applications*, 395:183–190, 2005.

J. Li, D. Li, C. Xiong, and S. Hoi. BLIP: Bootstrapping language-image pre-training for unified vision-language understanding and generation. In K. Chaudhuri, S. Jegelka, L. Song, C. Szepesvari, G. Niu, and S. Sabato, editors, *Proceedings of the 39th International Conference on Machine Learning*, volume 162 of *Proceedings of Machine Learning Research*, pages 12888–12900. PMLR, 17–23 Jul 2022a. URL <https://proceedings.mlr.press/v162/li22n.html>.

Q. Li, S. Haque, C. Anil, J. Lucas, R. B. Grosse, and J.-H. Jacobsen. Preventing gradient attenuation in Lipschitz constrained convolutional networks. In H. Wallach, H. Larochelle, A. Beygelzimer, F. d'Alché-Buc, E. Fox, and R. Garnett, editors, *Advances in Neural Information Processing Systems*, volume 32. Curran Associates, Inc., 2019a. URL https://proceedings.neurips.cc/paper_files/paper/2019/file/1ce3e6e3f452828e23a0c94572bef9d9-Paper.pdf.

Q. Li, C. Tai, and E. Weinan. Stochastic modified equations and dynamics of stochastic gradient algorithms I: Mathematical foundations. *Journal of Machine Learning Research*, 20(40):1–47, 2019b.

Y. Li and C. Xu. Trade-off between robustness and accuracy of vision transformers. In *Proceedings of the IEEE/CVF Conference on Computer Vision and Pattern Recognition*, pages 7558–7568, 2023.

Y. Li and Y. Yuan. Convergence analysis of two-layer neural networks with ReLU activation. In I. Guyon, U. V. Luxburg, S. Bengio, H. Wallach, R. Fergus, S. Vishwanathan, and R. Garnett, editors, *Advances in Neural Information Processing Systems*, volume 30. Curran Associates, Inc., 2017. URL https://proceedings.neurips.cc/paper_files/paper/2017/file/a96b65a721e561e1e3de768ac819ffbb-Paper.pdf.

Z. Li, F. Liu, W. Yang, S. Peng, and J. Zhou. A survey of convolutional neural networks: analysis, applications, and prospects. *IEEE transactions on neural networks and learning systems*, 33(12):6999–7019, 2021.

Z. Li, T. Wang, and S. Arora. What happens after SGD reaches zero loss? — A mathematical framework. In *International Conference on Learning Representations*, 2022b. URL <https://openreview.net/forum?id=siCt4xZn5Ve>.

Y. Lipman, R. T. Q. Chen, H. Ben-Hamu, M. Nickel, and M. Le. Flow matching for generative modeling. In *The Eleventh International Conference on Learning Representations*, 2023. URL <https://openreview.net/forum?id=PqvMRDCJT9t>.

M. Lukasik, S. Bhojanapalli, A. Menon, and S. Kumar. Does label smoothing mitigate label noise? In H. D. III and A. Singh, editors, *Proceedings of the 37th International Conference on Machine Learning*, volume 119 of *Proceedings of Machine Learning Research*, pages 6448–6458. PMLR, 13–18 Jul 2020. URL <https://proceedings.mlr.press/v119/lukasik20a.html>.

S. M. Lundberg and S.-I. Lee. A unified approach to interpreting model predictions. In I. Guyon, U. V. Luxburg, S. Bengio, H. Wallach, R. Fergus, S. Vishwanathan, and R. Garnett, editors, *Advances in Neural Information Processing Systems*, volume 30. Curran Associates, Inc., 2017.

C. Luo, Q. Lin, W. Xie, B. Wu, J. Xie, and L. Shen. Frequency-driven imperceptible adversarial attack on semantic similarity. In *Proceedings of the IEEE/CVF Conference on Computer Vision and Pattern Recognition*, pages 15315–15324, 2022.

A. L. Maas, A. Y. Hannun, and A. Y. Ng. Rectifier nonlinearities improve neural network acoustic models. In *ICML Workshop on Deep Learning for Audio, Speech and Language Processing*, 2013.

J. Macdonald, S. Wäldchen, S. Hauch, and G. Kutyniok. A rate-distortion framework for explaining neural network decisions. *arXiv preprint arXiv:1905.11092*, 2019.

A. Madry, A. Makelov, L. Schmidt, D. Tsipras, and A. Vladu. Towards deep learning models resistant to adversarial attacks. *International Conference on Learning Representations (ICLR)*, 2018.

J. R. Magnus and H. Neudecker. *Matrix differential calculus with applications in statistics and econometrics*. John Wiley & Sons, 2019.

S. Malladi, K. Lyu, A. Panigrahi, and S. Arora. On the SDEs and scaling rules for adaptive gradient algorithms. *Advances in Neural Information Processing Systems*, 35:7697–7711, 2022.

S. Mandt, M. D. Hoffman, D. M. Blei, et al. Continuous-time limit of stochastic gradient descent revisited. *NIPS-2015*, 2015.

S. Mandt, M. D. Hoffman, and D. M. Blei. Stochastic gradient descent as approximate Bayesian inference. *Journal of Machine Learning Research*, 18(134):1–35, 2017.

V. A. Marčenko and L. A. Pastur. Distribution of eigenvalues for some sets of random matrices. *Mathematics of the USSR-Sbornik*, 1(4):457, 1967.

J. Martens. New insights and perspectives on the natural gradient method. *Journal of Machine Learning Research*, 21(146):1–76, 2020.

A. Maurer. A vector-contraction inequality for Rademacher complexities. In *Algorithmic Learning Theory: 27th International Conference, ALT 2016, Bari, Italy, October 19–21, 2016, Proceedings*, page 3–17, Berlin, Heidelberg, 2016. Springer-Verlag. ISBN 978-3-319-46378-0. doi: 10.1007/978-3-319-46379-7_1. URL https://doi.org/10.1007/978-3-319-46379-7_1.

R. Mises and H. Pollaczek-Geiringer. Praktische verfahren der gleichungsauflösung. *ZAMM-Journal of Applied Mathematics and Mechanics/Zeitschrift für Angewandte Mathematik und Mechanik*, 9(1):58–77, 1929.

T. Miyato, T. Kataoka, M. Koyama, and Y. Yoshida. Spectral normalization for generative adversarial networks. In *International Conference on Learning Representations*, 2018. URL <https://openreview.net/forum?id=B1QRgziT->.

A. Modas, S.-M. Moosavi-Dezfooli, and P. Frossard. Sparsefool: A few pixels make a big difference. In *2019 IEEE/CVF Conference on Computer Vision and Pattern Recognition (CVPR)*, pages 9079–9088, 2019. doi: 10.1109/CVPR.2019.00930.

M. Mohri, A. Rostamizadeh, and A. Talwalkar. *Foundations of machine learning*. MIT Press, 2018.

P. Nair. Softmax is $1/2$ -Lipschitz: A tight bound across all ℓ_p norms. *arXiv preprint arXiv:2510.23012*, 2025.

V. Nair and G. E. Hinton. Rectified linear units improve restricted Boltzmann machines. In *Proceedings of the 27th International Conference on International Conference on Machine Learning*, ICML’10, page 807–814, Madison, WI, USA, 2010. Omnipress. ISBN 9781605589077.

N. Natarajan, I. S. Dhillon, P. K. Ravikumar, and A. Tewari. Learning with noisy labels. In C. Burges, L. Bottou, M. Welling, Z. Ghahramani, and K. Weinberger, editors, *Advances in Neural Information Processing Systems*, volume 26. Curran Associates, Inc., 2013.

F. Navarro. Necessary players, Myerson fairness and the equal treatment of equals. *Annals of Operations Research*, 280:111–119, 2019.

A. Neelakantan, L. Vilnis, Q. V. Le, I. Sutskever, L. Kaiser, K. Kurach, and J. Martens. Adding gradient noise improves learning for very deep networks. 2015. URL <https://arxiv.org/abs/1511.06807>.

B. Neyshabur, R. Tomioka, and N. Srebro. Norm-based capacity control in neural networks. In P. Grünwald, E. Hazan, and S. Kale, editors, *Proceedings of The 28th Conference on Learning Theory*, volume 40 of *Proceedings of Machine Learning Research*, pages 1376–1401, Paris, France, 03–06 Jul 2015. PMLR. URL <https://proceedings.mlr.press/v40/Neyshabur15.html>.

B. Neyshabur, S. Bhojanapalli, D. Mcallester, and N. Srebro. Exploring generalization in deep learning. In I. Guyon, U. V. Luxburg, S. Bengio, H. Wallach, R. Fergus, S. Vishwanathan, and R. Garnett, editors, *Advances in Neural Information Processing Systems*, volume 30. Curran Associates, Inc., 2017. URL https://proceedings.neurips.cc/paper_files/paper/2017/file/10ce03a1ed01077e3e289f3e53c72813-Paper.pdf.

A. Nguyen, A. Dosovitskiy, J. Yosinski, T. Brox, and J. Clune. Synthesizing the preferred inputs for neurons in neural networks via deep generator networks. In D. Lee, M. Sugiyama, U. Luxburg, I. Guyon, and R. Garnett, editors, *Advances in Neural Information Processing Systems*, volume 29. Curran Associates, Inc., 2016.

A. Nguyen, J. Yosinski, and J. Clune. Understanding neural networks via feature visualization: A survey. *Explainable AI: interpreting, explaining and visualizing deep learning*, pages 55–76, 2019.

M. A. Nielsen and I. L. Chuang. *Quantum computation and quantum information*. Cambridge University Press, 2010.

NIST. Artificial intelligence risk management framework, 2023. URL <https://www.nist.gov/itl/ai-risk-management-framework>.

B. Oksendal. *Stochastic differential equations: an introduction with applications*. Springer Science & Business Media, 2013.

OpenAI, J. Achiam, S. Adler, S. Agarwal, L. Ahmad, I. Akkaya, F. L. Aleman, D. Almeida, J. Altenschmidt, S. Altman, S. Anadkat, R. Avila, I. Babuschkin, S. Balaji, V. Balcom, P. Baltescu, H. Bao, M. Bavarian, J. Belgum, I. Bello, J. Berdine, G. Bernadett-Shapiro, C. Berner, L. Bogdonoff, O. Boiko, M. Boyd, A.-L. Brakman, G. Brockman, T. Brooks, M. Brundage, K. Button, T. Cai, R. Campbell, A. Cann, B. Carey, C. Carlson, R. Carmichael, B. Chan, C. Chang, F. Chantzis, D. Chen, S. Chen, R. Chen, J. Chen, M. Chen, B. Chess, C. Cho, C. Chu, H. W. Chung, D. Cummings,

J. Currier, Y. Dai, C. Decareaux, T. Degry, N. Deutsch, D. Deville, A. Dhar, D. Dohan, S. Dowling, S. Dunning, A. Ecoffet, A. Eleti, T. Eloundou, D. Farhi, L. Fedus, N. Felix, S. P. Fishman, J. Forte, I. Fulford, L. Gao, E. Georges, C. Gibson, V. Goel, T. Gogineni, G. Goh, R. Gontijo-Lopes, J. Gordon, M. Grafstein, S. Gray, R. Greene, J. Gross, S. S. Gu, Y. Guo, C. Hallacy, J. Han, J. Harris, Y. He, M. Heaton, J. Heidecke, C. Hesse, A. Hickey, W. Hickey, P. Hoeschele, B. Houghton, K. Hsu, S. Hu, X. Hu, J. Huizinga, S. Jain, S. Jain, J. Jang, A. Jiang, R. Jiang, H. Jin, D. Jin, S. Jomoto, B. Jonn, H. Jun, T. Kaftan, Łukasz Kaiser, A. Kamali, I. Kanitscheider, N. S. Keskar, T. Khan, L. Kilpatrick, J. W. Kim, C. Kim, Y. Kim, J. H. Kirchner, J. Kiros, M. Knight, D. Kokotajlo, Łukasz Kondraciuk, A. Kondrich, A. Konstantinidis, K. Kosic, G. Krueger, V. Kuo, M. Lampe, I. Lan, T. Lee, J. Leike, J. Leung, D. Levy, C. M. Li, R. Lim, M. Lin, S. Lin, M. Litwin, T. Lopez, R. Lowe, P. Lue, A. Makanju, K. Malfacini, S. Manning, T. Markov, Y. Markovski, B. Martin, K. Mayer, A. Mayne, B. McGrew, S. M. McKinney, C. McLeavey, P. McMillan, J. McNeil, D. Medina, A. Mehta, J. Menick, L. Metz, A. Mishchenko, P. Mishkin, V. Monaco, E. Morikawa, D. Mossing, T. Mu, M. Murati, O. Murk, D. Mély, A. Nair, R. Nakano, R. Nayak, A. Neelakantan, R. Ngo, H. Noh, L. Ouyang, C. O’Keefe, J. Pachocki, A. Paino, J. Palermo, A. Pantuliano, G. Parascandolo, J. Parish, E. Parparita, A. Passos, M. Pavlov, A. Peng, A. Perelman, F. de Avila Belbute Peres, M. Petrov, H. P. de Oliveira Pinto, Michael, Pokorny, M. Pokrass, V. H. Pong, T. Powell, A. Power, B. Power, E. Proehl, R. Puri, A. Radford, J. Rae, A. Ramesh, C. Raymond, F. Real, K. Rimbach, C. Ross, B. Rotsted, H. Roussez, N. Ryder, M. Saltarelli, T. Sanders, S. Santurkar, G. Sastry, H. Schmidt, D. Schnurr, J. Schulman, D. Selsam, K. Sheppard, T. Sherbakov, J. Shieh, S. Shoker, P. Shyam, S. Sidor, E. Sigler, M. Simens, J. Sitkin, K. Slama, I. Sohl, B. Sokolowsky, Y. Song, N. Staudacher, F. P. Such, N. Summers, I. Sutskever, J. Tang, N. Tezak, M. B. Thompson, P. Tillet, A. Tootoonchian, E. Tseng, P. Tuggle, N. Turley, J. Tworek, J. F. C. Uribe, A. Vallone, A. Vijayvergiya, C. Voss, C. Wainwright, J. J. Wang, A. Wang, B. Wang, J. Ward, J. Wei, C. Weinmann, A. Welihinda, P. Welinder, J. Weng, L. Weng, M. Wiethoff, D. Willner, C. Winter, S. Wolrich, H. Wong, L. Workman, S. Wu, J. Wu, M. Wu, K. Xiao, T. Xu, S. Yoo, K. Yu, Q. Yuan, W. Zaremba, R. Zellers, C. Zhang, M. Zhang, S. Zhao, T. Zheng, J. Zhuang, W. Zhuk, and B. Zoph. GPT-4 technical report, 2024. URL <https://arxiv.org/abs/2303.08774>.

A. V. Oppenheim. *Applications of digital signal processing*. Prentice-Hall, 1978. ISBN 0130391158, 9780130391155.

T. Pang, X. Yang, Y. Dong, H. Su, and J. Zhu. Bag of tricks for adversarial training. In *International Conference on Learning Representations*, 2021. URL <https://openreview.net/forum?id=Xb8xvrtB8Ce>.

A. Paszke, S. Gross, F. Massa, A. Lerer, J. Bradbury, G. Chanan, T. Killeen, Z. Lin, N. Gimelshein, L. Antiga, A. Desmaison, A. Köpf, E. Yang, Z. DeVito, M. Raison, A. Tejani, S. Chilamkurthy, B. Steiner, L. Fang, J. Bai, and S. Chintala. *PyTorch: an imperative style, high-performance deep learning library*. Curran Associates Inc., Red Hook, NY, USA, 2019.

G. Patrini, A. Rozza, A. K. Menon, R. Nock, and L. Qu. Making deep neural networks robust to label noise: A loss correction approach. In *2017 IEEE Conference on Computer Vision and Pattern Recognition (CVPR)*, pages 2233–2241, 2017. doi: 10.1109/CVPR.2017.240.

S. Paul and P.-Y. Chen. Vision transformers are robust learners. In *Proceedings of the AAAI conference on Artificial Intelligence*, volume 36, pages 2071–2081, 2022.

B. Perozzi, R. Al-Rfou, and S. Skiena. DeepWalk: online learning of social representations. In *Proceedings of the 20th ACM SIGKDD International Conference on Knowledge Discovery and Data Mining*, KDD ’14, page 701–710, New York, NY, USA, 2014. Association for Computing Machinery. ISBN 9781450329569. doi: 10.1145/2623330.2623732. URL <https://doi.org/10.1145/2623330.2623732>.

Y. Perugachi-Diaz, J. Tomczak, and S. Bhulai. Invertible DenseNets with concatenated LipSwish. In M. Ranzato, A. Beygelzimer, Y. Dauphin, P. Liang, and J. W. Vaughan, editors, *Advances in Neural Information Processing Systems*, volume 34, pages 17246–17257. Curran Associates, Inc., 2021.

J. Pomponi, S. Scardapane, and A. Uncini. Pixle: a fast and effective black-box attack based on rearranging pixels. In *2022 International Joint Conference on Neural Networks (IJCNN)*, pages 1–7. IEEE, 2022.

X. Qi, J. Wang, Y. Chen, Y. Shi, and L. Zhang. LipsFormer: Introducing Lipschitz continuity to vision transformers. In *The Eleventh International Conference on Learning Representations*, 2023. URL <https://openreview.net/forum?id=cHf1DcCwch3>.

A. Radford, J. Wu, R. Child, D. Luan, D. Amodei, and I. Sutskever. Language models are unsupervised multitask learners, 2019.

A. Radford, J. W. Kim, C. Hallacy, A. Ramesh, G. Goh, S. Agarwal, G. Sastry, A. Askell, P. Mishkin, J. Clark, G. Krueger, and I. Sutskever. Learning transferable visual models from natural language supervision. In M. Meila and T. Zhang, editors, *Proceedings of the 38th International Conference on Machine Learning*, volume 139 of *Proceedings of*

Machine Learning Research, pages 8748–8763. PMLR, 18–24 Jul 2021. URL <https://proceedings.mlr.press/v139/radford21a.html>.

N. Rahaman, A. Baratin, D. Arpit, F. Draxler, M. Lin, F. Hamprecht, Y. Bengio, and A. Courville. On the spectral bias of neural networks. In *International Conference on Machine Learning*, pages 5301–5310. PMLR, 2019.

P. Ramachandran, B. Zoph, and Q. V. Le. Searching for activation functions, 2018. URL <https://openreview.net/forum?id=SkBYYyZRZ>.

J. W. S. Rayleigh. *The theory of sound, Volume One*. Courier Corporation, 2013.

B. Recht, R. Roelofs, L. Schmidt, and V. Shankar. Do ImageNet classifiers generalize to ImageNet? In *International Conference on Machine Learning (ICML)*, pages 5389–5400. PMLR, 2019.

F. Rellich. *Perturbation theory of eigenvalue problems*. CRC Press, 1969. ISBN 0677006802, 9780677006802.

D. Rezende and S. Mohamed. Variational inference with normalizing flows. In F. Bach and D. Blei, editors, *Proceedings of the 32nd International Conference on Machine Learning*, volume 37 of *Proceedings of Machine Learning Research*, pages 1530–1538, Lille, France, 07–09 Jul 2015. PMLR. URL <https://proceedings.mlr.press/v37/rezende15.html>.

M. T. Ribeiro, S. Singh, and C. Guestrin. “Why Should I Trust You?”: Explaining the predictions of any classifier. In *Proceedings of the 22nd ACM SIGKDD International Conference on Knowledge Discovery and Data Mining*, KDD ’16, page 1135–1144, New York, NY, USA, 2016. Association for Computing Machinery. ISBN 9781450342322. doi: 10.1145/2939672.2939778. URL <https://doi.org/10.1145/2939672.2939778>.

H. Robbins and S. Monro. A stochastic approximation method. *The Annals of Mathematical Statistics*, 22(3):400–407, 1951. ISSN 00034851. URL <http://www.jstor.org/stable/2236626>.

E. A. Rocamora, G. Chrysos, and V. Cevher. Certified robustness under bounded Levenshtein distance. In *The Thirteenth International Conference on Learning Representations*, 2025. URL <https://openreview.net/forum?id=cd79pbXi4N>.

A. E. Roth. *The Shapley value: essays in honor of Lloyd S. Shapley*. Cambridge University Press, 1988.

W. Rudin. *Principles of Mathematical Analysis*. McGraw-Hill, 3 edition, 1976.

W. Rudin. *Real and Complex Analysis*. McGraw-Hill, New York, 3rd edition, 1987. ISBN 9780070542341.

J. J. Sakurai and J. Napolitano. *Modern quantum mechanics*. Cambridge University Press, 2020.

E. Schrödinger. Quantisierung als eigenwertproblem. *Annalen der physik*, 385(13):437–490, 1926.

H. Sedghi, V. Gupta, and P. M. Long. The singular values of convolutional layers. In *International Conference on Learning Representations*, 2019. URL <https://openreview.net/forum?id=rJevYoA9Fm>.

R. R. Selvaraju, M. Cogswell, A. Das, R. Vedantam, D. Parikh, and D. Batra. Grad-CAM: Visual explanations from deep networks via gradient-based localization. In *2017 IEEE International Conference on Computer Vision (ICCV)*, pages 618–626, 2017. doi: 10.1109/ICCV.2017.74.

S. Shalev-Shwartz and S. Ben-David. *Understanding machine learning: From theory to algorithms*. Cambridge University Press, 2014.

O. M. Shalit. Dilation theory: a guided tour. In *Operator theory, functional analysis and applications*, pages 551–623. Springer, 2021.

R. Shao, Z. Shi, J. Yi, P.-Y. Chen, and C.-J. Hsieh. On the adversarial robustness of vision transformers. *Transactions on Machine Learning Research*, 2022. ISSN 2835-8856. URL <https://openreview.net/forum?id=1E7K4n1Esk>.

A. Shrikumar, P. Greenside, and A. Kundaje. Learning important features through propagating activation differences. In D. Precup and Y. W. Teh, editors, *Proceedings of the 34th International Conference on Machine Learning*, volume 70 of *Proceedings of Machine Learning Research*, pages 3145–3153. PMLR, 06–11 Aug 2017. URL <https://proceedings.mlr.press/v70/shrikumar17a.html>.

U. Simsekli, L. Sagun, and M. Gurbuzbalaban. A tail-index analysis of stochastic gradient noise in deep neural networks. In K. Chaudhuri and R. Salakhutdinov, editors, *Proceedings of the 36th International Conference on Machine Learning*, volume 97 of *Proceedings of Machine Learning Research*, pages 5827–5837. PMLR, 09–15 Jun 2019. URL <https://proceedings.mlr.press/v97/simsekli19a.html>.

U. Simsekli, L. Zhu, Y. W. Teh, and M. Gurbuzbalaban. Fractional underdamped Langevin dynamics: Retargeting SGD with momentum under heavy-tailed gradient noise. In H. D. III and A. Singh, editors, *Proceedings of the 37th International Conference on Machine Learning*, volume 119 of *Proceedings of Machine Learning Research*, pages 8970–8980. PMLR, 13–18 Jul 2020. URL <https://proceedings.mlr.press/v119/simsekli20a.html>.

D. Smilkov, N. Thorat, B. Kim, F. Viégas, and M. Wattenberg. Smoothgrad: removing noise by adding noise. 2017. URL <https://arxiv.org/abs/1706.03825>.

J. Sokolić, R. Giryes, G. Sapiro, and M. R. D. Rodrigues. Robust large margin deep neural networks. *IEEE Transactions on Signal Processing*, 65(16):4265–4280, 2017. doi: 10.1109/TSP.2017.2708039.

Y. Song, J. Sohl-Dickstein, D. P. Kingma, A. Kumar, S. Ermon, and B. Poole. Score-based generative modeling through stochastic differential equations. In *International Conference on Learning Representations*, 2021. URL <https://openreview.net/forum?id=PxTIG12RRHS>.

M. Spivak. *Calculus on manifolds: a modern approach to classical theorems of advanced calculus*. CRC press, 2018.

E. M. Stein and R. Shakarchi. *Fourier analysis: an introduction*, volume 1. Princeton University Press, 2011.

G. W. Stewart and J.-g. Sun. Matrix perturbation theory. *Academic Press*, 1990.

P. Stoica, R. L. Moses, et al. *Spectral analysis of signals*, volume 452. Pearson Prentice Hall Upper Saddle River, NJ, 2005.

W. Su, S. Boyd, and E. J. Candès. A differential equation for modeling nesterov’s accelerated gradient method: Theory and insights. *Journal of Machine Learning Research*, 17(153):1–43, 2016. URL <http://jmlr.org/papers/v17/15-084.html>.

I. Sucholutsky, R. M. Battleday, K. M. Collins, R. Marjeh, J. Peterson, P. Singh, U. Bhatt, N. Jacoby, A. Weller, and T. L. Griffiths. On the informativeness of supervision signals. In R. J. Evans and I. Shpitser, editors, *Proceedings of the Thirty-Ninth Conference on Uncertainty in Artificial Intelligence*, volume 216 of *Proceedings of Machine Learning Research*, pages 2036–2046. PMLR, 31 Jul–04 Aug 2023. URL <https://proceedings.mlr.press/v216/sucholutsky23a.html>.

M. Sundararajan, A. Taly, and Q. Yan. Axiomatic attribution for deep networks. In D. Precup and Y. W. Teh, editors, *Proceedings of the 34th International Conference on Machine Learning*, volume 70 of *Proceedings of Machine Learning Research*, pages 3319–3328. PMLR, 06–11 Aug 2017. URL <https://proceedings.mlr.press/v70/sundararajan17a.html>.

R. S. Sutton, A. G. Barto, et al. *Reinforcement learning: An introduction*, volume 1. MIT Press, 1998.

C. Szegedy, W. Zaremba, I. Sutskever, J. Bruna, D. Erhan, I. J. Goodfellow, and R. Fergus. Intriguing properties of neural networks. In Y. Bengio and Y. LeCun, editors, *2nd International Conference on Learning Representations, ICLR 2014, Banff, AB, Canada, April 14-16, 2014, Conference Track Proceedings*, 2014. URL <http://arxiv.org/abs/1312.6199>.

M. Tan and Q. Le. EfficientNet: Rethinking model scaling for convolutional neural networks. In K. Chaudhuri and R. Salakhutdinov, editors, *Proceedings of the 36th International Conference on Machine Learning*, volume 97 of *Proceedings of Machine Learning Research*, pages 6105–6114. PMLR, 09–15 Jun 2019. URL <https://proceedings.mlr.press/v97/tan19a.html>.

T. Tao. *Topics in random matrix theory*, volume 132. American Mathematical Soc., 2012.

R. Taori, A. Dave, V. Shankar, N. Carlini, B. Recht, and L. Schmidt. Measuring robustness to natural distribution shifts in image classification. In H. Larochelle, M. Ranzato, R. Hadsell, M. Balcan, and H. Lin, editors, *Advances in Neural Information Processing Systems*, volume 33, pages 18583–18599. Curran Associates, Inc., 2020. URL https://proceedings.neurips.cc/paper_files/paper/2020/file/d8330f857a17c53d217014ee776bfd50-Paper.pdf.

H. Touvron, L. Martin, K. Stone, P. Albert, A. Almahairi, Y. Babaei, N. Bashlykov, S. Batra, P. Bhargava, S. Bhosale, et al. Llama: Open and efficient foundation language models. *arXiv preprint arXiv:2302.13971*, 2023.

C. A. Tracy and H. Widom. Level-spacing distributions and the Airy kernel. *Communications in Mathematical Physics*, 159:151–174, 1994.

A. Trockman and J. Z. Kolter. Orthogonalizing convolutional layers with the Cayley transform. In *International Conference on Learning Representations*, 2021. URL https://openreview.net/forum?id=Pbj8H_jEHYv.

D. Tsipras, S. Santurkar, L. Engstrom, A. Turner, and A. Madry. Robustness may be at odds with accuracy. In *International Conference on Learning Representations*, 2019. URL <https://openreview.net/forum?id=SyxAb30cY7>.

Y. Tsuzuku and I. Sato. On the structural sensitivity of deep convolutional networks to the directions of Fourier basis functions. In *2019 IEEE/CVF Conference on Computer Vision and Pattern Recognition (CVPR)*, pages 51–60, 2019. doi: 10.1109/CVPR.2019.00014.

Y. Tsuzuku, I. Sato, and M. Sugiyama. Lipschitz-margin training: scalable certification of perturbation invariance for deep neural networks. In *Proceedings of the 32nd International Conference on Neural Information Processing Systems, NIPS’18*, page 6542–6551, Red Hook, NY, USA, 2018. Curran Associates Inc.

Róisín Luo, A. Drimbarean, J. McDermott, and C. O’Riordan. Reclaiming Residual Knowledge: A Novel Paradigm to Low-Bit Quantization. In *The 35th British Machine Vision Conference, BMVC 2024, Glasgow, UK, November 25-28, 2024*. BMVA, 2024a. URL <https://arxiv.org/abs/2408.00923>.

Róisín Luo, J. McDermott, and C. O’Riordan. Interpreting Global Perturbation Robustness of Image Models using Axiomatic Spectral Importance Decomposition. *Transactions on Machine Learning Research (TMLR)*, 2024b. ISSN 2835-8856. URL <https://arxiv.org/abs/2408.01139>. Presented at The Thirteenth International Conference on Learning Representations (ICLR 2025), Singapore.

Róisín Luo, J. McDermott, C. Gagné, Q. Sun, and C. O’Riordan. Optimization-Induced Dynamics of Lipschitz Continuity in Neural Networks. Manuscript is under review at Journal of Machine Learning Research (JMLR), 2025a. URL <https://arxiv.org/abs/2506.18588>.

Róisín Luo, J. McDermott, and C. O’Riordan. Lipschitz Continuity in Deep Learning: A Systematic Review of Theoretical Foundations, Estimation Methods, Regularization Approaches and Certifiable Robustness. Manuscript is under review at *Transactions on Machine Learning Research (TMLR)*, 2025b.

Róisín Luo, C. O’Riordan, and J. McDermott. Higher-Order Singular-Value Derivatives of Real Rectangular Matrices. *Journal of Mathematical Analysis and Applications (JMAA)*, page 130236, 2025c. ISSN 0022-247X. doi: 10.1016/j.jmaa.2025.130236. URL <https://doi.org/10.1016/j.jmaa.2025.130236>.

R. Van Den Berg, L. Hasenclever, J. M. Tomczak, and M. Welling. Sylvester normalizing flows for variational inference. UAI, 2018.

A. Vaswani, N. Shazeer, N. Parmar, J. Uszkoreit, L. Jones, A. N. Gomez, L. u. Kaiser, and I. Polosukhin. Attention is all you need. In I. Guyon, U. V. Luxburg, S. Bengio, H. Wallach, R. Fergus, S. Vishwanathan, and R. Garnett, editors, *Advances in Neural Information Processing Systems*, volume 30. Curran Associates, Inc., 2017.

P. Veličković, G. Cucurull, A. Casanova, A. Romero, P. Liò, and Y. Bengio. Graph attention networks. In *International Conference on Learning Representations*, 2018. URL <https://openreview.net/forum?id=rJXMpikCZ>.

C. Villani et al. *Optimal transport: old and new*, volume 338. Springer, 2008.

A. Virmaux and K. Scaman. Lipschitz regularity of deep neural networks: analysis and efficient estimation. In S. Bengio, H. Wallach, H. Larochelle, K. Grauman, N. Cesa-Bianchi, and R. Garnett, editors, *Advances in Neural Information Processing Systems*, volume 31. Curran Associates, Inc., 2018. URL https://proceedings.neurips.cc/paper_files/paper/2018/file/d54e99a6c03704e95e6965532dec148b-Paper.pdf.

E. Vorontsov, C. Trabelsi, S. Kadouri, and C. Pal. On orthogonality and learning recurrent networks with long term dependencies. In D. Precup and Y. W. Teh, editors, *Proceedings of the 34th International Conference on Machine Learning*, volume 70 of *Proceedings of Machine Learning Research*, pages 3570–3578. PMLR, 06–11 Aug 2017. URL <https://proceedings.mlr.press/v70/vorontsov17a.html>.

J. Vuckovic, A. Baratin, and R. T. d. Combes. A mathematical theory of attention. 2020. URL <https://arxiv.org/abs/2007.02876>.

H. Wang, X. Wu, Z. Huang, and E. P. Xing. High-frequency component helps explain the generalization of convolutional neural networks. In *Proceedings of the IEEE/CVF Conference on Computer Vision and Pattern Recognition*, pages 8684–8694, 2020.

M. Welling and Y. W. Teh. Bayesian learning via stochastic gradient Langevin dynamics. In *Proceedings of the 28th International Conference on International Conference on Machine Learning*, ICML’11, page 681–688, Madison, WI, USA, 2011. Omnipress. ISBN 9781450306195.

L. Weng, H. Zhang, H. Chen, Z. Song, C.-J. Hsieh, L. Daniel, D. Boning, and I. Dhillon. Towards fast computation of certified robustness for ReLU networks. In *International Conference on Machine Learning*, pages 5276–5285. PMLR, 2018a.

T.-W. Weng, H. Zhang, P.-Y. Chen, J. Yi, D. Su, Y. Gao, C.-J. Hsieh, and L. Daniel. Evaluating the robustness of neural networks: An extreme value theory approach.

In *International Conference on Learning Representations*, 2018b. URL <https://openreview.net/forum?id=BkUH1MZ0b>.

S. Wisdom, T. Powers, J. Hershey, J. Le Roux, and L. Atlas. Full-capacity unitary recurrent neural networks. In D. Lee, M. Sugiyama, U. Luxburg, I. Guyon, and R. Garnett, editors, *Advances in Neural Information Processing Systems*, volume 29. Curran Associates, Inc., 2016. URL https://proceedings.neurips.cc/paper_files/paper/2016/file/d9ff90f4000eacd3a6c9cb27f78994cf-Paper.pdf.

T. Xiao, X. Wang, A. A. Efros, and T. Darrell. What should not be contrastive in contrastive learning. In *International Conference on Learning Representations*, 2021. URL <https://openreview.net/forum?id=CZ8Y3NzuVzO>.

K. Xu, W. Hu, J. Leskovec, and S. Jegelka. How powerful are graph neural networks? In *7th International Conference on Learning Representations, ICLR 2019, New Orleans, LA, USA, May 6-9, 2019*. OpenReview.net, 2019a. URL <https://openreview.net/forum?id=ryGs6iA5Km>.

Z.-Q. J. Xu, Y. Zhang, and Y. Xiao. Training behavior of deep neural network in frequency domain. In *Neural Information Processing: 26th International Conference, ICONIP 2019, Sydney, NSW, Australia, December 12–15, 2019, Proceedings, Part I*, page 264–274, Berlin, Heidelberg, 2019b. Springer-Verlag. ISBN 978-3-030-36707-7. doi: 10.1007/978-3-030-36708-4_22. URL https://doi.org/10.1007/978-3-030-36708-4_22.

Z.-Q. J. Xu, Y. Zhang, T. Luo, Y. Xiao, and Z. Ma. Frequency principle: Fourier analysis sheds light on deep neural networks. *Communications in Computational Physics*, 28(5):1746–1767, Nov. 2020. doi: 10.4208/cicp.OA-2020-0085. URL <https://global-sci.com/index.php/cicp/article/view/6896>.

D. Yin, R. Kannan, and P. Bartlett. Rademacher complexity for adversarially robust generalization. In K. Chaudhuri and R. Salakhutdinov, editors, *Proceedings of the 36th International Conference on Machine Learning*, volume 97 of *Proceedings of Machine Learning Research*, pages 7085–7094. PMLR, 09–15 Jun 2019. URL <https://proceedings.mlr.press/v97/yin19b.html>.

K. Yosida. *Functional analysis*. Springer Science & Business Media, 2012.

N. Yudin, A. Gaponov, S. Kudriashov, and M. Rakhuba. Pay attention to attention distribution: A new local Lipschitz bound for transformers. 2025. URL <https://arxiv.org/abs/2507.07814>.

M. D. Zeiler, D. Krishnan, G. W. Taylor, and R. Fergus. Deconvolutional networks. In *2010 IEEE Computer Society Conference on Computer Vision and Pattern Recognition*, pages 2528–2535, 2010. doi: 10.1109/CVPR.2010.5539957.

B. Zhang, D. Jiang, D. He, and L. Wang. Rethinking Lipschitz neural networks and certified robustness: a Boolean function perspective. In *Proceedings of the 36th International Conference on Neural Information Processing Systems*, NIPS ’22, Red Hook, NY, USA, 2022. Curran Associates Inc. ISBN 9781713871088.

C. Zhang, S. Bengio, M. Hardt, B. Recht, and O. Vinyals. Understanding deep learning (still) requires rethinking generalization. *Commun. ACM*, 64(3):107–115, Feb. 2021. ISSN 0001-0782. doi: 10.1145/3446776. URL <https://doi.org/10.1145/3446776>.

Z. Zhang, X. Shu, B. Yu, T. Liu, J. Zhao, Q. Li, and L. Guo. Distilling knowledge from well-informed soft labels for neural relation extraction. In *Proceedings of the AAAI Conference on Artificial Intelligence*, volume 34, pages 9620–9627, 2020.

S. Zheng, Y. Song, T. Leung, and I. Goodfellow. Improving the robustness of deep neural networks via stability training. In *2016 IEEE Conference on Computer Vision and Pattern Recognition (CVPR)*, pages 4480–4488, 2016. doi: 10.1109/CVPR.2016.485.

B. Zhou, A. Khosla, A. Lapedriza, A. Oliva, and A. Torralba. Learning deep features for discriminative localization. In *2016 IEEE Conference on Computer Vision and Pattern Recognition (CVPR)*, pages 2921–2929, 2016. doi: 10.1109/CVPR.2016.319.

D. Zhou, Z. Yu, E. Xie, C. Xiao, A. Anandkumar, J. Feng, and J. M. Alvarez. Understanding the robustness in vision transformers. In K. Chaudhuri, S. Jegelka, L. Song, C. Szepesvari, G. Niu, and S. Sabato, editors, *Proceedings of the 39th International Conference on Machine Learning*, volume 162 of *Proceedings of Machine Learning Research*, pages 27378–27394. PMLR, 17–23 Jul 2022. URL <https://proceedings.mlr.press/v162/zhou22m.html>.

Z. Zhu, J. Wu, B. Yu, L. Wu, and J. Ma. The anisotropic noise in stochastic gradient descent: Its behavior of escaping from sharp minima and regularization effects. In K. Chaudhuri and R. Salakhutdinov, editors, *Proceedings of the 36th International Conference on Machine Learning*, volume 97 of *Proceedings of Machine Learning Research*, pages 7654–7663. PMLR, 09–15 Jun 2019. URL <https://proceedings.mlr.press/v97/zhu19e.html>.